Development of active tumor targeting systems for delivery of siRNA and drugs into breast and colorectal cancer

by

Igor Moura Paiva

A thesis submitted in partial fulfillment of the requirements for the degree of

Doctor of Philosophy

in

Pharmaceutical Sciences

Faculty of Pharmacy and Pharmaceutical Sciences

University of Alberta

Abstract

Active targeting strategies have been pursued to improve the efficacy and safety of cancer therapeutics and theranostics. The significant benefit of tumor homing ligands conjugated to small molecules versus nanoparticle delivery systems in enhancing drug delivery to the tumor is still a matter of debate in the literature. The central hypothesis of this thesis was that ligand molecules specific to cancer cell-surface biomarkers, can enhance homing and interaction of drugs as well as nano-drug delivery systems with tumors leading to an increased therapeutic index for the incorporated drug. To test this hypothesis, in the first research project of this thesis, the biodistribution of a breast cancer-specific engineered peptide (C18.4DK) conjugated to Cy5.5 (C18.4DK-Cy5.5) was evaluated in mice carrying orthotopic breast MDA-MB-231 tumors, where a preferential accumulation of conjugated Cy5.5 in the tumor was observed, especially two hours after intravenous injection, with rapid clearance from all other organs except kidneys and liver. Next, we examined the validity of P18.4 peptide conjugation on polymeric micellar nanoplatforms, based on poly(ethylene oxide)-*block*-poly(ε-caprolactone-*grafted*-polyamines) (PEO-*b*-PCL-*g*-PA), for specific siRNA delivery to tumor versus normal cells. We also investigated the capacity of GE11 modified polymeric micelles based on PEO-PCL and its derivative PEO-poly(a-benzyl carboxylate-ε-caprolactone) (PEO-PBCL) in targeting epidermal growth factor receptor (EGFR) overexpressing colorectal cancer models making the comparison with plain or mock peptide modified micelles. For this purpose, traceable micelles were generated using two strategies: by attaching the fluorophore Cy5.5 into the PCL/PBCL block for near-infrared (NIR) imaging; or by incorporating a positron emission tomography (PET) contrast agent, i.e., ^{64}Cu, into the micellar shell-forming portion. Both imaging studies indicated that the EGFR-targeting peptide GE11 positively impacted nanoparticle accumulation into EGFR-expressing colorectal cancer (CRC) subcutaneous or orthotopic xenografts in mice. GE11 modification also enhanced the therapeutic activity of a novel inhibitor of DNA repair, denoted as A83B4C63, encapsulated in PEO-PBCL micelles in reducing the tumor burden in a PTEN negative CRC orthotopic tumor model via synthetic

lethality. Finally, modification of polymeric micelles with full-length monoclonal antibody ligands targeting EGFR (i.e., Panitumumab), or carcinoembryonic antigen-related cell adhesion molecule 6 (CEACAM6) was examined and shown to increase micellar association with both HCT116 colorectal cancer cellular populations (i.e., monolayer and spheroid cultures), respectively, when compared to the non-modified micellar counterparts. In conclusion, our results provided a consistent body of evidence showing that the use of tumor-targeting peptide and antibody-based ligands to be an efficient approach for enhancing specificity and delivery of therapeutic cargos (e.g., small molecules), or nanoparticles encapsulating small molecule drugs or siRNA, into breast tumor and CRC models. Nevertheless, the choice of the tumor-targeting ligand and cargo (nanoparticle, versus small molecule) affects the extent and kinetics of tumor interaction and accumulation.

Preface

Chapter two of this thesis has been published as Raghuwanshi, Y., Etayash, H., Soudy, R., Paiva, I.M., Lavasanifar, A., Kaur, K. (2017). **Proteolytically stable cyclic decapeptide for breast cancer cell targeting**. *J. Med. Chem.* 60, 4893-4903. First, second, and third authors were responsible for the *in vitro* work, while I was entirely responsible for the *in vivo* part, which was an independent study. Dr. Lavasanifar and Dr. Kaur were the supervisors and the ones who corrected the manuscript.

Chapter three will be submitted for publication as Paiva, I.M., Vakili, M.R., Ghasemi, N., Soudy, R., Kaur, K., Lavasanifar, A. **Towards development of nanocarriers for tumor cell-specific siRNA delivery**. Most of the experiments were carried out by me, excepting part of the GPC analysis (Ghasemi, N.), and peptide synthesis (Soudy, R.). Dr. Vakili and Dr. Lavasanifar contributed to the supervision and corrections of the manuscript.

Chapter four has been accepted with revisions to be published in Molecular Pharmaceutics (ACS, mp-2019-010434) as Paiva, I.M., Mattingly, S., Wuest, M., Vakili, M.R., Leier, S., Weinfeld, M., Lavasanifar, A., Wuest, F. **Synthesis and analysis of ^{64}Cu-labeled GE11-modified polymeric micellar nanoparticles for EGFR-targeted molecular imaging in a colorectal cancer model**. The radiolabelling work was performed by Mattingly, S., and Leier, S., while Wuest, M. was/will be responsible for the PET imaging. I was responsible for preparing the micellar nanoparticles, and I also did the *in vitro* work and most of the manuscript writing. Dr. Lavasanifar and Dr. Wuest contributed to their supervision, edits, and corrections.

Chapter five will be submitted for publication as Paiva, I.M., Sadat, S., Soleimani, A., Shrine, Z., Vakili, M.R., Paladino, M., Martin, G., Tabatabaei-Dakhili, S.A., Velázquez-Martínez, C.A., Jirik, F., Hall, D.G., Weinfeld, M., Lavasanifar, A. **GE11-modified polymeric micelles for targeted delivery of novel inhibitors of DNA repair to EGFR-expressing orthotopic colorectal cancer xenografts in mice**. This study was a multi-lab investigation. The research group from Dr. Dennis Hall (including Paladino, M.) contributed to the drug synthesis. The contribution of Dr. Carlos Velázquez-Martínez's lab (including Tabatabaei-Dakhili, S.A.) was regarding the analysis using molecular dynamics. Genetic modification of cancer cells and the development of orthotopic colorectal cancer mouse model were carried out in Dr. Frank Jirik's lab (including Martin, G.). I performed and/or led the main experiments in this study. Dr. Weinfeld and Dr. Lavasanifar were the supervisors and Dr. Lavasanifar also helped to prepare the manuscript.

Dedication

To my parents (José Rubéns and Nelita), wife (Keila), and daughter (Teresa),

whom have been my foundation and strength throughout this journey.

"... quaecumque vera, quaecumque pudica, quaecumque justa, quaecumque sancta, quaecumque amabilia, quaecumque bonae famae, si qua virtus, si qua laus disciplinae, haec cogitate."

(✝ *Philippians 4:8* ✝)

Acknowledgements

Firstly, I would like to express my deepest appreciation towards my supervisor, Dr. Afsaneh Lavasanifar, for her extraordinary example, guidance, and support during these five and a half years. The training with her has constantly shaped me towards excellence. I am really thankful to have had the opportunity to be at her side, learning little by little to become an independent researcher and a better person.

I would like to thank my supervisory committee members, Dr. Hasan Uludag and Dr. Raymond Lai, for their fruitful comments and suggestions throughout these years. I would also like to thank Dr. Raimar Loebenberg for his support, especially in the teaching assistantship.

I sincerely thank Dr. Michael Weinfeld for his kind guidance and Dr. Mohammad Reza Vakili for having introduced me to the chemistry world as well as for his assistance and valuable pieces of advice. I would specifically like to show my gratitude towards my labmates, Dr. Forugh, Nasim, Hanan, Sadat, Waleed, and many others, for their positive energy, helpful discussions, and enjoyable talks.

Lastly, a heartfelt thanks to my beloved wife, for always standing by my side. A huge thanks to all my family and friends, especially to my mom, dad, brother, and sister, for always providing encouragement and motivation. Without their unconditional support, none of this would have ever been possible.

Table of Contents

x

List of Tables

List of Figures

List of Abbreviations

aa	amino acid
Ab	antibody
ABCB1	ATP-binding cassette transporter
acPEO	acetal poly(ethylene oxide)
ACPYPE	AnteChamber PYthon Parser interface
ACUC	Animal Care and Use Committee
ADC	antibody-drug conjugate
ADCC	antibody-dependent cellular cytotoxicity
AGO2	argonaute protein 2
AMP	antimicrobial peptide
ANOVA	analysis of variance
BBB	blood brain barrier
BCA	Bicinchoninic acid
BCL	α-benzyl carboxylate-ϵ-caprolactone
BIRC5	baculoviral inhibitor of apoptosis repeat-containing 5
BiTE	bispecific T-cell engager
BOC	benzotriazol hexafluorophosphate
bp	nucleotide base-pair
bsAb	bi-specific heterodimeric antibody
BSC	best supportive care
CAR-T	chimeric antigen receptor T-cells
Cas9	CRISPR-associate nuclease 9
CCAC	Canadian Council on Animal Care
CD	cluster of differentiation
$CDCl_3$	deuterated chloroform
CDR	complementarity-determining region
CEACAM6	carcinoembryonic antigen-related cell adhesion molecule 6
C/EBPα	enhancer-binding protein alpha
CH	constable heavy domain
CMC	critical micellar concentration

CPP	cell penetrating peptide
CRC	colorectal cancer
CRISPR	clustered regularly interspaced short palindromic repeats
crRNA	CRISPR ribonucleic acid
CSC	cancer stem-like cells
CTL	cytotoxic T-cell
DCC	N,N-dicylcohexyl carbodiimide
DCM	dichloromethane
DFS	disease-free survival
DIPEA	N,N-diisopropylethylamine
DLS	dynamic light scattering
DMF	N,N,-dimethylformamide
DMAc	N,N-dimethylacetamide
DMSO	dimethyl sulfoxide
DNA	deoxyribonucleic acid
dn/dc	refractive index increment
Dox	doxorubicin
DPBS	Dulbecco's phosphate-buffered saline
DP	degree of polymerization
DT	N,N-dimethyldipropylenetriamine
ECGS	endothelial cell growth supplement
ECM	tumor extracellular matrix
EDV	EnGeneIC^{TM} Dream Vector
EE	encapsulation efficiency
EGFR	epidermal growth factor receptor
EGM	endothelial cell growth media
EPR	enhanced permeation and retention effect
Fab	antigen-binding fragment
FAM	5-carboxyfluorescein
FBP	folate-binding protein
FBS	fetal bovine serum
Fc	crystallisable fragment

FcγR	Fc gamma receptor
FDA	Food and Drug Administration (United States of America)
FN3	fibronectin type III domain
GnRH	gonadotropin-releasing hormone
GPC	gel permeation chromatography
GRB2	growth factor receptor-bound protein 2
ΔG^0	change in free energy
hcAb	heavy chain-only antibody
HCTU	hexafluorophosphate
hEGF	human epidermal growth factor
HER2	human epidermal growth factor receptor 2
HIV	human immunodeficiency virus
HK	high molecular weight kininogen
HOBt	hydroxybenzotriazole
HUVEC	human umbilical vein endothelial cells
^{1}H-NMR	proton nuclear magnetic resonance
Ig	immunoglobulin
kcps	kilo counts per second
K_D	constant of dissociation
kDa	kilo daltons
KRT1 / K1	keratin-1
mAb	monoclonal antibody
MALDI-TOF	matrix-assisted laser desorption ionization time-of-flight
MAP	maximum a posteriori
MBL	mannose-binding lectin
MCL-1	myeloid cell leukemia-1
MD	Molecular Dynamic
MEGM	mammary epithelial cell medium
MFI	mean/median fluorescence intensity
MIP	maximum intensity projection
miRNA	micro ribonucleic acid
MMPBSA	molecular mechanics Poisson-Boltzmann surface area

Mn	number average molecular weight
mRNA	messenger ribonucleic acid
MTT	3-(4,5-Dimethylthiazol-2 yl)-2,5-diphenyltetrazolium bromide
Mw	weight average molecular weight
MWCO	molecular weight cut-off
NEAAs	nonessential amino acids
NHS	N-hydroxysuccinimide
NIR	near infrared
NK	natural killer cells
NMM	N-methylmorpholine
NOTA	2-S-(4-aminobenzyl)-1,4,7-triazacyclononane-1,4,7-triacetic acid
NP	nanoparticle
PA	polyamines
PARP	poly(ADP-ribose) polymerase
PDC	peptide-drug conjugate
PDI	polydispersity index
PD-1	programmed cell death protein 1
PD-L1	programmed cell death ligand 1
PEG-*b*-PLA	poly(ethylene glycol)-*block*-poly(lactic acid)
PEO-*b*-PBCL	poly(ethylene oxide)-*block*-poly(α-benzyl carboxylate ε-caprolactone)
PEO-*b*-PBCL-*b*-PPC	PEO-*b*-PBCL-*block*-poly(α-propargyl carboxylate-ε-caprolactone)
PEO-*b*-PCL	poly(ethylene oxide)-*block*-poly(ε-caprolactone)
PEO-*b*-PCL-*b*-PPC	PEO-*b*-PCL-*block*-poly(α-propargyl carboxylate-ε-caprolactone)
PET	positron emission tomography
PFS	progression-free survival
P-gp	P-glycoprotein
PhSiH3	phenylsilane
PLC	phospholipase C-g1
PME	particle mesh Ewald
PMNP	polymeric micellar nanoparticle
PMSF	phenylmethylsulfonyl fluoride
PNKP	polynucleotide kinase/phosphatase

PSMA	prostate-specific membrane antigen
PTEN	phosphatase and tensin homologue
RAM	Rink amide resin
ra-siRNA	repeat-associated siRNA
RES	reticuloendothelial system
RISC	RNA-induced silencing complex
RITA	RNA-induced transcriptional activation
RMSD	root mean square deviation
RMSF	root mean square fluctuation
RNAi	RNA interference
ROI	regions of interest
RP-HPLC	reversed-phase high-performance liquid chromatography
RT-PCR	real-time polymerase chain reaction
saRNA	small activating ribonucleic acid
scnRN	scan ribonucleic acid
SCR	scramble sequence
SD	standard deviation
SDS	sodium dodecyl sulfate
SDS-PAGE	sodium dodecyl sulfate polyacrylamide gel electrophoresis
SELEX	systematic evolution of ligands by exponential enrichment
SEM	standard error of the mean
shRNA	short hairpin ribonucleic acid
SH3	sarcoma-homology 3
siRNA	small interfering ribonucleic acid
SLS	static Light Scattering
SOS1	son of sevenless homolog 1
$Sn(Oct)_2$	stannous octoate
SP	spermine
SPPS	solid phase peptide synthesis
SPECT	single-photon computed tomography
SUV	standardized uptake value
TAA	tumor-associated antigen

TAT	viral transactivator of transcription
TFA	trifluoroacetic acid
TGF-α	transforming growth factor-alfa
THF	tetrahydrofuran
TIPS	triisopropyl silane
TLR	toll-like receptors
TME	tumor microenvironment
tncRNA	tiny non-coding ribonucleic acid
TNF	tumor necrosis factor
tracrRNA	trans-acting crRNA
TRAIL	tumor necrosis factor (TNF)-related apoptosis-inducing ligand
TPGS	D-alpha-tocopheryl polyethylene glycol succinate
$t_{1/2}$	half-life
scFv	single-chain variable fragment
VEGF	vascular endothelial growth factor
VH	variable heavy domain
VHH	variable heavy homodimers chain in camelids
VL	variable light domain
VNAR	variable new antigen receptor in cartilaginous fish
ZP	ζ-potential

Chapter One

Introduction

1.1 Overview of tumor microenvironment

The word "tumor" is originated from Latin and means swelling;[1] however, solid tumors are more than simply growing masses of proliferating cancer cells. Instead, they are complex tissues composed of intricate three-dimensional architecture, containing multiple distinct cellular types that participate in heterotypic interactions with one another. Besides cancer cells (i.e., parenchymal compartment), tumor microenvironment (TME) is also composed of a stromal compartment that comprises endothelial-based cellular structures, including arteries, veins, and capillaries, as well as endothelial-related cells, such as lymphatics. Pericytes represent another example of non-cancerous cells in tumors, normally found wrapping around endothelial tubing of blood vessels. Cancer-associated fibroblasts provide structural support to epithelial tissues as well as myofibroblasts. Additionally, inflammatory immune cells, such as natural killer (NK), mast, and myeloid dendritic cells, macrophages, T- and B-lymphocytes, neutrophils, have been extensively reported within tumoral tissues. Though the profile of cell composition and/or infiltration of those cells is highly variable.[2,3]

Tumor extracellular matrix (ECM) is made up of soluble components (e.g., growth factors and metabolites) and by a network of fiber biopolymers, such as proteoglycans, glycoproteins, collagen, elastin, fibronectin, and other elements. Stromal stiffness consists of a classic characteristic of tumors, which can greatly influence the reprogramming of cancer cells. A lax and porous ECM has been correlated with better prognosis and early stages in cancer development, whereas the increase in stromal rigidity has been tightly associated with higher chances of cancer cell migration and poor response to therapies. In very stiff tumor ECM, the interstitial pressure is majorly elevated, leading to frequent blood extravasation, hemorrhage, and formation of hypoxic and necrotic areas. Moreover, significant desmoplasia is observed in the latter scenario, especially due to the increase in the content of type I collagen and glycoprotein, cross-linking of reticulin, and decrease in proteoglycans, resulting in very low

diffusion rates of chemotherapeutic agents into the tumor core in comparison with tumors containing soft ECM.[4,5]

The impact of TME in modulating tumor development and progression has been proved to be pivotal for maintaining cellular malignancy. Bussard and Smith[6] have reported that non-metastatic (HTB-132™ cells) and metastatic (HTB-26™ cells) breast cancer cells transplanted into a healthy mammary gland microenvironment (CRL-4010™ cells) were redirected to behave without forming tumors and, at the same time, contributing to the healthy tissue development. Cancer cell populations within tumor are known to be quite heterogeneous, from a genetic point of view, and the presence of subpopulations of cancer stem-like cells (CSC) confers even more diversity to this pathological condition. CSCs are extremely plastic, which means that a single, genetically homogeneous population of cells within a tumor may be phenotypically heterogeneous due to the presence of cells in distinct stages of differentiation. Some biomarkers for identification of CSC subsets in a cell population, for example, are CD44, CD133, and CD66c. In the context of chemotherapy resistance, CSCs are mainly responsible for cancer relapse, especially because of those subpopulations in the sleep-like quiescent state, which are capable of restoring the tumor development after a while. Therefore, given the complexity of cancers, success in curbing this disease cannot be achieved by a straightforward avenue, so that diversified therapeutic and diagnostic strategies may be one of the main keys for improving outcomes.[2,5,7]

1.2 Therapeutic and homing agents in oncology

1.2.1 Small molecules

In principle, small molecules can bind to proteins, nucleic acids, polysaccharides, and lipids, and this binding has the potential to be used for interference into biological processes, blocking or activating the function(s) in which the target is involved. However, the vast majority of successful drugs rely on the binding into proteins, especially because of the difficulty to obtain potent compounds against the latter nucleic acids, polysaccharides, and lipids. Prominent protein-based drug targets comprise enzymes, receptors, and ion channels. To be clinically relevant, small-molecule drugs have to present high selectivity and affinity to the proposed protein, with a constant of dissociation (K_D) in nanomolar range or lower. There is a relationship between the energy of the interaction and the K_D, described as the following:

$$\Delta G^0 = -RT\ln(1/K_D)$$

Where ΔG^0 is the change in free energy due to the interaction, R is gas constant (1.99 cal/mol degree), and T is the temperature in Kelvin.[8–10]

Many characteristics make these compounds advantageous, including their relatively simpler and cheaper production when compared to biologics, and feasible generation of high-throughput chemical libraries that allow the identification of more potent and selective drug candidates to known or new molecular targets for cancer treatment. On the other hand, the main drawback of conventional drugs consists of the fact that they are not equipped to receive any feedback from the body. Thus, they keep acting into the patients regardless of the physiological condition of different organs and/or tissues. The loading of small molecules into nano-sized delivery systems significantly improves this condition, since the treatment is passively directed to the site of disease and distribution to healthy regions are restricted. Tumors, inflamed sites, and liver are the most favorable locations for directing nanoparticle-based treatments.[9,11] In the following sections, examples about how small molecule drugs, applied in cancer treatment, can benefit macromolecular or nano-delivery systems will be briefly discussed.

1.2.1.1 Agonists and partial agonists

Both classes of drugs are defined as compounds that stimulate the intrinsic activity of a specific protein, which in most of the cases, corresponds to an enzymatic-based function. The use of this approach, using small molecules, is not as common as the employment of antagonistic compounds that block their targets, instead.[12] For cancer treatment, agonists of toll-like receptors (TLR), especially TLR3, 4, 7/8, and 9, have been included in a list containing therapeutic agents with the highest potential to treat cancer, by the US National Cancer Institute. Imiquimod, marketed in a cream formulation (imiquimod 5%, Aldara®), is a synthetic imidazoquinoline that targets TLR7/8. Aldara® is especially indicated in cases of primary skin malignancies (i.e., superficial basal cell carcinoma) and premalignant conditions (i.e., actinic keratosis). Its antitumor effect is related to the inhibition of angiogenesis and natural killer cell-mediated cytotoxicity. Local TLR7 activation by imiquimod can alter the tumor microenvironment and increase inflammatory processes in the region, with promising cancer immunotherapeutic properties.[13]

The activation of receptors specific for tumor necrosis factor (TNF)-related apoptosis-inducing ligand (TRAIL) by employing small molecules has also been identified as a promising anticancer treatment. Targeting the death receptors DR4 and DR5 (TRAIL-receptor 1 and 2, respectively) has shown to selectively eliminate tumor cells while sparing normal ones since, although these two receptors are usually expressed on a wide variety of normal and tumor cell types, a preferential induction on tumor cells have been robustly detected. Bioymifi, A2C2, and ONC201 are examples of small compounds that are capable of inducing apoptosis through the agonistic effect on DR5.[14–16]

1.2.1.2 Antagonists

The use of therapeutic antagonists is much more common in cancer treatment than agonists. Antagonists can be categorized based on their binding site on the target protein and its relation to the protein's natural ligand (e.g., competitive, non-competitive, antagonisms following Gaddum and Schild

equations), nature of the binding (e.g., reversible, irreversible), and function of the targeted protein (e.g., dehydrogenase, topoisomerase inhibitors). Despite their abundance, improvement in the safety and efficacy of existing drugs and the discovery of new compounds is extremely difficult. Most inhibitors act by binding to their targets at similar regions to endogenous ligands or substrates (i.e., at the catalytic domain), in a competitive fashion; however, this is known to provide a limited approach for effective long-term inhibition. In general, tumors rapidly develop resistance towards ATP competitive small molecules, such as Erlotinib, a reversible inhibitor of epidermal growth factor receptor (EGFR), whereas treatment with the EGFR inhibitor Afatinib prevents acquired resistance mechanisms due to its covalent bond with the receptor. Drug development programs are established with specific targeted metabolic pathways and/or individual enzymes for targeting and, as a rule, the higher the drug potency, the lower the dose required to achieve efficacy and, consequently, the risk of side effects are reduced.[17–21]

1.2.1.3 Small molecules with tumor-homing properties

One of the main hurdles of traditional cancer treatments involves the destruction of healthy tissues with high replicating rates, such as gastrointestinal epithelia, hair follicles, and other non-cancerous regions. Taking advantage of the affinity that some small molecules possess towards overexpressed receptors on cancer cells, targeted therapies provide more selectivity to tumors, avoiding off-targets. The specific role of tumor-homing molecules is to enhance receptor-mediated endocytosis of cytotoxic agents, which are conjugated or loaded in delivery systems bearing these entities. Many nutrients indispensable for cell survival, such as folate, cobalamin, and biotin have been extensively employed for this purpose since their receptors are usually upregulated in different cancers.[22,23] Moreover, some analogs of N-acetylaspartyl glutamate, which is a natural substrate of prostate-specific membrane antigen (PSMA), have been used as homing ligands for tumor imaging and targeted treatments.[24]

1.2.1.4 Phototherapeutic approaches

Organic small molecules constitute a major representative of photodynamic therapy agents, and more recently, their photothermal therapeutic properties have also been explored. Both strategies are sophisticated methods to locally and specifically eliminate tumors. The activation of photosensitizers by a specific light source, with an appropriate wavelength and energy, triggers the generation of a harsh environment in the tumor and tumor vicinities through either oxygen reactive species or hyperthermia. In general, the use of compounds that excite at long-wavelength lights (> 700 nm), more specifically at the near-infrared (NIR) region, are ideal for *in vivo* studies, especially because of their high capacity to pass through tissues and reach deep cells and/or organs. Although Cy5.5 fluorophore does not present any phototherapeutic activity, its property to be excited even in deep tissues has been widely explored for biomedical imaging purposes, since it confers high-resolution measurements in small animal models of labeled delivery systems for biodistribution investigations. Furthermore, several oncologic photodynamic agents are already available in clinics, namely porphyrin-based compounds, aminolevulinic acid, and phthalocyanines.[25–27] More recently, an organic based-molecule also gained approval for photothermal therapy from the U.S. Food and Drug Administration (FDA). Indocyanine green, a cyanine dye (Cy7) that absorbs at 700–900 nm, has been able to increase the temperature up to 48.5 °C at the tumor site, by directed NIR light irradiation, leading human hepatocellular carcinoma xenografts in mice to cell apoptosis.[28]

Small molecules represent a versatile class of therapeutics, as briefly presented in this section. In the current era of biologics, led by antibody-based biopharmaceutical companies, the potential of this class of molecules that were the first ones employed in cancer therapy is far from being saturated. With the combined advances in computing simulation and high throughput screening methodologies for drug

discovery, together with the dynamic progress in cancer biology, encouraging outcomes can still be expected for improving patient's condition.[29,30]

1.2.2 Peptides

Short sequences of amino acid residues have profoundly impacted our current modern pharmaceutical industry, back in the first half of the 1900s. A good example is insulin (51-mer peptide) that was considered a "miracle drug", and widely contributed to advancements in the field of biologics.[31] Peptides are considered great alternatives to be used for cancer therapy. They tend to bind stronger to the protein target than small molecules, and at the same time, do not have issues regarding immunogenicity and 3D-folding stability, that is observed for protein and antibody-based therapeutics. Many antimicrobial peptides (AMPs) from naturally-occurring defense systems, as well as their synthetic analogs, have been identified with anti-cancer activity, such as cathelicidin, pleurocidin, buforin, and others. Their mechanism of cytotoxicity is related to the formation of pores in plasma and mitochondria membranes of malignant cells.[32,33]

Linear peptides that contain 2–10 amino acid residues are known to be flexible structures in solution, whereas once the length of linear peptides extends to 10-20, secondary structures begin to be formed, such as α-helices, turns, and β-strands. The short *in vivo* half-life of peptides is one of the major limitations among peptidic sequences applied for cancer therapy and diagnosis. Their clearance from the bloodstream and enzymatic digestion in the blood, kidneys and/or liver can take place within minutes to hours after intravenous administration. Some strategies have successfully been implemented to improve the pharmacokinetic profile of some peptidic sequences, including pegylation, cyclization, and introduction of D-amino acids.[34–36]

1.2.2.1 Engineered peptides

Synthetic and engineered peptidic sequences can be designed for mimicking naturally occurring hormones, and additionally, for improving peptide stability and binding affinity. Somatostatin analogs illustrate such strategies in a very interesting way. Somatostatin is a natural peptide, composed of 14 amino acid residues (AGCKNFFWKTFTSC), and has a very rapid half-life (~ 3 min). Its 8-mer analog octreotide (fCFwKTCT-ol), available as Sandostatin®, possesses longer half-life than its precursor (up to 2 h), mainly because of the incorporation of two D-amino acid residues (lower-case letters), and the replacement of a L-threonine in the C-terminus by a L-threninol residue (i.e., carboxylate end was substituted by an aldehyde group), as depicted in **Figure 1.1**. Cysteine residues were also maintained for the molecule cyclization via a disulfide bond, as well as the essential amino acids for specific binding to somatostatin receptors. The cytostatic activity of octreotide has been observed against several cancers, including gastroenteropancreatic- and neuro-endocrine ones, known to overexpress somatostatin receptor subtype II on their plasma membrane.[37,38]

Analogs for gonadotropin-releasing hormone (GnRH, 10-mer) is another example of engineered peptides, used in oncology, that were developed for enhancing stability against degradation. More interestingly, in this case, the structural modifications were carried out to produce peptidic agonists (leuprolide or Lupron®) and antagonists (Degarelix or Firmagon®). In the first sequence, the similarity with the parental sequence (GnRH type I) was maintained, while in the latter one, more amino acid residues were modified, as described by Henninot, Collins, and Nuss.[31] Both peptides are employed in clinical practice for treating cancer, particularly against hormone-responsive prostate cancer.[31,34]
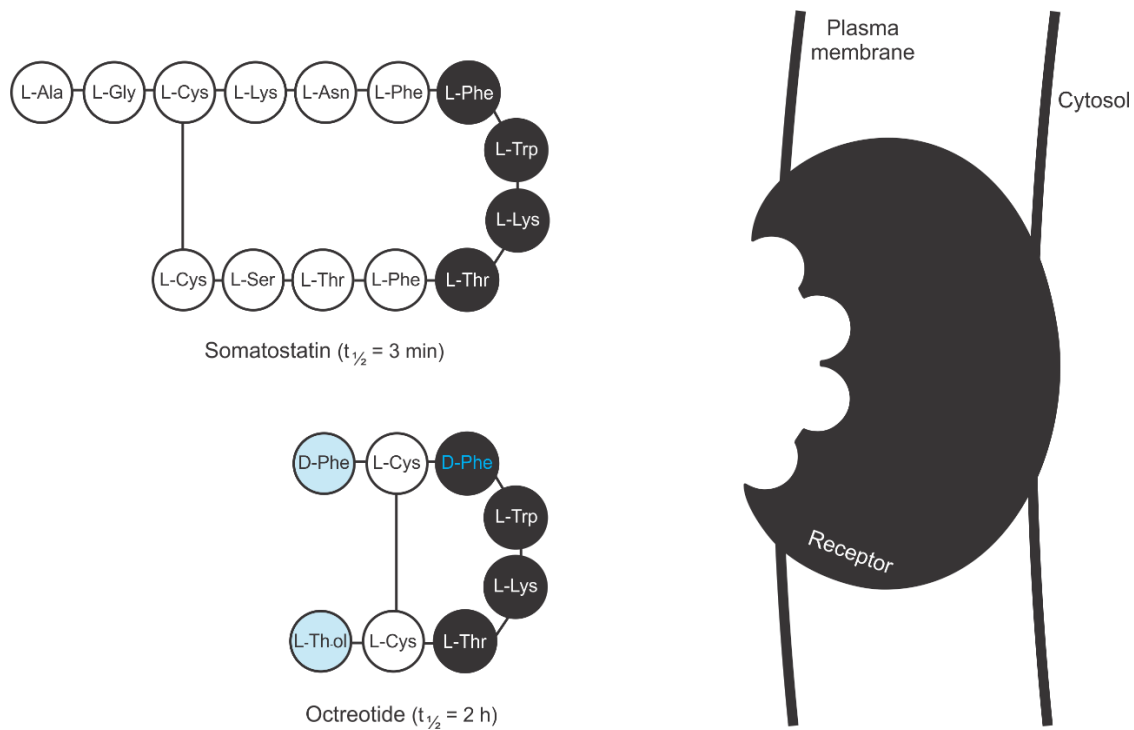
Figure 1.1. Scheme representing structural similarities between Somatostatin (top left panel) and its analog Octreotide (bottom left panel). Both peptides can interact with Somatostatin receptor (at the right) through the highlighted amino acid residues (in black). The engineered peptidic sequence of Octreotide is more stable in biological fluids, resulting in a higher half-life ($t_{1/2}$) in blood circulation. (Adapted from Reference 38).

1.2.2.2 Peptide Vaccines

Antitumor peptide vaccines are derived from tumor-associated antigens (TAAs), that are capable of inducing tumor-specific cytotoxic T-cell (CTL)-mediated cytolysis. Additionally, the immune response to these peptide vaccines stimulates the production of memory T cells, offering the promise of long-lasting immune protection, which translates into disease-free survival (DFS) for patients. Accumulating evidence has indicated that this novel therapeutic approach is capable of circumventing the poorly immunogenic and highly immunosuppressive nature of most tumors, though some studies have also pointed out its

limitations in providing clinical benefits for patients. One of the challenges in this area may be the concomitant deactivation of tumor-derived immunosuppressive factors that allow success in disease development. Some studies have shown that the tumor progression is promoted when tumors are transplanted in immunocompetent animals, while tumor development seems to be much delayed or lacking in immunodeficient hosts.[39–42]

Recently, a phase I/IIa trial, using a peptide vaccine derived from folate-binding protein (FBP), has indicated to be effective in preventing recurrence in high-risk ovarian and endometrial cancer. The elevated expression of FBP among malignant cells, but not in normal tissues, together with the fact that FBP is highly immunogenic, makes this candidate an excellent target for immunotherapy. Patients received the denoted E39 peptide vaccine, a 9-mer peptidic portion of FBP (EIWTHSYKV, position 191-199). Because of the concern regarding tolerance and possible reduction in immunologic memory over time, an attenuated version (i.e., less immunogenic) of that peptide was also given, called E39' or J65 (EIWTFSTKV). Interestingly, this study concluded that predefined groups of subjects need to be selected for optimal effectiveness, since patients who completed therapy for primary disease (low FBP), presented an impressive clinical outcome, with a high rate of DFS (90%). On the contrary, patients treated for recurrent disease showed no benefit, even at higher doses.[40]

1.2.2.3 Tumor-homing peptides

As previously mentioned for small molecules, the main characteristic of peptidic sequences with affinity to cancer markers is not essential to activate or block the targeted receptor but enhance cell uptake of therapeutics. The first generation of tumor-homing peptides was identified for targeting α_v integrins and aminopeptidase N receptors, via RGD and NGR motifs, respectively. Two basic strategies have been used for selecting relevant sequences. The first one focuses on the screening of peptidic sequences capable of binding to a given cell population, without targeting any specific receptor. The

second one uses a purified protein target, which is known to be relevant and overexpressed on the desired type of tumor.[43]

1.2.2.4 Cell-penetrating peptides

Functional cell membranes are complex structures basically composed of a bilayer of phospholipids with associated proteins,[44] and are pivotal for selective diffusion of cargoes into the cell, serving as a barrier for dangerous particles (e.g., pathogens) and allowing the internalization of beneficial substances (e.g., nutrients). Cell-penetrating peptides (CPPs) possesses an impressive ability to pass through cell membranes, and their transduction activity may have different mechanisms. According to the transient-pore model, CPPs are considered to directly penetrate through the formation of either "toroidal" or "barrel-stave" pores. In the carpet-like model, the interaction between CPPs and plasma membranes is based on their charges, leading to a transient increase in membrane fluidity. The inverted-micelle mechanism relies on the formation of invaginations from the lipid bilayer, followed by the peptide engulfment.[45]

CPPs are classified in cationic, amphipathic, and hydrophobic sequences. Cationic CPPs are abundant in arginine and lysine amino acid residues, and present an excellent affinity to the plasma membrane, as well as to negatively charged glycoproteins on the cell surface. A significant amount of peptidic sequences belonging to this class are derived from the transactivator of transcription (TAT) protein, discovered from human immunodeficiency virus (HIV). In 1997, the classical truncated version of TAT (RKKRRQRRR) that enabled cell entry was identified.[46]

Amphipathic CPPs, as the name describes, contain hydrophobic portions, which are usually formed by the presence of valine, alanine, leucine, and isoleucine, and polar regions composed of cationic or anionic amino acid residues. Several sequences in this class are an assembly of peptides, different in nature, through covalent coupling (e.g., multiple antigen peptides). Amphipathic peptides in high

concentrations near the membrane surface, tend to form transient secondary structures, which may favor their cell uptake through different mechanisms.[47,48]

Hydrophobic CPPs present a smaller number of identified sequences compared to cationic and amphipathic peptides, and they are also less studied. Predominantly, they are formed by nonpolar amino acids, so that their translocation across the cell membrane may be driven by an energy-independent pathway.[48]

In conclusion, some important classes of peptides have been presented here, highlighting a wide variety of roles in cancer treatment and detection. This class of molecules is limited by its often poor pharmacokinetic profile as well as larger molecular weight and lower conformational flexibility compared to small molecules. Even so, therapeutic and diagnostic agents based on peptidic sequences are still very attractive compounds because of their higher specificity towards the selected target. Studies on peptidomimetics have offered a great alternative for the development of molecules that retain the peptide specificity, and at the same time, possessing an improved capacity to cross cellular membranes, which is the case for sequences rich in charged amino acid residues.[49,50]

1.2.3 Nucleic acids

The specific base-pairing (bp) between purines and pyrimidines was first proposed by Watson and Crick in 1953, who also reported the alpha-helix conformation of double-stranded nucleotides.[51] Alternatively, other non-canonical nucleotide structures have also been observed, such as the one identified by Karst Hoogsteen, which allows the formation of triple-stranded molecules. Recently, Conde *et al.*[52] have reported on a self-assembled RNA-triple-helix hydrogel scaffold for therapeutically regulating the expression of proteins in the tumor microenvironment. Therapeutics based on nucleic acids for cancer treatment have been enticing drug developers, especially because of the potency and versatility of such molecules, the prospect of suppressing genes encoding proteins that are "undruggable" by classical small molecules, and the possibility for making "programmable" therapeutics that can be re-targeted without changing *in vivo* pharmacokinetics. However, one of the main obstacles for naked nucleotides (i.e., without the aid of delivery systems) to reach cellular cytosol and/or nucleus relies on their anionic charge, conferred by the phosphate groups throughout their backbone, which makes the interaction with anionic phospholipids on the plasma membrane very challenging. Therefore, advancements in this area have been tightly associated with the development of efficient and safe biomaterials for this purpose.[53–55]

1.2.3.1 Messenger ribonucleic acid (mRNA)

This category of molecules (~ 1,000–15,000 bp) has been extensively characterized and is one of the major players in the central dogma of molecular biology that states: DNA is transcribed into mRNA, which is translated into protein.[56] One of the first exogenous mRNA molecules to be successfully delivered to cells was in 1978, through a nano-formulation based on large unilamellar liposomes.[57] mRNA therapeutics holds the potential to revolutionize protein replacement therapies and cancer vaccination. In its most straightforward application, mRNA can be transfected to the cell target and, after reaching the cytosol, induce the protein synthesis that its nucleotide sequence is encoded for. In comparison with

protein therapeutics for protein replacement, mRNA can be more effective on a per molecule basis, since one mRNA molecule can generate many copies of the protein over hours or days. A most clinically advanced application of mRNA drugs is their potential to serve as an alternative to traditional vaccination strategies. Many clinical studies have already demonstrated that transfection of mRNAs, encoding tumor-associated antigens (TAAs), to dendritic cells can efficiently elicit cytotoxic T cells in order to target and eliminate cancers. The biopharmaceutical company BioNTech GmbH, for instance, has six different formulations under clinical trials using mRNA molecules encoding one or more TAAs to treat a variety of cancers, including melanoma, breast, lung, bladder, and squamous carcinoma.[58,59]

1.2.3.2 Non-coding RNAs

Post-transcriptional gene downregulation via RNA interference (RNAi) is an important endogenous process for animals, plants, and microorganisms, being part of the regulatory machinery for many biochemical, cellular pathways.[60] MicroRNAs (miRNAs) are noncoding RNAs, ranging from 19–25 bp in length. Endogenously, they are initially produced as a long and imperfect hairpin transcript, called primary miRNA (~ 80 bp). Then, still in the nucleus, this single-stranded nucleotide is shortened by the action of nucleases in a microprocessor complex, finally generating the miRNA that bears only one stem-loop hairpin, and a 2-bp overhang at the 3' end for its exportation to the cytosol. Subsequently, the molecule is further processed by Dicer nuclease, producing double-stranded RNA. The dsRNA associated with a protein complex containing dicer, argonaute, and transactivating response RNA-binding protein, forming the RNA-induced silencing complex (RISC), which is responsible, ultimately, for cleaving the targeted mRNA.[61,62] Taking advantage of this naturally-occurring RNAi pathway, numerous synthetic RNA therapeutics have been employed in clinical trials or as FDA-approved medicines, namely short interference RNA (siRNA),[63] miRNA (miR),[64] and short hairpin RNA (shRNA).[65] So far, none of these types of therapies has reached the market for cancer treatment, though two siRNA-based medicines have

recently been approved. Patisiran® (Alnylam Pharmaceuticals Inc.) is the first-ever therapeutics based on RNAi being indicated to treat transthyretin (TTR) amyloidosis by reducing the levels of a mutated protein that accumulates and impacts heart and nerve system. Subsequently, Givosiran® (Alnylam Pharmaceuticals Inc.) also reached the market, indicated for acute hepatic porphyria, leading to downregulation of delta-ALA synthase 1 and reduction of its neurotoxic metabolites.[66,67]

Contrarily to RNAi function, small activating RNA (saRNA) is a type of double-stranded RNA that induces gene expression. Similar in length to RNAi molecules (i.e., ~ 21 bp), saRNAs target specific promoter regions in the DNA in order to stimulate transcription of the desired gene. Their canonical mechanism of upregulation starts with the binding to argonaute 2 (AGO2) in the cytoplasm. Then, AGO2-bound saRNA is translocated into the nucleus and binds either directly to DNA or chromatin-bound RNA. A protein complex, called RNA-induced transcriptional activation (RITA), is formed for inducing transcription. Since the identification of this novel concept, saRNAs have quickly emerged as a powerful oligotherapeutic tool for cancer therapy.[68] Currently, there is an ongoing clinical trial for hepatocellular carcinoma treatment using saRNA targeting CCAAT enhancer-binding protein alpha (C/EBPα), which is a known tumor suppressor player. Preclinical studies on a cirrhotic rat model with multifocal liver tumors showed that the tumor burden decreased by 80% after the increase in C/EBPα levels by treatment with saRNA, which was injected three times intravenously in a polyplex-based formulation.[69,70]

Furthermore, different families of non-coding small RNAs have been found in various organisms, especially among *D. melanogaster* and *C. elegans*. Many of these molecules, such as repeat-associated siRNAs (ra-siRNAs), tiny non-coding RNAs (tncRNAs), scan RNAs (scnRNAs), and others, were found to be originated from transposons, viruses, and repetitive sequences. So far, none of them has been observed in mammals, and there is a possibility that some of these novel RNAs may have a different mechanism of action compared to the traditional microRNAs. Thus, new avenues for alternative targeting strategies can be explored by further understanding their functions.[71,72] A successful example that confirms the potential

of those poorly known RNAs is the clustered regularly interspaced short palindromic repeats (CRISPR) technologies.

CRISPR/Cas9 type II system was first identified as an adaptive immune mechanism from *Streptococcus pyogenes*, and then successfully implemented in mammalian cells as a powerful gene-editing tool, especially due to their relative simplicity compared to CRISPR/Cas types I and III.[73,74] CRISPR associate nuclease 9 (Cas9) contains a CRISPR RNA (crRNA), that guides the recognition of the target site for the site-specific double-stranded DNA break, subsequent gene insertion or deletion, and DNA repair. However, crRNA needs to be activated in a process mediated by trans-acting crRNA (tracrRNA). More recently, a novel and simpler type II mechanism of genome editing was identified in *Prevotella disiens* and *Francisella novicida*, denoted CRISPR/Cpf1 or CRISPR/Cas12a. In this case, Cas12a is only dependent on the guidance of crRNA for the site-specific cleavage, not requiring the mediation of tracrRNA.[73,75]

The first clinical trial that employed CRISPR/Cas9 was conducted by a team led by the oncologist Lu You at the Sichuan University (China),[76] aiming for the treatment of metastatic non-small-cell lung cancer. In that study, immune cells from the recipient's blood were extracted, cultured, and the gene encoding programmed cell death protein 1 (PD-1) was disabled. Then, they were re-introduced intravenously to the patient. The outcome of this trial was overall considered successful regarding the safety of the treatment, though some adverse effects such as acute fever and hepatic dysfunction were reported.[77] The axis PD-1/ PD-ligand 1 (PD-L1) has been considered the most promising target for checkpoint inhibitor therapy, given its notorious clinical efficacy of monoclonal antibodies anti-PD-1 or anti-PD-L1 in the treatment of advanced cancers. PD-1 is mainly expressed on the plasma membrane of T cells, and upon the binding with PD-L1, usually overexpressed in malignant cells, PD-1 is phosphorylated, and signaling mediated by this protein is inhibited, which would lead to T cells activation and subsequent tumor elimination. Similar *ex vivo* gene-editing techniques using CRISPR/Cas9 on extracted immune cells have been assessed in other clinical trials.[76,78,79]

1.2.3.3 Deoxyribonucleic acid (DNA)

Compared to the transient effect of the aforementioned therapeutic RNAs, DNA-based medicines are remarkable in the capability of providing a more stable genetic modification in the transfected cells. Both therapeutics based on DNA and mRNA molecules present a similar function, which consists of changing the gene expression with comparable levels of efficiency. However, while DNA has the disadvantageous requirement for nuclear localization, mRNA is a much more labile compound, and with higher immunogenicity.[80] Plasmid constructs inserted into the cellular nucleus start producing the designed transcripts, which can be noncoding RNAs in the case of silencing strategies, or mRNA sequences encoding a specific protein of interest. Among different cellular players to be targeted in cancer, there is a trend for silencing anti-apoptotic proteins, and on the opposite direction, for increasing the expression of pro-apoptotic ones. Apoptosis is a programmed cell death that can be mainly mediated by mitochondria (i.e., intrinsic pathway) and by death-inducing receptors (i.e., extrinsic pathway). For instance, many papers have shown that delivery of plasmids encoding shRNA against survivin (**Figure 1.2**), also called baculoviral inhibitor of apoptosis repeat-containing 5 (BIRC5), effectively contribute for treating cancers as monotherapy or in combination with drugs.[81–85] Hu *et al*.[81] have shown interesting preclinical data using this strategy on ovarian cancer. A polyplex system composed of β-cyclodextrin covalently grafted along the backbone of polyethyleneimine was developed for co-delivery of paclitaxel and plasmid encoding RNAi targeting BIRC5. Mice bearing SKOV-3 xenografts were treated with 4 injections, and the tumor volume among the groups that received the combination therapy was significantly smaller than the control groups.

Plasmid region:

5'-GATCC GGACCACCGCATCTCTACA TTCAAGACG TGTAGAGATGCGGTGGTCC TTTTTTGAATTC A -3'

Transcription

shRNA:

G G A C C A C C G C A U C U C U A C A U U C A

C C U G G U G G C G U A G A G A U G U G C A G

U U

mRNA:
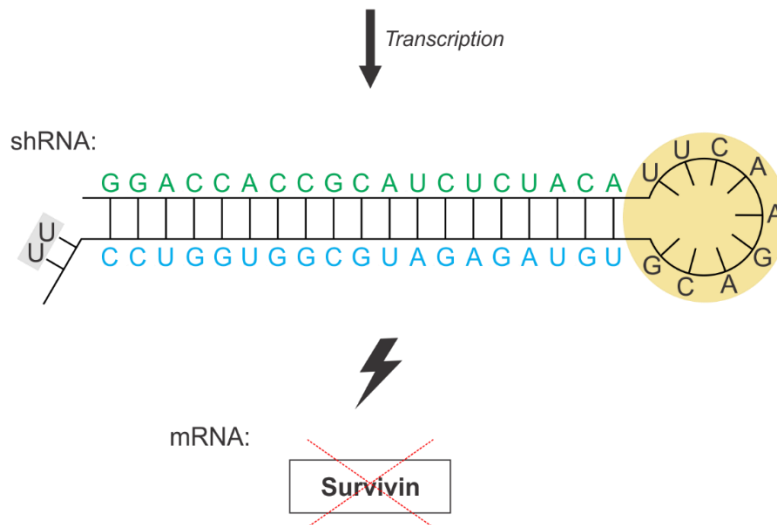
Survivin

Figure 1.2. Nucleotide sequences employed for downregulating the expression of the anti-apoptotic protein survivin. (Top panel): Portion in the plasmid DNA construct that transcribes into short-hairpin RNA, leading to the downregulation of survivin (BIRC5). (Created based on Reference 82).

1.2.3.4 Aptamers

Aptamers are synthetic DNA or RNA ligands, ranging from 20 to 60 oligonucleotides, and are highly capable of binding to target molecules, particularly proteins and receptors with affinity and specificity. The interaction between aptamers and their selected target takes place through pi-stacking of aromatic rings, electrostatic and van der Waals forces, and/or by the formation of hydrogen bonds. Oligonucleotides specific for a given cell surface receptor are screened by a method called SELEX (systematic evolution of ligands by exponential enrichment). In this process, the target of interest is incubated with an initial pool, containing 10^{14}-10^{15} different combinations of nucleotidic sequences. Non-binding candidates are removed, and the bound oligonucleotides are recovered, amplified, and used for

the next selection cycle. After several rounds, the resultant sequences are identified by sequencing, and individual aptamers are validated through further rounds of incubation with the targeted protein.[86,87]

Two major noteworthy concerns involving this class of ligand are aptamer degradation and cross-specificity. Nuclease activity in biological fluids, particularly in blood, has the potential to cleave oligonucleotides very rapidly. Some modifications in their structure can increase nuclease resistance, minimally impacting their binding affinity. The most common and effective structural improvements consist of modifying their 3'- and 5'-nucleotide ends. On the other hand, the obstacle regarding cross-specificity can be addressed by applying stringent SELEX protocols, especially by introducing a SELEX negative selection step, using off-target proteins that share similar structures and/or folding, compared to the targeted protein.[88]

To sum up this section, therapeutics based on nucleotides are still being fully consolidated in the clinics, mainly because they are relatively novel compounds. Comparing with small molecules and peptides, their efficiency is strictly dependent on nanocarriers for protection, permeation through the cell membrane, and escape from the endosome. This perhaps consists of the main limitation of this type of molecules, since although the effect of small molecules and peptides can be enhanced by using nano-delivery systems, they do not present the same level of dependence as the nucleotides.

1.2.4 Antibodies

Organisms naturally produce antibody (Ab) molecules as part of the humoral immune response against invaders. They are secreted by plasma cells, a differentiated B cell, after a sophisticated process of production that includes foreign epitope recognition, random genetic recombination, and class switching reorganization.[89] Therapeutic Ab consists of the largest class of medicines under clinical trials nowadays, and the fastest-growing sector in the pharmaceutical industry. Because of their versatility and efficiency for targeting different molecules, they have been successful for the treatment of a variety of diseases, including rheumatoid arthritis, Crohn disease, respiratory syncytial virus infection, and most importantly for the scope of this thesis, cancers.[90–92]

The first reports about human antibody production and purification start in the 1920s.[93] Basically, the process included animal immunization using human antigens and blood extraction from challenged animals. As those antibodies are a repertoire of different clones of plasma cells (i.e., polyclonal antibodies), they recognize the given antigen through different epitopes. Then, because of heterogeneity in their amino acid composition and sequence as well as the strength of their binding to antigens, this type of biological could not be standardized and consequently could not be considered as a biopharmaceutical product.[89,91] The breakthrough of this field started with hybridoma technology, which made the production of monoclonal antibodies (mAb) possible. The importance of this achievement was so expressive that the inventors were awarded the Nobel Prize of Medicine, and just ten years after the discovery, the first biopharmaceutics came to the market. Orthoclone OKT3, a full mouse antibody targeted at the CD3 receptor of T cells, was approved by the FDA in 1986 for treatment of acute glucocorticoid-resistant rejection in organ transplantation.[90,94]

1.2.4.1 Whole antibody

Also called immunoglobulins (Ig), antibodies are tetrameric multi-domain glycoproteins containing two copies of heavy and two light chains. There are five classes of Ig's (A, D, E, G, and M), although the current mAb biopharmaceutics are only IgG molecules. Their heavy chains (~ 50 kDa) are bound to each other by disulfide bonds, and each one has one light chain (~ 25 kDa) also connected through S-S bonds (~ 150 kDa in total). The IgG's are further classified into four subclasses: IgG1, IgG2, IgG3, and IgG4. Besides, the antibody molecules are classified based on the functions of their regions. The antigen-binding fragment (Fab) is the portion where the antigen is recognized, called variable domain, consisting of heavy and light domains (i.e., VH, VL, CH1, and CL). On the other hand, there is a constant portion, called fragment crystallizable (Fc) region, which has only heavy chain segments (i.e., CH2 and CH3).[95] This part is responsible for interacting with Fc receptors from immune cells. The Fab and Fc portions of IgG isoforms are separated by a linker composed of polysaccharides, giving them more flexibility, while some isoforms are more rigid structures (e.g., IgM and IgE) since they lack this hinge region.[96]

Each IgG molecule usually contains a total of 12 intra-chain disulfide bonds as well as 2 more inter-chain bonds linking the heavy and light chains. Depending on the subclass, the antibody may contain 2-8 inter-chain S-S bonds connecting the two heavy chains. However, those classical disulfide bond structures have been challenged, since recombinant and human monoclonal IgG antibodies must be extensively analyzed for the development and standardization of biologics, using, non-expected disulfide bonds have been revealed, especially among IgG2 and IgG4 subclasses. Free sulfhydryl groups have been detected, even though cysteine residues are more likely to be found in the disulfide-bonded state. Also, the presence of structural disulfide variants, such as trisulfide bond formation or thioether linkages has been observed.[97]

The antibody molecule stability is extremely important for developing this type of biological formulation and is widely known that disulfide bonds play a crucial role in this regard. Degradation or abnormality among disulfide bonds may cause changes in the proper protein folding, leading to loss of stability and aggregation as well as worsening the binding activity and the pharmacokinetic parameters. These bonds can be degraded through different mechanisms, including α- and β-elimination reaction, and direct attack of the sulfur atom by hydroxyl anions. Free sulfhydryl groups may also react with dehydroalanines, forming non-reducible cross-linked species as well as contributing to antibody hinge region fragmentation.[97–99]

Another important characteristic of monoclonal antibodies is the presence of certain types of N-linked sugars. Several studies have shown that IgG glycoforms significantly impact stability and interaction with Fc receptors. Human IgGs carry most of the N-linked glycans in the CH_2 domain, more specifically at the conserved sequons Asn_{297}-Ser/Thr. Additional oligosaccharides might also be found in other regions, usually associated with random appearances of similar repetitions in amino acid sequence, which is found constitutively in the Fc region. A common pendant saccharide among recombinant mAb molecules seems to be fucose. In the absence of this monosaccharide, a significant increase in antibody-dependent cellular cytotoxicity (ADCC) is observed, since non-fucosylated immunoglobulins bind with better affinity to the Fc receptor (type IIIa), which is highly desirable in the therapeutic context.[100,101]

1.2.4.1.1 Chimeric, humanized, and human mAb

Because of the extreme high immunogenicity of murine mAbs and other non-human proteins, the first approach adopted to circumvent this problem was the creation of chimeras by fusing murine VH and VL domains, responsible for the binding activity, with human constant domains (i.e., CH1, CH2, CH3, and CL), leading to the development of the first generation of humanized biologicals, called chimeric mAbs. Erbitux® (cetuximab) and Rituxan® (rituximab) are examples of this class of molecules and are well-

established medicines, targeting epidermal growth factor receptor (EGFR) and the cluster of differentiation 20 (CD-20), respectively.[102–104]

In the second generation, the replacement of murine-derived regions (or other species) to human amino acid sequences was enlarged compared to the chimeric antibodies. The only non-human region in humanized mAbs is the antigen-binding site (i.e., paratope), which is usually composed of a set of six complementarity-determining regions (CDRs), namely L1, L2, L3, H1, H2, and H3. Other humanization techniques have been developed to generate humanized antibodies; however, the CDR grafting was considered the gold standard approach in the production of these therapeutics.[103–105]

The total elimination of murine protein sequences has further reduced the issue of immunogenicity since human anti-humanized antibodies can still be verified among ~ 9% of humanized mAbs clinically in used. In fact, fully human mAbs have proven to be a safer medicine, presenting a lower frequency of related immune responses and hypersensitivity reactions. The anti-EGFR panitumumab (Vectibix®) is a human mAb that is FDA-approved approved for the treatment of colorectal cancer.[103,104] In the first clinical study that Vectibix® was tested as a monotherapy, an unselected population of mCRC patients received the medication. The progression-free survival (PFS) was 8 weeks versus 7.3 weeks for the best supportive care (BSC). However, after the identification that panitumumab efficacy correlates with the KRAS exon 2 mutation (codon 12 and 13), another study restricting the treatment for patients with KRAS WT tumors was conducted. Then, a clear improvement in overall survival was observed with PFS = 12.3 weeks, while the PFS was 7.3 weeks in the BSC arm.[106]

1.2.4.2 Ig-derived ligands

Since immunoglobulins are modular entities, separation of mAb into specific domains has been widely performed through biochemical or genetic methods. The antigen-binding fragment (Fab, ~ 50 KDa) was the first class of Ab-derived biologics approved for clinical use. Removal of Fc portion significantly

reduces potential off-targets observed by whole mAb, in a context of tumor-homing strategies, especially because Fc gamma receptors (e.g., FcγR) are naturally expressed by several healthy cells throughout the body, including vascular endothelium, monocytes, and macrophages, as well as by some cellular barrier sites, such as intestinal epithelium, glomerular filter in the kidneys, and blood-brain barrier.[102,107]

The fragmentation process drastically influences the physiochemical features of these molecules. Single-chain variable fragment (scFv) consists of the smallest functional fragment possibly derived from a human immunoglobulin molecule (~ 25 KDa), and it is composed of one variable region from the heavy (VH) and another one from the light (VL) chain. These two domains are joined together by a flexible peptide linker, forming a fused construct.[108,109] However, the hydrophobic regions of VH and VL chains often dissociate from one another, which can cause aggregation and poor solubility, since those exposed hydrophobic faces are prone to associate with other hydrophobic surfaces.[110]

A further reduction in size of Ig-derived fragments was still possible to be accomplished due to the existence of stable and soluble heavy chain-only antibodies (hcAb) in some species. The Fab portion of hcAbs has naturally contracted in just one single domain, which is known to occur in camelid, such as dromedary camels and llamas (variable heavy homodimers, VHH) or in cartilaginous fish, mainly among sharks (variable new antigen receptor, VNAR). Antibody fragments obtained from hcAb, called nanobodies, are advantageous due to their small size (~ 12 KDa) and great solubility and stability.[109,111,112] Interestingly, modified versions of full human nanobodies were developed through genetic engineering, but issues regarding aggregation were observed, similarly to scFv. Replacement of some amino acid residues in the hydrophobic interface (**Figure 1.3**), mimicking the camelid antibody structure, seems to be a great alternative to improve water solubility and, at the same time, circumvent problems of immunogenicity. This substitution process was coined camelization and is employed to generate nanobody-based human VH or VL.[110,111]
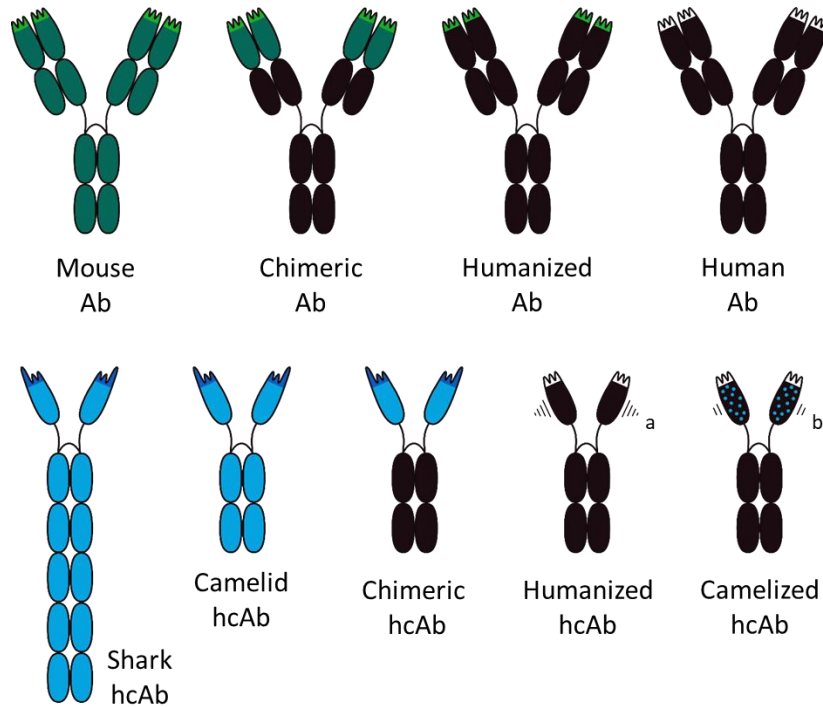
Figure 1.3. Antibody structures (Ab) from different species, highlighting their complementarity-determining regions (top portion of each molecule). (a): Regions containing high levels of hydrophobicity in the humanized heavy chain-only antibodies (hcAb), which makes this type of molecule unstable in aqueous solution and prone to form aggregates. (b): Partial replacement of hydrophobic amino acid residues, conserved in human VH and VL, to more hydrophilic residues derived from camelids (blue dots), aiming the increase in water solubility and, consequently, prolonging their half-life in blood circulation (Created based on References 81,91, and 93).

1.2.4.2.1 Bi-specific antibodies

The most straightforward way to obtain bi-specific heterodimeric antibody structures (bsAb) is to assemble from two different IgG molecules or Fab portions using biochemical techniques through reduction/oxidation of disulfide bonds, followed by affinity chromatography. However, such approach does not allow large-scale bsAb production. Ideally, the desired bi-specific IgG molecules should be produced in one cell line. The main problem associated with bsAb development through cellular co-expression of two different VH and VL variable domains is the possibility of non-desired recombinations, commonly referred to as chain-association issue. Several genetic and cellular engineering strategies, such as quadroma technology, knobs-into-holes, CrossMab, common heavy chain, and common light-chain strategies, have been implemented to produce optimized bsAb structures. A biparatopic bsAb is a molecule that instead of targeting two different proteins, is designed to simultaneously bind to two non-overlapping epitopes on the same target, increasing the binding strength of the ligand.[113–115]

Blinatumomab (trade name Blincyto®, Amgen, Inc.) is a first-in-class bispecific T-cell engager (BiTE) therapeutics, primarily indicated in relapsed/refractory acute lymphoblastic leukemia. BiTE molecules are characterized by mediating the interaction between the cytotoxic T-cells and cancer cells. In the case of Blinatumomab, which consists of two fused scFv portions, the bsAb construct has dual specificity for CD19 and CD3. CD19 was selected as target antigen based on its frequent expression among malignant B cells and its impact on proliferation and survival of B cells, whereas CD3 moities are abundant on the surface of T-cells. The primary clinical study that was the basis for its indication against acute lymphoblastic leukemia involved 185 evaluable adults in a single-arm trial. The complete remission (CR) rate was 32%, and the median duration of response was 6.7 months. The standard of care for this condition used to be intensive combination chemotherapy with disappointing outcomes.[116,117]

1.2.4.3 Non Ig-derived ligands

Numerous non-antibody synthetic constructs have been identified as great binding-scaffolds, since their reduced complexity in structure and folding, when compared to immunoglobulins. As reviewed by Vazquez-Lombardi et al.,[118] such molecules have been reported to be under pre- and clinical trials for therapeutic and diagnostic purposes, majorly focusing on cancer and inflammatory diseases. An extensive list of this broad class of ligands, but not comprehensive, is included here together with a brief description: (i) Affibody: a non-cysteine three-helix bundle domain, derived from B-domain in the IgG-binding region of staphylococcal protein A;[119,120] (ii) Affilin: a polypeptide sequence folded in a highly compact α/β structure, derived from ubiquitin (~ 76-mer);[121] (iii) Anticalin: a protein fragment derived from lipocalin protein family and dominated by a β-barrel folding;[122] (iv) Adnectin: also called monobody, is based on the fibronectin type III (FN3) domain, having an Ig-fold (i.e., two β-sheets packed against each other) and no disulfide bonds.[123] (v): Fynomer: a small protein (~ 7 KDa), derived from amino acids 83–156 of the sarcoma-homology 3 (SH3) domain of FYN tyrosine kinase;[124] (vi) Kunitz domain: its folding is formed by two-stranded antiparallel β-sheet and two α-helices, being stabilized by three pairs of disulfide bonds;[125] (vii) Obody: derived from a bacterial aspartyl tRNA synthetase, has a unique binding site formed by a combination of concave β-sheet and four loops;[126] (viii) Repebody: based on immune response of jawless vertebrates, consists of highly-diverse leucine-rich repeats (each containing 20–29 aa) in a horseshoe-shaped solenoid fold.[126]

In a comparison study reported by Orlova et al., an affibody specific for anti-human epidermal growth factor receptor 2 (HER-2) and Trastuzumab, a full-length monoclonal antibody anti-HER-2, were evaluated as tracers for in vivo PET imaging. The biodistribution analysis of both [124]I-radiolabelled molecules after i.v. injection into mice bearing NCI-N87 cells (gastric carcinoma) revealed that the affibody provided a better contrast (i.e., tumor-to-organ ratio) in HER-2 imaging than Trastuzumab. However, the

total uptake radioactivity was higher using the monoclonal antibody, confirming the prolonged blood circulation of immunoglobulins and pointing out the rapid clearance of affibodies.[127]

1.2.4.4 Cell expressing antibodies: CAR-T

Chimeric T-cell receptors were first denoted as "T-body" molecules by Eshhar *et al.*,[128] who contributed to the development of plasmid constructs encoding artificial antibody-like structures to be expressed in T cells. The updated term for this approach is chimeric antigen receptor T-cells (CAR-T). As a type of adoptive cell transfer, the preparation of CAR T-cells starts with the isolation and *ex vivo* expansion of T-lymphocytes from the patient's peripheral blood, followed by their genetic manipulation and re-infusion back into the patient. In 2017, a significant milestone was achieved in the treatment of blood cancers, due to the FDA-approval of the first two CAR T-cell therapies, Tisagenlecleucel (Kymriah®) and Axicabtagene Ciloleucel (Yescarta®).[129,130]

Structurally, these chimeric antibody-like structures are composed of an antigen-binding ectodomain, a transmembrane domain, and an endodomain that transmits T-cell activation signals. In most of the cases, a scFv construct is included in the designed plasmid, since the Fab portion is more challenging to be expressed, especially because Fab is the product of two genes. On the other side of the molecule, the signaling moiety is derived from cytoplasmic regions of endogenous T-cell receptors, more specifically, the ζ domain of CD3 complex. The most recent generations of CARs have additional costimulatory domains, such as CD28, CD137, and others, to further enhance the activation of cytotoxic function of effector T-cells against the targeted tumor cells.[131,132]

In one of the clinical studies used as the basis for the approval of Yescarta®, which is a CD19-targeted CAR T-cell therapy, 111 patients with diffuse large B-cell lymphoma, primary mediastinal B-cell lymphoma, or transformed follicular lymphoma were enrolled in the trial. Genetic modification of autologous cells was successfully achieved in 110 patients (99%), and the re-introduction of modified T-

cells was performed in 101 participants (91%). Impressively, the objective response rate was 82%, and the complete response rate was 54%. With such positive clinical responses, many other studies in other types of cancer were also conducted, especially to treat solid malignancies, since they represent the majority of cancer-related morbidity and mortality. However, the overall outcomes so far have not paralleled the success seen in liquid cancers.[130,133]

In conclusion, antibody molecules have been extensively used in cancer therapy and diagnosis, and given their high levels of safety and efficacy on preclinical and clinical trials. They present an excellent rate of translation from bench to bedside. A drawback of such therapies that is important to recognize comes from their proper 3D folding and conformation. Aggregation, denaturation, and other modifications on the antibody structure can seriously compromise their capacity to bind to the therapeutic targets. In this field, the formulation aspect of view need to be carefully investigated, and guidelines strictly followed in order to maintain molecule stability.[97,98,134]

1.2.5 Proteins, carbohydrates, and other molecules

Some well-recognized tumor-homing ligands have greatly impacted the development of targeted-therapeutics. Transferrin, a glycosylated serum protein,[135] and hyaluronic acid, an anionic glycosaminoglycan polysaccharide,[136] as well as other entities,[137] are examples of such molecules. Among few active-targeting drug nanocarriers that have reached clinical trials so far, transferrin has been the selected ligand for at least two of them (as indicated in **Table 1.1**). This accounts for a large proportion, given the plethora of ligands currently available for this purpose, and emphasizes that non-immunogenicity, non-toxicity, and biodegradability are valuable properties in this field. Though the prospect of having only one versatile platform that could simultaneously target a broad range of cancers, which is the case for transferrin, also seems to be very appealing to clinicians and manufacturers.[138,139]

Another interesting class of molecules to be discussed include some surfactants, commonly employed in drug delivery systems, such as poloxamers, tweens, spans, and vitamin E D-α-tocopheryl polyethylene glycol succinate (TPGS). Besides their properties of improving drug solubility, stability, permeability, and release profile, they also have been characterized with the ability to inhibit the activity of P-glycoprotein (P-gp) or ATP-binding cassette transporter (ABCB1). P-gp is one of the primary causes of multidrug resistance since this transporter can pump several chemotherapeutic agents out of the cell, decreasing intracellular drug accumulation in tumors and, consequently, reducing cytotoxic effects of cancer therapies.[140] Lipid nanoparticles have already been successfully explored because of the dual function of their amphiphilic molecules since they efficiently and specifically deliver the payload to the tumor site and, at the same time, target and block P-gp for preventing the efflux of the drug from cancer cells.[141]

Different studies have investigated the mechanism of P-gp inhibition by TPGS using Caco-2 monolayers to measure the transport pattern of Rhodamine dye through separate compartments. Several lengths of PEG have been evaluated and molecular weights near 1,000-2,000 g/mol seem to have the best

activity in this regard. Its mechanism of action still remains unclear, especially if P-gp ATPase inhibition was achieved via direct interaction of TPGS, via an indirect allosteric modulation of the P-gp function, or via steric blocking of substrate binding. Rigidification or fluidization of the P-gp membrane environment produced by TPGS at P-gp active concentrations has also the capacity to rule out as the main cause for inhibition. Similarly to lipid nanoparticles, these studies are quite interesting since they open novel possibilities for pharmaceutical excipients, not only relying on their technological properties to encapsulate and/or solubilize drugs but also targeting specific receptors that can enhance the activity of drugs inside the cells.[142,143]

1.3 Nano- and small-sized targeted drug formulations in oncology

1.3.1 Passive targeting of nanoparticles

Although nanomedicine is regarded as a relatively novel therapeutic approach, some nano-scaled products have been commercially available for over 100 years. This is the case, for instance, of colloidal silver dispersions that have been used for multiple purposes, especially because of their antimicrobial and wound healing properties.[144] The boom in the applied nanotechnology for cancer therapy started in 1986, with a Japanese report describing the phenomenon in which nanoparticles preferentially accumulate in solid tumors.[145] The fundamental features of this effect, called enhanced permeation and retention (EPR), consist of hyperpermeability of tumor vasculature and impairment of lymphatic drainage capacity.[146–148] EPR effect concept has shaped modern drug delivery, since has been served as the rational basis for numerous passively targeted drug nanocarriers, including some FDA-approved ones such as Doxil®, Onivyde®, Abraxane®, Marqibo®, and DaunoXome®.[148–150]

The side effects of small chemotherapeutic molecules are widely known to be devastating since these compounds attack all parts of the body indiscriminately. In clinical practice, the expectations from conventional chemotherapy are that cancer will recede before excessive harm is done to the patients. Thus, there was an optimistic belief that the passive accumulation of nanoparticles, carrying those potent cytotoxic drugs, would revolutionize the treatment of solid tumors. However, the EPR effect has shown to be a non-straightforward answer to enhance therapy specificity, and despite a massive number of positive pre-clinical data in this area, the translation into new clinical therapies has been more challenging than initially thought.[147,151] One of the main obstacles in the development of drug nanocarriers from bench-to-bedside is the lack of more realistic tumor models. Ethical and financial restrictions significantly limit the use of larger animal models (e.g., non-human primates), and the fast-growing xenografted murine models, in which tumor volume can sometimes reach nearly 10% of the mouse's body, do not recapitulate the majority of solid tumors in humans.[151–153]

Some physicochemical properties of drug nanocarriers, namely size, shape, and surface properties (i.e., charge, stealth coating), can greatly influence the pattern of their tumor accumulation.[150] In the literature, there is a controversial threshold (< 200 nm), more or less established, regarding hydrodynamic particle diameter for suitable extravasation into solid tumors. However, fluorescent-labeled nanoparticles, made up of poly(ethylene glycol)-poly(lactic acid) (PEG-PLA), with a size of ~ 110 nm accumulated 50-fold more efficiently into tumors than the counterparts of ~ 160 nm. The later ones had a visible higher signal intensity among organs of the reticuloendothelial system (RES), especially in the liver that contains specialized macrophages in its sinusoidal walls (i.e., Kupffer cells), known to recognize opsonins adsorbed on the nanoparticle surfaces, engulfing them.[154] Another important parameter to be considered in this matter is the shape of nanoparticles. Geng *et al.*[155] compared spherical and worm-like micellar nanostructures, based on poly(ethylene oxide)-poly(ε-caprolactone) (PEO-PCL), and their observation was that the worm-like filomicelles persisted in the blood circulation of rats ten times longer than their spherical-shaped micelles. Interestingly, long worm-like filomicelles were found to have a great ability to escape *in vitro* phagocytosis compared to short worm-like and spherical micellar nanoparticles.

Incorporation of hydrophilic surface layer on passively targeted drug nanocarriers is an efficient stealth coating strategy to avoid RES recognition, extend their circulation half-life and, consequently, enhance the chance for tumor extravasation via EPR effect. There are many entities suitable for stealth coatings, such as polysaccharides, polyglycerols, polyoxazolines, and polybetaines, but the most common polymer used is PEG (or PEO, depending on the molecular weight). When the density of the PEG surface layer is relatively low, the polymer is arranged in a mushroom-like coil structure, and as the PEG density increases, a brush model is observed since the PEG chains tend to avoid overlapping with other PEG molecules. Doxil®, a PEGylated doxorubicin liposomal formulation, was the first drug nanocarrier to obtain FDA approval after only five years from its reported development. Nevertheless, some disadvantages of pegylation have to be pondered, including the so-called "PEG dilemma". Even though PEG coating is

beneficial in some aspects, it also prevents cell interaction once nanoparticles reach the tumor site; and once cell uptake occurs, the endosomal escape is compromised. In addition to that, the hand-foot syndrome is a painful side effect associated with PEG, and repeated injections lead to induction of the IgM response and subsequent complement system activation.[149,156]

Nanotechnology may not solve all the problems in cancer therapy; however, it is undoubtedly the case that the improvements are encouraging.[151] For example, mice bearing MCF-7 tumor xenografts were treated (i.v. injections) with a polymeric nano-formulation containing paclitaxel (i.e., poly(beta-amino ester) and poly(lactide-*co*-glycolide)), and around 0.6% of the dose reached the tumor site, whereas when the free drug was administered, only 0.2% of the initial drug amount was able to be delivered into the tumor.[157] Similarly, a small improvement was sufficient for Vyxeos® FDA approval, a liposomal formulation of daunorubicin and cytarabine. The overall survival of patients with poor-prognosis acute myeloid leukemia treated with free form is ~ 5.9 months, and with Vyxeos® is ~ 9.6 months.[158] From the first clinically approved nanomedicine in 1995 (Doxil®) to the latest one in 2018 (Apealea®), there are at least 15 drug nano-formulations on the market for cancer treatment, which reflects that the process of optimization and improvement is slowly being conceived in this field.[138]

1.3.2 Active targeting of nanoparticles

The central mechanism behind active tumor-targeted drug nanocarriers relies on the binding of molecules, present on nanoparticle's surface, to specific epitopes from tumor-biomarkers exposed on plasma membrane, in order to augment intracellular delivery of payloads into cancer cellular cytosol.[139] The structure repertoire of ligand entities varies significantly and includes small molecules (e.g., folate), sugars (e.g., lactose), proteins, aptamers, peptides, and antibodies. Binding interaction between ligand and cell receptor is known to be strongly dependant on a certain level of physical proximity from both

entities. Also, since the present strategy does not contribute to higher permeation into solid tumors, it has been considered as a complementary step to the size-based passive diffusion.[139,151]

Surface-modified nanocarriers have robustly shown to contribute to enhancing the specificity of chemotherapeutic agents, especially because these systems possess the distinguished ability to be internalized by cancer cells at greater extents, in comparison with normal cells.[159] One of the major problems related to passive tumor-targeting resides in the vast heterogeneity within and between tumor microenvironments. Once plain surface nanoparticles extravasate into tumors, their cargo is delivered indiscriminately to different cellular, including arteries, veins, capillaries, lymphatics, pericytes, cancer-associated fibroblasts, myofibroblasts, adipocytes, natural killer (NK) and mast cells, macrophages (M1, M2), T- and B-lymphocytes, neutrophils, myeloid dendritic cells, and others besides cancer cells.[2,3] Therefore, advancements in the understanding of tumor biology has led to an individualized, patient-oriented selection of cancer markers, allowing drug nanocarriers to be highly specific to receptors overexpressed by particular cancerous cell populations, avoiding those non-cancerous cells.[151,153]

Nonetheless, some factors related to the behavior of surface-decorated delivery systems in blood circulation have been identified to affect their targeting efficiency. Protein corona coating, formed by adsorption of serum proteins and opsonins, can drastically modify the design of such systems since it prevents a proper interaction with cell receptors by covering the ligands decorated on the surface of nanocarriers, which ultimately, can lead to the inability of such systems to target cancer cells at the tumor site. This phenomenon is particularly more prejudicial to constructs based on active tumor-targeting when compared to the ones based on passive-targeting since stealth-coating strategies do not entirely cover the surface. Oh *et al.*,[160] have recently developed a corona shield strategy that remarkably reduced serum protein coating and macrophage uptake by conjugating glutathione-S-transferase on mesoporous silica nanoparticle, which was fused in an affibody structure specific for human epidermal growth factor receptor 2 (HER2). Recognition by RES consists of a limiting factor against accumulation into solid tumors,

and even though pegylation is usually applied, the exposed tumor-targeting ligands are prone to be identified as antigens. The flow rate of nanomaterials has been characterized to be extremely slow in the liver sinusoid for increasing the chance of interaction and uptake by hepatic Kupffer, endothelial, and B-cells. Macrophage depletion in murine models using chemical treatments (e.g., clodronate and propamidine), has shown to enhance tumor accumulation of nanoparticles by 150 times.[161,162]

So far, no active-targeted nanocarrier has been approved for clinical use. Few of them have already reached clinical trials, as indicated in **Table 1.1**. Interestingly, from the total of 13 formulations that were subjected to clinical trials phase I, positive outcomes were observed in 8, and patients are still being recruited for testing 2 formulations (EGFR EDV-mit and EGFR EDV-dox). Only in 3 trials the study was terminated due to a negative outcome: MM-310 was identified to have significant toxicity as a side effect, Lipovaxin-MM was rejected because of low efficacy, and CALAA-01 was terminated by unclear reasons since its administration was well tolerated in all doses tested. Clinical trials phase II or III have been conducted for 5 actively targeted nano-formulations, 2 studies were terminated since the efficacy was low (MM-302 and BIND-014), and the status for 3 trials is still ongoing (SGT-53, MBP-426, and C225-IL-dox). Therefore, even though there is no active cellular targeting nano-approaches in the market so far, increase interest for developing more specific nanocarriers towards particular cancer cell subsets within the tumor microenvironment can be clearly seen in the scientific community.[163–173]

Table 1.1. Background information on actively-targeted drug nanocarriers that have reached clinical trials.

Code (ID)	Payload	Ligand	NP type	NP composition	Conjugation chemistry (ligand-NP)	Indication	Status / (selected trial)	Outcome
SGT-94	RB94 plasmid	Anti-transferrin scFv	Liposome	DOTAP, CHOL	Non-covalent complexation	Solid tumors	Phase I (NCT01517464)	Positive
SGT-53	p53 plasmid + free temozolomide	Anti-transferrin scFv	Liposome	DOTAP, DOPE, DOPE-MPB	C-end cysteine + DOPE-maleimide	Glioblastoma and pancreatic cancer	Phase II (NCT02340156)	Ongoing
MCC-465	Doxorubicin	Anti-keratin 8/18 F(ab')$_2$	Liposome	DPPC, CHOL, DPPE, PEG(5K)-SH	Thiolated amine (2-iminothiolane) + DPPE-maleimide	Gastric cancer	Phase I (N/A)	Positive
MBP-426	Oxaliplatin + free leucovorin/5-FU	Transferrin	Liposome	DSPC, CHOL, DSPE-PEG(2K), DSPE-PEG(3K)	Amine (lysine) + PEG-COOH (carbodiimide/S-NHS)	Gastric, esophageal adenocarcinoma	Phase Ib/II (NCT00964080)	Ongoing
MM-302	Doxorubicin + free trastuzumab	Anti-HER2 scFv	Liposome	HSPC, CHOL, DSPE-PEG(1.9K)	C-end cysteine + PEG-maleimide	HER2-positive breast cancer	Phase II/III (NCT02213744)	Negative
MM-310	Docetaxel prodrug	Anti-EphA2 scFv	Liposome	NOF, HSPC, CHOL, DSG-PEG (2K), DSPE-PEG(2K)	C-end cysteine + PEG-maleimide	Solid tumors	Phase I (NCT03076372)	Negative
C225-IL-dox	Doxorubicin	Anti-EGFR Fab'	Liposome	HSPC, CHOL, DSPE- PEG(2K)	Reduced thiols + PEG-maleimide	Glioblastoma	Phase I (NCT03603379)	Ongoing
Lipovaxin-MM	OVA-dominant epitope (peptide SIINFEKL)	CD11c and DEC-205 scFv	Vesicle + liposome	Human cell membrane vesicles + Ni^{2+}-NTA$_3$-DTDA, POPC, PC-BODIPY	Histidine tag + Metal-chelator	Malignant melanoma	Phase I (NCT01052142)	Negative
BIND-014	Docetaxel	PSMA-targeting pentanedioic acid (ACUPA)	Polymeric nanoparticle	PLA-PEG(5K)	Amine + PEG-COOH (carbodiimide)	Prostate cancer	Phase II (NCT01812746)	Negative
CALAA-01	anti-RRM2 siRNA	Transferrin	Polymeric nanoparticle	B-cyclodextrin-polycation, adamantane-PEG(5K)	Aldehyde (asparagine-N-linked sugar) + PEG-NH$_2$ Imine reduction (NaBH$_3$CN)	Solid tumors	Phase I (NCT00689065)	Unknown
EGFR EDV-mit	Mitoxantrone	Anti-EGFR bsAb (arm A)	EnGeneIC delivery vector	Bacterial chromosome-free nanocell	Anti-nanocell bsAb (arm B)	Solid or CNS tumors	Phase I (NCT02687386)	Ongoing
EGFR EDV-dox	Doxorubicin	Anti-EGFR bsAb (arm A)	EnGeneIC delivery vector	Bacterial chromosome-free nanocell	Anti-nanocell bsAb (arm B)	Glioblastoma	Phase I (NCT02766699)	Ongoing
Rexin-G	Human cyclin G1 plasmid	Collagen-binding motif (viral envelope)	Viral vector	Moloney murine leukemia retrovirus (MoMLV)	N/A	Pancreatic Cancer, Osteosarcoma	Phase II (NCT00572130)	Positive

1.3.3 Active targeting of small drug conjugates

Side effects of small-molecule drug formulations intravenously administered are notorious and deleterious for patients, due to their lack of specificity to cancers. In this class of tumor-targeted treatments, cytotoxic chemotherapeutic agents are covalently conjugated with tumor-specific ligands. This approach has shown to be extremely efficient in enhancing drug delivery to cancers, sparing normal cells from the off-target effects, and at the same time solving some limitations encountered in most of the small therapeutic molecules, namely water solubility, plasma instability, and fast renal clearance.[174,175] One important characteristic of this class is the fact that, in this case, drug formulations are usually below ~ 10 nm[176] and, in consequence, they do not rely on EPR effect, being referred as non-EPR approaches.[151]

Antibody-drug conjugates (ADC) represent a relatively novel class of protein-based therapeutic agents that are increasingly achieving clinical and regulatory success. Currently, more than 100 ADCs are under clinical trials against cancers, and 4 FDA-approved ADCs are on the market for cancer therapy, including Mylotarg® (i.e., humanized anti-CD33 mAb conjugated with the DNA-damaging agent calicheamicin), Adcetris® (i.e., chimeric anti-CD30 mAb conjugated with the microtubule disrupting agent MMAE), Kadcyla® (i.e., humanized anti-HER2 conjugated with the microtubule disrupting agent DM1), and Besponsa® (i.e., humanized anti-CD22 mAb conjugated with the DNA-damaging agent calicheamicin). Interestingly, the cytotoxic compounds conjugated into these systems, such as auristatins and maytansinoids are ~ 1000-fold more potent than standard chemotherapeutic agents, displaying IC50 values at sub-nanomolar (nM) range versus the latter ones that often display IC50 values at low micromolar (µM) range.[174,175] The research for developing these super potent cytotoxic agents has sparked great interest, especially on DNA-damaging agents. For instance, Vadastuximab Talirine (SGN-CD33A, Seattle genetics Inc.) was a CD33-targeted novel therapy against acute myeloid leukemia, in which its cytotoxic payload was composed of pyrrolobenzodiazepine dimers, a molecule ~10-fold more potent

than auristatins and maytansinoids. However, despite its impressive activity in preclinical and early clinical trials, the medication failed in phase III due to issues of safety.[177,178]

Some limitations of ADCs, such as their large size, three-dimensional folding, and off-target issues due to the affinity of Fc portion towards normal cells and tissues in the body, have encouraged the development of other forms of therapeutic conjugates, especially the use of peptidic sequences, though investigation in this area is recent and has been progressing in a slower pace.[179] Moreover, numerous other types of ligands have been employed for this drug conjugation strategy, including aptamers, nanobodies, affibodies and other tumor-targeting entities.[180–182]

Peptide-drug conjugates (PDCs) share the same rationale of ADCs; however, their pharmacokinetic profile is prominently distinct from one another. Their differences in size lead to rapid renal clearance and a shorter plasma half-life of PDCs in comparison with ADCs, whereas high penetration rates cannot be achieved in tight tissues by using the latter formulations. For instance, novel drug delivery systems based on PDC have shown that chemotherapy agents' translocation to the brain can be carried out following systemic administration. Certain types of peptides, namely cell-penetrating peptides (CPP), can greatly contribute to the crossing through the blood-brain barrier (BBB).[183,184] Li *et al*.,[184] reported on a formulation strategy for enhancing the delivery of placlitaxel into the brain by using an intracranial model of U87 glioblastoma in nude mice. The drug was covalently attached to one peptide related to a lipoprotein expressed in the brain as well as to a CPP sequence. A significant higher translocation of paclitaxel into the brain was observed in comparison with the free cytotoxic agent.

The chemistry of drug conjugates should be carefully selected so that functional groups, nature, and site of the coupling do not contribute to reducing drug potency and ligand affinity. The most common conjugation strategies related to antibody-like molecules, as corroborated by the **Table 1.1** (in the column named "conjugation chemistry"), comprise reactions between primary amines with carboxylate groups by amide bond formation using carbodiimide chemistry, as well as between maleimide groups with thiols.

In this latter reaction, sulphydryls are commonly generated by reacting primary amines of lysine residues from proteins or peptides with 2-iminothiolane (i.e., Traut's reagent). Linkers serve as the connector of drug and ligand molecules. Non-cleavable linkers are advantageous for their binding stability since it minimizes the risk of early drug release in the blood, which would cause an elevation in side effects. On the other hand, the benefit of using cleavable linkers is their responsive drug release upon certain conditions, such as pH modification, enzymatic or reducing agent activity, which can provide higher drug concentration to the targeted region, especially if the antibody targets a non-internalized receptor, such as CD20. In a preclinical study on an ADC composed of anti-HER2 mAb and DM1 drug, the reduceable disulfide link chemistry was compared with the non-cleavable linker formed by thioether. The results indicated that the non-reducible linker offered a better cytotoxic efficacy against the transplanted breast tumor models, improved pharmacokinetics, and reduced toxicity over the disulfide cleavable strategy.[185–187]

1.4 Thesis Proposal

The central hypothesis of this thesis was that ligand molecules specific to cancer cell-surface biomarkers, can enhance homing and interaction of drugs as well as nano-drug delivery systems with tumors leading to an increased therapeutic index for the incorporated drug.

1.4.1 Rationale and significance

Targeting of drugs to tumor can be achieved by exploiting the physiological differences between tumor and healthy tissues and/or cells by active or passive means. This encompasses the use of nano-delivery systems of 10-200 nm in size that can take advantage of the physical barrier of continuous vasculature at normal tissues versus the angiogenic vasculature at the tumor site, to preferentially accumulate at the tumor and release the encapsulated cargo at the vicinity of tumor cells. This strategy; however, does have its own limitations: i) it does not ensure proper **internalization** of drug within the tumor cells; ii) it will not provide means for **specific interaction** of the drug with cancer cells within the heterogeneous tumor microenvironment; iii) it may not achieve **sufficient homing and retaining** of the drug with the tumor tissue; and/or iv) it may hinder **deep penetration** of the therapeutic molecule within the tumor mass due to nanoscopic size. This approach is presented as option A in figure 1-4, where the box represents the cargo and the trolley is the carrier.

Our research group and others have pursued the development of ligand modified drugs and drug delivery systems, to account for the above shortcomings of tumor targeting by nano-delivery systems (represented as option B and C in figure 1.4, respectively). The key represents the ligand, that takes advantage of aberrant expression of their target receptors on the surface of cancer versus normal tissues to achieve tumor-targeted drug delivery. The hypothesis of this thesis was that peptide/protein-based ligands with specificity to cancer cell-surface biomarkers, can enhance the interaction of drugs as well as nano-delivery systems of small molecules or siRNA with tumor over normal cells leading to an increased

therapeutic index for the incorporated therapeutic agent.

In the first two research chapters of this thesis, two engineered analogs of P160 peptide, a peptide originally developed by phage display and known to specifically target breast cancer and glioblastoma cells, namely C18.4DK and P18.4, were used. Both peptidic sequences retain most of the amino acid residues from their parent P160 peptide, but are engineered to show improved stability in biologic fluids. These peptides, are found to target Keratin 1 (KRT1), an intermediate filament protein that contributes to the formation of cellular cytoskeleton. In general, keratins are described as cytosolic frameworks, arranged in pairs with equal amounts of type I and II (e.g., K1/K10, K5/K14, and K8/K18). Interestingly, KRT1 does not fully fall into this generalized description, since its occurrence without heterodimer pairing is commonly observed, and also various studies have indicated that this protein can function as a cell-surface receptor for different molecules, such as high molecular weight kininogen (HK)[188], mannose-binding lectin (MBL),[189] and viral nucleoprotein.[190] Its upregulation has been reported as a pattern in several types of cancer, including breast cancer, melanoma, neuroblastoma, and nasopharyngeal carcinoma. Moreover, KRT1 has been associated with resistance to chemotherapeutic agents, including platinum compounds, vincristine, docetaxel, and 5-fluorouracil.[191–193] In chapter two of this thesis, the success of cancer-targeting peptide ligands in enhancing tumor delivery and retention of conjugated small molecules was assessed (option B in Figure 1.4). In this context, we explored whether modification of a model hydrophobic molecule, Cy5.5 fluorescent probe, with C18.4DK can enhance its tumor accumulation and retention in an orthotopic tumor model of triple-negative breast cancer.

In chapter three, we explored the success of engineered peptide ligands based on P160 in enhancing tumor versus normal cell specificity of nano-siRNA delivery systems. In this regard, another engineered derivative of P160, known as P18.4, was pursued to enhance the specific delivery of a siRNA cargo by polymeric micelles containing polyamine (PA) groups in their core, to cancer versus angiogenic vessel cells (Option C, Figure 1.4). Previous reports have employed this peptidic sequence for enhancing

tumor affinity of different systems, such as polymer- and lipid-based nanocarriers for the delivery of drugs[194,195] and plasmid.[196]

Targeting the epidermal growth factor receptor (EGFR) was the chosen approach in chapters 4, 5, and 6 of this thesis. Two EGFR-specific ligands were employed for surface modifying our micellar nanostructures: GE11 peptide (Chapter 4 and 5), which has been widely utilized in pre-clinical studies for several cancer-related applications; and Panitumumab, which is an FDA-approved, fully human monoclonal antibody (brand name Vectibix®) (Chapter 6). This receptor corresponds to a classical target in oncology, given the deep understanding of its crucial roles in cancer development and progression, though still unraveled functions of EGFR have been still recognized. The canonical activation starts with the binding with its endogenous ligands that leads to receptor dimerization and induction of signaling cascade pathways by activation of the cytosolic tyrosine kinase domain. At least three main EGFR-dependent pathways provide support for malignant features, including the one via phosphatidylinositol 3-kinase (PI3K) triggering to Akt activation and suppression of apoptosis. Secondly, cell cycle progression is promoted through growth factor receptor-bound protein 2 (GRB2) and son of sevenless homolog 1 (SOS1) that induce the activation of p21^{ras}. And the third pathway is via phosphorylation of phospholipase C-g1 (PLC), leading to PIP$_2$-related actin reorganization, which ultimately contributes to cell migration and invasion.[197–199] In Chapters 4 and 5, we explored the role of GE11 modification of polymeric micellar surface in enhancing the homing and retention of these nano-delivery systems in either subcutaneous or orthotopic CRC models by two PET or NIR imaging techniques, respectively. The benefit of this approach in increasing the anticancer activity of a novel inhibitor of DNA repair in monotherapy of PTEN negative CRC models was also explored (Option C in Figure 1.4). In literature, there are many studies on drug nano-formulations that use GE11 peptide to enhance tumor homing and therapeutic activity, including carriers containing doxorubicin,[200] gemcitabine,[201] and cisplatin.[202]

In Chapter 6, the use of a clinical monoclonal antibody against EGFR, rather than a peptide ligand

for the purpose of cancer-targeting, was pursued. Another monoclonal antibody was employed for targeting carcinoembryonic antigen-related cell adhesion molecule 6 (CEACAM6), also called CD66c. This protein is anchored to the plasma membrane and seems not to have transmembrane and intracellular domains. Its overexpression has been associated with worse prognosis and high risk of relapse. Its overexpression promotes migration and invasion as well as chemoresistance (e.g., gemcitabine). Moreover, CEACAM6 has been identified to be involved in colorectal cancer (CRC) growth and in the formation of CSC populations, being indicated as a potential target for cancer stem cell-directed therapies.[203–205]
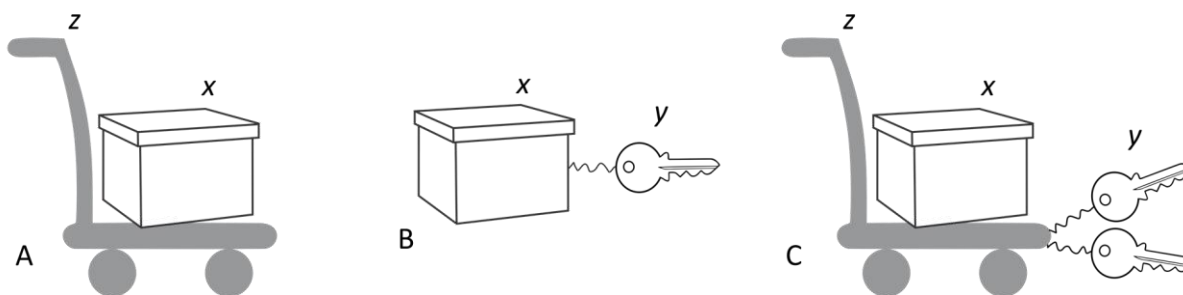
Figure 1.4. Schematic representation of different tumor-targeting strategies used in this thesis, pointing out the major components that were modified among different delivery systems. (x = Payload): Cy5.5 (model drug), siRNA (against MCL-1), and A83B4C63 (PNKP inhibitor); (y = Ligand): Keratin-1-targeting peptidic sequences (i.e., C18.4DK and P18.4), EGFR-targeting peptide (i.e., GE11), EGFR-targeting monoclonal antibody (Vectibix), and anti-CD66c monoclonal antibody; (z = nanocarrier): Polymeric micelles based on PEO-b-PCL and PEO-b-PBCL as well as polyplex micelles composed of PEO-b-P(CL-g-SP) and PEO-b-P(CL-g-DT).

1.4.2 Working hypotheses

1) Modifying the fluorophore-based model drug Cy5.5 with C18.4DK cyclic peptide will contribute to increasing fluorescence signals from the small traceable molecule in MDA-MB-231 xenografts, implanted orthotopically in mice.

2) Covalently conjugating P18.4 peptide to the shell of PEO-P(CL-PA) micelles will enhance the delivery to MDA-MB-435 cancer cells over normal angiogenic HUVEC cells.

3) GE11 modification of polymeric micellar surface will allow preferred accumulation and retention of nanocarrier in EGFR overexpressing subcutaneous or orthotopic CRC tumors.

4) GE11 modification of polymeric micellar surface can lead to enhanced anti-cancer activity of encapsulated cargo in EGFR overexpressing CRC tumors.

5) Surface modification of polymeric micelles with monoclonal antibodies against EGFR or CD66c can enhance specificity of the delivery system for its target cells, overexpressing the above cancer biomarkers.

1.4.3 Specific objectives

1) To assess the biodistribution profile of Cy5.5 conjugated C18.4DK after systemic administration in an orthotopic MDA-MB-231 mice model.

2) To assess the effect of P18.4 surface-modification of PEO-*b*-P(CL-*g*-polyamines) micelles on the specificity and transfection efficiency of complexed siRNA in target cancer cells.

3) To assess the effect of ^{64}Cu labeled GE11 modification of polymeric micellar surfaces, formed by PEO-*b*-PBCL copolymers, containing EGFR-targeting GE11 peptide or mock HW12 peptide, and track their fate through PET imaging on ectopic biodistribution of polymeric micelles in subcutaneous HCT116 colorectal mouse model by PET imaging.

4) To assess the effect of GE11 modification of Cy5.5 labeled polymeric micelles on the biodistribution of polymeric micelles in the orthotopic HCT116 model by IVIS imaging.

5) To assess the effect of GE11 modification of polymeric micelles on anticancer activity of the encapsulated novel inhibitor of DNA repair in an orthotopic HCT116 tumor model.

6) To develop mAb modified polymeric micelles and assess the role of mAb modification on increasing the specificity of polymeric micelles for target cells overexpressing the target receptor.

Chapter Two

Near-infrared optical imaging of proteolytically stable cyclic decapeptide for tumor targeting using a breast cancer orthotopic mouse model

A version of this chapter has been published in

Journal of Medicinal Chemistry 2017, 60(12):4893-4903.

2.1 Introduction

Selective delivery of chemotherapeutic drugs to cancer cells is needed to avoid toxic side effects on the healthy cells and tissues. Among different strategies, the use of ligand molecules such as antibodies, tumor homing peptides, and aptamers that target specific receptors on particular types of cancer cells has been particularly effective for selective drug delivery.[207–209] These targeting ligands do not often exhibit anti-cancer properties; however, their conjugation to anticancer drugs or drug carriers such as micelles and liposomes enhances the efficacy and therapeutic index of the chemotherapeutics.[210–212] Peptides as drug carriers are believed to be one of the effective approaches to deliver chemotherapeutic agents to the tumor site.[213,214] Despite lacking sufficient stability due to rapid renal clearance, peptides have unique advantages as drug carriers.

Numerous peptides have been identified by phage display for targeting breast cancer cells and have been reported to show promising outcome for targeted delivery of drugs to tumors.[214–217] One such peptide is the dodecapeptide P160, which was identified by random peptide phage display by Zhang *et al*. in 2001 (**Figure 2.1**).[218] Specifically, P160 was isolated via selection rounds of a phage library on the human WAC 2 neuroblastoma cell line. The authors demonstrated a high affinity to MDA-MB-435 and WAC2 cells and low binding to primary HUVEC cells. In another study, it was shown that when intravenously injected, ^{131}I-labeled P160 preferentially accumulated in tumors than in normal organs like heart, liver, spleen, lung, kidney, muscle, and brain.[219] The stability studies for this peptidic sequence in human serum, however, revealed complete degradation by serum proteases after 4 h.

In order to improve specific binding to breast cancer cells, analogs of peptide P160 were screened using a peptide array–whole cell-binding assay.[220] A library of 70 peptide sequences was synthesized on cellulose membrane and screened against human breast cancer cell lines that led to the identification of P18 (**Figure 2.1**), a decapeptide that showed better binding to breast cancer cells than its precursor. A proteolytically stable analog of P18 peptide, namely peptide 18.4 (WxEAAYQrFL), was obtained by

substituting two labile amino acid residues with D-amino acids.[221] P18.4 was found to be safe, with minimal cellular toxicity.[194,195,221] Besides, an analog to P18.4 with r8k substitution (WxEAAYQkFL) was designed to facilitate side-chain attachment of doxorubicin (Dox) and synthesize peptide−Dox conjugate.[222] The conjugate functions as a breast cancer prodrug to selectively target and deliver chemotherapeutic agents to breast tumors with reduced delivery to normal cells. Peptide−Dox conjugates, developed by attaching doxorubicin via an ester linkage, enhanced drug selectivity 40 times more in breast cancer cells than the noncancerous cells compared to the free doxorubicin.[221,222] Recently, we found that P160 and its derivatives bind to 67 kDa keratin 1 (KRT1) on the breast cancer cell surface.[223] Affinity column chromatography followed by tandem mass spectrometry and proteomics was used to identify the target receptor for P160 and P18.4, which is highly expressed on breast cancer cells. Surface plasmon resonance was used to confirm the binding specificity of the peptide to a fragment of KRT1 (387−496 aa, Mw = 38 kDa), and the Kd values found were ~ 1.1 μM and 0.98 μM for P160 and P18.4, respectively.[223]

Our research group has designed a cyclic analog of peptide P18.4 in order to enhance the affinity and specificity toward breast cancer cell lines while maintaining the proteolytic stability. Also, the D-amino acid residues have been eliminated from the peptidic sequence, and as hypothesized, the cyclization imparted sufficient stability to the peptide structure. Therefore, this novel sequence, denoted by C18.4DK, has shown to present excellent stability toward proteolytic degradation. The results show that the present peptide analog display higher uptake by breast cancer cells when compared to the uptake data by noncancerous cells. The focus of this chapter was to investigate the *in vivo* biodistribution of C18.4DK conjugates with the near-infrared (NIR) fluorophore Cy5.5. Mice carrying orthotopic breast MDA-MB-231 tumors were intravenously injected with C18.4DK and monitored to follow the fate of these traceable conjugates, which may be considered as a prototype of a tumor-targeted drug-peptide delivery system.

2.2 Materials and Methods

2.2.1 Materials

Rink amide resin (RAM), O-(1H-6-chlorobenzotriazole-1-yl)-1,1,3,3-tetramethyluronium hexafluorophosphate (HCTU), and the Fmoc-amino acids were purchased from NovaBiochem (San Diego, CA, USA). Piperidine, N,N,-dimethylformamide (DMF), N-methylmorpholine (NMM), trifluoroacetic acid (TFA), phenylsilane (PhSiH3), hydroxybenzotriazole (HOBt), benzotriazol-1-yloxytris(dimethylamino)phosphonium hexafluorophosphate (BOC) and all other chemicals were purchased from Sigma-Aldrich and were used as received unless otherwise stated. The peptide synthesis was performed manually in small plastic columns with a frit at their base for solvent removal under suction and a cap with septum at the top for the addition of reagents. Cy5.5-NHS ester and D-luciferin (potassium salt) were obtained from Molecular Probes (Eugene, OR, USA). Matrigel basement membrane matrix was purchased from BD Biosciences (Franklin Lakes, NJ, USA). Cell culture media, fetal bovine serum (FBS), sodium pyruvate, L-glutamine, nonessential amino acids (NEAAs), penicillin–streptomycin, trypsin EDTA, Dulbecco's phosphate-buffered saline (DPBS), and penicillin–streptomycin–fungizone were purchased from Gibco/Life Technologies (Burlington, ON, Canada).

2.2.2 Cell culture

Cell lines (except HUVEC and luciferase-expressing MDA-MB-231) were purchased from ATCC and cultured in a humidified incubator at 37 °C in 5% CO_2. DMEM supplemented with 10% FBS, 100 IU/mL penicillin, and 100 IU/mL streptomycin was used to culture MCF-7 and MDA-MB-231 cancer cell lines, whereas MDA-MB-435 was cultured in RPMI-1640 media (10% FBS, 100 IU/mL penicillin, and 100 IU/mL streptomycin). The noncancerous human MCF-10A cell line was cultured in mammary epithelial cell medium (MEGM kit from Lonza, USA) supplemented with cytokines, bovine brain extract (BPE), hydrocortisone, human epidermal growth factor (hEGF), insulin, fetal bovine serum (FBS), and

gentamicin/amphotericin-B. Human umbilical vein endothelial cells (HUVEC), a kind gift from the laboratory of Sandra Davidge, University of Alberta, were cultivated in endothelial cell growth media (EGM kit from Lonza, USA) containing 20% FCS, 2 mmol/L glutamine, 100 IU/mL penicillin, 100 IU/mL streptomycin, and 2 ng/mL basic fibroblast growth factor (Roche Diagnostics, Mannheim, Germany). The luciferase-expressing human breast cancer cell line MDA-MB-231 (clone D3H2LN) was received as a gift from the laboratory of Dr. Mary Hitt (University of Alberta). The MDA-MB-231- D3H2LN-luc+ cells were grown in MEM medium supplemented with 10% FBS, 1 mM sodium pyruvate, 0.1 mM NEAAs, 2 mM L-glutamine, 100 IU/mL penicillin, 100 µg/mL streptomycin, and 0.25 µg/mL Fungizone® at 37 °C in 5% CO_2 atmosphere.

2.2.3 Peptide synthesis

The C18.4DK was assembled by solid-phase peptide synthesis (SPPS) method. The side chains of the amino acids were protected as follows: tert-butyl (tBu) for tyrosine, trityl (Trt) for glutamine and 2-acetyldimedone (Dde) for lysine. SSPS was carried out using Fmoc chemistry on RAM resin (substitution 0.79 mmol/g; scale 0.2 mmol), as described previously with some variations.[220,224] Briefly, a solution of orthogonally protected N-α-Fmoc-L-glutamic acid α-allyl ester (Fmoc-Glu-OAll, 3 equiv.), HCTU (3 equiv.), and NMM (3 equiv.) in DMF was added to pre-swelled RAM resin, and the reaction was left for 2 h. The Fmoc protecting group of the coupled amino acid was removed using 20% piperidine in DMF, and the presence of free amino group was confirmed by Kaiser test.[225] After coupling all the remaining amino acids, deallylation was done with palladium (PPh$_3$)$_4$ (0.16 equiv.) and PhSiH3 (16 equiv.) in DCM for 2 h in a gastight syringe with septum. The reaction mixture was washed with diethyldithiocarbamic acid sodium salt followed by Fmoc group removal. Next, the on-resin cyclization was done using BOP (1.95 equiv.), HOBt, (2 equiv.), and NMM (4.5 equiv.) in DMF for 2 h. Removal of Dde protecting group from the side chain of lysine was achieved by treatment with hydrazine monohydrate in DMF (2:98) for 3 min. Cy5.5-

NHS ester was coupled to the lysine side chain to give the labeled cyclic peptide. A mixture of the dye (0.3 mM) and DIPEA (0.15 mM) in anhydrous DMF (1 mL) was stirred for 48 h at room temperature in the dark. After completion of the reaction, Cy5.5-labeled C18.4DK was washed three times with DMF and isopropanol and dried completely. The peptide was fully deprotected and cleaved from the resin with TFA−TIPS−H$_2$O (95:2.5:2.5) at room temperature for 2 h and washed with TFA−DCM (1:9). The acid washings were precipitated by ice-cold diethyl ether. The precipitate was collected by centrifugation and again washed with ice-cold dry diethyl ether. The crude peptide was dissolved in water and purified using reversed-phase (RP) HPLC (Varian Prostar 210, USA), using a Vydac C18 semipreparative (1 cm × 25 cm, 5 µm) column. The flow rate was 2 mL/min with a gradient of 15−55% ACN/water (0.1% TFA) in 35 minutes, and detection was performed by UV absorbance at 214 nm. Mass spectra were recorded on a matrix-assisted laser desorption ionization time-of-flight (MALDI-TOF) Voyager spectrometer (Applied Biosystems, USA).

2.2.4 *In vitro* cellular uptake

Flow cytometry analysis was used to evaluate the uptake of fluorescent-labeled C18.4DK against three human breast cancer cell lines (MCF-7, MDA-MB-231, and MDA-MB-435) and two noncancerous cell lines (MCF-10A and HUVEC). Cell lines were grown in 75 cm^2 culture flasks until a confluence of ~ 80% was achieved. The medium was then aspirated, and cells were washed with PBS (pH 7.4). The cells were dislodged using 0.25% of trypsin−EDTA solution and, if needed, kept at 37 °C for a few minutes to trypsinize them completely. The trypsin was then deactivated using a small volume of FBS-containing growth medium. The suspended cells were collected in a Falcon tube and centrifuged at 500g for 5 min. The resultant pellet was resuspended in medium, and the cells were counted using a hemocytometer. Based on the number of cells, an appropriate volume of medium was added, and cells were seeded in a 12-well tissue culture plate at a density of 1×10^6 in 1 mL of culture medium at 37 °C for 24 h in a

humidified CO_2 incubator. After 24 h, the medium was aspirated, and the cells were washed twice with PBS. Cells were incubated in serum-free medium containing the peptide at a concentration of 1 µM for 30 min at 37 °C. After 30 min of incubation, the cells were thoroughly washed three times with PBS to remove unbound peptide. The cells were then detached, further washed in FACS solution (2% FBS in PBS) and centrifuged at 500g for 5 min. Cell pellets were finally resuspended in FACS solution and analyzed using BD LSR-Fortessa flow cytometer. The unlabeled cells were used as a control, and their autofluorescence represents the cutoff point value, and thus, differentiates them from fluorescent-positive cells. The experiment was performed in triplicates, and 10,000 events were recorded for each sample.

2.2.5 Orthotopic breast cancer mouse model

Female athymic NIH-III mice (4–6 weeks old) were purchased from Charles River (Wilmington, MA, USA). The animal studies were conducted in accordance with the guidelines of the Canadian Council on Animal Care (CCAC) with approval from the Animal Care and Use Committee (ACUC) of the University of Alberta (Edmonton, AB, Canada). Mice were kept on the 2014S Teklad Global 14% protein rodent maintenance diet, which is low on chlorophyll to improve optical imaging clarity. To establish the orthotopic mammary fat pad tumor model, mice were injected with 2×10^6 MDA-MB-231-D3H2LN-luc+ cells in 50 µL solution of 50% Matrigel basement membrane matrix (BD Biosciences, Franklin Lakes, NJ, USA), into the left abdominal mammary fat pad.[226] The mice were used when the tumors reached a size of 300 mm^3 (2 weeks after injection).

2.2.6 Tracking peptide in mice bearing breast MDA-MB-231 tumors

Saline or Cy5.5-labeled C18.4DK in a dose of 3.9 µg per mouse (equivalent to a concentration of 0.1 mg/kg of Cy5.5) [227] was injected to the mice via the tail vein. The animals were then scanned at different time intervals (0.5, 2, 6, and 24 h) using IVIS Spectrum preclinical *in vivo* imaging system (PerkinElmer, Waltham, MA, USA). Three mice per each group were used in all timepoints. For tracking

the *in vivo* bioluminescence, luciferin solution in DPBS (150 mg/kg) was subcutaneously injected into the back neck of each mouse 15 min prior to the imaging procedure. Animals were imaged for 0.5 s, 10 bin, level B. For scanning the fluorescence from the Cy5.5-labeled peptide, mice were imaged for 0.5 s, 10 bin, level B at an excitation and emission wavelength of 680 and 720 nm, respectively. Spectral unmixing was used to analyze the images and perform the autofluorescence subtraction. At defined time intervals (1, 4, and 24 h) following peptide injection, animals were euthanized (n = 3 for each time point); tumor, liver, spleen, and kidneys were excised and soaked in a 12-well plate containing luciferin (300 μg/mL). The organs were then imaged using the IVIS Spectrum imaging system. For *ex vivo* fluorescence imaging, animals were imaged for 0.5 s, 10 bin, level B at an excitation and emission wavelength of 680 and 720 nm, respectively. For bioluminescence imaging, animals were imaged for 0.5 s, 10 bin, level B and the radiant efficiency of the treated groups was subtracted by the signal obtained from the saline group.
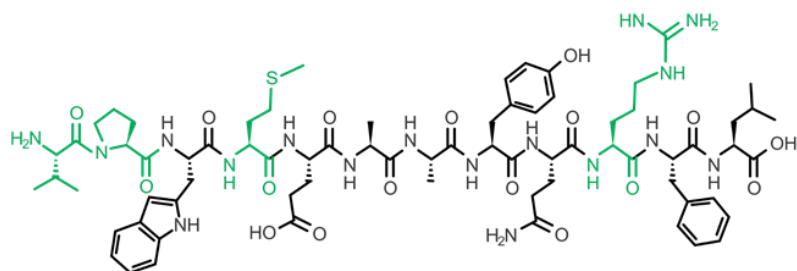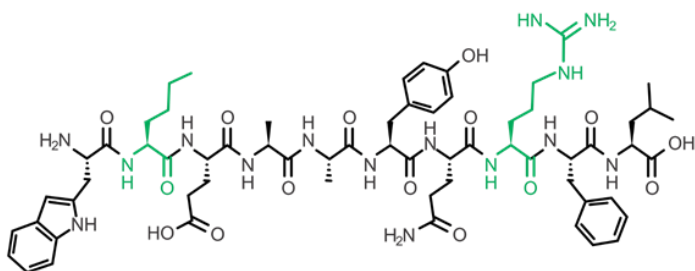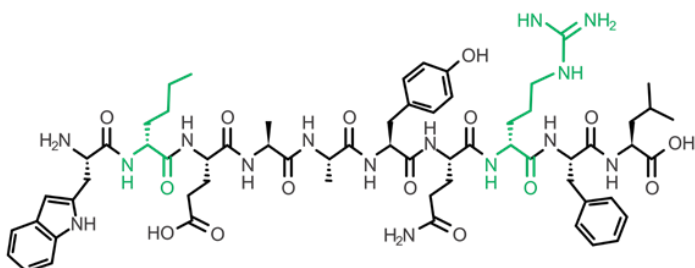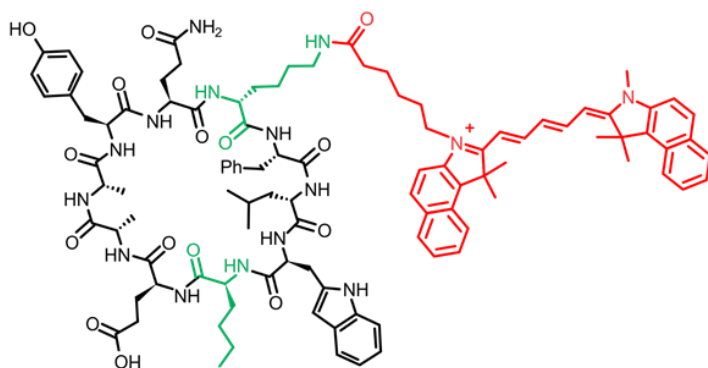
Figure 2.1. Chemical structure and important considerations about the Cy5.5-tagged C18.4DK. All the precursors of this new peptidic analog are also displayed. The amino acid residues highlighted in green were modified, and the NIR fluorophore Cy5.5 is shown in red. *D-amino acids are shown with lower case letters, and "x" represents Nle (norleucine).

2.3 Results and discussion

2.3.1 Preparation of the synthetic peptide

Peptide P18.4 is a positively charged (net charge of +1 in physiological pH) linear decapeptide with two D-amino acids, which confers high stability in biological fluids (i.e., human serum and mouse liver homogenate).[221] Here, we have designed a cyclic analog of that peptide, denoted as C18.4DK (**Figure 2.1**). The design strategy involved the replacement of D-norleucine (x) and D-arginine (r) to L-norleucine (X) and D-lysine (k) amino acid residues, respectively. The cyclization of this peptidic sequence was proven to be efficient for reducing proteolytic degradation (**Figure 2.S1**) while maintaining the breast cancer cell targeting properties.

C18.4DK was synthesized following stepwise solid-phase peptide synthesis on Rink amide resin as the polymeric support. The first amino acid residue coupled into the resin was Fmoc-Glu-OAll through the side chain of glutamic acid. That allyl-protected carboxylate served, after the peptide assembly, as the linker for the peptide on-resin cyclization. Moreover, the Dde-protected amine group from the lysine side chain was used by coupling the NIR-fluorophore Cy5.5 into the peptide. For the preparation of labeled linear peptides, the N-terminal amino group of Trp residue was used to attach β-alanine and FITC. Peptidic products were purified using RP-HPLC, and a yield of ~ 71% was obtained. The elution time was found to be at ~ 28.1 min (**Figure 2.2A**), which is considerably longer than the P18.4 peptide (~ 25.9 min), suggesting that a higher hydrophobicity than its precursor. Results from MALDI-TOF (**Figure 2.2B**) revealed that the observed mass $[M + H]^{+1}$ was 1250.5 (calculated $[M + H]^{+1}$ = 1250.5).
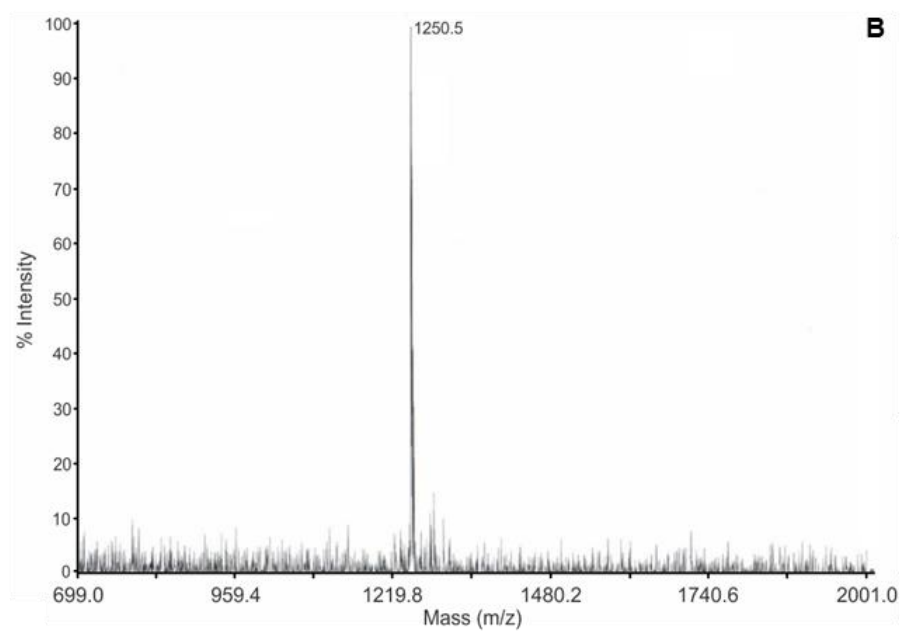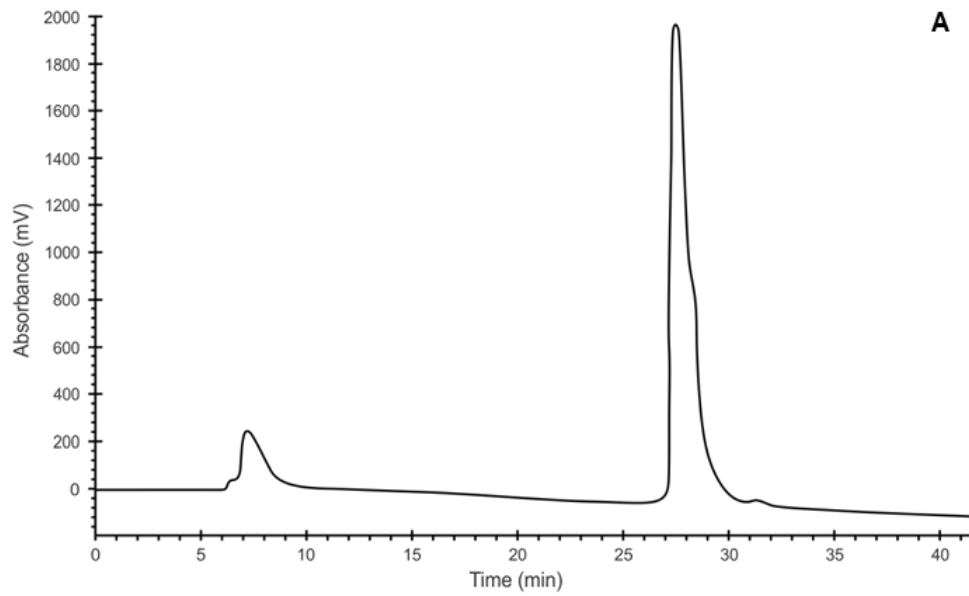
Figure 2.2. Analysis of C18.4DK. (A): HPLC chromatograms using 15-55% gradient of acetonitrile/water with a flow rate of 2 mL/min. (B): MALDI-TOF mass spectra showing the [M+H]$^{+1}$ for the peptide mass.

2.3.2 *In vitro* cell uptake studies

Cell binding and uptake of C18.4DK were investigated using flow cytometry assay. The peptide internalization was poorly accomplished among the noncancerous cell lines HUVEC and MCF-10A so that the fluorescence intensities were close to the untreated groups. On the contrary, the tumor-targeting ability of C18.4DK (at 1 μM) was prominent ($p < 0.05$) among the breast cancer cell lines MDA-MB-435, MDA-MB-231, and MCF-7, especially when the results are compared to the linearized version of this amino acid sequence. Cyclization of the peptide may have led to an increase in hydrophobicity, due to the head-to-tail peptide bond formation, and consequently, enhanced plasma membrane permeability and cellular uptake of the peptidic sequence. Previous studies have shown that cyclization reduces the hydrogen bonding and hydrodynamic radius in solution and increases peptide lipophilicity, thereby, enhancing permeability through lipid-based membranes, which could ultimately result in high cell uptake.[228,229]

Flow cytometry was also employed to determine the binding specificity of C18.4DK using a competitive binding assay (data not shown).[206] The breast cancer cells MCF-7 or MDA-MB-231 were treated in the presence or absence of unlabeled peptide in excess (50-fold). After 30 min, a decrease in % (percent) of fluorescent-positive cells was observed when the cells were incubated with unlabeled peptides. This finding suggested the conjecture that cell uptake of peptides can be reduced when the putative receptor is preoccupied with an excess of ligand. Besides, we have previously shown that conjugation of doxorubicin through the lysine side chain amino group, from the linearized peptidic sequence of C18.4DK, has not impaired the binding specificity and cell uptake of the peptide-drug conjugate in breast cancer cells.[222]
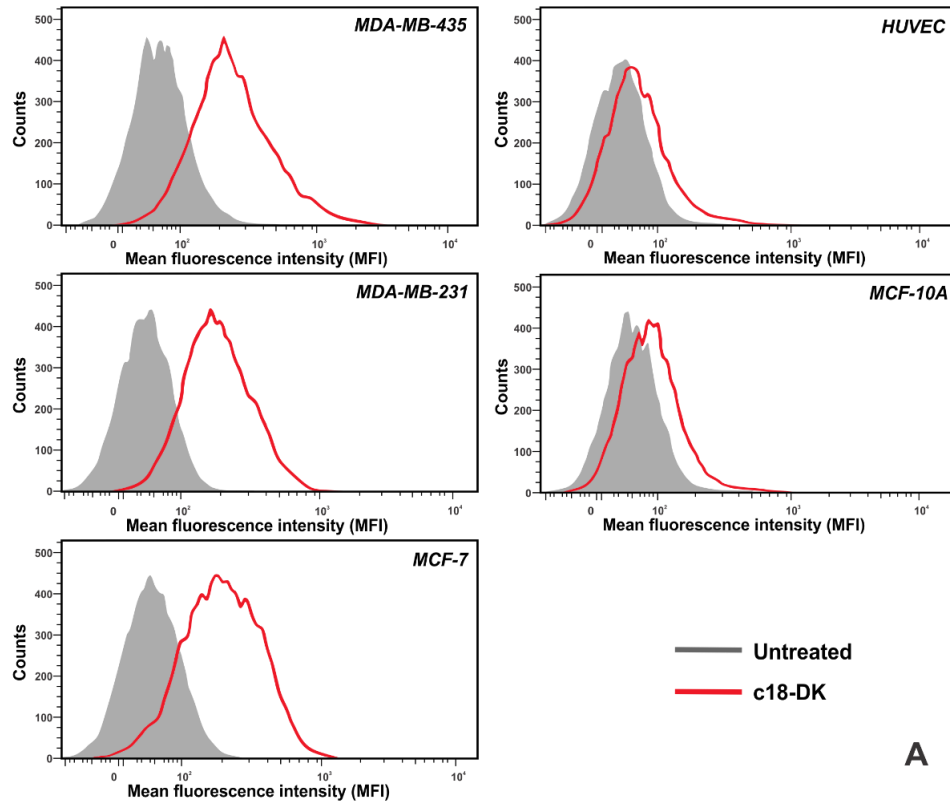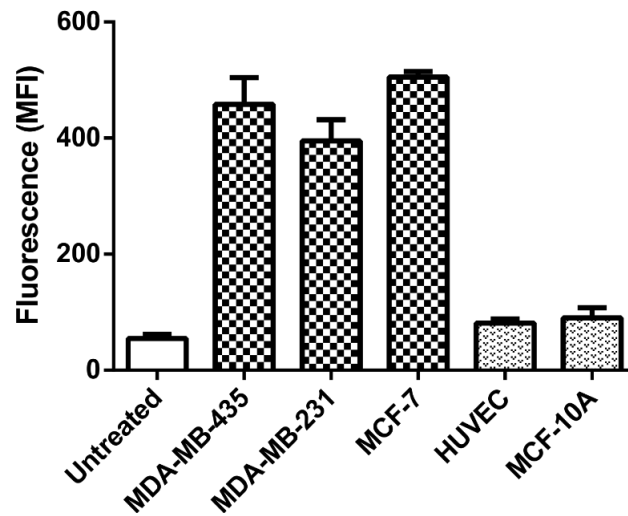
Figure 2.3. C18.4DK uptake by breast cancer (MDA-MB-435, MDA-MB-231, and MCF-7) and non-cancerous (HUVEC and MCF-10A) cell lines, measured by flow cytometry. The peptide concentration was 1 µM, and treated cells were incubated for 30 min at 37 °C. (A): Fluorescence signal from C18.4DK is shown in red, and autofluorescence from the cells in grey. (B): The mean fluorescence intensity (MFI) graph summarizes the histograms and the data were obtained from three independent experiments ± SD.

2.3.3 *In vivo* tracking of the Cy5.5-labeled C18.4DK in live mice

The luciferase-expressing MDA-MB-231 cell line was used in animal studies to be able to visualize the presence of primary and potential metastatic tumors in the animals in this experiment. Bioluminescence imaging of different organs yielded negative results, indicating the absence of noticeable tumor metastasis in other organs (**Figure 2.10A**) under current experimental conditions.

The results of this imaging study in live animals showed the labeled C18.4DK to distribute to several organs nonspecifically within 0.5 h but cleared very rapidly from these organs (within 2 h) as well. At the 2 h time point, the peptide was mainly observed in the liver, kidney, spleen, and orthotopic breast tumor location (**Figure 2.6** and **Figure 2.9-2.11**). *Ex vivo* data following excision of the tumor confirmed these results and showed the presence of the peptide in the tumor tissue at 2 h after injection (**Figure 2.10B**). At 6 h, the peptide was cleared from the tumor but was still observed in potential sites of its elimination, i.e., kidneys and liver, up to 24 h after injection (**Figure 2.7** and **Figure 2.10B**). The preferential tumor accumulation of cyclic peptide 7 at 2 h after injection, in spite of its clearance from other organs, may be attributed to the existence of specific interaction between this peptide and its receptors present only in tumor tissue. A previous study has reported on the biodistribution of P160 peptide, where 1 h following intravenous injection of ^{131}I-labeled P160 to mice carrying subcutaneous MDA-MB-435 tumors, nonspecific distributions in lung, spleen, liver, kidney, and the tumor were seen.[219] In that study, following perfusion of the mice with 0.9% NaCl, peptide uptake in all organs was reduced, but it stayed the same in the tumor, pointing to better peptide interaction with the tumor tissue. We have seen the peptide to be washed quickly (< 2 h after injection) off the nonspecific organs but stay in the tumor at the same time, which is in line with what reported earlier for P160 peptide biodistribution. We plan to investigate the tissue distribution of C18.4DK versus its linearized version in primary and metastatic breast tumor models before and after perfusion of different tissues in future studies.
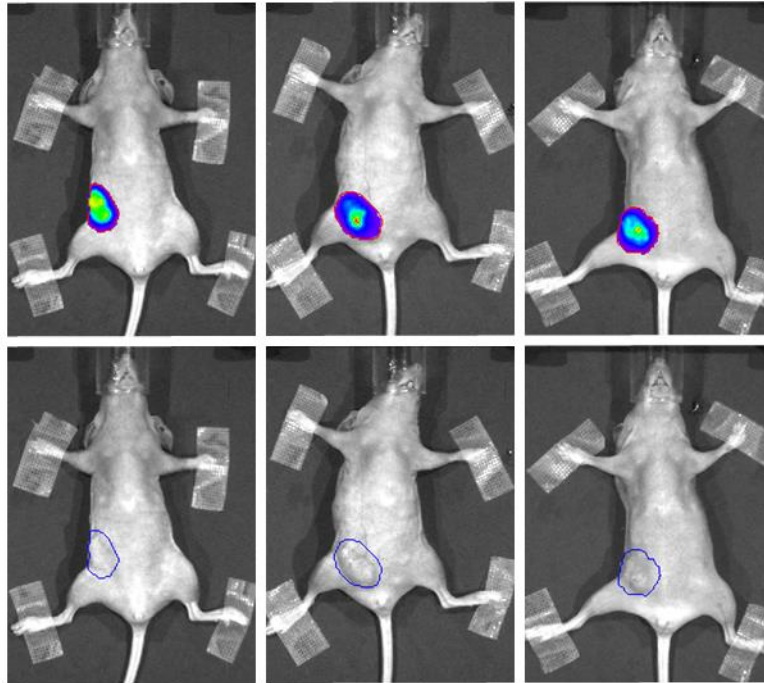
Figure 2.4. *In vivo* study after saline injection. The upper images show the luminescence signal from the MDA-MB-231 luciferase positive cell line after luciferin injection. The bottom images show the absence of fluorescence signal, as there was no Cy5.5-tagged C18.4DK peptide in the circulation.
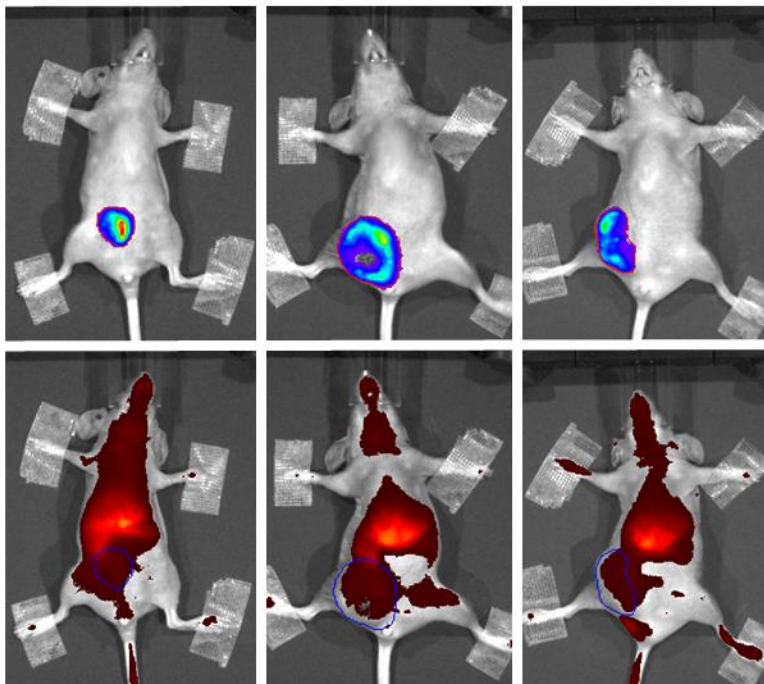
Figure 2.5. *In vivo* study after 0.5 h post-i.v. injection. The upper images show the luminescence signal from the MDA-MB-231 luciferase positive cell line after luciferin injection. The bottom images show the fluorescence signal from the Cy5.5-tagged C18.4DK peptide.
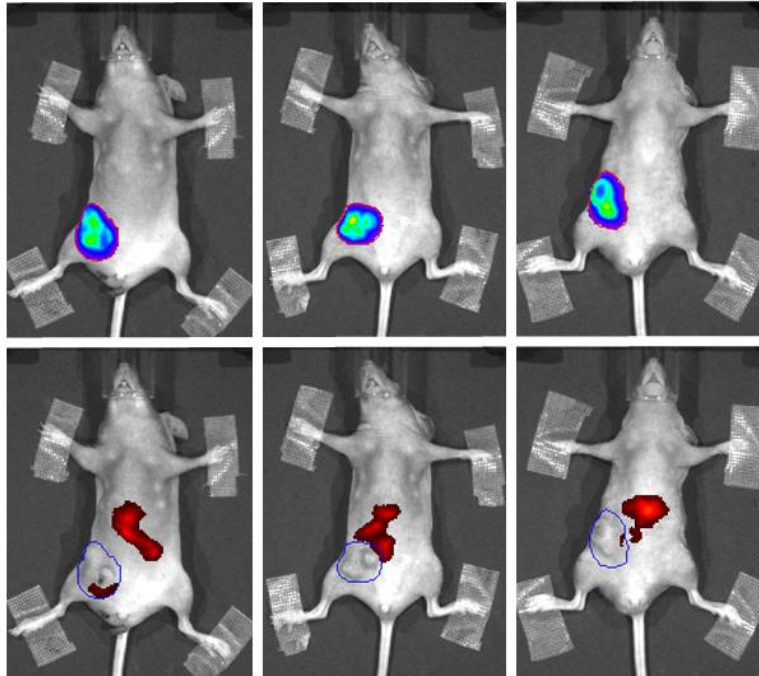
Figure 2.6. *In vivo* study after 2 h post-i.v. injection. The upper images show the luminescence signal from the MDA-MB-231 luciferase positive cell line after luciferin injection. The bottom images show the fluorescence signal from the Cy5.5-tagged C18.4DK peptide.
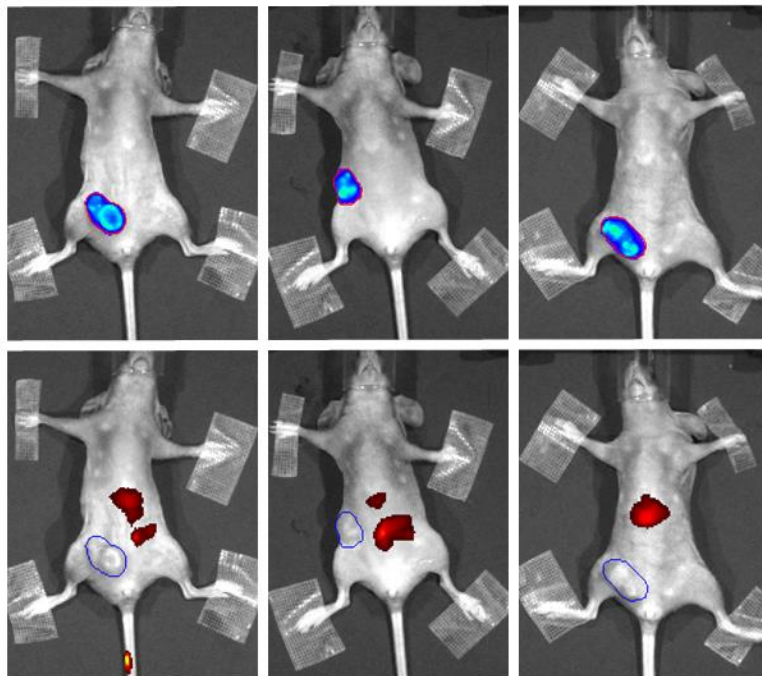
Figure 2.7. *In vivo* study after 6 h post-i.v. injection. The upper images show the luminescence signal from the MDA-MB-231 luciferase positive cell line after luciferin injection. The bottom images show the fluorescence signal from the Cy5.5-tagged C18.4DK peptide.
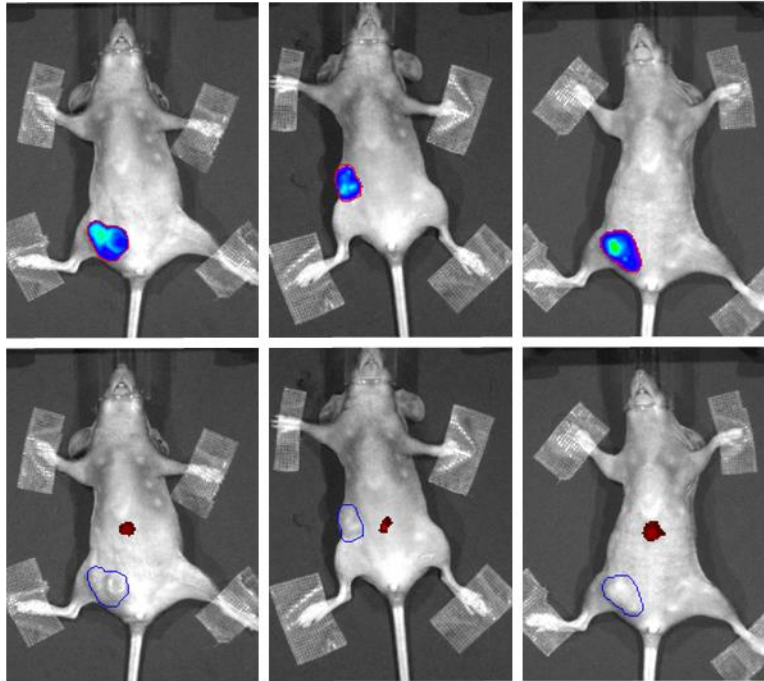
Figure 2.8. *In vivo* study after 24 h post-i.v. injection. The upper images show the luminescence signal from the MDA-MB-231 luciferase positive cell line after luciferin injection. The bottom images show the fluorescence signal from the Cy5.5-tagged C18.4DK peptide.
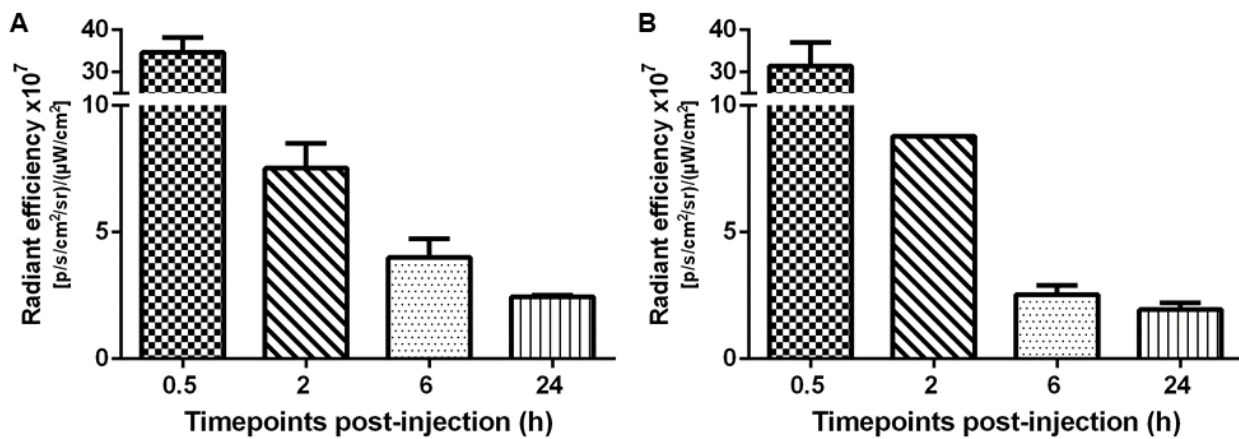
Figure 2.9. Peptide accumulation in the tumor site at different time points after i.v. injection. (A): *In vivo* fluorescence intensity at the tumor site according to the luminescence signal. (B): *Ex vivo* study using the excised tumor.
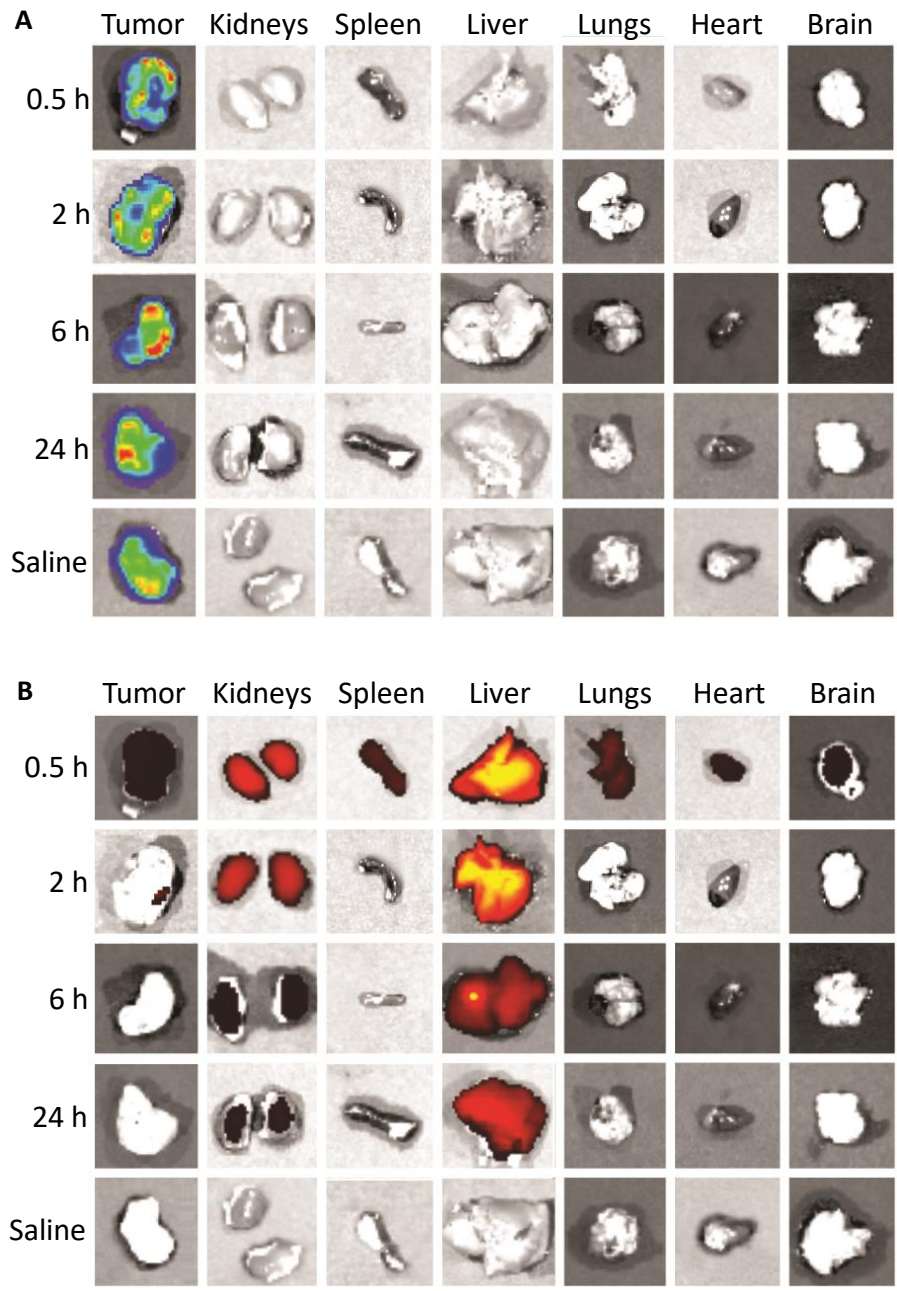
Figure 2.10. *Ex vivo* study after different timepoints. (A): Luminescence signal from the MDA-MB-231 luciferase positive cell line after luciferin injection. (B): Fluorescence signal from the Cy5.5-tagged C18.4DK peptide followed by i.v. injection.
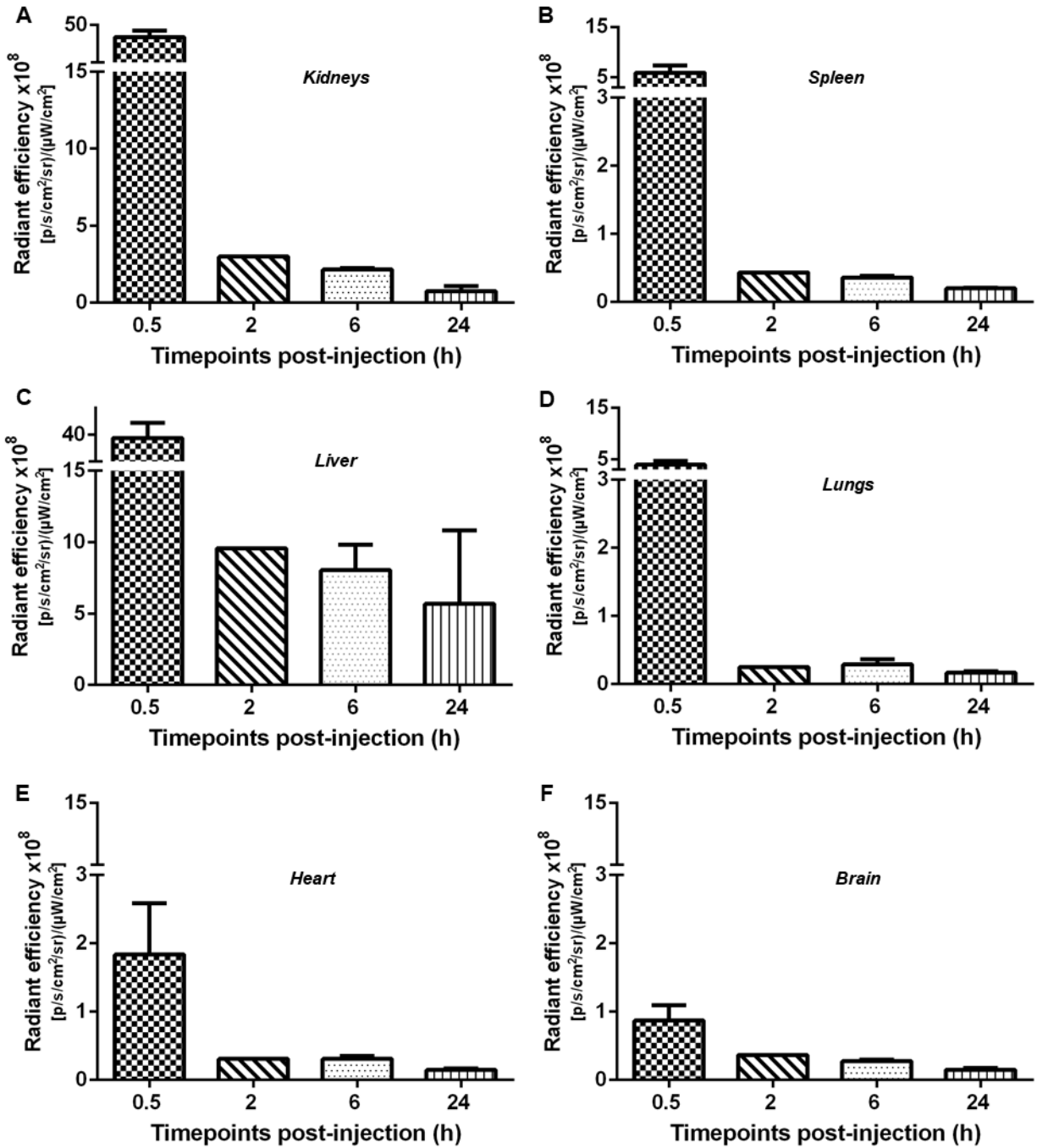
Figure 2.11. Biodistribution of the peptide C18.4DK among (A): kidneys, (B): spleen, (C): liver, (D): Lungs, (E): Heart, and (F): brain, at different time points after i.v. injection.

2.5 Conclusions

The study highlights the design of a novel proteolytically stable cyclic peptide for breast cancer targeting that can be conjugated to chemotherapeutic agents, drug nanocarriers and other systems, in order to increase specificity and efficacy of cancer treatments. Cyclization seemed to have conferred conformational restriction, higher hydrophobicity, and enhancement in the affinity and selectivity toward the target breast cancer cells. *In vivo* biodistribution studies in mice carrying orthotopic breast MDA-MB-231 tumors showed that, although C18.4DK accumulates rapidly and non-specifically throughout the mouse body, its clearance from the tumor site was slower than the other organs, especially at 2 h after injection. Liver and kidneys were the organs with the highest accumulation since they are the potential elimination sites. These results are encouraging and support our conjecture that peptide−drug conjugate could be delivered to the tumor site, followed by the release of the drug and quick removal of the peptide from the body. In our previous study,[222] the linearized version of C18.4DK conjugated with doxorubicin displayed a short half-life of ~ 2 h, when incubated with human serum. New chemistries for conjugating C18.4DK to doxorubicin are currently being investigated to impart better pharmacokinetic profile, which would be useful for cell studies and therapeutic efficacy assessment using mice bearing breast cancer xenografts.

2.6 Supplementary information
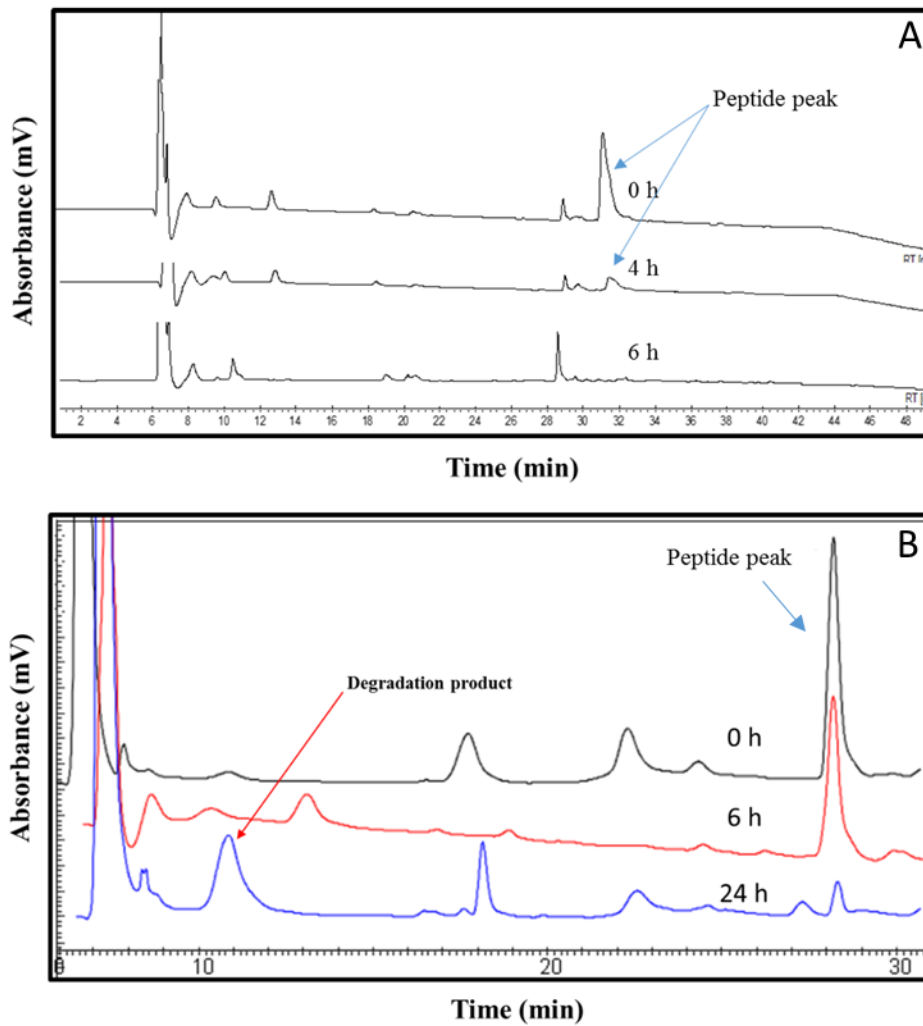
Figure 2.S1. Proteolytic stability assessment of (A): C18.4DK-related, and (B): C18.4DK peptide sequences (i.e., cWXEAAYQkFL and cWXEAAYQ̲KFL, respectively) after incubation with human serum. Peptides were incubated with serum for different time intervals at 37 °C, prior to the RP-HPLC analysis. Peptides eluted around 30-31 min (control) or 27-28 min (C18.4DK) and most of the remaining peaks came from the medium.

Chapter Three

Towards development of nanocarriers for tumor cell-specific siRNA delivery

A version of this chapter will be submitted for publication.

3.1 Introduction

During the past few decades, the understanding of the scientific community over the molecular mediators of cancer etiology, pathology, and progression has robustly expanded.[2,230] The rapid growth of knowledge in this area is partly owed to the development of tools for post-translational silencing of genetic mediators of cancer development, growth, and aggression, which acts by specific downregulating proteins of interest, including RNAi technology.[231] The application of this powerful technology as a therapeutic agent in cancer has met several roadblocks, however.

One of the major unmet needs in this context is the need for efficient and safe tools for the systemic administration of RNAi therapeutics.[232–234] A recent review[235] has shown that in the majority (61%) of all clinical trials involving RNA therapeutics (registered at ClinicalTrials.gov), local administration was chosen over systemic methods, and within those studies, 64% employed naked RNA. Naked nucleotides were also employed in almost half (43%) of the studies using intravenous infusion.[235,236] RNA molecules are well known to present several issues when injected without any carrier, namely rapid degradation by nucleases (even if delivered directly to the target tissue), significant systemic clearance through kidneys, and negligible cell internalization due to their anionic charge, resulting ultimately in a poor activity. On the other hand, delivery systems of nucleic acids show nonspecific toxicity, restricted interaction with receptors in the cell membrane, and limited access to intracellular and molecular targets of nucleic acids of interest.[54,231] These drawbacks are perhaps reflected in the limited use of RNA carriers in clinical trials of these agents.

Our research group has reported on a polymeric micellar nano-system for *in vivo* siRNA delivery to tumors following systemic administration.[237] Downregulation of myeloid cell leukemia-1 (MCL-1) in MDA-MB-435 tumors has been targeted in that report. The anti-apoptotic Bcl-2 family member, MCL-1, has been identified as an important molecular target for different cancers. Upregulation of this protein has been associated with the promotion of cell survival, poor prognosis of cancer patients as well as

resistance to drugs.[238,239] In fact, some reports have identified that the knockdown of MCL-1, as a monotherapy, decreases cell proliferation.[237,240] Moreover, its disruption has shown to sensitize cellular response to many chemotherapeutics, such as paclitaxel,[241,242] doxorubicin,[243,244] etoposide,[245] and osimertinib.[246] We have shown modification of the shell in micellar siRNA delivery systems by RGD4C peptide, to lead to a significant enhancement in tumor accumulation and transfection efficiency of MCL-1 siRNA in MDA-MB-435 cells, *in vitro*. Accordingly, following intravenous administration of RGD4C modified micelles of MCL-1 siRNA, MCL-1 silencing in the MDA-MB-435 xenografts reached 40%, whereas the downregulation was only 20%, on average, for the animals treated with plain polyplex micelles.[237]

Accumulation into solid tumors by nano-sized delivery systems through enhanced permeation and retention (EPR) effect can contribute to increasing the specificity of the loaded therapeutic agents for tumor.[247] However, the high cellular heterogeneity within tumor microenvironment still makes these nanocarriers incapable of specific interaction with cancer over normal cells within the tumor site. Surface modification of nanomedicines with cancer-targeting ligands is particularly important to further enhance the specificity of treatments, once they reach the tumor site through passive diffusion. The uptake of nano-carriers of siRNA by non-cancerous cells, such as fibroblasts, pericytes, immune cells, endothelial cells, present in the tumor tissue can be reduced through modification of nano-delivery systems with cancer-specific ligands, thereby the intratumoral distribution of delivered siRNA towards cancer cells.[2] Peptidic sequences are of particular interest as cancer-specific ligands for this purpose. This is especially due to the ease of engineering of peptide sequences that can be employed to enhance their affinity to the target and stability in biologic fluids.[194,223]

3.2 Methods

3.2.1 Materials

Spermine (SP), N,N-dimethyldipropylenetriamine (DT), methoxy polyethylene oxide (mPEO, 5 KDa), N,N-dicylcohexyl carbodiimide (DCC), N-hydroxysuccinimide (NHS), N,N-diisopropylethylamine (DIPEA), triisopropyl silane (TIPS), trifluoroacetic acid (TFA), tetrahydrofuran (THF), anhydrous dimethylformamide (DMF), dichloromethane (DCM), deuterated chloroform (CDCl$_3$), and 3-(4,5-Dimethylthiazol-2 yl)-2,5-diphenyltetrazolium bromide (MTT) were obtained from Sigma Aldrich (MO, USA). Spectra/Por dialysis tubing (#3, molecular weight cut-off = 3.5 KDa) was provided by Spectrum Laboratories Inc. (CA, USA). α-Benzyl carboxylate-ε-caprolactone (BCL) monomer was synthesized by Alberta Research Chemicals Inc. (AB, Canada). Stannous octoate was purchased from MP Biomedicals Inc. (HE, Germany), which was further purified by azeotropic distillation under reduced pressure. All other chemicals were reagent grade. Cell culture media RPMI 1640, penicillin/streptomycin, fetal bovine serum, trypsin with ethylenediaminetetraacetic acid (trypsin/EDTA), and phosphate-buffered saline (PBS) were purchased from GIBCO (NY, USA). Scrambled and myeloid cell leukemia-1 (MCL-1) siRNA sequences were purchased from Qiagen (CA, USA). 5-carboxyfluorescein(FAM)-labeled siRNA was supplied from Ambion (TX, USA).

3.2.2 Cell lines

The MDA-MB-435 cell line was obtained from Dr. Robert Clark's lab (Georgetown University, USA), and the medium used was RPMI 1640 supplemented with 10% FBS, 1% penicillin/streptomycin (P/S). For HUVEC cells, obtained from Dr. Nadia Jahroudi's lab (Faculty of Medicine, University of Alberta), cell growth was carried out using gelatin (0.2%)-coated dishes. The medium was M199 supplemented with 20% FBS, 2% P/S, 2 mM L-glutamine, and 1% ECGS (endothelial cell growth supplement). Both cells were incubated in 5% CO$_2$ at 37 °C until the desired confluence.

3.2.3 Preparation of acetal-PEO homopolymer

The preparation of acetal-poly(ethylene oxide) (acPEO), which contains two distinct terminal functional groups (i.e., acetal in one end and hydroxyl in the other end), was accomplished according to a method previously reported[248] with some modifications. Briefly, potassium-naphthalene complex was prepared right before the synthesis of the polymer by reacting naphthalene (12.9 mmol) and potassium (14.7 mmol) in anhydrous THF, under argon, for 24 h at room temperature. For polymerization of ethylene oxide, a specific amount of potassium-naphthalene (2 mmol) solution resulted from the reaction mentioned above was added dropwise to a solution of 3,3-diethoxy propanol (2 mmol) in 40 mL dry THF, under argon, for 10 minutes at room temperature. The reaction container was cooled to around zero, and then ethylene oxide (228 mmol) was added into the solution under argon atmosphere. The reaction container was left at room temperature for 24 h under Ar atmosphere. The polymerization reaction was quenched by adding ~ 2 mL acidified ethanol. The polymer was recovered by precipitation in ethyl ether and further purified with THF dissolution followed by re-precipitation in ethyl ether. Finally, acPEO was vacuum dried and stored at -20 °C until use.

3.2.4 Synthesis of di-block copolymers with grafted polyamines

Acetal poly(ethylene oxide)-*b*-poly(α-carboxyl-ε-caprolactone-*g*-dimethyldipropylenetriamine) (acPEO-*b*-P(CL-*g*-DT)), and methoxy poly(ethylene oxide)-*b*-poly(α-carboxyl-ε-caprolactone-*g*-spermine) (mPEO-*b*-P(CL-*g*-SP)) were prepared according to previous reports.[237,249] Briefly, in the first step, poly(ethylene oxide)-*b*-poly(α-benzyl carboxylate-ε-caprolactone) (mPEO-*b*-PBCL or acPEO-*b*-PBCL) were prepared by bulk polymerization of α-benzyl carboxylate-ε-caprolactone (BCL) with a macroinitiator such as mPEO or acPEO at 140 °C for 4 h, using stannous octoate as the catalyst. In the second step, benzyl groups were removed through reduction in the presence of pd on charcoal at a constant stream of hydrogen gas, forming methoxy or acetal poly(ethylene oxide)-*b*-poly(α-carboxyl-ε-caprolactone) (mPEO-

b-PCCL or acPEO-*b*-PCCL, respectively). In the third step, the pendant carboxylic acid groups of PCCL were activated using DCC/NHS in anhydrous THF and then conjugated to SP or DT under stirring in anhydrous DMF at room temperature for 24h. The resulting product was dialyzed (MWCO = 3.5 KDa) against N,N-dimethylacetamide (DMAc) for 24 h, then water for 7 h and freeze-dried and stored at -20 °C until use.

3.2.5 Peptide synthesis and conjugation into acPEO-*b*-P(CL-*g*-DT) copolymer

Synthesis of P18.4 peptide (WxEAAYQrFL) was carried out on 2-chlorotrityl-chloride resin (0.2 mmol, 1 mmol/g), as described by Soudy *et al*..[221] Briefly, the first Fmoc-amino acid, leucine, was coupled to the solid phase using DIPEA for 6 hours. The other amino acid residues were added using an automated peptide synthesizer (Tribute, Protein Technology, Inc., USA). After completion of the synthesis, peptides were cleaved from the resin and all protecting groups were removed using cleavage mixture (90:9% TFA/DCM, 1% TIPS) at room temperature for 90 minutes, followed by washing the resin twice with cleavage reagent. The cleaved peptide combined with TFA washes was concentrated by rotary evaporation. Cold diethyl ether (~ 40 mL) was added to precipitate the peptide and then centrifuged. Crude peptides were dissolved in water and purified using reversed-phase HPLC (Varian Prostar 210, CA, USA). MALDI-TOF mass characterization was carried out using a Voyager spectrometer (Applied Biosystems, MA, USA).

The P18.4 peptide was conjugated into the acPEO-*b*-P(CL-*g*-DP) copolymer, as previously reported.[237,250] In short, micellization was performed by dissolving the copolymer in acetone, and in a dropwise manner, the polymer solution was transferred into deionized distilled water under constant stirring. After acetone evaporation, the micellar solution was acidified to pH 2 (using 0.5 M hydrochloric acid) and stirred for 1 hour at room temperature to convert acetal aldehyde groups. The resulting solution was neutralized with sodium hydroxide (0.5 M) and buffered with PBS. Then, the peptide with a molar ratio of 1:3 of the peptide to the polymer was added to the solution and stirred for 2 h at room

temperature. Sodium cyanoborohydride (NaBH$_3$CN, 10 equiv.) was added into the reaction and stirred for 24 h. The conjugation efficiency of the peptide to polymeric micelles was determined by reversed-phase HPLC method, using a Varian Prostar 210 System measuring the unreacted peptide concentration. The stationary phase was the μBondapack C18 analytical column (10 μm 3.9× 300 mm, Waters Corp., MA, USA), while the mobile phase consisted of 0.1% TFA (aqueous, solution A) and acetonitrile (solution B), using the following gradient flow (1 mL/min): (i) 100% A for 1 min, (ii) linear gradient from 100% A to 60% A in 20 min, (iii) linear gradient from 60% A to 0% A in 4 min, (iv) 0% A for 2 min, (v) linear gradient from 0% A to 100% A in 4 min, and (vi) 100% A for 5 min. Detection was performed at 214 nm using a Varian 335 detector (Varian Inc., Australia). The concentration of unreacted peptide was quantified based on a calibration curve with known concentrations of P18.4 peptide (0.5-1000 μg/mL). The amount of conjugated peptide was calculated by subtracting the amount of unreacted peptide from the initial amount of the peptide. The unreacted peptide was then removed through dialysis (MWCO = 3.5 KDa) against deionized distilled water (48 hours) and lyophilized.

3.2.6 Polymer characterization

Proton nuclear magnetic resonance (^{1}H NMR) was used to characterize the synthesized copolymers. All samples, including the intermediate products, were dissolved in deuterated chloroform (CDCl$_3$) at a concentration of 5-10 mg/mL. Their spectra were recorded using the Bruker Avance III 600 MHz spectrometer (Bruker BioSpin Corporation, MA, USA). The data were processed using the Bruker software TopSpin 3.5. Based on the integration of proton signals from the poly(ethylene oxide) and poly(caprolactone) segments (-CH$_2$CH$_2$O-, δ = 3.65 ppm and -OCH$_2$-, δ = 4.05 ppm, respectively), degree of polymerization (DP) of PCL blocks was calculated, and they were used to determine the number average molecular weight (Mn) of block copolymers. Moreover, the ratio of integration for the signals of the selected methylene hydrogens of the polyamines (-NHCH$_2$- δ = 2.1–3.2) to the selected methylene

hydrogens of the PCL segments (-OCH$_2$-, δ = 4.05 ppm) was used to estimate the polyamine substitution levels.

Gel permeation chromatography (GPC) was used to determine the weight (Mw) and number (Mn) average molecular weight, and the molar-mass dispersity (Ð, Mw/Mn). The measurements were performed on a system equipped with a triple detector array (Viscotek Corp., TX, USA), connected to two Waters columns (Strygel HR2 and Strygel HR4E). The mobile phase was 0.22 µm filtered THF (HPLC grade) at a flow rate of 0.8 mL/min. The injection volume was 20 µL at a polymer concentration of 5-10 mg/mL. Molecular weights were calculated based on polystyrene standards (3.7, 5.0, 9.9, 13.0, and 76.0 KDa) using the universal calibration.

3.2.7 Preparation of micelles, siRNA micelleplexes, and their characterization

Polymeric micelles were formed through self-assembly of block copolymers using dialysis method.[251] To sum up, polymers or a mixture of polymers were dissolved in DMF, added dropwise into deionized distilled water under constant stirring at room temperature for 2 h and then the organic solvent was removed through dialysis (MWCO 3.5 KDa) against deionized distilled water. Polymeric micelles were then centrifuged and filtered through a 0.22 µm membrane to remove possible aggregates. For siRNA complexation, mPEO-*b*-P(CL-*g*-SP) copolymers or the combination of mPEO-*b*-P(CL-*g*-SP)/acPEO-*b*-P(CL-*g*-DT) or mPEO-*b*-P(CL-*g*-SP)/P18.4-PEO-*b*-P(CL-*g*-DT) in a molar ratio of 2:1, were used to prepare the polyplex micelles. The formed polymeric micelles were incubated with siRNA solution at 37 °C for 30 min in 0.1 M HEPES buffer (pH 6.5).

Polymeric micelles formed without siRNA complexation were denoted Mic-PCCL or Mic-SP, and their composition was copolymers by themselves, either mPEO-*b*-PCCL or mPEO-*b*-P(CL-*g*-SP), respectively. In contrast, micelleplexes were composed of mPEO-*b*-P(CL-*g*-SP)/siRNA, called Mic-SP-plex.

The non-targeted and the targeted versions were coined as Plain-Mix-plex and P18.4-Mix-plex, respectively, as described in Table 2 and S2.

The self-assembled structures were characterized for their hydrodynamic size, ζ-potential (ZP), and critical micellar concentration (CMC), using Zeta-Sizer Nano (Malvern Instruments Ltd., Malvern, UK). Dynamic light scattering (DLS) analyses were performed at a scattering angle of 173° at 25 °C.

3.2.8 Gel retardation assay

The binding between siRNA and the polymeric micelles was assessed by agarose gel electrophoresis. Micelleplexes were prepared by mixing 8 μL of 0.1 M HEPES buffer (pH 6.5) with 4 μL of scrambled siRNA (containing 2 μg siRNA) and 8 μL of serially-diluted concentrations of polymeric micelles (containing polymer:siRNA ratios w/w ranging from 0:1 to 16:1). After 30 min of incubation at 37 °C, 4 μL of 6x sample buffer (50% glycerol, 1% bromophenol blue, and 1% xylene cyanol in TBE buffer) was added, and the samples were loaded into a 2% agarose gel containing RedSafeTM (1X) nucleic acid staining solution (iNtRON Biotechnology Inc., Korea). Electrophoresis was performed at 70 mV for 15 min, and the resulting gels were recorded under UV-illumination.

The polyplex micelles were also challenged regarding their ability to release siRNA in the presence of the competing polyanionic heparin. For this purpose, only the polymer:siRNA ratio of 16:1 (w/w) was used, and the micellar complexes were incubated with increasing concentrations of heparin sulfate (0.1, 0.8, 1.5, 3.0, and 6.0 mg/mL) at 37 °C for 1 h. Samples were resolved in agarose gel using the same method described above.

The protective role of polyplex micelles (both Plain-Mix-plex and P18.4-Mix-plex) against siRNA degradation in the presence of fetal bovine serum (FBS) was also evaluated. Different polymer:siRNA ratios (from 0:1 to 16:1) were used, and the formed micelleplexes were incubated with 25% FBS at 37 °C

for 24 h. After that, samples were incubated for 1 h with an excess of heparin (6.0 mg/mL). Intact free siRNA percentage was estimated by resolving the samples through the agarose gel.

All the pictures captured under UV-illumination, after electrophoresis, were processed using the ImageQuantTM TL software (GE Healthcare, Bucks, UK). The density of each band was determined, and the percentage of bound and or released siRNA was calculated based on the controls. Experiments were performed at least in triplicate.

3.2.9 Effect of micelles and micelleplexes on cellular metabolic activity

MDA-MB-435 cells were treated with mPEO-*b*-P(CL-*g*-SP)/siRNA micelleplexes at a polymer:siRNA ratio of 16:1 (Mic-SP-plex's), using a scrambled siRNA sequence and siRNA doses of 100, 200, and 300 nM, or with micelles formed by mPEO-*b*-PCCL copolymers (Mic-PCCL's), in a polymer concentration equivalent to complexes containing 100, 200, and 300 nM siRNA. Similarly, treatments composed of non-targeted (Plain-Mix-plex) and targeted (P18.4-Mix-plex) mixed micelle polyplexes were also assessed. The micellar structures were incubated with MDA-MB-435 cells for 3 h. After that, an aliquot of 20 µL of MTT solution (5 mg/mL in PBS) was added to each well and incubated at 37 °C for 2 h. Then, the medium was removed, 100 µL of DMSO was added, and the optical density was measured at 570 nm using a Synergy H1 Multi-Mode microplate reader (BioTek Instruments, VT, USA). The % cell viability was calculated based on the MTT absorbance in treated cells over that for the untreated cells. The presented data correspond to at least three independent measurements.

3.2.10 Cell uptake assessment

Flow cytometry was used to compare the level of siRNA delivery to MDA-MB-435 and HUVEC cells among polyplex micelles containing the peptide P18.4 (P18.4-Mix-plex) with their plain counterparts (Plain-Mix-plex). The experiments were carried out using 5-carboxyfluorescein (FAM)-labeled scrambled siRNA. Confluent cells (~ 70%) were treated in triplicate in 24-well plates with 50 nM siRNA at a

polymer:siRNA ratio of 16:1 (w/w). After 24 h, cells were trypsinized, washed in PBS three times, fixed in 2% paraformaldehyde solution, and subjected to flow cytometry using a FACS CANTO II flow cytometer (Becton Dickinson, CA, USA). Single cells were properly gated, and the median fluorescence intensity (MFI) from the FAM-siRNA was quantified after a minimum of 10,000 events. Moreover, another flow cytometry technique was used to confirm siRNA delivery profiles. For this experiment, in addition to the FAM fluorescence (green), nucleus and endosomes were also stained with Hoechst NucBlue® (Invitrogen, CA, USA) and LysoTracker® Deep Red (Life Technologies, NY, USA), respectively. The data were acquired using ImageStreamX® Mark II imaging flow cytometer (Amnis/EMD Millipore, WA, USA) using 1,000 events. All experiments were performed in triplicate.

3.2.11 Assessment of MCL-1 downregulation by RT-PCR

Cells were treated with P18.4-Mix-plex and Plain-Mix-plex, using 100, 200, and 300 nM of scrambled or MCL-1 siRNA (polymer:siRNA ratio = 16:1, w/w), in a 6-well plate for 48 h. After that, the total RNA was extracted using RNeasy and QIAshredder (Qiagen, Hilden, Germany) according to the manufacturer's recommendations. cDNA was synthesized according to Invitrogen's protocol. Briefly, 200 ng/μL RNA was reacted with a first mix (containing Oligo dT, random primer, and dNTP) and then heated to 65 °C for 5 min. After that, a second mix was added (containing 5 x buffer, DTT, and RNAout), and the samples were heated at 37 °C for 2 min. Lastly, the reverse transcriptase M-MLV was added. A thermocycling of 25 °C for 10 min, 37 °C for 50 min, and 70 °C for 15 min were then applied to the samples. GAPDH was used as the endogenous housekeeping gene (forward sequence: 5'-CAC ATG GCC TCC AAG GAG TAA-3' and reverse sequence: 5'-TGA GGG TCT CTC TCT TCC TCT TGT-3'). For MCL-1, the primers used were the following: forward sequence: 5'- CCT TTG TGG CTA AAC ACT TGA AG-3' and reverse sequence: 5'- CGA GAA CGT CTG TGA TAC TTT CTG-3'. The SYBR® Green qPCR Mastermix (Applied Biosystems, CA, USA) and primers (3.2 μM per sample) were added together with the cDNA of each sample. Real-time PCR

was performed on a RT-PCR (real-time polymerase chain reaction) StepOnePlus™ system (Applied Biosystems, MA, USA). Lipofectamine 2000 (Life Technologies Corporation, CA, USA) was used as a positive control (following the vendor's protocols) and naked siRNA as a negative control. The experiments were performed in triplicate.

3.2.12 Measuring MCL-1 downregulation by western blot

Confluent MDA-MB-435 cells (~ 70%), in 6-well plates, were treated with scrambled and MCL-1 siRNA using peptide-targeted (P18.4-Mix-plex) and non-targeted (Plain-Mix-plex) polyplex micelles in a polymer:siRNA ratio of 16:1 (w/w). After 48 h treatment, total protein extraction was performed by cell lysis with RIPA buffer (including 0.05% protease inhibitor and 0.05% phosphatase inhibitor, EMD Millipore). Protein concentration was determined using the PierceTM BCA Protein Assay Kit (Thermo Scientific, IL, USA). Cell lysates were then treated with SDS and 2-mercaptoethanol, and an equal protein amount of each sample was resolved on SDS-PAGE, followed by the transferring to a nitrocellulose membrane. The membrane was probed with anti-MCL-1 (1:1000, Santa Cruz, # 66026), and anti-β-actin (1:1000, CST, #58169) diluted in 5% BSA in TBS-T buffer. These antibodies were probed with anti-mouse IgG conjugated with horseradish peroxidase (1:1000, Cell Signaling, #7076). The membrane was washed three times with TBS-T after secondary antibody treatment. The bands on the membrane were visualized with PierceTM ECL western blotting substrate (Thermo Scientific, IL, USA) and then exposed to X-ray films (Fuji Films, TY, Japan). Finally, the density of each band was calculated using the ImageQuant TL software. Lipofectamine 2000 and naked siRNA were used as the controls.

3.2.13 Statistical analysis

Statistical analyses were carried out using Graphpad Prism 8.0 (Graphpad Software Inc., La Jolla, CA, USA). Statistical analysis was performed using unpaired Student's t-test or one-way analysis of

variance (ANOVA) followed by Tukey's posthoc test. Data were presented as mean ± standard error of the mean, and the level of significance was set at $p < 0.05$.

3.3 Results

3.3.1 Characterization of PEO-*b*-P(CL-*g*-PA)s

The structure of all synthesized copolymers was characterized by ^{1}H NMR and GPC, and the results are reported in **Table 3.1**, **Table 3.S1**, and **Figure 3.S1**. The degrees of polymerizations (DP) of the PCL segments of the synthesized polymers were calculated by comparing integration values of the methylene protons of (-CH$_2$-CH$_2$O-) corresponding to PEO (δ = 3.65 ppm) and the methylene protons (-CH$_2$O-) of the PCCL (δ = 4.05 ppm) segments. This calculation revealed that the DP of the three synthesized mPEO-*b*-P(CL-*g*-SP) copolymers were around 10, 15, and 20, whereas the DP for acPEO-*b*-P(CL-*g*-DT) copolymer was 12. Similarly, the percentage of SP or DT substitutions on the synthesized polymers were estimated by comparing the ratios of the area under the peaks for protons of polyamines at δ = 2.1–3.2 ppm to -CH$_2$O- of PCCL at δ = 4.05 ppm segments. The estimated percentage of SP or DT substitutions were 27, 55, and 50% for mPEO-*b*-P(CL-*g*-SP) copolymers with DP of 10, 15, and 20, respectively. This corresponded to a number average molecular weight of 7.5, 8.4, and 10.0 KDa according to the ^{1}H-NMR analysis, which was close to the Mn values obtained from the GPC analysis (8.9, 8.8, and 9.4 KDa). Regarding acPEO-*b*-P(CL-*g*-DT) copolymer, 33% of polyamine substitution was observed, and its Mn determined by ^{1}H-NMR and GPC were 6.0 and 6.5 KDa, respectively.

Table 3.1. Characterization of copolymers used for preparing the polyplex micellar structures.

Polymers	Mn (KDa)[1]	SP/DT * conj. (mol%)[1]	Mn (KDa)[2]	Mw (KDa)[2]	Mw/Mn[2]
PEO$_{114}$-b-P(CL-g-SP)$_{10}$	7.500	27	8.900	9.900	1.12
PEO$_{114}$-b-P(CL-g-SP)$_{15}$	8.400	55	8.800	10.100	1.15
PEO$_{114}$-b-P(CL-g-SP)$_{20}$	10.000	50	9.400	10.900	1.15
acPEO$_{101}$-b-P(CL-g-DT)$_{12}$	6.000	33	6.500	6.600	1.02

[1] Based on ^{1}H-NMR;
[2] Based on GPC;
* Molar % conjugation of SP and DT.

The reaction yield of P18.4 peptide synthesis was 63%. A highly pure P18.4 peptide (> 95%) was obtained by the purification of the synthesized P18.4 peptide. MALDI-TOF analysis showed a [M + H]$^+$ at m/z 1,367.9 (calculated 1,367.7). The conjugating reaction of P18.4 peptide with the acPEO-b-P(CL-g-DT) block copolymer had an efficiency of 87%, quantified by HPLC (**Figure 3.S2**). The molar percentage of peptide conjugation was 29% (i.e., 29 moles peptide per 100 moles block copolymer).
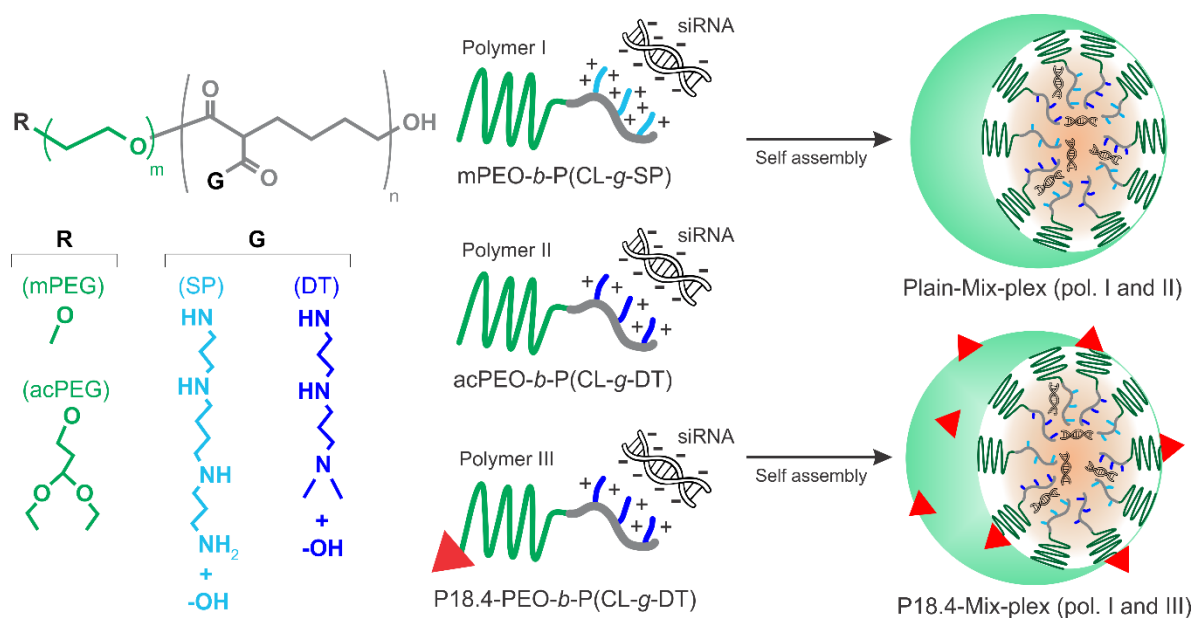
Figure 3.1. Preparation of polyplex micelles formed by complexation between different block copolymers and siRNA.

3.3.2 Characterization of polymeric micelles and micelleplexes

The formation of micelles, using mPEO-*b*-P(CL-*g*-SP) (Mic-SP) alone without siRNA, or polyplex micelles following incubation of siRNA with mPEO-*b*-P(CL-*g*-SP) (Mic-SP-plex) were confirmed by DLS and ZP measurements (**Table 3.2** and **Table 3.S2**). The micellar structures presented a polydispersity index below 0.3, indicating a narrow size distribution, and their average diameters ranged from 64 to 147 nm. For Mic-SP samples that do not contain siRNA, no correlation between the DP and particle size was observed. In contrast, for Mic-SP-plex samples that contained siRNA, block copolymers with higher DP led to the formation of smaller micelles. The ZP of polyplex micelles were slightly negative. This was in contrast to Mic-SP structures, which had no siRNA complex, which showed positive ZP values. No correlation between DP or SP substitution and ZP was found among Mic-SP samples. As there was no significant difference in ZP between Mic-SP$_{10}$ and Mic-SP$_{15}$ as well as Mic-SP$_{10}$ and Mic-SP$_{20}$, only the difference in ZP between Mic-SP$_{15}$ and Mic-SP$_{20}$ was statistically significant. The ZP of Mic-SP-plex$_{10}$, Mic-SP-plex$_{15,}$ and Mic-SP-plex$_{20}$ were also not statistically different.

For mixed polyplex micelles, plain-Mix-plex, and P18.4-Mix-plex, composed of siRNA and a mixture of mPEO-*b*-P(CL-*g*-SP)/acPEO-*b*-P(CL-*g*-DT) or mPEO-*b*-P(CL-*g*-SP)/P18.4-PEO-*b*-P(CL-*g*-DT), were found to have similar physico-chemical properties. As shown in **Table 3.2**, although their hydrodynamic diameters were equivalent (i.e., ~ 77-80 nm), the peptide decoration seems to have reduced the ZP of these micelleplexes, may be due to the unreacted acetal groups or differences in micellar rearrangement that exposed some carboxylate groups closer to the surface.

Table 3.2. Characterization of polymeric micelles and polyplex micelles with siRNA.

Micellar composition	ID	Size (nm)*	PDI	CMC (µM)*	ZP (mV)*
mPEO-*b*-P(CL-*g*-SP)$_{10}$	Mic-SP$_{10}$	(33.6 ± 4.6)	0.53	-	19.9 ± 0.74 [w,y]
mPEO-*b*-P(CL-*g*-SP)$_{15}$	Mic-SP$_{15}$	(74.1 ± 5.1)	0.45	-	18.2 ± 0.39 [w]
mPEO-*b*-P(CL-*g*-SP)$_{20}$	Mic-SP$_{20}$	(59.8 ± 3.7)	0.48	-	20.5 ± 0.96 [y]
mPEO-*b*-P(CL-*g*-SP)$_{10}$/siRNA	Mic-SP-plex$_{10}$	146.7 ± 3.3 [a]	0.32	15.25 ± 0.07 [a]	-4.50 ± 0.16 [a]
mPEO-*b*-P(CL-*g*-SP)$_{15}$/siRNA	Mic-SP-plex$_{15}$	103.4 ± 0.5 [b]	0.27	13.01 ± 0.25 [b]	-4.51 ± 0.23 [a]
mPEO-*b*-P(CL-*g*-SP)$_{20}$/siRNA	Mic-SP-plex$_{20}$	64.2 ± 1.6 [c]	0.22	4.01 ± 0.03 [c]	-3.78 ± 0.22 [a]
Plain Mix Micelle/siRNA [1]	Plain-Mix-plex	77.4 ± 1.1 [d]	0.25	7.61 ± 0.37 [d]	-4.12 ± 0.11 [a]
P18.4 Mix Micelle/siRNA [2]	P18.4-Mix-plex	80.2 ± 0.5 [d]	0.24	7.41 ± 0.06 [d]	-1.38 ± 0.43 [b]

[1] Polymer composition: mPEO$_{114}$-*b*-P(CL-*g*-SP)$_{20}$ / acPEO$_{101}$-*b*-P(CL-*g*-DT)$_{12}$ = molar ratio 2:1

[2] Polymer composition: mPEO$_{114}$-*b*-P(CL-*g*-SP)$_{20}$ / P18.4-PEO$_{101}$-*b*-P(CL-*g*-DT)$_{12}$ = molar ratio 2:1

( ) Values in brackets: Result quality of these DLS analyses indicate "refer to quality".

* Letters superscripted in the columns indicate the results after one-way ANOVA and Tukey's posthoc test. Averages with the same letters indicate no significant difference ($P > 0.05$), and different letters indicate statistical significance ($P < 0.001$).

The micellar thermodynamic stability, reflected by measured CMCs, was dependent on the DP of copolymers that formed the Mic-SP-plex. Polyplex micelles composed of mPEO-*b*-P(CL-*g*-SP)$_{10}$ had the lowest stability (CMC ~ 15 µM), while mPEO-*b*-P(CL-*g*-SP)$_{20}$ presented the best outcome (CMC ~ 4 µM). The CMC values for non-targeted (Plain-Mix-plex) and targeted (P18.4-Mix-plex) mixed micelleplexes were similar (CMC ~ 7 µM). Formation of mixed micelles through the addition of the DT-containing copolymer to Mic-SP-Plex$_{20}$, seemed to have increased the CMC of mixed micelles compared to Mic-SP-plex$_{20}$. This may reflect the lower DP of the PCCL backbone in the P(CL-*g*-DT) copolymer used for the formation of mixed micelleplexes (DP = 12).

Mic-SP micelles, without siRNA complexation, were found to be kinetically not stable as the presence of a destabilizing agent, i.e., SDS, reduced their count rate rapidly over time, indicating rapid

micellar disassembly (**Figure 3.S3**). This can be attributed to the presence of highly positive charged moieties in the micellar core in these structures.

3.3.3 The effect of micellar composition on siRNA binding, release, and protection against degradation

Gel retardation assay was used to understand the capacity of the prepared polyplex micelles in interacting with scrambled 21-bp sequences of siRNA. Mic-SP-plex samples with higher DP of PCCL segment were able to bind siRNA at a lower amount of polymer. Total siRNA binding (i.e., ~ 100%) was achieved at polymer:siRNA ratios of 8:1, 4: 1, and 2:1 for Mic-SP-plex$_{10}$, Mic-SP-plex$_{15}$, and Mic-SP-plex$_{20}$, respectively (**Figure 3.2A** and **Figure 3.S4**).

The siRNA release profile of Mic-SP-plex's under low concentrations of heparin showed that the group with the highest binding capacity (Mic-SP-plex$_{20}$) was the one that required the highest amount of heparin to achieve the siRNA decomplexation from the micelles. However, at the 3 mg/mL heparin, all groups had nearly 100% siRNA released (**Figure 3.2B** and **Figure 3.S4**).
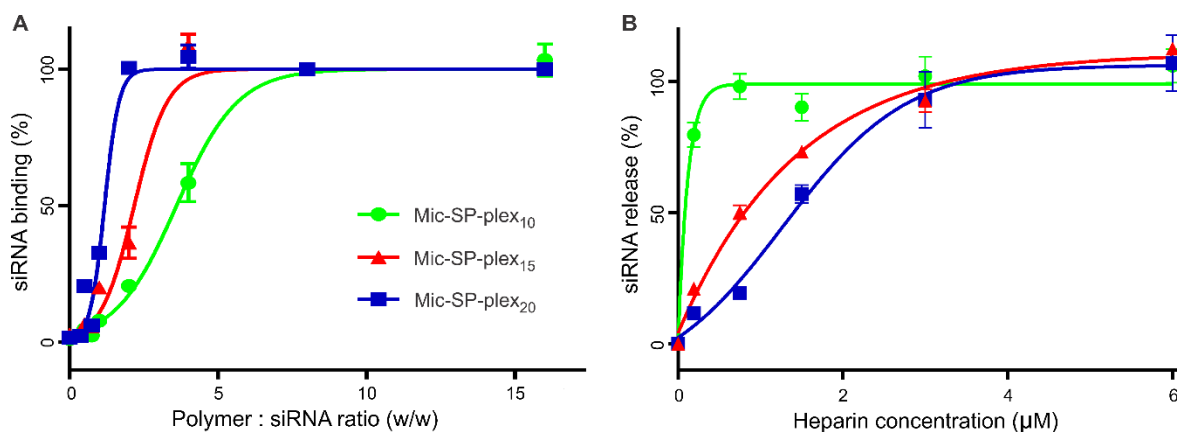
Figure 3.2. Complexation between siRNA and polymeric micelles composed of mPEO-*b*-P(CL-*g*-SP) were tested with different polymer chain lengths. (A): The profile of siRNA binding was investigated using increasing polymer:siRNA ratios (from 0:1 to 16:1). (B): siRNA release was determined with the polymer:siRNA ratio of 16:1 varying heparin concentrations of 0, 0.1, 0.8, 1.5, 3.0, and 6.0 mg/mL. Mic-

SP-plex10, Mic-SP-plex15, and Mic-SP-plex20 were represented by green, red, and blue colors, respectively (n=3). The representative raw gel retardation data used for this analysis is shown in Figure 3.4S.

When comparing Plain-Mix-plex and P18.4-Mix-plex samples, the former showed a slightly stronger complexation with siRNA. Even though the peptide surface modification seemed to have reduced the binding capacity, both micellar constructs were able to reach ~ 100% siRNA binding at a polymer:siRNA ratio of 4:1 (**Figure 3.3A** and **Figure 3.S5**). Similarly, the release profile between non-targeted and P18.4-targeted micelleplexes reflected and confirmed the siRNA binding data. As seen in Figure 3B, at a heparin concentration of ≤ 1.5 mg/mL, Plain-Mix-plex required a higher heparin amount for achieving the same siRNA partial release (**Figure 3.S5**). However, at higher heparin concentration (≥ 3 mg/mL), 100% siRNA release was achieved for both mixed polyplex micelles.

The serum is well known to be rich in nucleases that can degrade the siRNA molecules. In fact, our data confirmed that free siRNA was not stable in 25% FBS, being completely degraded after 24 h incubation, as seen by the absence of signals in the first well for both gels (**Figure 3.3C** and **Figure 3.S5**). Mixed micelleplexes without or with peptides on their surface, showed similar protection capacity. In line with the results of siRNA binding and release, the increase in polymer:siRNA ratio for both micellar structures led to an enhancement in siRNA protection against degradation by serum.
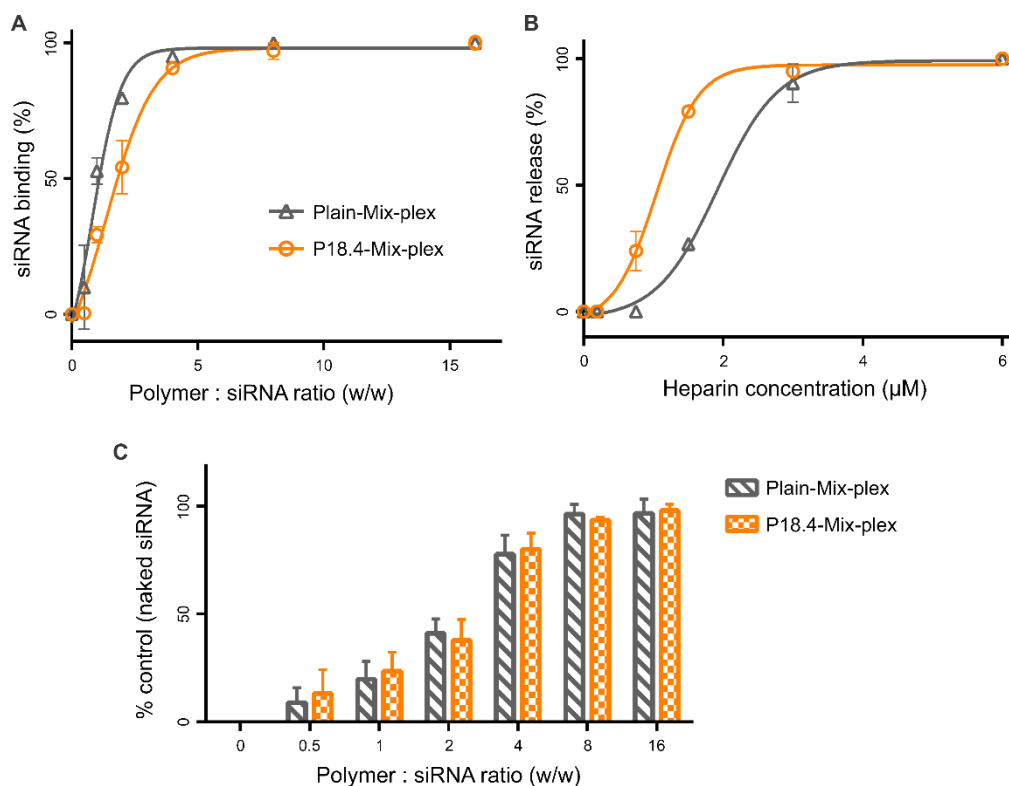
Figure 3.3. Assessment of siRNA binding, release, and protection against degradation by serum among plain and P18.4 polyplex micelles. (A): Profile of complexation between siRNA and micelleplexes composed of different polymer:siRNA ratios (from 0:1 to 16:1). (B): siRNA release from the polyplex micelles with a polymer:siRNA ratio of 16:1 in the presence of increasing amounts of heparin (from 0 to 6.0 mg/mL). (C): siRNA protection against degradation through incubation with FBS (25%, w/v). The intensity of bands on the gels indicated that the siRNA was successfully protected by non-targeted (grey color) and P18.4-targeted (orange color) micelleplexes. The representative raw gel retardation data used for this analysis is shown in Figure 3.5S.

3.3.4 The effect of micellar composition on cell metabolic activity

Mixed polyplex micelles (either Plain-Mix-plex or P18.4-Mix-plex) showed a positive and similar dose-response in terms of cytotoxicity with increasing siRNA and polymer concentrations (**Figure 3.4**). In comparison to mix-micelle/siRNA complexes, Mic-SP-plex, composed of only mPEO-*b*-P(CL-*g*-SP) copolymers, showed higher cytotoxicity at similar siRNA doses (data not shown). This reflects higher

cytotoxicity of SP compared to the DT substituent since the Mix-plex preparations were constituted of mPEO-*b*-P(CL-*g*-SP) and acPEO-*b*-P(CL-*g*-DT) copolymers.
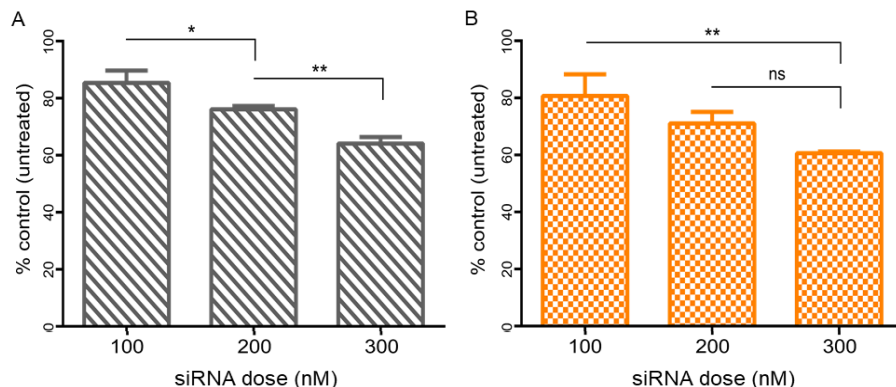
Figure 3.4. Metabolic activity of MDA-MB-435 cells was evaluated after 48 h treatment with (A) Plain-Mix-plex or (B) P18.4-Mix-plex. Their composition was scrambled siRNA, mPEO-*b*-P(CL-*g*-SP), and acPEO-*b*-P(CL-*g*-DT) or P18.4-PEO-*b*-P(CL-*g*-DT). The polymer:siRNA ratio used was 16:1. Bars in the graphs represent the mean ± SEM (n = 3). Differences were compared using one-way ANOVA followed by Tukey's posthoc test (* p < 0.05; ** p < 0.01; ns p > 0.05).

3.3.5 Cell uptake

Our flow cytometry data suggest that the P18.4 peptide surface modification significantly enhanced the association of siRNA with the MDA-MB-435 cells through an energy-dependent mechanism over HUVEC cells (**Figure 3.5A** and **Figure 3.5B**). As seen in **Figure 5B**, when the incubation temperature was 4°C, there was a negligible siRNA uptake by the cells, and this uptake did not change through the incorporation of siRNA in plain or P18.4-modified micelles. When the incubation was conducted at 37°C, plain micelleplexes, containing FAM-siRNA, showed an increase in the fluorescence of cells upon incubation. A further enhancement in FAM-siRNA cell uptake by treating the cells with P18.4-targeted polyplex micelles was achieved which was statistically higher than that of plain micelles at 37 °C (**Figure 3.5B**, p < 0.001; one-way ANOVA, Tukey's posthoc test). This was in contrast to HUVEC cells that did not

show any significant difference upon incubation with P18.4 modified micelleplexes compared to plain ones at the same time frame (**Figure 3.5A**). Free siRNA molecules were not taken up significantly by the cells, irrespective of the incubation temperature, due to their negative charge.
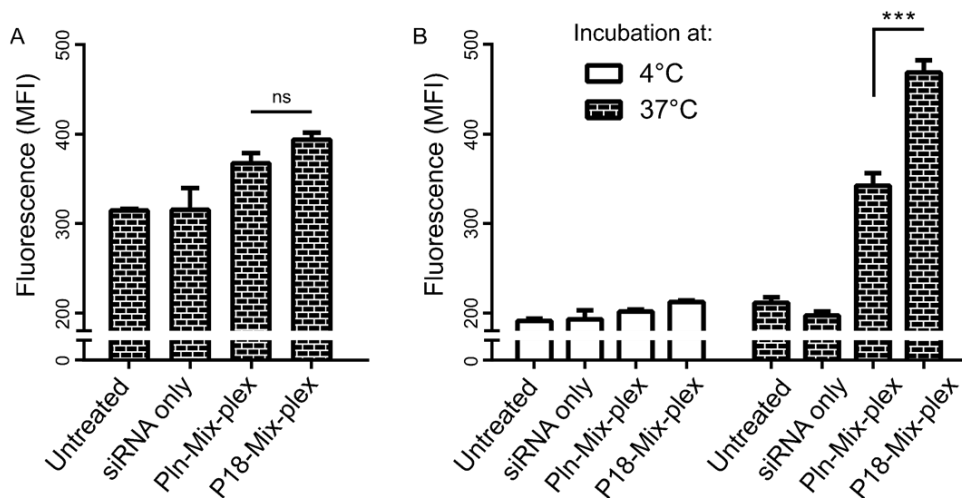
Figure 3.5. Uptake of polyplex micelles containing FAM-siRNA by (A) HUVECs at 37 °C; and (B) MDA-MB-435 cells at 4 and 37 °C. Bar graphs show the median fluorescence intensity (MFI). The outcomes correspond only to signals from single cells after 3 h post-treatment. Bars are the mean ± SEM (n = 3). *** Significance after unpaired Student's t-test (p < 0.001).

Furthermore, imaging flow cytometry was used to investigate the cellular internalization of polymer/siRNA micelleplexes in MDA-MB-435 cells (**Figure 3.6**). Similar to the results of flow cytometry, an enhancement in siRNA cell uptake was observed for P18.4-targeted micelleplexes compared to plain ones (p < 0.05; one-way ANOVA, Tukey's posthoc test), which confirms the effect of peptide surface modification on enhancing siRNA internalization by MDA-MB-435 cells.
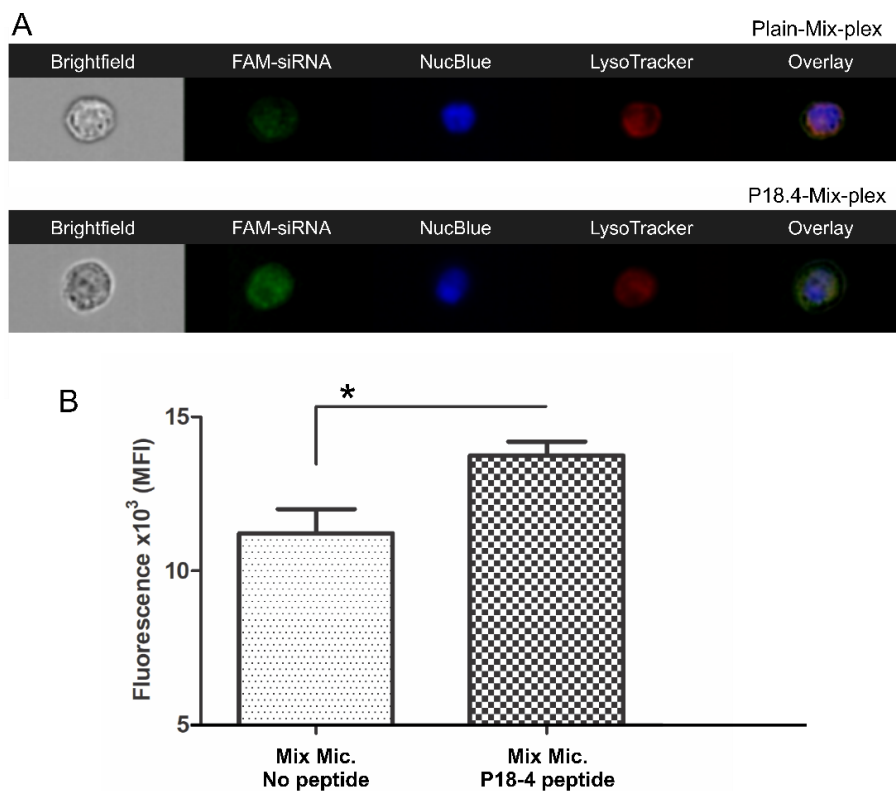
Figure 3.6. Cellular uptake and distribution of FAM-siRNA, complexed into the micellar constructs, using MDA-MB-435 cells. (A): Images represent FAM-siRNA (green), Hoechst (blue), LysoTracker (red), and their merged images. (B): Graphic bars represent the mean ± SEM (n = 3). * Significance after unpaired Student's t-test (p < 0.05).

3.3.6 MCL-1 down regulation through treatment with polyplex micelles

The delivery of MCL-1 siRNA was evaluated by measuring the expression of MCL-1 in MDA-MB-435 cells at both mRNA and protein levels. Treatments using the scrambled siRNA sequence did not change the MCL-1 expression, as expected (**Figure 3.7A**). When the actual MCL-1 siRNA sequence was employed, a siRNA dose of 300 nM was required to observed reduction at the mRNA and protein MCL-1 levels after 48 h treatment (**Figure 3.7B**). Among the other groups that received lower siRNA doses, lipofectamine was the only delivery system capable of bringing down MCL-1 mRNA (by ~ 60%). The silencing effect of plain micelleplexes (300 nM siRNA, polymer:siRNA = 16:1) was ~ 75%, whereas for the

P18.4-targeted micelleplexes (300 nM siRNA, polymer:siRNA = 16:1), the downregulation was around 80%. A trend towards better transfection efficiency at this siRNA dose was observed for P18.4 modified micelles compared to plain ones, that did not reach statistical significance under current experimental conditions (**Figure 3.7**).
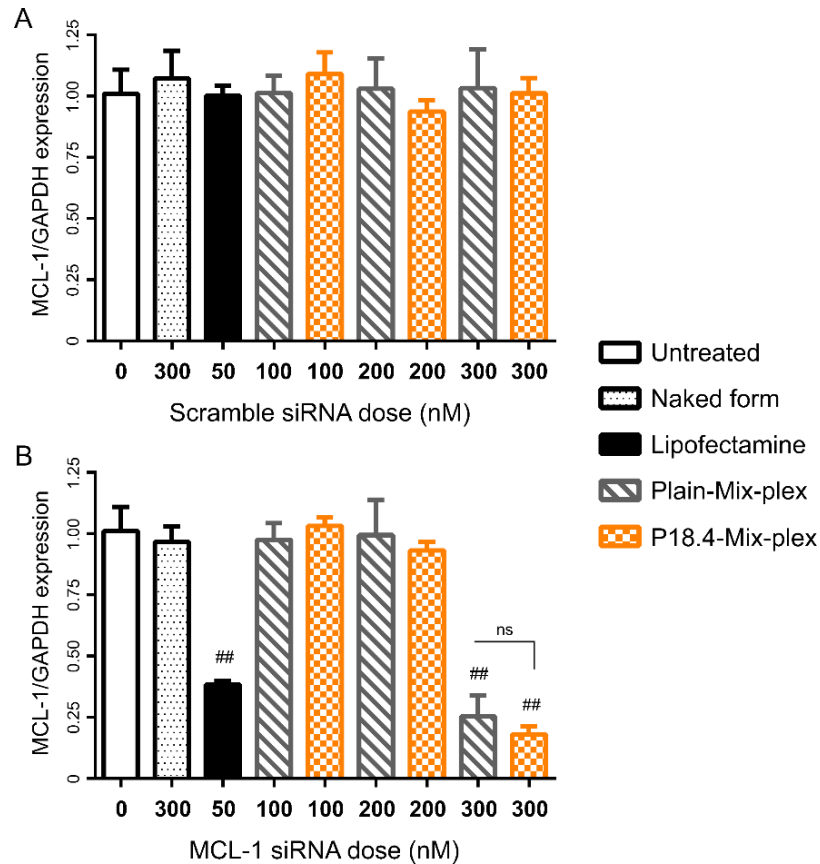
Figure 3.7. Expression of MCL-1, at mRNA level, in MDA-MB-435 cells treated with different micelleplexes for 48 h (polymer:siRNA ratio = 16:1). (A): Scrambled siRNA sequence was used as a negative control and (B): MCL-1 siRNA as the test groups. Bars represent the mean ± SEM (n = 3). ##: Significant difference between scramble and MCL-1 siRNA complexed with the indicated nanoparticle types. ns: No significance between Plain-Mix-plex and P18.4-Mix-plex.

Western blot results corroborated the observation at the mRNA levels, mostly because of the short half-life (~ 1 h) of MCL-1.[252] Interestingly, this data indicated that at the siRNA dose of 200 nM, some

silencing activity among groups treated with both polyplex micelles were observed, and the strong reduction in MCL-1 expression was noticeably high at siRNA dose of 300 nM (**Figure 3.8**). Nevertheless, no difference between transfection of MCL-1 siRNA between P18.4 modified and plain micelles were observed at the protein level under the experimental conditions here.
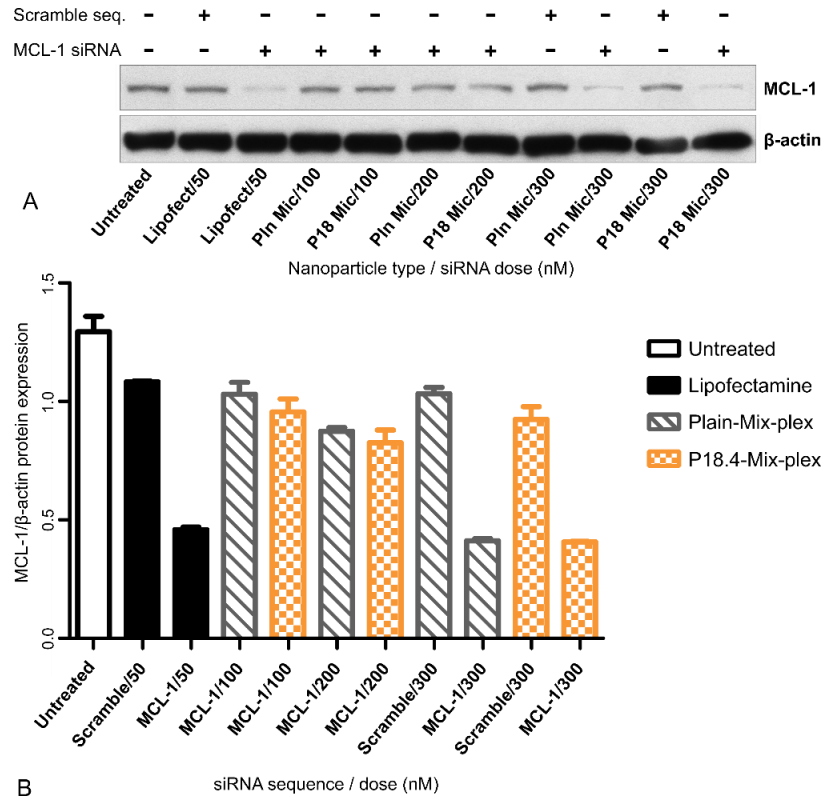
Figure 3.8. MCL-1 protein expression in MDA-MB-435 cells after 48 h treatment with different siRNA doses (polymer:siRNA ratio = 16:1). (A): Panel shows the bands of MCL-1 and β-actin, indicating when scrambled or MCL-1 siRNA sequences were used for each well. (B): Graphic representation of the western blot data. Bar values were calculated from the density of bands for each treatment.

3.4 Discussion

Nano-carriers based on polycaprolactone (PCL) have been the focus of much interest in drug delivery; however, because of the absence of cationic charged entities, these poly(ester)s may not provide adequate means for the accommodation of nucleic acid-based therapeutics. Thus, positively-charged entities need to be attached to PEO-*b*-PCL copolymers in order to make them capable of complexation with siRNA and similar structures. Several studies have reported on different chemical strategies for solving this problem, including the introduction of polyarginine (PEO$_{114}$-*Dlink$_m$*-*b*-Poly(Arg)$_9$-*b*-PCL$_{27}$),[253] poly(2-aminoethyl ethylene phosphate) (PEO$_{45}$-*b*-PCL$_{80}$-*b*-PPEEA$_{10}$),[254] and polyethyleneimine (PEO$_{90}$-*b*-PEI$_{46}$-*b*-PCL$_{20}$),[255,256] as well as the formation of mixed polyplex micelles containing a combination of PEI$_{47}$-PCL$_{14}$ with PEO$_{84}$-PGA$_{52}$ (polyglutamic acid),[257] or PEO$_{45}$-*b*-PCL$_{18}$ with DOTAP (1,2-dioleoyl-3-trimethylammonium-propane).[258]

In the present study, we report on the optimization of polymeric micelleplexes based on PEO-poly(ester)s grafted with polyamines, for siRNA delivery, first. For this purpose, we synthesized polymers with varied DP in the PCL backbone (i.e., DP of 20, 15, and 10). In these series of polymers, SP conjugation was similar between PEO-*b*-P(CL-*g*-SP)s (~ 50-55%). The polyamine conjugation level was, however, lower in polymers of DP 10 (~ 27%). Our data, showed longer PCCL backbones, to introduce enhanced stability to the PEO-*b*-P(CL-*g*-SP) micelleplexes. This was despite a higher number of substituted SP on polymers with DP 20 (approximately 10 SP molecules per polymer chain for polymers with DP 20 on average versus 8 SP molecules on average for polymers with DP 15). The observation may be a reflection of higher hydrophobicity of the core in PEO-*b*-P(CL-*g*-SP) micelles of higher DP for PCL-*g*-SP. It may also be due to a 1:1 balance between the free COOH groups on the P(CL-*g*-SP) and free primary amine of SP substituent leading to the stabilization of P(CL-*g*-SP) core upon complexation with siRNA.

Based on the above observation, PEO-*b*-P(CL-*g*-SP)s with DP of 20 were selected for further studies involving P18.4 modification of micellar siRNA nano-delivery systems. Peptide modification of

micellar complexes of siRNA was achieved through the formation of mixed micelles using a mixture of PEO-*b*-P(CL-*g*-SP)$_{20}$ with P18.4-PEO-*b*-P(CL-*g*-DT) as reported previously by our group for RGD4C modified micelle complexes of siRNA.[237] The PEO-*b*-P(CL-*g*-DT) copolymers were considered advantageous over PEO-*b*-P(CL-*g*-SP) ones for peptide conjugation, owing to the possibility of side Schiff base reactions between aldehyde functionalized and the free amine groups on the SP substituents.[259]

Our research group has previously assessed the use of different grafted polyamines into the PCL block copolymer for siRNA delivery. We found polyamines containing secondary and primary amine groups (e.g., SP) to be more efficient in delivering siRNA into the cell cytosol, compared to the copolymers grafted with polyamines with secondary and tertiary amine groups (e.g., DT).[249] The molecular origin of the proton sponge effect has been attributed to the differential ionization behavior of the tertiary and secondary amine group relative to the primary amine, which tends to initiate first.[260] In the current study, P18.4 modification of micelles through mixing of P18.4-PEO-*b*-P(CL-*g*-DT), which does not have primary amines in its structure, slightly affected the siRNA binding (**Figure 3.3A**), and release from the micellar-siRNA complexes (**Figure 3.3B**). The effect was more noticeable on siRNA release, though. Nevertheless, both structures (plain versus P18.4 modified ones) protected complexed siRNA to the same extent against FBS degrading effects (**Figure 3.3C**). Both systems showed dose-dependent non-specific cytotoxicity against MDA-MB-435 cells, which reached 65-70% cell viability at a siRNA dose of 300 nM and polymer to siRNA w/w ratio of 16:1 following 48 h incubation (**Figure 3.4**).

Of note is the advantage of P18.4 as a targeting ligand on delivery systems because of its high stability in biological fluids. Our data showed micellar surface modification with the tumor-targeting peptide P18.4 to be a promising strategy to make siRNA delivery more specific for MDA-MB-435 cancer cells as opposed to HUVEC cells (model for endothelial cells). This was evident from an increase in the uptake of siRNA by MDA-MB-435 cells when treated by P18.4 modified siRNA micellar complexes over plain ones (**Figure 3.5B**, and **Figure 3.6**). In contrast, the siRNA uptake did not significantly change in

HUVEC cells by P18.4 modification of micelles (**Figure 3.5A**). The findings were in line with previous findings for P18.4-modified PEO-PBCL and PEO-PCL micelles, which did not carry cationic segments in their core structures.[250] Here, the observation on the polyamine containing micelles points to the adequate coverage of polyamine segments in the micellar core, by the micellar shell structures prepared in this study and the role of P18.4 modification in shifting the cellular entry of micelleplexes towards receptor-mediated endocytosis.

Despite the increase in cell uptake, P18.4 modification on the micellar surface did not significantly affect the transfection efficiency of MCL-1 siRNA by its micellar complexes, at studied doses (**Figure 7** and **Figure 8**). This may reflect the similarity in the interaction of plain and P18.4 micellar siRNA complexes with endosomal membrane, restricting siRNA access to the cytosol for both systems despite higher cell uptake of P18.4 modified ones, or be simply an artifact of the current experimental conditions. Further studies are required to clarify the reason behind this observation. Nevertheless, the increased specificity of delivery systems to tumor versus endothelial cells is still envisioned to benefit the intra-tumoral distribution and specificity of silencing activity of P18.4 modified siRNA micelleplexes for tumor cells, *in vivo*. The validity of this hypothesis needs to be examined in future studies in 3D models containing tumor epithelial and endothelial cells and/or *in vivo* models.

3.5 Conclusion

In polymers under this study, those with longer PCL-SP backbone (DP = 20) were shown to be more suitable for siRNA delivery due to the enhanced stability of micelleplexes. P18.4 modification of polymeric micellar siRNA complexes based on PEO-*b*-P(CL-*g*-SP)$_{20}$ increased the specificity of delivered siRNA to tumor versus endothelial cells. The increase in siRNA interaction with cancer cells, however, did not affect the transfection efficiency of delivered siRNA against MCL-1 expression under current experimental conditions. It needs to be determined if this change in specificity, can benefit siRNA intratumoral distribution to epithelial tumor cells versus endothelial cells.

3.6 Supplementary Information
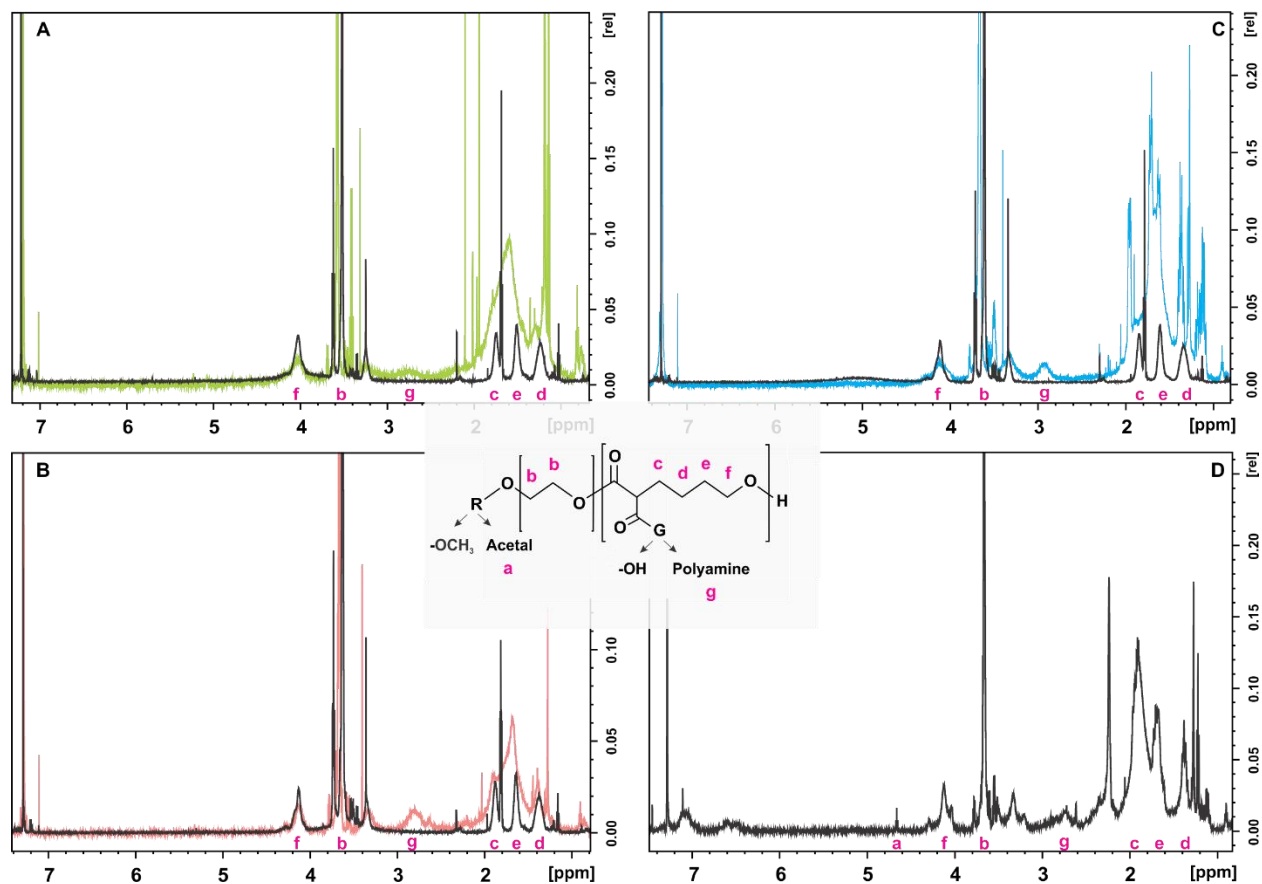
Figure 3.S1. ^{1}H-NMR spectra of the synthesized block copolymers. (A): mPEO$_{114}$-*b*-PCCL$_{10}$ (black line) and mPEO$_{114}$-*b*-P(CL-*g*-SP)$_{10}$ (green line); (B): mPEO$_{114}$-*b*-PCCL$_{15}$ (black line) and mPEO$_{114}$-*b*-P(CL-*g*-SP)$_{15}$ (red line); (C): mPEO$_{114}$-*b*-PCCL$_{20}$ (black line) and mPEO$_{114}$-*b*-P(CL-*g*-SP)$_{20}$ (blue line); (D): acPEO-*b*-P(CL-*g*-DT). Middle panel contains the structure of the copolymer backbone indicating the main proton signal assignments (pink letters).
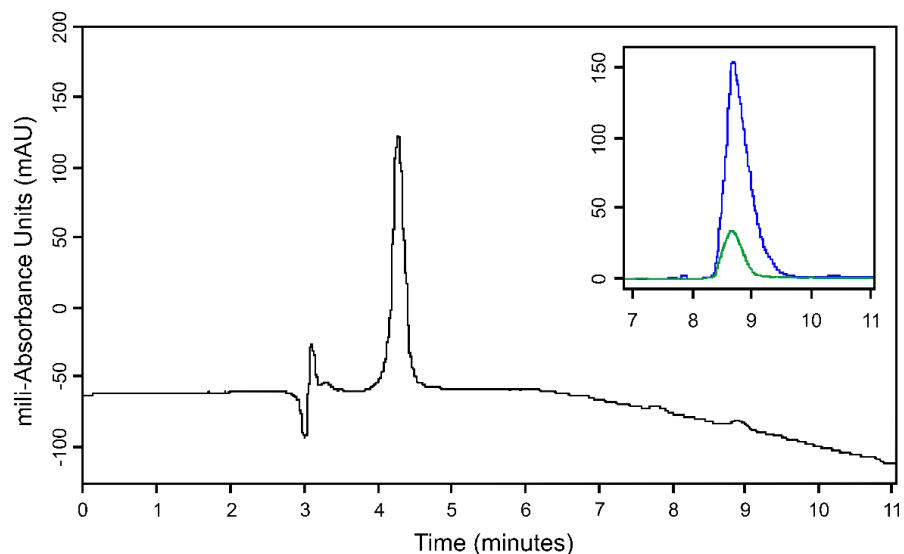
Figure 3.S2. Representative HPLC chromatogram used for assessing the reaction of P18.4 peptide and acPEO-*b*-P(CL-*g*-DT) copolymers. Conjugated peptides were determined by subtracting the amount of free unreacted peptide after 24 h reaction (green line) from the initial peptide added at time zero (blue line). The main panel shows the sample after 48 h dialysis against water to remove the unreacted peptides (black line).

Table 3.S1. Characterization of PEO-PCCL copolymers used for preparing polyamine-grafted block copolymers.

Polymers	Mn (KDa) [1]	Mn (KDa) [2]	Mw (KDa) [2]	Mw/Mn [2]
mPEO$_{114}$-*b*-PCCL$_{10}$	7.200	8.400	9.700	1.15
mPEO$_{114}$-*b*-PCCL$_{15}$	7.900	8.900	9.900	1.11
mPEO$_{114}$-*b*-PCCL$_{20}$	9.500	10.700	16.000	1.50

[1] Based on ^{1}H-NMR; [2] Based on GPC.

Table 3.S2. Characterization of micelles composed of PEO-PCCL copolymers used for preparing polyamine-grafted block copolymers.

Micellar composition	ID	Size (nm)	PDI	CMC (µM)	ZP (mV)
mPEO-*b*-PCCL$_{10}$	Mic-PCCL$_{10}$	70.2 ± 2.6	0.48	8.95 ± 0.11	-3.51 ± 0.16
mPEO-*b*-PCCL$_{15}$	Mic-PCCL$_{15}$	117.9 ± 0.7	0.26	8.05 ± 0.06	-3.81 ± 0.05
mPEO-*b*-PCCL$_{20}$	Mic-PCCL$_{20}$	134.6 ± 3.1	0.21	4.44 ± 0.03	-3.94 ± 0.02
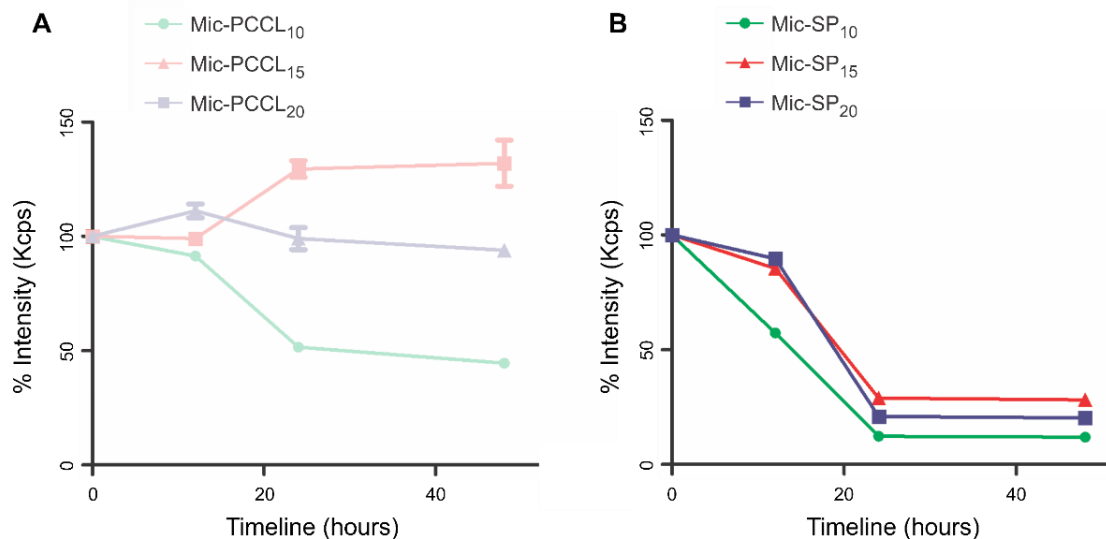
Figure 3.S3. Kinetic stability of micelles incubated with sodium dodecyl sulfate (SDS), a micellar destabilizing agent. The count rates (Kcps) of polymeric micelles, composed of (A): mPEO-*b*-PCCL and (B): mPEO-*b*-P(CL-*g*-SP) copolymers with no siRNA complexation, were measured at different timepoints.
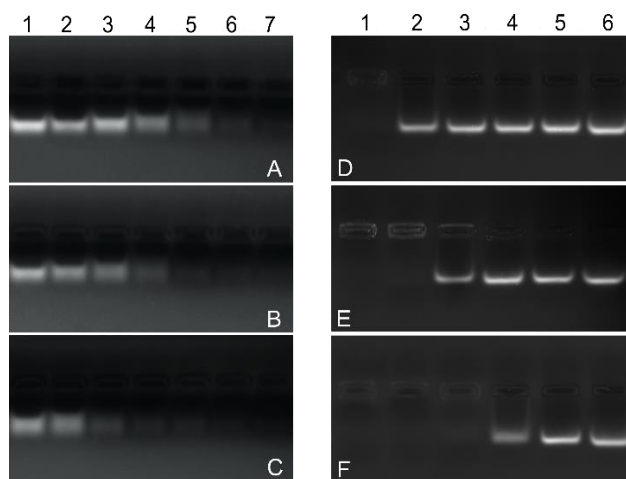
Figure 3.S4. Profile of siRNA binding was evaluated using polyplex micelles composed of (A) mPEO-*b*-P(CL-*g*-SP)$_{20}$, (B) mPEO-*b*-P(CL-*g*-SP)$_{15}$, and (C) mPEO-*b*-P(CL-*g*-SP)$_{10}$ and with different polymer/siRNA ratios (well#1: 0/1; well#2: 0.5/1; well#3: 1/1; well#4: 2/1; well#5: 4/1; well#6: 8/1; and well#7: 16/1). On the right panels, siRNA release was analyzed using (D) Mic-SP-plex$_{20}$, (E) Mic-SP-plex$_{15}$, and (F) Mic-SP-plex$_{10}$. In this case, the polymer/siRNA ratio was fixed to 16:1, varying heparin concentration (well#1: 0 mg/mL; well#2: 0.1 mg/mL; well#3: 0.8 mg/mL; well#4: 1.5 mg/mL; well#5: 3 mg/mL; and well#6: 6 mg/mL).
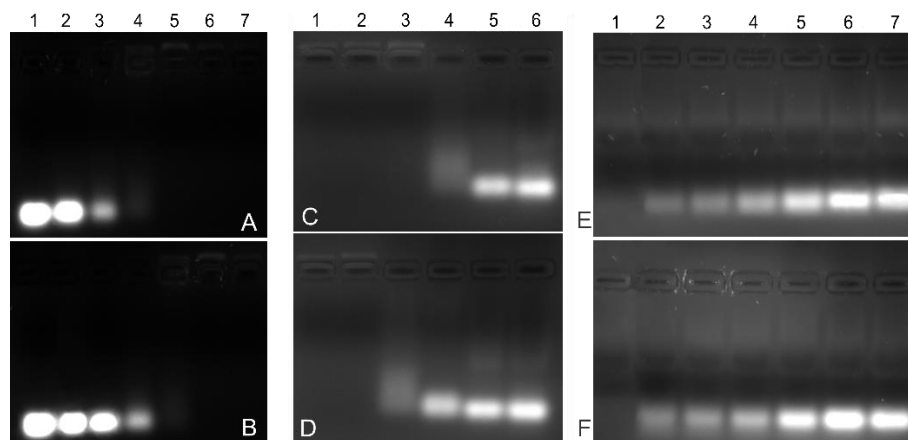
Figure 3.S5. The siRNA binding was investigated using Plain-Mix-plex (A) and P18.4-Mix-plex (B), and increasing polymer/siRNA ratios (well#1: 0/1; well#2: 0.5/1; well#3: 1/1; well#4: 2/1; well#5: 4/1; well#6: 8/1; and well#7: 16/1) were tested. The siRNA release profile was assessed between Plain-Mix-plex (C) and P18.4-Mix-plex (D) with a constant polymer/siRNA ratio (16/1) using different amounts of heparin (well#1: 0 mg/mL; well#2: 0.1 mg/mL; well#3: 0.8 mg/mL; well#4: 1.5 mg/mL; well#5: 3 mg/mL; and well#6: 6 mg/mL). The siRNA protection against degradation in serum (FBS, 25% w/v) was compared between plain (E) and P18.4 (F) polyplex micelles formed in increasing polymer/siRNA ratios (well#1: 0/1; well#2: 0.5/1; well#3: 1/1; well#4: 2/1; well#5: 4/1; well#6: 8/1; and well#7: 16/1). After 24 h incubation 6 mg/mL of heparin was used to release the protected payloads.

Chapter Four

Synthesis and analysis of ^{64}Cu-labeled GE11-modified polymeric micellar nanoparticles for EGFR-targeted molecular imaging in a colorectal cancer model

A version of this chapter has been accepted with revisions in

Molecular Pharmaceutics (submission ID: mp-2019-010434).

4.1 Introduction

Nanoparticles (NPs) can be surface-modified to effectively serve as an *in vivo* biosensor or drug delivery agent. Decoration of NPs with a broad variety of contrast agents, including fluorophores and radionuclides, allow their use as imaging agents for magnetic resonance imaging, computed tomography, ultrasound, optical imaging, single-photon computed tomography (SPECT) and positron emission tomography (PET). The incorporation of radionuclides onto the surface of NPs can produce traceable nanosystems with potential applications as targeted therapeutics and diagnostics in many different diseases, including cancer. Depending on the type of the attached radionuclide, radiolabeled nanosystems can be applied as non-invasive imaging probes for PET using positron emitters such as ^{64}Cu ($t_{1/2}$ ~ 12.7 h), ^{89}Zr ($t_{1/2}$ ~ 3.3 d) or ^{124}I ($t_{1/2}$ ~ 4.8 d), or as therapeutic agents, e.g. for brachytherapy,[261] using therapeutic radioisotopes e.g. ^{125}I ($t_{1/2}$ ~ 60 d), ^{192}Ir ($t_{1/2}$ ~ 74 h) or ^{60}Co ($t_{1/2}$ ~ 5.26 y). In some cases, PET can be combined with other imaging modalities based on the physical properties of the NP platform.[262] In addition to the general passive targeting properties of NPs through the enhanced permeability and retention (EPR) effect, the NPs surface can be decorated with various tumor-targeting vectors for directed delivery to specific cancer biomarkers expressed on the surface of cancer cells. It is also possible to load chemo-therapeutic drugs into the interior of the nanosystems allowing their delivery to cancer tissue, *in vivo*. A NP containing a PET isotope on the surface and a therapeutic payload embedded in the NPs would allow exact *in vivo* tracking of NPs by PET imaging to identify the optimal timeframe in which particles are maximally concentrated in the desired target tissue, facilitating the delivery and controlled release of the drug. The radioisotope ^{64}Cu ($t_{1/2}$ ~ 12.7 h) has a half-life which is compatible with the typical long biological half-life of NPs.[263] ^{64}Cu is readily available through the ^{64}Ni(p,n)^{64}Cu nuclear reaction using small biomedical cyclotrons, and ^{64}Cu emits low energy positrons as well as therapeutically relevant β^- particles. Consequently, ^{64}Cu is well-suited for the radiolabeling of NPs to monitor their biodistribution, stability, and clearance profile *in vivo* while also offering opportunities for potential therapeutic applications.

Polymeric micellar NPs (PMNPs), formed through self-assembly of polyethylene oxide (PEO)-*block*-poly(ester)s present a core/shell structure in which hydrophobic molecules, such as chemotherapeutic, photodynamic and contrast agents, can be encapsulated as a payload to facilitate cancer treatment and/or diagnosis. The main advantage of poly(ester)s, especially polycaprolactones (PCL) lies in their high versatility. Pendant functional groups (e.g., carboxylates, alkynes, acrylates, or halogens) have been successfully attached to the PCL backbone in order to improve crucial polymer properties and/or to tailor for specific applications.[264–266] In earlier studies, our research group has reported on PEO-*b*-poly(α-benzyl carboxylate-ε-caprolactone), PEO-*b*-PBCL, and demonstrated it to be superior to its parental di-block copolymer PEO-poly(ε-caprolactone), PEO-*b*-PCL, especially with regard to micelle stability, *in vivo*.[250] Moreover, those PMNPs containing a PBCL core were found to have both a higher capacity for encapsulating hydrophobic small molecules as well as more desirable release properties.[267]

The EPR effect is a well-known mechanism by which nano-sized particles passively diffuse and accumulate into the vicinity of solid tumors. Although this passive targeting phenomenon plays the most significant role in NP tumor accumulation, only a small portion (~ 1 %) of the injected dose is actually delivered into the tumor.[148] Because of the constant build-up of interstitial fluid, dysfunctional lymphatic drainage, and consequent high intratumoral pressure, there may be a reverse gradient of NP permeation over time. Furthermore, the tumor microenvironment is quite heterogeneous, characterized by the presence of immune inflammatory cells, endothelial cells, fibroblasts, pericytes and others. Therefore, surface modification of NPs using tumor-targeted ligands seems to be a promising strategy to circumvent some of these obstacles.[2,247]

Overexpression of epidermal growth factor receptor (EGFR) represents an established and extensively studied typical biomarker of rapidly proliferating and highly aggressive types of cancers, including colorectal cancer (CRC).[2,268,269] In the past, investigators have used different molecular entities

such as small molecules, nucleic acids, peptides, proteins, monoclonal antibodies and antibody fragments to target EGFR, *in vivo*. Most of the targeting vectors bind to the extracellular domains of EGFR, competing with endogenous ligands such as EGF, TGF-α, epiregulin, and others,[270] and block downstream signaling pathways and/or mark cancer cells for eradication by the immune system.[201,271–277] EGFR is overexpressed in many types of cancers and several EGFR ligands, particularly 12-mer peptide GE11, have been used for targeted cancer therapy,[200,278–281] diagnosis,[227,282–286] and/or both.[287–289] The peptide sequence of GE11 (YHWYGYTPQNVI) shows good binding affinity to EGFR (K_d = 22 nM) without triggering dimerization and mitosis like its endogenous ligand, EGF.[279] Various DOTA- and NOTA-decorated GE11 peptides were labeled with ^{68}Ga, ^{64}Cu, and ^{111}In for PET and SPECT imaging.[282,283,285,286,290] However, none of the radiolabeled GE11 peptides were stable *in vitro* or *in vivo,* limiting their application as EGFR imaging agents.[286,291]

To date, most studies with ^{64}Cu-labeled NP platforms were directed towards specific targeting of various receptor proteins associated with tumor vasculature and angiogenesis, such as integrins, membrane glycoprotein endoglin, or vascular endothelial growth factor (VEGF) receptor.[292–298] Few studies have reported the use of ^{64}Cu-labeled NPs for EGFR targeting. Recently Yang *et al.* described the preparation of gold/iron oxide nanoparticles decorated with an EGFR-targeting affibody, where EGFR-directed molecular targeting was demonstrated though specific blocking studies *in vivo*.[299] Moreover, current literature revealed that radiolabeling of NPs with ^{64}Cu was mainly accomplished with various NOTA- or DOTA-decorated NP platforms according to a post-labeling approach.[300]

The goal of the present study was the synthesis and analysis of ^{64}Cu-labeled NPs prepared by a pre-labeling approach to avoid the modification of the NP surface with a ^{64}Cu binding chelator. This was accomplished by an *in situ* formed ^{64}Cu-NOTA complex containing a diazonium salt motif for subsequent azo coupling to tyrosine residues of EGFR-targeting GE11 peptide or mock peptide HW12 present on the surface of PEO-*b*-PBCL PMNPs. Recently we have successfully applied this labeling technique to other

macromolecules.[301,302] The present study describes the first application of this novel radiolabeling approach to NPs. ^{64}Cu-labeled and GE11-decorated PMNPs were analyzed with PET in the EGFR-expressing HCT116 colon cancer model, *in vivo*.

4.2 Methods

4.2.1 Materials

Methoxy-polyethylene oxide (mPEO, 5,000 Da), ethylene oxide (≥99.9%), 3,3-diethoxy propanol, ascorbic acid, and fetal bovine serum (FBS) were purchased from Sigma (St. Louis, MO, USA). α-Benzyl carboxylate-ε-caprolactone and α-propargyl carboxylate-ε-caprolactone were obtained from Alberta Research Chemicals Inc. (Edmonton, AB, Canada). Stannous octoate was acquired from MP Biomedicals Inc. (Tuttlingen, Germany) and further purified by vacuum distillation. Peptides GE11 (YHWYGYTPQNVI) and HW12 (HYPYAHPTHPSW) were obtained after custom synthesis by Biomatik LLC (Wilmington, DE, USA). [^{64}Cu]CuCl$_2$ was purchased from Washington University School of Medicine (St. Louis MO, USA). Dialysis tubing (MWCO - 3.5 kDa) was purchased from Spectrum Laboratories (Rancho Dominguez, CA, USA). 2-S-(4-Aminobenzyl)-1,4,7-triazacyclononane-1,4,7-triacetic acid was purchased from Macrocyclics, Inc. (Plano, TX, USA). All other chemicals were reagent grade.

4.2.2 Cell lines

Colorectal cancer cell lines with different levels of EGFR expression, HCT116 (CCL-247[TM]) and SW620 (CCL-227[TM]) cells (i.e., EGFR positive and negative, respectively), were obtained from American Type Culture Collection (ATCC, Manassas, VA, USA). Cell growth was done in Dulbecco's Modified Eagle medium (DMEM) supplemented with 10% FBS, 100 u/mL penicillin, and 100 mg/mL streptomycin at 37 °C and 5% CO$_2$.

4.2.3 Peptide and fluorophore conjugation into the block copolymers

Di-block copolymers poly(ethylene oxide)-*block*-poly(α-benzyl carboxylate-ε-caprolactone) (PEO-*b*-PBCL), containing methoxy-PEO (mPEO) or acetal-PEO (acPEO), and tri-block copolymer poly(ethylene oxide)-*block*-poly(α-benzyl carboxylate-ε-caprolactone)-*block*-poly(α-propargyl carboxylate-ε-caprolactone) (PEO-*b*-PBCL-*b*-PPC) were synthesized as previously reported.[250] Briefly, either mPEO or acPEO was used as the initiator for ring-opening bulk polymerization. The reaction was performed under vacuum at 140 °C for 4 h, using stannous octoate (4 drops) as the catalyst. Ring-opening solution polymerization was done to add the third block under reflux with dry toluene for 30 h and with mPEO-*b*-PBCL as macroinitiator.

GE11 and HW12 peptides were covalently attached to the di-block copolymers containing a terminal acetal group from PEO. Polymeric micelles were prepared through co-solvent evaporation method (5 mg/mL). The micellar solution was then acidified to pH 2 (0.5 M HCl) and stirred for 2 h at room temperature. Solution pH was re-adjusted to pH 7 (0.5 M NaOH) and buffered (PBS, pH 7.4). Peptide solution (1% DMSO) was added to the micelles in a peptide:polymer ratio of 1:5 (mol/mol), under constant stirring, for 2 h. Then, $NaBH_3CN$ (10 eq.) was added to the reaction and incubated for 24 h. The resulting micellar solution was dialyzed against water and lyophilized.

Copolymers conjugated with near-infrared (NIR) fluorophore Cy5.5 were prepared using azide-alkyne click chemistry. The triblock copolymer PEO-*b*-PBCL-*b*-PPC (10 µmol) was dissolved in degassed DMSO under constant stirring. A solution of Cy5.5-azide (1 µmol in DMSO) was added followed by ascorbic acid (0.5 µmol) and degassed with argon for30 s. Finally, the Cu-TBTA complex solution (10 mM) was added followed by another argon purge for 30 s. The sealed stirring reaction mixture was incubated at room temperature in the dark for 16 h. Then, the non-reacted dye was washed off by dialysis against DMSO for 24 h. The DMSO was removed by dialysis against water for 24 h and lyophilized.

4.2.4 Characterization of block copolymers

The number average molecular weight ($M_{n, Pol}$) of copolymers was determined by 600 MHz ^{1}H NMR (Bruker Avance III instrument, Billerica, MA, USA) in deuterated chloroform. The degree of polymerization (DP) of PBCL segments was calculated from the peak intensity of methylene protons from PEO block (-CH_2CH_2O-, δ = 3.65 ppm) compared with protons of the methylene group from the PBCL backbones (-OCH_2-, δ = 4.05 ppm). For triblock copolymers, containing propargyl grafts, the length of the third block PPC was determined by comparing proton peak intensity from PEO (-CH_2CH_2O-, δ = 3.65 ppm) with methylene protons from PPC (-OCH_2-, δ = 4.75 ppm). GE11 and HW12 conjugation to acPEO-*b*-PBCL was determined by reverse-phase UV-HPLC (Varian Prostar 210 System). A μBondapak (Waters Corp, Billerica, MA, USA) C-18 analytical column (10 μm, 3.9×300 mm) was used with a gradient of acetonitrile:water (10–70% for a 45 min run time) at a flow rate of 1 mL/min. Detection was performed at 214 nm using a ProStar 335 PDA module (Agilent Technologies, Santa Clara, CA, USA). The grafting of Cy5.5 into the triblock copolymers PEO-*b*-PBCL-*b*-PCC was measured by fluorescence using Synergy H1 multi-mode microplate reader (BioTek Instruments Inc., Winooski, VT, USA) with excitation/emission wavelengths of 673 nm/707 nm.

4.2.5 Preparation of PMNPs

Micellization was carried out by co-solvent evaporation method.[250] Briefly, acetone was used to dissolve the appropriate mix of mPEO-*b*-PBCL and GE11-PEO-*b*-PBCL or HW12-PEO-*b*-PBCL, resulting in 10% (mol/mol) peptide density of total polymer amount. Then the polymer mixtures were added dropwise in double distilled water under stirring (aiming for 10 mg/mL polymer concentration) and incubated overnight without a cap at room temperature with constant agitation. Cy5.5-tagged polymeric micelles were prepared for the *in vitro* cell uptake studies through mixing of tri-block copolymer PEO-*b*-

PBCL-*b*-P(PC-*g*-Cy5.5) with the other copolymers. The amount of Cy5.5 dye in the mixed micelles was 0.4 µg per mg polymer.

4.2.6 Nanoparticle characterization

The size distribution of PMNPs and ζ-potential were measured before and after radiolabeling by dynamic light scattering (DLS) using the Zetasizer Instrument Nano-ZS (Malvern Instruments, Worcestershire, UK). Measurements were made at 25 °C with a scattering angle of 173°. This equipment was also used for determining the molecular weight of PMNPs ($M_{w, NP}$), running a Static Light Scattering (SLS) method. For SLS measurements, different concentrations of PMNP samples were studied applying the Rayleigh equation. Pure toluene was chosen as a reference and the refractive index increment (dn/dc) for the micellar solutions was estimated based on previous studies. The number of unimeric polymer chains that forms one micelle (i.e., aggregation number) was determined by dividing the molecular weight of PMNPs by the number average molecular weight of the synthesized block copolymers ($M_{n, POL}$), obtained from NMR.

4.2.7 *In vitro* cellular uptake studies by colorectal cancer cells

For flow cytometry, HCT116 and SW620 cells were seeded into 12-well plates ($1–1.2 \times 10^5$ cells/well) and incubated at 37 °C for 24 h to reach 70% confluence. Cy5.5-tagged PMNPs were added in a concentration equivalent to 0.2 µg/mL Cy5.5 (triplicate). For competition experiments, both cell lines were pre-treated with excess free GE11 (1.5 mg/mL) for 30 min prior to the addition of GE11-PMNPs. After incubation for 3 h at 37°C, cells were washed three times with PBS, detached from the plates with trypsin, and fixed using 4% paraformaldehyde. The fluorescence signal was recorded using a LSR-Fortessa X20 (BD Biosciences, Franklin Lakes, NJ) and cell-associated Cy5.5 median fluorescence intensity (MFI) was used for PMNP uptake quantification.

For confocal microscopy studies, cells were seeded into 24-well plates containing round cover slips (0.2 mm thickness) at densities of 4-5 × 10^4 cells/well and incubated at 37 °C for 24 h, until 50% confluence. Cy5.5-tagged PMNPs were added (see above). Fixed cells on cover-slips were prepared in DAPI-containing mounting media. Slides were set in the dark for 24 h. Analysis of cell-associated Cy5.5 was carried out on a Zeiss LSM 710 confocal microscope (Carl Zeiss Microscope systems, Jena, Germany) using blue (Ex: 405 nm; Em: 410-500 nm) and red (Ex: 633 nm; Em: 633-744 nm) filters with 40× magnification. Images were analyzed using Zen 2012 software (Carl Zeiss Microscope Systems, Jena, Germany).

4.2.8 Radiolabeling

[^{64}Cu]CuCl$_2$ (10-15 µL in 0.1 N HCl) was buffered by 50 µL 0.1 M NH$_4$OAc (pH 5.5), transferred to a microcentrifuge tube, then, 20 µg of chelator 2-S-(4-aminobenzyl)-1,4,7-triazacyclononane-1,4,7-triacetic acid (NOTA-Bn-NH$_2$) in 2 µL NH$_4$OAc (0.1 M, pH 5.5) was added to the aqueous [^{64}Cu]Cu(OAc)$_2$ solution. The mixture was shaken (thermoshaker; 750 rpm, 37 °C) for 15 min. Chelation of ^{64}Cu was monitored by reverse phase thin layer chromatography (radio-TLC) using MeOH:1M NH$_4$OAc (9:1) observing for R$_f$ ~ 0.3 for ^{64}Cu-NOTA-Bn-NH$_2$. The chelation mixture was cooled to 0°C (ice bath), acidified (pH ~ 1) using 100 µL of 1N HCl (trace metal grade), and 10 µL of sodium nitrite solution was added (aq., 2 M). The mixture was held at 0 °C (occasional shaking for 5 min) to complete conversion of the amine group by acid-mediated nitrosation-diazotization.

Radiolabeling of PMNPs started with the addition of 70 µL of a solution of GE11- or HW12-micelles (10 mg/mL in 0.1 M borate buffered saline, pH 8.8) to the crude nitrosation-diazotization mixture, followed by 80 µL of 1N NaOH to correct to pH 8-9. The coupling reaction was maintained at 0°C (occasional shaking for ~ 30 min) and was monitored by reverse phase radio-TLC (solvent system as above, ^{64}Cu-NOTA-PMNP R$_f$ ~ 0). ^{64}Cu-labeled micelles were separated from labeling precursors by size exclusion

chromatography (Bio-rad 10DG desalting column) pre-equilibrated and gravity eluted with 1X PBS. Fractions (400 µL) were collected and measured for activity using an Atomlab 400 dose calibrator and radiochemical purity by determined by radio-TLC.

4.2.9 *In vivo* PET experiments

All animal experiments were carried out in accordance with guidelines of the Canadian Council on Animal Care (CCAC) and approved (AC 18235) by the local Animal Care Committee of the Cross Cancer Institute. HCT116 cells ($\sim 1 \times 10^6$) were subcutaneously injected into the upper left flank of female NIH-III nude mice (Charles River, Saint-Constant, QC, Canada). After 3-4 weeks of tumor growth reaching an average tumor size of $\sim 300 - 500$ mm^3, mice were injected intravenously with 5–8 MBq of radiolabeled ^{64}Cu-labeled GE11- or HW12-PMNPs in 130-180 µL sodium acetate. For initial *in vivo* experiments normal BALB/c mice were used. Radioactivity present in the injection solution was determined using a dose calibrator (Atomlab 300; Biodex Medical Systems, Upton, NY, USA). Static PET acquisitions of 30–60 min duration were performed at 2 h, 24 h, and 48 h post-injection. Each mouse was anesthetized under isoflurane in 100% O$_2$ and maintained at a constant temperature of 37 °C. Mice were immobilized in a prone position, in the center of the field view of an INVEON® PET scanner (Siemens Preclinical Solutions, Knoxville, TN, USA). No correction for partial volume effects was performed. Image files were reconstructed using maximum a posteriori (MAP) reconstruction mode and further processed using the Rover v.2.0.51 software (ABX, Radeberg, Germany). Masks defining 3D regions of interest (ROI) were set and defined by 50% thresholding. Mean and maximum standardized uptake values SUV$_{mean}$ or SUV$_{max}$ = (activity / mL tissue) / (injected activity/body weight), in milliliters per kilogram were calculated for each region of interest (ROI).

4.2.10 Statistical analysis

All *in vitro* data are expressed as means ± SEM from n experiments. Graphs were constructed using GraphPad Prism® 5.04 (GraphPad Software, La Jolla, CA, USA). Statistical differences were tested by Student's t-test and were considered significant for $p < 0.05$ (*), $p < 0.01$ (**) and $p < 0.001$ (***).

4.3 Results

4.3.1 Characterization of copolymers and PMNPs

The number average molecular weight ($M_{n, Pol}$) among the synthesized block copolymers mPEO-*b*-PBCL, acPEO-*b*-PBCL, and mPEO-*b*-PBCL-*b*-PPC was 10,224; 12,280; and 11,060 g/mol, respectively (**Table 4.S1** and **Figure 4.S1**). The degree of polymerization (DP) for mPEO-*b*-PBCL was 20.1, and for acPEO-*b*-PBCL was 22.9. The DP of PBCL and PPC segments from the tri-block copolymer was 15.5 and 3.5, which together formed the micellar core (DP = 19). In our previous study,[250] high stability of polymeric micelles formed by PEO-*b*-PBCL copolymers with DP ~ 20 was shown, and because of that, the aim in this work was to achieve similar polymer lengths. **Table 4.1** shows that the PMNPs had a narrow, low polydispersity index (PDI ~ 0.3).

Table 4.1. Characterization of non-labeled and ^{64}Cu-labeled PMNPs.

PMNP	Size distribution (nm)	PDI	ζ-Potential (mV)	$M_{w, NP}$ x 10^3 (g/mol)	Aggregation number
HW12-NP	49.92 ± 0.32	0.27	8.65 ± 1.48	1660 ± 63.9	151
GE11-NP	45.30 ± 0.07	0.19	-7.90 ± 0.17	1720 ± 50.0	157
^{64}Cu-HW12-NP	53.16 ± 0.76	0.36	1.36 ± 0.77	-	-
^{64}Cu-GE11-NP	53.54 ± 0.31	0.16	-5.13 ± 0.68	-	-

Before radiolabeling with ^{64}Cu, HW12-micelles were found to have a slightly larger particle size (~50 nm) than GE11-micelles (~45 nm). After the radiolabeling, both PMNPs showed similar hydrodynamic diameters, although an increase in PDI and micellar size was observed. ^{64}Cu labeling minimally affected the micellar structures, as seen in the size distribution histogram (**Figure 4.2C** and **Figure 4.2F**). Zeta-potential data revealed that the charge was positive for HW12-micelles but negative for GE11-micelles, and radio-coupling conditions reduced their charges. Both micelles presented comparable molecular weights ($M_{w\ NP}$), and aggregation number, in which the analysis indicated that one single PMNP is composed of about 150 unimeric block copolymers.

4.3.2 *In vitro* cell uptake study

Flow cytometry indicated that Cy5.5-tagged HW12- and GE11-PMNPs were internalized by EGFR-negative cell line SW620 at similar levels (**Figure 4.1A**), whereas their internalization profiles in EGFR-positive HCT116 cell line were significantly different from one another (**Figure 4.1B**). Internalization of HW12-PMNPs by HCT116 cells was comparable to that of control micelles lacking the peptide surface decoration (data not shown), likely due to the fact that the HW12 peptide does not have binding specificity for EGFR. In contrast, GE11-PMNPs were present inside HCT116 cells with a significantly higher fluorescence signal ($p < 0.001$, one-way ANOVA, Tukey's posthoc test). Their median fluorescence intensity (MFI) was 8,240 ± 287 for HW12-PMNPs versus 15,690 ± 385 for GE11-PMNPs, which represented an increase of ~ 90% in internalization. The same pattern was observed qualitatively through confocal microscopy experiments, as shown in **Figure 4.1C**.

Pre-treatment with GE11 (1 µM) reduced HCT116 cell uptake of GE11-PMNPs to similar levels to those observed for HW12-PMNPs. This competitive blocking experiment represented further evidence that the conjugation of GE11 to PMNPs enhanced EGRF-directed targeting, resulting in increased

internalization into EGFR-expressing cell line HCT116. Moreover, competition with free GE11 did not change the uptake of GE11-PMNPs in EGFR negative SW620 cells (**Figure 4.1A** and **Figure 4.1B**).
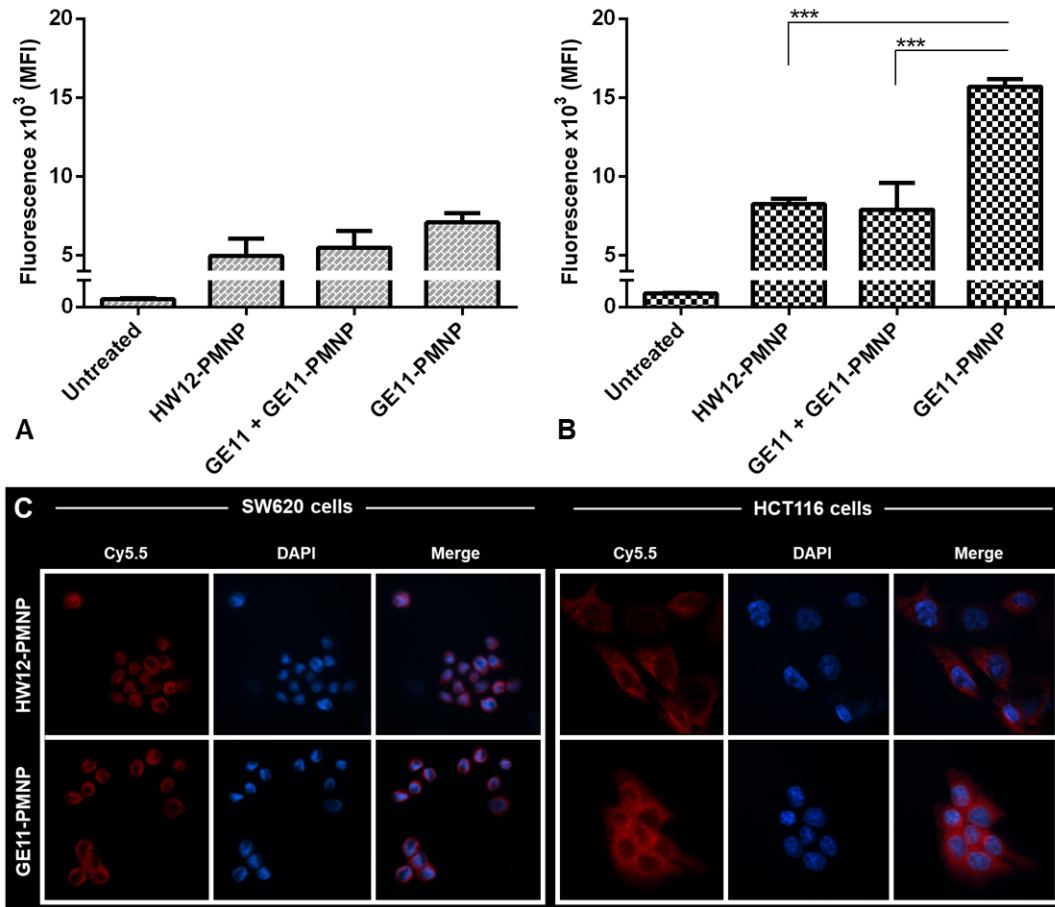
Figure 4.1. *In vitro* cell uptake studies. CRC SW620 and HCT116 cells were incubated with Cy5.5-tagged PMNP for 3 h at 37 °C. MFI was collected by flow cytometry from ~ 10,000 single-cell events, using (A) SW620 and (B) HCT116 cells. (C): Confocal microscopic images represent the PMNPs in red (Cy5.5), the nucleus in blue (DAPI), and their combination (merged together).

4.3.3 Radiolabeling of polymeric micellar nanoparticles

Figure 4.2 summarizes the overall scheme for the synthesis of the ^{64}Cu-labeled GE11- and HW12-peptide modified PMNPs, as well as their analysis through particle size distribution. Conjugation of peptide-decorated PMNPs and pre-labeling of ^{64}Cu-NOTA-Bn-NH$_2$ was accomplished by nitrosation-diazotization chemistry to form a reactive diazonium salt (^{64}Cu-NOTA-N$_2^+$) *in situ*, which enabled azo coupling to tyrosine residues[303] present in both the GE11 and HW12 peptide sequences (**Scheme 4.1**).
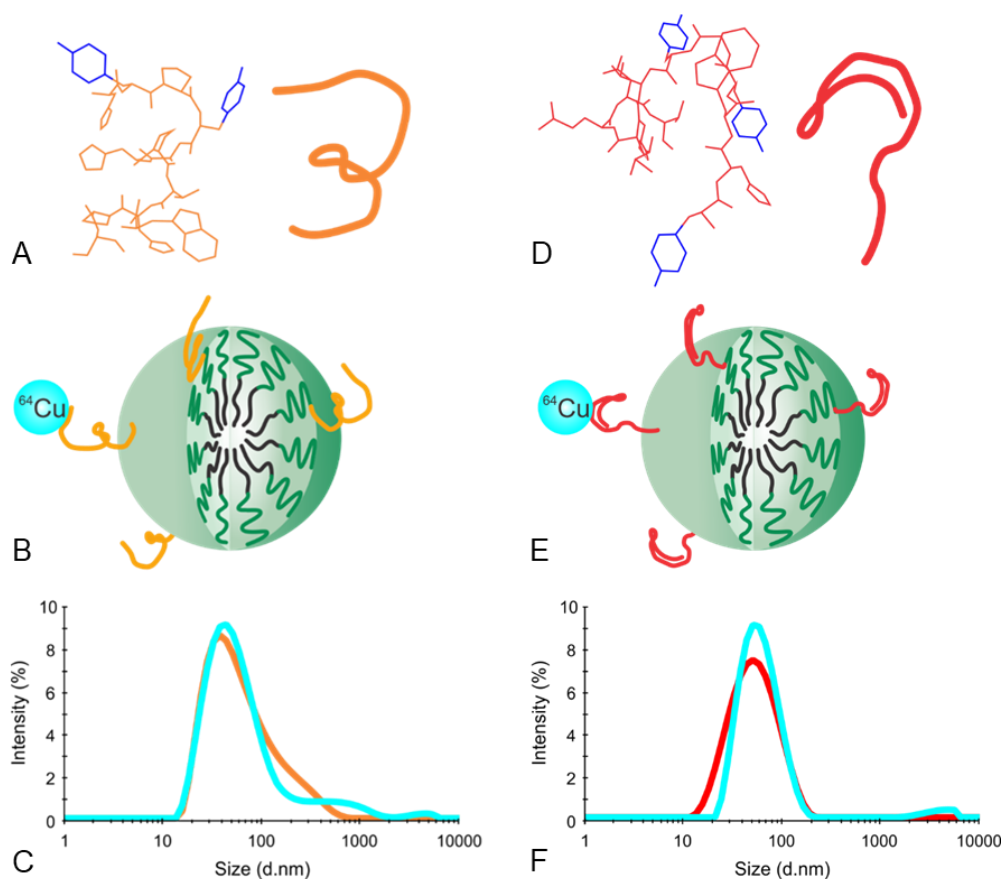
Figure 4.2. Preparation of ^{64}Cu-labeled PMNPs. (Top panels): Predicted 3D conformation of (A) HW12 and (D) GE11 peptides. The proposed folding for both peptidic sequences was obtained by using PEP-FOLD3 server. The simplified chemical structures, on the left side, emphasize the tyrosine (Y) residues in blue. (Middle panels): Representation of (B) ^{64}Cu- HW12-PMNPs and (E) ^{64}Cu-GE11-PMNPs conjugated through and peptides, respectively. (Bottom panels): Particle size distribution of (C) HW12-PMNPs and (F) GE11-PMNPs before (orange or red lines) and after (turquoise lines) ^{64}Cu-NOTA conjugation.

The nature and geometry of the coordination of ^{64}Cu in NOTA chelators are still not fully understood. The illustration of the reaction sequence displayed in **Scheme 4.1** reflects the proposed major isomer for the ^{64}Cu-NOTA-Bn-NH$_2$ complex according to a recent publication by Schlesinger *et al.*.[304] Mild reaction conditions (aqueous, 4 °C, pH 8-9, 30 min) were sufficient to achieve coupling, and purification was done by size exclusion chromatography with an average decay-corrected radiochemical yield of 23% and a radiochemical purity of >98 % as determined by radio-TLC.
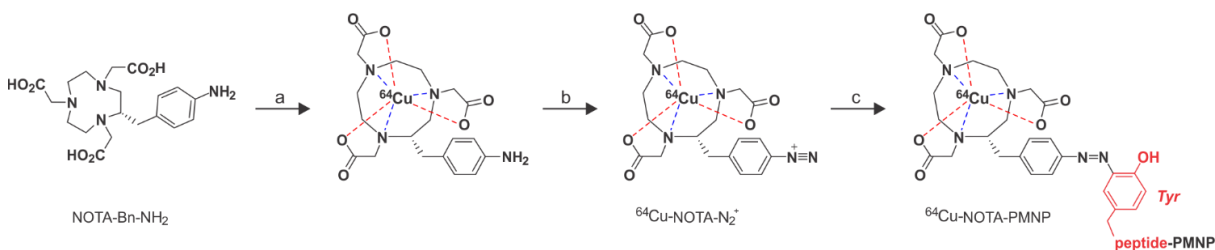
Figure 4.3. NP radiolabeling with ^{64}Cu, reagents and conditions: (a) [^{64}Cu]CuCl$_2$, 0.1M NH$_4$OAc (pH 5.5), 15 min, 37 °C; (b) NaNO$_2$, HCl, pH 1, 5 min, 4 °C; (c) GE11- or HW12-PMNPs, 0.1M borate buffered saline (pH 8-9), 15 min, 4 °C, 23% isolated decay-corrected radiochemical yield.

4.3.4 *In vivo* uptake and clearance profile of PMNPs in normal mice

The *in vivo* uptake and clearance profile of ^{64}Cu-NOTA-GE11-PMNPs was first analyzed with PET using normal BALB/c mice at three-time points over a time course of 48 hours. **Figure 4.4** shows representative PET images after 2 h, 24 h and 48 h post-injection as well as selected organ accumulation and clearance of the radiolabeled micelles. The image and semi-quantitative data revealed that the ^{64}Cu-NOTA-GE11-PMNPs showed somewhat delayed clearance from the blood pool as analyzed over the region of the heart. It was also evident that the renal clearance was negligible, and the main clearance pathway occurred through the hepatobiliary system with slow clearance from the liver and a steady accumulation

in the spleen, which acts as a storage organ for larger particles such as PMNPs and delays their hepatobiliary clearance.

In contrast to the typical biodistribution profile of radiolabeled NPs as presented in Scheme 3, we also performed comparative biodistribution studies with small ^{64}Cu-labeled compounds [^{64}Cu]Cu(OAc)$_2$ and ^{64}Cu-NOTA-Bn-NH$_2$ demonstrating rapid elimination of [^{64}Cu]Cu(OAc)$_2$ via the intestinal tract and an exclusively renal clearance profile for ^{64}Cu-NOTA-Bn-NH$_2$, respectively (**Figure 4.S3**). Both complexes are characterized by fast blood clearance.

Concerns were recently raised in the literature about the stability of micelles administered below their critical micellar concentration,[305] as would be the case for the present ^{64}Cu-labeled PMNP formulations. In light of these concerns and as a control experiment, we also assessed the biodistribution profile of ^{64}Cu-NOTA-GE11-PMNPs in the presence of non-targeted (peptide-free) PMNPs in a "doped" formulation. Except for slightly higher liver retention, no notable differences in the organ distribution profile was observed (**Figure 4.S4**). Given this indirect evidence of PMNP stability at low concentrations, further *in vivo* analysis of ^{64}Cu-NOTA-GE11- and ^{64}Cu-NOTA-HW12-PMNPs was continued without "doping".

64Cu-NOTA-Ge11-PMNPs
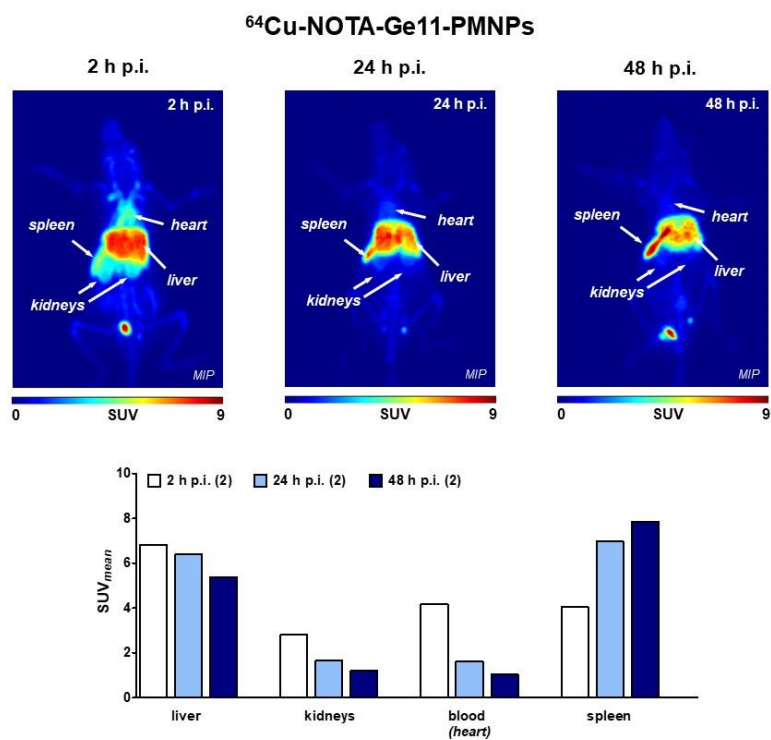
Figure 4.4. Representative PET images (*MIP - maximum intensity projection*) and selected organ uptake and clearance profiles after injection of 64Cu-NOTA-GE11-PMNPs into normal BALB/c mice at 2 h, 24 h, and 48 h post injection (p.i.). Data are shown as mean standardized uptake values (SUV$_{mean}$) and mean values from 2 experiments.

4.3.5 *In vivo* analysis of PMNPs in EGFR expressing colorectal HCT116 cancer model

64Cu-NOTA-GE11-PMNPs and, as a non-EGFR-targeting control, 64Cu-NOTA-HW12-PMNPs, were analyzed in NIH III nude mice bearing HCT116 tumors. The colorectal HCT116 cancer cell line has been found to overexpress EGFR.[267] **Figure 4.5** depicts representative PET images after injection of either 64Cu-NOTA-HW12-PMNPs or 64Cu-NOTA-GE11-PMNPs at 2 h, 24 h, and 48 h post-injection. The PET data indicated that both the EGFR-targeting and non-targeting micelles exhibited increasing tumor accumulation reaching enhanced tumor-to-muscle ratios over time, likely based on the EPR effect. Tumor uptake at 24 h and 48 h post-injection revealed a small enhancement in the tumor tissue for the targeting 64Cu-NOTA-GE11-PMNPs versus the non-targeting 64Cu-NOTA-HW12-PMNPs. As the semi-quantitative

SUV data analysis shows, the difference in uptake between the two types of micelles was most prominent at the 24 h time point, resulting in 24 or 28% increase for the targeting micelles depending on the analysis as SUV_{mean} or SUV_{max}. The latter analysis revealed a statistical significance between 1.48 ± 0.06 (n = 3) for ^{64}Cu-NOTA-HW12-PMNPs and 1.90 ± 0.09 (n = 4) for ^{64}Cu-NOTA-GE11-PMNPs (p < 0.05). However, at 48 h post-injection, only a trend in higher accumulation of EFGR-targeting NPs could be observed. Muscle retention, an indicator of off-target accumulation, was very low and did not change over the time course of 48 h. These PET data point towards specific EGFR-targeting in these HCT116 tumors when peptide GE11 is present on the surface of PMNPs.
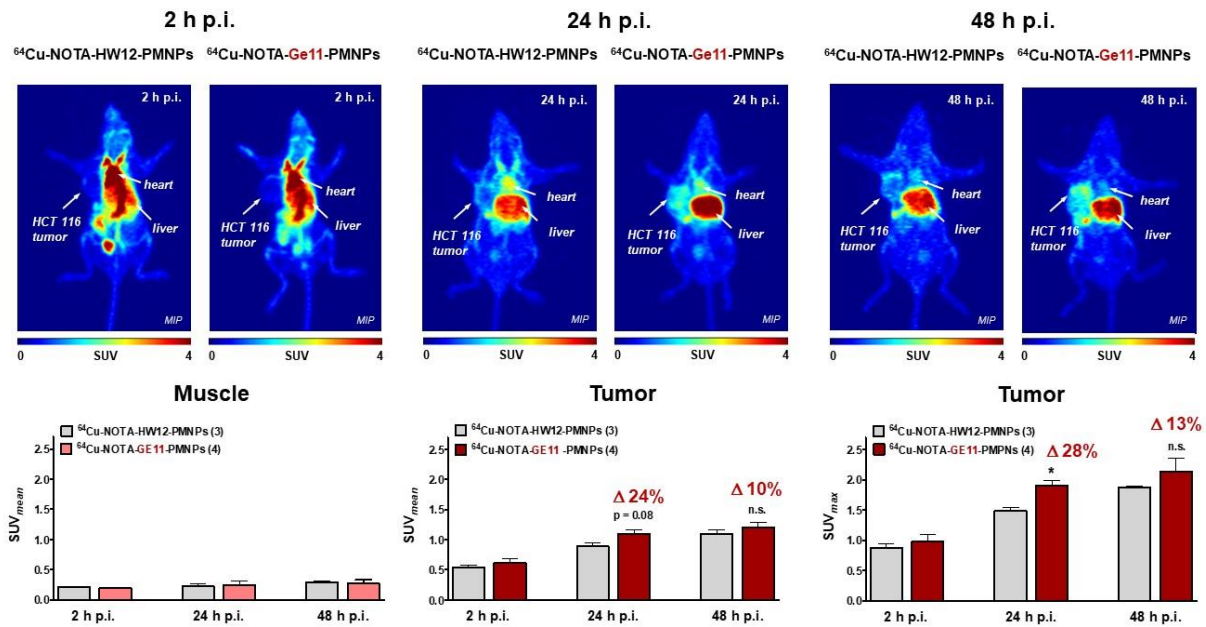
Figure 4.5. Top: Representative PET images (*MIP – maximum intensity projections*) of HCT116 tumor-bearing NIH-III mice at 2 h, 24 h, and 48 h p.i. of ^{64}Cu-NOTA-HW12-PMNPs (left) or ^{64}Cu-NOTA-GE11-PMNPs (right). Bottom: Analysis of mean and maximum standardized uptake values (SUV_{mean} - muscle and tumor; SUV_{max} - tumor only) for the selected time points post-injection. Comparison between ^{64}Cu-NOTA-HW12-PMNPs and ^{64}Cu-NOTA-GE11-PMNPs. Data are shown as mean ± SEM from n experiments.

4.4 Discussion

The main results of the present study are that GE11-decorated PMNPs showed a significantly higher internalization into EGFR expressing HCT116 cells as well as a significantly higher HCT116 tumor uptake after 24 h post-injection as analyzed with the ^{64}Cu-radiolabeled PMNPs. The *in vitro* and *in vivo* uptake patterns for the HW12-conjugated PMNPs were significantly lower. This finding confirms the concept of specific targeting of EGFR using modified nanoparticles to increase the delivery of therapeutic payloads to EGFR expressing cancer cells for chemo- or radiotherapy. Our research group is focused on the design and synthesis of new imidopiperidine compounds as inhibitors of DNA repair enzyme polynucleotide kinase/phosphatase (PNKP) for treating colorectal cancer.[267] Recently, we have found that micellar nanocarriers based on PEO-*b*-PBCL copolymers were superior at loading PNKP inhibitor candidates than micellar systems alone formed by PEO-*b*-PCL copolymers. The physical entrapment of those small-molecules was found to be more efficient in the micellar nanoparticle core, which may be due to the abundance of benzyl groups in the micellar core, given their somewhat slower drug release profile.[267]

In the present study, in order to investigate the *in vivo* fate of GE11-modified PMNPs composed of PEO-*b*-PBCL copolymers, a novel pre-labeling strategy with ^{64}Cu was applied for both the GE11-PMNPs as well as non-EGFR-targeting HW12-PMNPs. This radiolabeling technique allowed for *A)* labeling of (a not further modified) peptide conjugated NP, which could also be loaded with a drug payload in its core in the future; and *B)* semi-quantitatively analyze their *in vivo* profile regarding EGFR expressing colon tumor uptake and clearance pattern over time.

Numerous studies have been reported in the literature regarding the use of GE11 peptide as a surface modifier for different types of NPs to boost the delivery of drugs,[200,201] photodynamic agents,[278] and genes[279,280] into EGFR-overexpressing tumors while sparing normal tissues/organs. PEGylated self-assembled micellar NPs have been surface modified with GE11 for *in vivo* delivery of doxorubicin,[200]

gemcitabine,[201] and chlorin e6[278] into ovarian (SKOV3 cells), pancreatic (MIA PaCa-2 cells), or colorectal (HCT116 cells) mouse cancer models. In these examples, all tumors showed therapeutic effects reducing tumor volumes and resulting in longer survival in the GE11-containing treatment groups versus the non-targeted controls.[200,201,278] Moreover, the delivery of plasmid constructs, encoding for sodium iodide symporter to HuH7 hepatocellular tumors, was significantly enhanced by GE11-NPs composed of PEG-poly(ethylenimine). Sodium iodide symporter specific PET tracer [124]I was used to measure transfection, and the surface-decorated polyplexes showed the best results.[287,289]

To the best of our knowledge, this study describes, for the first time the functional and semi-quantitative analysis of radiolabeled GE11-decorated NPs, *in vivo*. The present PET data revealed a significantly higher accumulation of the ^{64}Cu-labeled GE11-PMNPs into HCT116 tumor xenografts compared to the non-targeting control, HW12-PMNPs. The analysis of the clearance pattern *in vivo* revealed a delayed blood and liver clearance of the radiolabeled NPs, which leads to their continuous delivery to the target site resulting in a more favorable delivery and release of payloads for therapeutic applications. In contrast, rapid renal elimination was observed in tumor-bearing mice after injection of ^{125}I-GE11,[279] ^{64}Cu-NOTA-GE11,[286] and other GE11-based radiolabeled constructs not attached to a nanocarrier.[284,285] This observation can be attributed to the smaller size of the radiotracers in the aforementioned studies, which are below the cut-off (~ 10 nm size) for renal clearance through the highly size-selective glomerular filtration.[306]

4.5 Conclusions

We have demonstrated that azo coupling of ^{64}Cu-NOTA-N$_2^+$ to tyrosine residues of GE11-tagged PMNPs leads to radiolabeled nanocarriers that accumulate in subcutaneous colorectal tumors in mice. Radiolabeled PMNPs were shown to exhibit a desirable longer residence period in the blood pool and a significant uptake in EGFR-expressing tumor tissue. The nonspecific tumor targeting of radiolabeled PMNPs, mediated by the EPR effect, was dominant as compared to the specific targeting, a common observation for particles of this size (~ 50 nm).[307] Nevertheless, the incorporation of peptide GE11 into the surface of PMNPs resulted in an increase of specific targeting to EGFR-expressing tumors. The difference in maximum uptake values between GE11-tagged *versus* HW12-tagged (negative control) PMNPs at 24 h was statistically significant.

Given our future intention to add a drug delivery component to this nanosystem, the targeting vector (GE11) also seems to have a positive effect on tumor cell internalization of PMNPs, as suggested by the fluorescence confocal microscopy data. This could provide an important advantage for future therapeutic applications. As demonstrated with the successful radiolabeling of PMNPs with radiometal ^{64}Cu, the described azo coupling pre-labeling approach represents a highly versatile labeling tool to study the uptake and metabolism of nanoscale carriers containing tyrosine residues with PET *in vivo*. Azo coupling chemistry is a convergent labeling strategy in which stably-chelated ^{64}Cu can be incorporated into a variety of tyrosine containing nanostructures under mild and aqueous conditions. The PMNPs used in the present experiments, customized for immune system evasion and prolonged circulation, have the capacity for encapsulating hydrophobic drugs and, therefore, are promising candidates for serving the pharmaceutical role for combining chemo- and radiotherapies, including diagnostic monitoring of their delivery. Radiolabeled PMNPs are also suitable drug delivery vectors as they can be used to assess the most optimal time for maximal drug delivery and release to the target tissue. The simultaneous

administration of drug-loaded PMNPs with radiolabeled NPs would allow for an image-guided therapy strategy *in vivo*.

4.6 Supplementary Information

Table 4.S1. Polymer characterization by ^{1}H-NMR. Number average molecular weight (Mn) and degree of polymerization (DP) per segment of block copolymers were determined.

Block copolymers	$M_{n, Pol}$ (g/mol)	DP per copolymer segments		
		PEO	PBCL	PPC
[mPEO]$_{114}$-*b*-[PBCL]$_{20}$	10,200	114.0	20.1	-
[acPEO]$_{161}$-*b*-[PBCL]$_{23}$	12,300	161.5	22.9	-
[mPEO]$_{114}$-*b*-[PBCL]$_{16}$-*b*-[PPC]$_4$	11,100	114.0	15.5	3.5
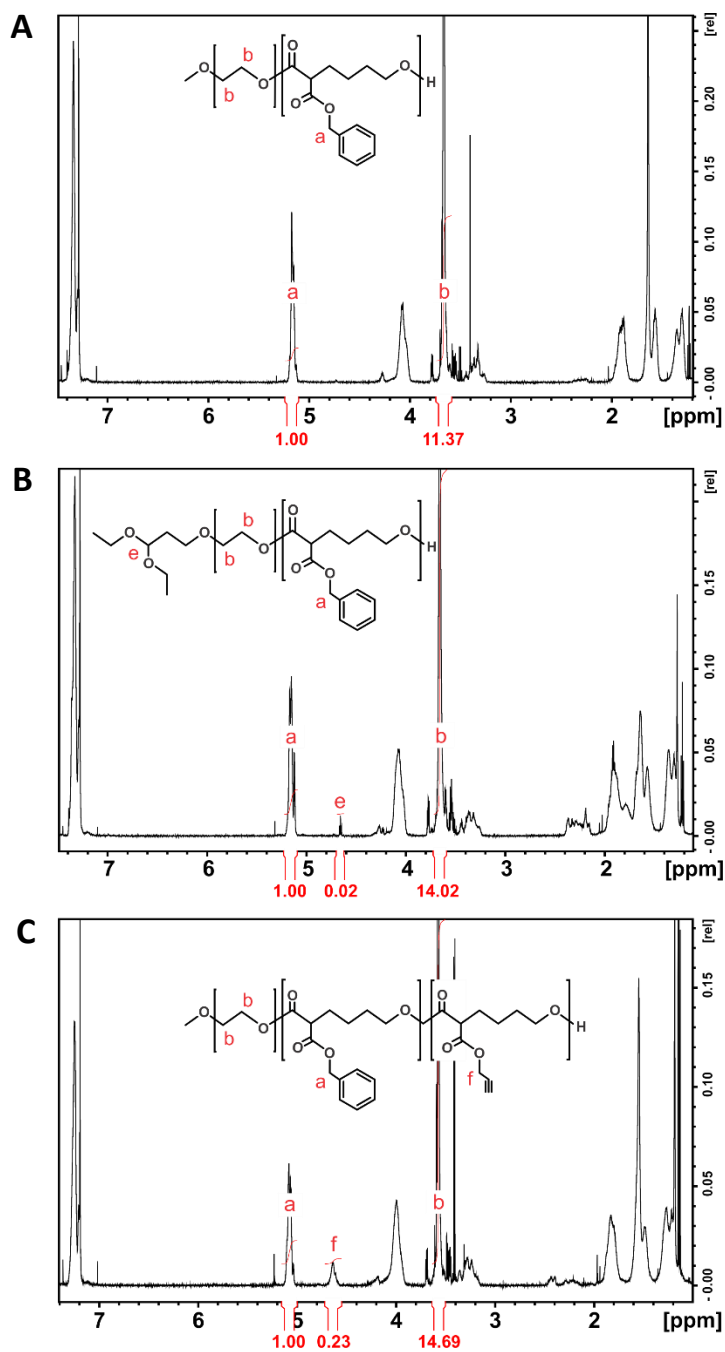
Figure 4.S1. ^{1}H-NMR spectra of the synthesized block copolymers used for forming the PMNPs. (A): mPEO-*b*-PBCL; (B): acPEO-*b*-PBCL; (C): mPEO-*b*-PBCL-*b*-PPC. Selected proton signals and their integration are highlighted in red.
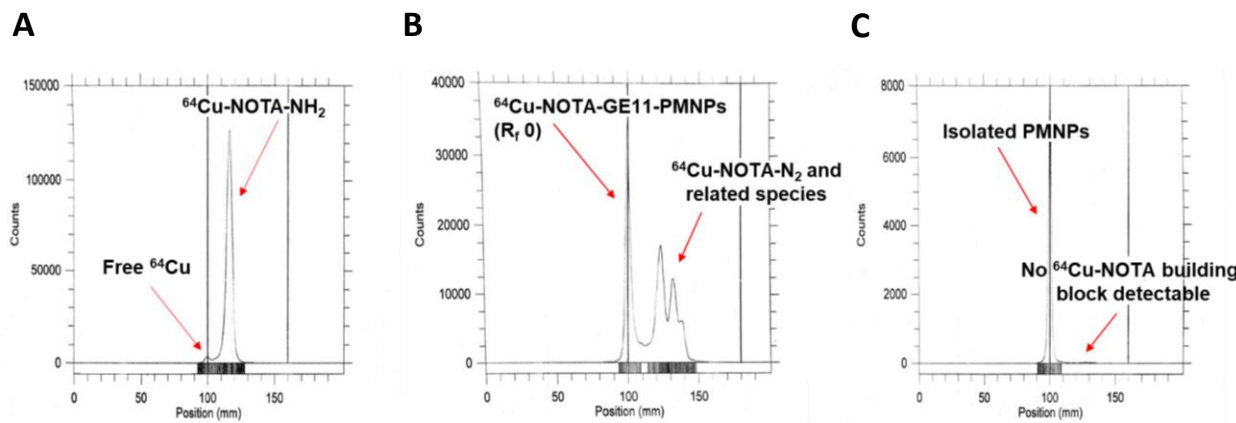
Figure 4.S2. Radio-TLCs of (A) ^{64}Cu-NOTA, (B) reaction post-NP addition, and (C) isolated PMNPs.
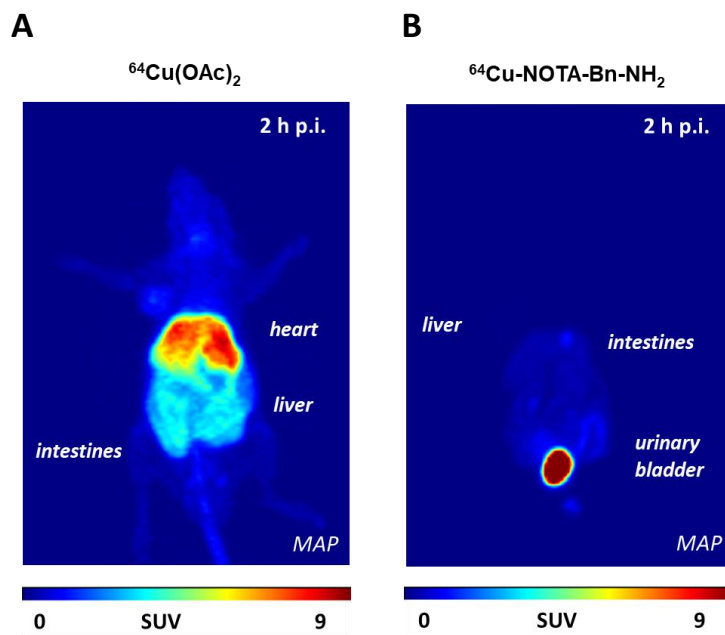
Figure 4.S3. *In vivo* PET images of (A) ^{64}Cu acetate and (B) ^{64}Cu chelated by NOTA-Bn-NH$_2$.
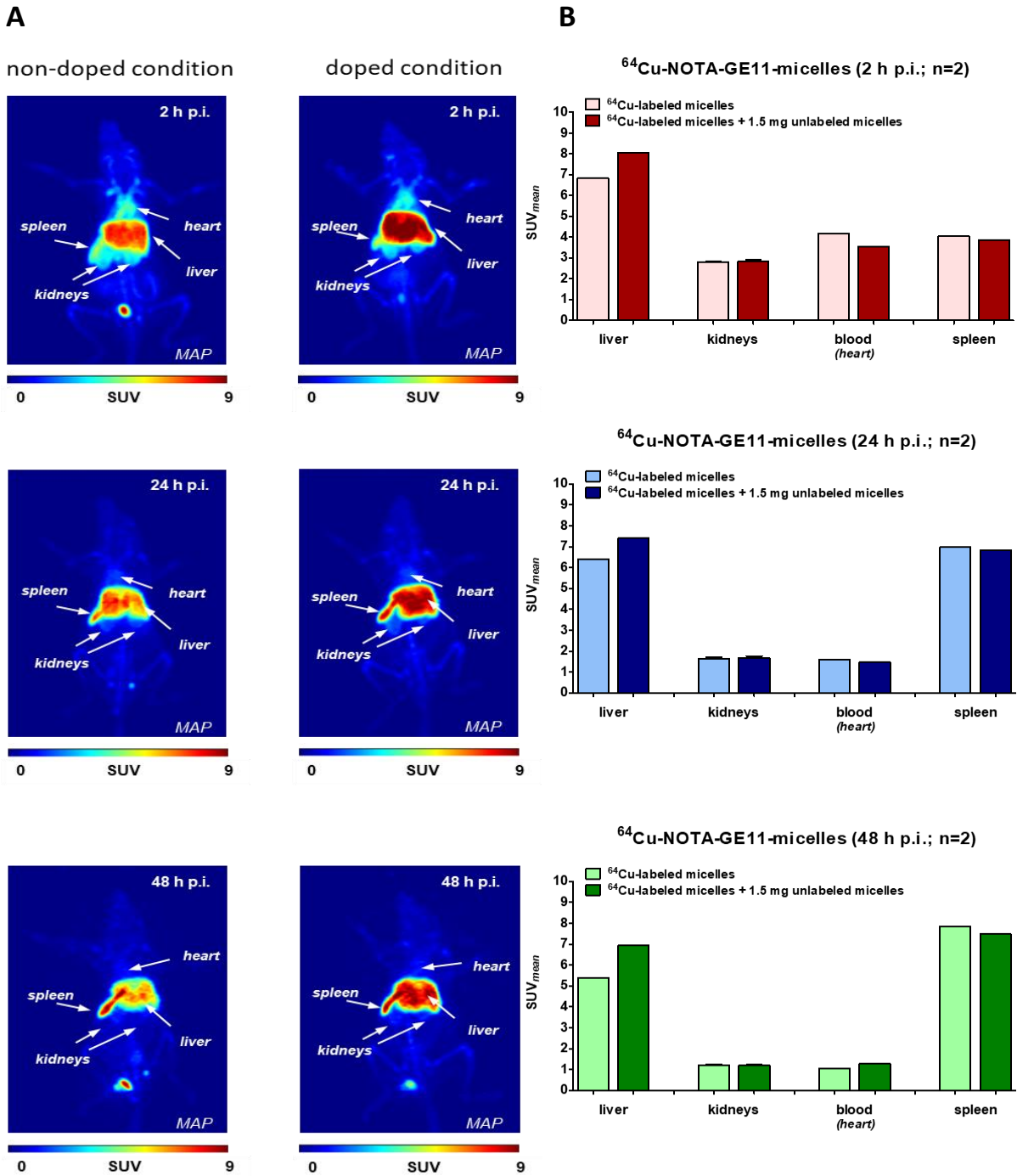
Figure 4.S4. PET images of BALB/c mice over 48 h p.i. of (A) ^{64}Cu-NOTA-GE11-PMNPs versus the same doped with 1.5 mg of non-targeted (peptide free) micelles. (B): The corresponding selected organ distributions.

Chapter five

GE11-modified polymeric micelles for targeted delivery of novel inhibitors of

DNA repair to EGFR-expressing orthotopic colorectal cancer xenografts in mice

A version of this chapter will be submitted for publication.

5.1 Introduction

Colorectal cancer (CRC) affects nearly 1.4 million people worldwide.[308–310] Surgical resection remains the first line of treatment, which may be complemented by radiologic management and assessment.[311] Nevertheless, over 60% of CRC patients will eventually relapse or develop *de novo* metastatic disease. Then, different chemotherapy agents, including 5-fluorouracil (5-FU), irinotecan, oxaliplatin, as well as their combinations, such as FOLFOX (leucovorin, 5-FU, and oxaliplatin), FOLFIRI (leucovorin, 5-FU, and irinotecan), and XELOX regimen (oxaliplatin and capecitabine) have been successfully implemented. More recently, therapeutic strategies have been majorly focussing on inhibiting epidermal growth factor receptor (EGFR), either as a monotherapy or in combination with those standard cytotoxic agents, due to the fact that EGFR is highly expressed among 60-80% of CRC patients.[312–314] This highlights the need for the development of new treatments for CRC, especially for the aggressive and metastatic form of the disease.

Long circulating nanoparticles are known to have a capacity for passive accumulation in solid tumors through enhanced permeation and retention (EPR) effect. Modification of nanoparticles using ligands specific for EGFR has been exploited mainly to enhance their homing and retention in the tumor site and increase nanocarrier cell internalization in tumors that overexpress this receptor.[315–318] The dodecapeptide GE11 (YHWYGYTPQNVI), is a peptide ligand specific for EGFR, which was originally identified by screening a phage display library against the purified receptor, in 2005.[279] Peptides are, in general, considered advantageous over other targeting ligands for surface modification of nanoparticle, because they can be easily synthesized and further engineered for target specificity and/or stability against degradation in biological fluids. Peptide binding to the target protein/receptor usually does not require the formation of tertiary structures, as observed with full-length antibody, single-chain variable fragment, diabody, nanobody, and other derivatives.[315,319,320] Also, the high immunogenicity of these large molecular-weight ligands makes short peptides a very attractive alternative for targeting EGFR.[321]

Besides GE11, another short amino acid sequence (6-mer), denoted by D4, has been identified to have high specificity to EGFR. Some studies have indicated that their binding site along the EGFR molecule differs substantially; whereas D4 binds to a pocket far from the EGF pocket, GE11 binds near to this region.[281,322] However, both peptidic sequences are known to have a weaker binding capacity when compared to the physiological ligand EGF and some antibody-based molecules, which may lead the break of the binding over time. However, since EGFR is an internalizing receptor, the micelle disconnection from the receptor in the endosome may be advantageous for the delivery of payloads to other cell compartments. Moreover, this weaker binding compared to EGF indicates that GE11 is unable to compete with EGF, and thus its effect is not related to starving cells.[323,324]

GE11 has been explored in several studies for enhancing nano-delivery of payloads, such as nucleic acids,[279,325,326] drugs,[200,201,326] and photodynamic agents[278] into EGFR-overexpressing tumor cells. Interestingly, the great augmentation in cell uptake rates observed when employing this peptide seems to be due to an EGFR-dependent actin-driven endocytic pathway. Interaction between GE11-modified nanoparticles and EGFR-expressing cells was shown to change the receptor level on the cell membrane minimally and not to activate the receptor dimerization and signaling. The latter is paramount for cancer therapy since a low mitogenic activity is desired in order to avoid cell proliferation by EGFR ligands.[325]

In the current research, we explored the use of GE11-modified polymeric micelles based on poly(ethylene oxide)-*block*-poly(ε-caprolatone) (PEO-*b*-PCL) and poly(ethylene oxide)-*block*-poly(α-benzyl carboxylate-ε-caprolatone) (PEO-*b*-PBCL) for targeted drug delivery to EGFR expressing colorectal cancer (CRC) cells, *in vitro*, and CRC orthotopic model, *in vivo*. We then evaluated the therapeutic activity of a novel inhibitor of DNA repair enzyme, i.e., polynucleotide kinase/phosphatase (PNKP), delivered by plain and GE11 polymeric micellar nanocarriers, in EGFR-overexpressing CRC cells harboring deficiency in the expression of a tumor suppressor protein, phosphatase and tensin homolog (PTEN). Downregulation of PTEN occurs in approximately one-third of colorectal cancers and is associated with more aggressive

128

phenotypes.[327] Deficiency in PTEN concomitantly with downregulation of poly(ADP-ribose) polymerase (PARP)[328] or PNKP,[329] is known to lead to cellular synthetic lethality. Thus, specific delivery of PNKP inhibitors to CRC cells deficient of PTEN through the use of nanoparticles is expected to provide two simultaneous strategies for targeting of these toxic compounds to aggressive cancer cells while keeping normal cells safe.

A83B4C63 is a poorly soluble novel inhibitor of PNKP, developed by our research group. Our earlier results have shown the success of polymeric micelles based on PEO-PCL and PEO-PBCL as solubilizing agents for this lead compound, preserving its inhibitory activity against intracellular PNKP, leading to specific cell death in PTEN negative CRC cells, both *in vitro* and *in vivo* in subcutaneous CRC models.[267,330] The current study explored the potential of PEO-PBCL micellar formulations of A83B4C63, particularly those with GE11 surface modifications, in targeted intracellular drug delivery to EGFR overexpressing CRCs harboring PTEN deficiency, *in vitro* and in orthotopic CRC models.

5.2 Methods

5.2.1 Cell Culture

Methoxy-poly(ethylene oxide) (PEO, 5,000 Da), ethylene oxide (≥99.9%), 3,3-diethoxy propanol, ascorbic acid, fetal bovine serum (FBS), and phenylmethylsulfonyl fluoride (PMSF) were purchased from Sigma (St. Louis, MO, USA). ε-Caprolactone was acquired from Lancaster Synthesis (Lancashire, England) and extra purified by vacuum distillation. The α-carbon modified-ε-caprolactone monomers, i.e., α-benzyl carboxylate-ε-caprolactone and α-propargyl carboxylate-ε-caprolactone, were obtained from Alberta Research Chemicals Inc. (Edmonton, Canada). Stannous octoate was purchased from MP Biomedicals Inc. (Tuttlingen, Germany) and distilled for further purification. Copper(II)-TBTA complex and Cy5.5-azide were acquired from Lumiprobe (Hallandale Beach, FL, USA). Cell culture media DMEM, DMEM:F12, sodium pyruvate, L-glutamine, non-essential amino acids, and penicillin-streptomycin were purchased from

GIBCO Life Technologies (Burlington, ON, Canada). Lipofectamine[TM] 2000 reagent was bought from Invitrogen (Carlsbad, CA, USA). Protease and phosphatase Inhibitor Cocktails (#535140 and #524625, respectively) were from Millipore (Burlington, MA, USA). Antibody against EGFR (#ab52894) was obtained from Abcam Inc. (Toronto, ON, Canada), anti-β-actin (#cst-4970), and horseradish peroxidase-conjugated anti-rabbit antibody was from Cell Signaling Technology (Danvers, MA, USA). Bicinchoninic acid (BCA) protein assay kit and Pierce ECL Western Blotting Substrate (#32106) was purchased from ThermoScientific (Rockford, IL, USA). The PNKP inhibitor, A83B4C63, was synthesized by Dr. Marco Paladino (Faculty of Science – Chemistry Department, University of Alberta). Peptide GE11 (YHWYGYTPQNVI) was acquired from Biomatik LLC (Wilmington, DE, USA). XenoLight D-Luciferin potassium salt bioluminescent substrate was purchased from PerkinElmer (Waltham, MA, USA). The mouse food was the 2014S Teklad Global 14% Protein Rodent Maintenance Diet, from Harlan Labs (Indianapolis, IN, USA). Dialysis tubing (MWCO - 3.5 kDa) was purchased from Spectrum Laboratories (Rancho Dominguez, CA, USA). The toluene, from Caledon (Halton Hills, ON, Canada) was dried by refluxing under H_2SO_4 before use. All other chemicals were reagent grade.

5.2.2 Synthesis of heterobifunctional polyethylene oxide

Synthesis of acetal-polyethylene oxide (acPEO, Mn ~ 5,000) was performed based on the method described by Nagasaki et al.[248] with some modifications. Briefly, potassium naphthalene, used as a catalyst, was freshly prepared before the polymerization. Pure naphthalene (12.9 mmol) and potassium (14.7 mmol) were added into 50 mL anhydrous THF. The reaction was protected under argon gas and kept running for 24 hours. Then, 3,3-diethoxy propanol (2 mmol) was dissolved in 40 mL dry THF, and 7 mL of the prepared catalyst (~ 2 mmol) was added dropwise into the reaction solution to activate the initiator. The flask was purged with argon, and after 10 min of stirring, the flask was transferred into an ice water bath. Ethylene oxide (228 mmol) was added to the reaction solution. After 48 hours, the polymerization

was quenched by acidified ethanol. ac-PEO was recovered by precipitation in ethyl ether. The product was further purified by precipitation in diethyl ether. The composition and the degree of polymerization were confirmed by ^{1}H-NMR (Bruker Advance III 600 MHz Spectrometer, Bruker Corporation, Billerica, MA).

5.2.3 Synthesis of peptide-conjugated polymers

The end hydroxyl group from synthesized acPEO was used to initiate the synthesis of the acPEO-*b*-PCL and acPEO-*b*-PBCL, which was carried out by bulk ring-opening polymerization of ε-caprolactone or BCL, respectively.[266] For peptide conjugation, micelles were prepared, by co-solvent evaporation, at a block copolymer concentration of 5 mg/mL. The pH was then adjusted to 2.0 using HCl (0.5 M solution). Micelles were then incubated at room temperature under stirring. After 2 h, the pH was re-adjusted to 7.4 with NaOH, followed by buffering the micellar solution using PBS (10X, pH 7.4). An aqueous peptide solution in 1% DMSO was prepared and added, under constant stirring, at a peptide:polymer ratio (mol/mol) of 1:3. After 2 h reaction, NaBH$_3$CN was added and the reaction was left for 24 h at room temperature under constant stirring. The resulting micellar solution was extensively dialyzed against distilled water and lyophilized. The molar conjugation percent of GE11 peptide into the copolymers was determined by reverse-phase HPLC measuring unreacted peptide concentration (Varian Prostar 210 System, Microsorb-MV 5 μm C18–100 Å column, a gradient of 0.1% trifluoroacetic acid/acetonitrile).[259]

5.2.4 Synthesis of three-block copolymers for Cy5.5 conjugation

The diblock copolymers PEO-*b*-PCL and PEO-*b*-PBCL were used as the macroinitiator for the ring-opening polymerization of α-propargyl carboxylate-ε-caprolactone monomer as reported before.[266] The copolymers were added together with PC in a 25 mL round bottom flask previously filled with 5 mL dry toluene under constant stirring. Stannous octoate was added to the flask and refluxed for 30 h. The reaction was stopped by cooling the system to room temperature. Both products, PEO-*b*-PCL-*b*-PPC or

PEO-*b*-PBCL-*b*-PPC, were then precipitated in hexane, and the supernatant was discarded. Lastly, the copolymers were dissolved in THF and further purified with ether followed by drying under vacuum.

The near-infrared (NIR) dye Cy5.5, having an azide group (Cy5.5-azide), was conjugated to both triblock copolymers through azide-alkyne click chemistry.[250] Briefly, the pendant alkyne from PPC reacted with Cy5.5-azide, using Cu(I) as the catalyst. The triblock copolymers were dissolved in degassed DMSO. Also, Cy5.5-azide, ascorbic acid, and Cu(II) TBTA complex were added to the mixture under constant stirring. The reaction was performed at room temperature, under argon for 16 h in the dark. After incubation, the mixture was separated from the non-reacted dye by dialysis against DMSO for 24 h followed by dialysis against water for 24 h and lyophilization. The conjugation efficiency of Cy5.5-azide to the copolymers was determined by fluorescence spectroscopy using a Synergy H1 Hybrid Multi-Mode Microplate Reader (BioTek), measuring the excitation at 673 nm and emission at 707 nm.

5.2.5 Characterization of synthesized block copolymers

Number molecular weight (Mn) of diblock copolymers was determined by ^{1}H NMR by comparing the integration from methylene hydrogen signals of PCL or PBCL segments (-OCH$_2$-, δ = 4.05 ppm) to the ones from PEO segment (-CH$_2$CH$_2$O-, δ = 3.65 ppm). In order to estimate the degree of polymerization of PPC, the area under the curve from PPC (-OCH$_2$-, δ = 4.75 ppm) was compared to that of the methylene hydrogens from PEO (-CH$_2$CH$_2$O-, δ = 3.65 ppm).

5.2.6 Preparation and characterization of empty and drug-loaded polymeric micelles

Polymeric micelles (PCL- or PBCL-based ones) containing conjugated Cy5.5, were prepared by mixing the synthesized block copolymers in the proportion described in **Table 5.S1**. The concentration of Cy5.5 dye in the mix micelles was 0.4 µg/mg of polymer, whereas the GE11 density was 5-20% mol/mol of the polymer (depending on the peptide feed ratio).

The A83B4C63 was physically encapsulated into the polymeric micelles by dissolving it (3 mg) together with the block copolymers (10 mg) in acetone. The ratio of unmodified and GE11 modified block copolymers used in the micellar composition was the same as what reported in **Table 5.S1**. Then, the polymer/drug solution in acetone was transferred dropwise to double distilled water (10 mL) under constant stirring and kept overnight. The obtained micellar solutions were centrifuged at 11,600 × g for 5 min and then filtered through 0.22 µm membrane, in order to remove free un-encapsulated compounds and/or possible polymeric aggregates.

Zeta-potential (ZP) of the prepared polymeric micelles was measured by Zetasizer Nano (ZEN3600, Malvern Instruments, Worcestershire, UK). This equipment was also used for dynamic light scattering (DLS) experiments, in which micellar particle size distribution, micellar thermodynamic stability, and micellar kinetic stability in the presence of sodium dodecyl sulfate (SDS) were determined, as reported before.[331,332] For CMC measurements, polymeric micelles were prepared in different concentrations (ranging from 0.49 to 500 µg/mL), and the count rate of scattered light was recorded. For the determination of micellar kinetic stability, polymeric micelles were prepared to have a concentration of 2 mg/mL and incubated with the micellar destabilizing agent SDS at a concentration of 6.7 mg/mL. All DLS analyses were made at 25.0 ± 0.1 °C with a 173° scattering angle on identical polymer mixtures described in **Figure 5.1** and **Table 5.S1** without Cy5.5 to avoid interference in the DLS readings.

5.2.7 *In vitro* release of the encapsulated A83B4C63

The *in vitro* release of A83B4C63 from the polymeric micelles was assessed through the equilibrium dialysis method. Sets of dialysis tubing were prepared in triplicate, containing 2 mL of each micellar formulation. The release study was carried out in 300 mL distilled water at 37 °C for 48 h and shaking at 65 rpm in a water bath system (Julabo SW 22, Seelbach, Germany). At selected time points (0, 1, 2, 4, 6, 8, 24, and 48 hours), aliquots of 200 µL were collected from inside the dialysis bags. The drug

was quantified using reversed-phase chromatography (Varian Prostar 210 HPLC System) coupled with a Microsorb-MV 5 μm C18–100 Å column (4.6 × 250 mm). The sample injection was 20 μL, the mobile phase was 0.1% trifluoroacetic acid and acetonitrile, and the flow rate was 0.7 mL/min at room temperature. Detection was performed at 280 nm, using a Varian 335 Photodiode Array HPLC detector (Varian Inc.).

5.2.8 Molecular modeling of binding between EGFR and its ligands GE11 and EGF

The structure of the extracellular domain of human epidermal growth factor (EGF) was obtained from the Protein Data Bank (PDB_ID: 1NQL) with a resolution of 2.8 Å.[333] The structure was refined and repaired by adding missing side-chains and assigning partial charges using Chimera.[334] Autoligand module of Autodock was used to identify the possible binding site for GE11, by scanning the highest affinity binding pockets on the surface of the protein.[335] The 3D structure of GE11 was built and prepared using the DOCKPREP module of Chimera, in the framework of the AMBER99SB forcefield. The docking protocol was performed using Autodock Vina by "boxing" the identified binding pocket into a grid of 100 x 100 x 100 Å, with a spacing of 0.375 Å.[336] To increase the accuracy of the docking, a total of 24 runs were performed with exhaustiveness of 40.

Before performing the Molecular Dynamic (MD) Simulations, the structure of GE11 was parameterized using AnteChamber PYthon Parser interfacE (ACPYPE).[337] In order to predict the stability of GE11 in the predicted binding site, and to calculate the binding free energy of the binding interactions, we used the GROMACS 5.1.5 package to perform a series of 20 ns-long MD simulations for the structure of (a) isolated GE11; (b) EGFR/GE11; and (c) EGFR/EGF complex.[338] The MD simulation of GE11 was carried out to obtain the most stable conformation of the molecule for both docking and the subsequent MD simulation. The simulation system was solvated in a box having 1 nm distance from each side, with TIP3P water molecules. Then, the system was neutralized using NaCl to reach a theoretical concentration of 0.15 M. The energy of the system was initially minimized using the AMBER99SB-ILDN force field, followed by

heating to 300° K, and equilibration (500 ps) using the Berendsen Thermostat. After that, a series of 20 ns-long production runs were performed for both complexes using periodic boundary conditions. Particle Mesh Ewald (PME) algorithm was used to calculate long-range interactions. All visualizations were carried out using the Schrodinger's PyMOL package (Molecular Graphics System, Version ~1.8, 2015). Finally, the molecular mechanics Poisson-Boltzmann surface area (MMPBSA) module of gromacs was used to compute the free energy of GE11 binding interactions in the last 5 ns of each simulation.[339] All the graphs were plotted using Grace and Prism version 7.00 for Mac, GraphPad Software, La Jolla California USA.

5.2.9 Cell lines

Colorectal cancer cell lines HCT116 and SW620 (wild type) were purchased from the American Type Culture Collection (ATCC). The cells were grown in Dulbecco's Modified Eagle Medium supplemented with 10% FBS, 1% penicillin-streptomycin solution at 37°C in 5% CO_2 atmosphere. Two approaches were used for genetically modifying the HCT116 cell line. For luciferase expression, cells were transfected with pEGFPLuc2 vector (developed in Dr. Jirik lab, University of Calgary) using Lipofectamine^{TM} 2000 reagent. The clones producing the EGFP-Luc2 fusion protein were maintained in similar conditions as described above, except for the growth medium (DMEM:F12) and the additional antibiotic (G418, 500 μg/ml).[340] On the other hand, for PTEN deletion, a Cre-LoxP system was used (developed in Dr. Waldman lab, Georgetown University). Briefly, the linearized PTEN targeting vector was introduced into the cells using the same transfection agent previously mentioned. Individual colonies were obtained, expanded, and the G418-resistant clones were tested for the presence of a heterozygous knockout. After excision of the IRES-neo^R gene with adeno-cre, heterozygous knockout clones were then re-transfected with Aat II-linearized PTEN targeting vector to delete the remaining allele. Finally, G418-resistant clones were tested for the presence of homozygous knockouts [341]. For all the cells (i.e., wild-type and the modified ones), the EGFR expression profile was assessed by western blot.

5.2.10 *In vitro* cellular uptake studies

CRC cell lines HCT116 and SW620 were seeded into 12-well plates until reaching 70% confluence. GE11 modified, and plain mixed micelles containing Cy5.5 covalently attached to the core-forming segment were added in a concentration equivalent of 0.2 µg/mL of Cy5.5 in each well in triplicate and incubated for 3 h at 37 °C. After the incubation time, cells were washed three times with cold PBS and trypsinized. A 4% paraformaldehyde in PBS solution was added to fix the cells, and 10,000 events of single cells were recorded using the LSR-Fortessa X20 (BD Biosciences, Franklin Lakes, NJ). The cell-associated Cy5.5 was excited using a red-diode laser (635 nm), and the FL4 channel (675 nm) was used to detect the cell-associated median fluorescence intensity.

For confocal microscopy studies, the above CRC cells were seeded into 24-well plates containing round coverslips (0.2 mm thickness) at densities of 4-5 × 10^4 cells/well and incubated at 37 °C for 24 h until they are 50% confluent. Cy5.5-labeled plain or GE11 modified PEO-PBCL micelles (0.2 µg/mL Cy5.5) were added to the wells in triplicate and incubated for 3 h at 37 °C. After that, cells were washed three times with cold PBS and fixed for 10 minutes using 4% paraformaldehyde. Then, the cover-slips were removed and were inverted on a slide with a drop of mounting media containing DAPI. The slides were allowed to cure in the dark for 24 h. The analysis of cell-associated Cy5.5 was carried out by an inverted confocal microscope, Quorum WaveFX spinning disk confocal system (Quorum Technologies Inc., Guelph, Canada). Images were acquired in an oil immersion lens with 40× objective. Fluorophores were excited at 405 nm (for DAPI) and 633 nm (for Cy5's). The emitted fluorescence was detected through spectral channels between 410-500 nm and 633-744 nm for blue and red fluorescence, respectively. The images were acquired and analyzed using Volocity software (Perkin Elmer, Waltham, MA, USA).

5.2.11 Western Blot

Expression of EGFR by SW620 and HCT116 cell lines as well as HCT116-luc2+PTEN+/+ and HCT116-luc2+ *PTEN-/-* was evaluated at the protein level. Cells were seeded in 6-well plates, and once 70% confluence was reached, they were washed with PBS and lysed (in RIPA buffer). The lysis buffer was supplemented with phenylmethylsulfonyl fluoride (PMSF), protease and phosphatase inhibitor, and the cell lysates were incubated for 30 min on ice, followed by centrifugation at 21,000 × g for 20 min. After protein quantification, using a BCA protein assay kit, an equal amount of protein was resolved through gel electrophoresis and transferred to a nitrocellulose membrane. Membranes were probed with rabbit antibodies against EGFR and β-actin. Finally, protein revelation was done using peroxidase-conjugated anti-rabbit IgG and detected by chemiluminescence.

5.2.12 Cell proliferation assays

In vitro viability of CRC cells following treatment with A83B4C63 and its encapsulated form in plain and GE11 micelles was evaluated by measuring cellular metabolic activity and luminescence signal of HCT116-luc2+ *PTEN-/-* cells. Cells were seeded in a 96-well plate, and once 70% confluence was reached, cells were treated with increasing concentrations of A83B4C63 as part of different formulations. For 3-(4,5-dimethylthiazol-2-yl)-2,5-diphenyl tetrazolium bromide (MTT) assay, 20 μL MTT solution (5 mg/mL) was added to treated cells and incubated at 37°C for 2 h. The medium was then replaced by 100 μL DMSO, and the absorbance was read at 570 nm (Synergy H1 Hybrid Reader, Biotek). For the second measurement, cells were treated for 5 min with D-luciferin (20 mg/mL), and the luciferase activity was recorded by luminescence using the IVIS Imaging System (Caliper Life Sciences; Alameda, CA).

5.2.13 Animal models

Athymic NIH-III mice were purchased from Charles River (Wilmington, MA). All animal studies were conducted in accordance with the guidelines of the Canadian Council on Animal Care (CCAC) with

approval from the Animal Care and Use Committee (ACUC) of the University of Alberta (Edmonton, AB, Canada) and University of Calgary (Calgary, AB, Canada). Mice were fed using the 2014S Teklad Global 14% protein rodent maintenance diet in order to minimize fluorescence interference from chlorophyll. The orthotopic CRC mouse model was developed similarly to the one described previously with some modifications.[342] In summary, the intestine of each mouse was taken out by surgery, and 50 µL solution containing 0.5×10^6 HCT116-luc2+ cells and 50% Matrigel Basement Membrane Matrix (BD Biosciences, Franklin Lakes, NJ) was injected in their cecum wall. When the tumors become detectable by luminescence measurement, the treatments were initiated. Animals were monitored daily for any sign of abnormal behavior or weight loss.

5.2.14 *In vivo* imaging and tissue biodistribution study

Animals were injected through tail vein i.v. administration, with the following Cy5.5-tagged mix micelles: PEO-PCL, GE11-PCL, PEO-PBCL, and GE11-PBCL (**Table 5.S1**). The micellar concentration was 250 mg/kg of body weight (equivalent to 0.1 mg/kg of free Cy5.5), as described in our previous report.[250] At different time-points after injection (2, 6, and 24 h), fluorescence and luminescence signals were measured using the Xenogen IVIS Imaging System instrument (Caliper Life Sciences; Alameda, CA). For bioluminescence imaging, D-luciferin (150 mg/kg) was subcutaneously injected into the mice 5 minutes prior to the measurements. Animal images and readings were analyzed with Living Image 3.0 software (Caliper Life Sciences; Alameda, CA). Lastly, at 24 h post-injection, mice were euthanized for *ex vivo* studies. Tumors and other organs (liver, kidneys, lung, intestine, spleen, heart, and brain) were excised, incubated in D-luciferin solution (300 µg/mL) and imaged for fluorescence and bioluminescence using the IVIS instrument.

5.2.15 *In vivo* therapeutic activity of A83B4C63 loaded into micelles

Mice were treated (tail vein i.v. administration) with 25 mg/Kg of A83B4C63 physically loaded into PEO-PBCL and GE11-PBCL micelles, six times every other day. The tumor growth was monitored every 3-5 days through luminescence measurement, after 7 minutes of D-luciferin (150 mg/kg) subcutaneous injection (Xenogen IVIS Imaging System instrument, Caliper Life Sciences). The measurement of tumor volume using a caliper was not feasible since, in this orthotopic CRC mouse model, tumors got developed deep. A threshold of 2 x 10^7 p/s/cm^2/sr for luminescence by primary tumors was established as the endpoint for the study. Images and intensities were processed using the Living Image 3.0 software (Caliper Life Sciences; Alameda, CA).

5.2.16 Statistics

Data were presented as mean ± standard error of the mean (SEM). When suitable, the data were analyzed for statistical significance using unpaired student's t-test or one-way analysis of variance (ANOVA) followed by Tukey's *posthoc* test. The minimum level of significance was set for p < 0.05.

5.3 Results

5.3.1 Characterization of synthesized block copolymers and associated micelles

The characteristics of block copolymers under study are summarized in **Table 5.1**. PEO-PCL and PEO-PBCL block copolymers used in the study had a number average molecular weight (Mn) of 7,800 and 10,900 g/mol, respectively, based on ^{1}H NMR analysis (**Figure S5.1**). This corresponds approximately to the calculated degree of polymerization (DP) of 25, initially designed for both PCL and PBCL segments. The molar conjugation of peptide to polymer in GE11-PEO-PCL and GE11-PEO-PBCL was 79 and 70 % (i.e., there is around 79-70 mol of peptide per 100 mol block copolymers, respectively, as determined by HPLC with UV detector. For PEO-PCL-P(CL-*g*-Cy5.5) and PEO-PBCL-P(CL-*g*-Cy5.5), fluorescent spectroscopy confirmed the attachment of Cy5.5 into the PPC segments, and the quantification results showed the Cy5.5 molar conjugation percentage to the polymer was 2.4% and 5.9%, respectively. The DP of PCL and PBCL remained around 24-25 in GE11 or Cy5.5 modified block copolymers as determined by ^{1}H NMR (**Table 5.1**).

For NIR imaging studies, as depicted in **Figure 5.1**, the Cy5.5-labelled polymeric micelles termed as GE11-PCL micelles were prepared by mixing PEO-*b*-PCL (6.8 mg), GE11-PEO-*b*-PCL (1.2 mg), and PEO-*b*-PCL-*b*-P(CL-*g*-Cy5.5) (2.0 mg). While GE11-PBCL micelles preparation was performed by combination of PEO-*b*-PBCL (8.0 mg), GE11-PEO-*b*-PBCL (1.4 mg), and PEO-*b*-PBCL-*b*-P(CL-*g*-Cy5.5) (0.6 mg). Control micelles, having no peptide decoration, were made up similarly, but without mixing the GE11-containing block copolymers with their composition listed in **Table 5.S1**.
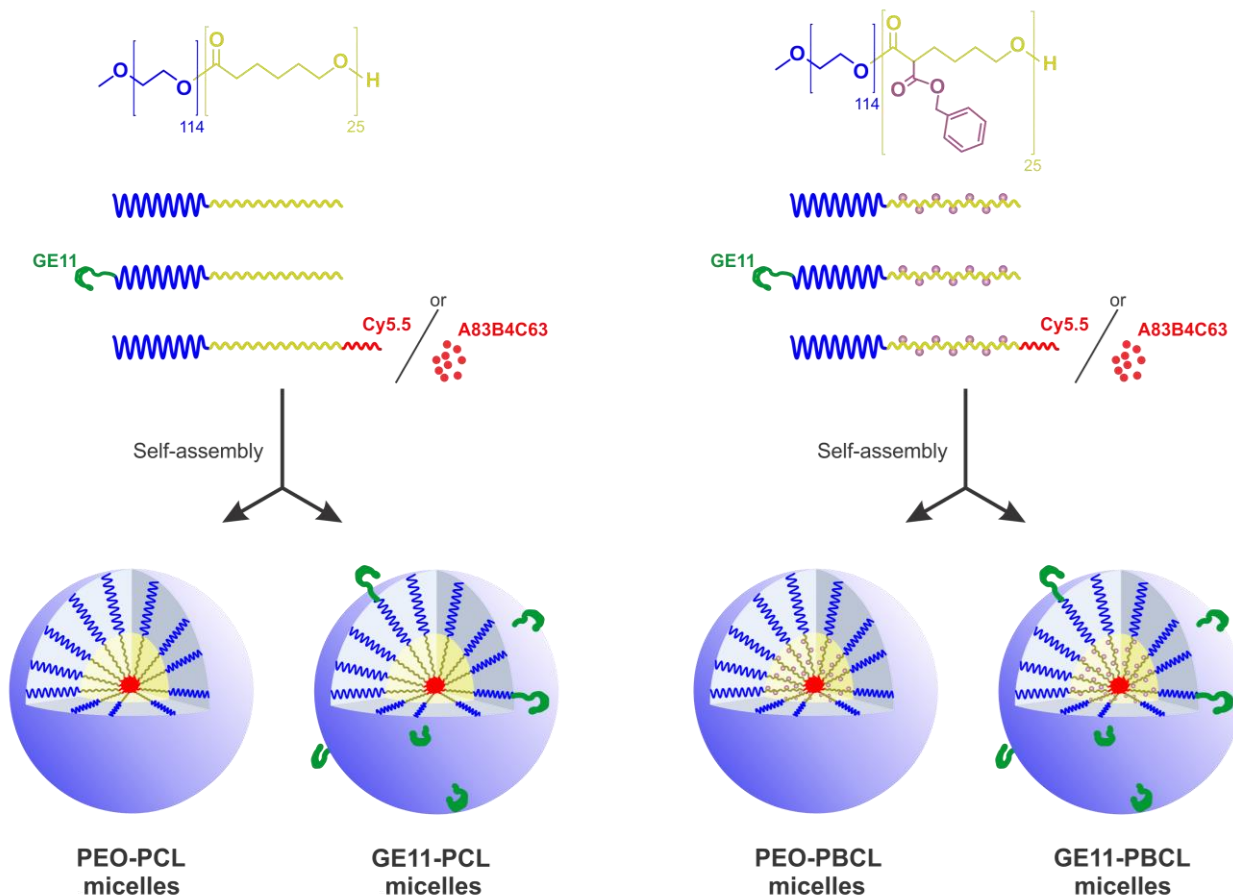
Figure 5.1. The model for the preparation of GE11-modified mixed micelles either tagged with Cy5.5 or physically loaded with A83B4C63 compound.

For assessment of anti-cancer activity, GE11-modified mixed micelles were prepared through a combination of PEO-*b*-PCL or PEO-*b*-PBCL and their corresponding GE11-modified copolymer counterparts, together with A83B4C63 compound, which were dissolved in acetone prior to the micellization. Plain micelles carrying A83B4C63 were prepared using PEO-*b*-PCL or PEO-*b*-PBCL alone. The composition of block copolymers for each micellar formulation is listed in **Table 5.S1**. A co-solvent evaporation method was used for the micellization process.

Table 5.1. Polymer composition of the prepared mixed micelles.

Block copolymers	Mn (g/mol)	Degree of polymerization (DP) per segment			Cy5.5 conj. (molar % ± SD)	GE11 conj. (molar % ± SD)
		PEO	P(B)CL	PPC		
PEO-*b*-PCL	7,800	114	24.5	-	-	-
GE11-PEO-*b*-PCL	9,300	123	24.3	-	-	78.7% ± 2.5
PEO-*b*-PCL-*b*-P(CL-*g*-Cy5.5)	9,700	114	23.7	2.9	2.4 ± 0.3	-
PEO-*b*-PBCL	10,900	114	23.6	-	-	-
GE11-PEO-*b*-PBCL	12,600	123	24.4	-	-	70.2% ± 2.2
PEO-*b*-PBCL-*b*-P(CL-*g*-Cy5.5)	13,200	114	25.3	2.7	5.9 ± 1.1	-

The characteristics of prepared micellar formulations are summarized in **Table 5.2**. All polymeric micelles used in this study showed a low polydispersity index (PDI < 0.3). The PBCL-based micelles (~ 41 nm) were statistically smaller in diameter than the PCL-based ones (~ 55 nm) ($p < 0.05$; unpaired t-test). The incorporation of A83B4C63 into micellar structure did not affect particle size among PBCL-based micelles ($p > 0.05$; one-way ANOVA, Tukey's *posthoc* test), though this measurement was significantly affected by A83B4C63 incorporation in PCL-based ones ($p < 0.05$; one-way ANOVA, Tukey's *posthoc* test), and that change did not follow a specific trend. The average diameter of plain micelles versus GE11 micelles showed that the peptide incorporation contributed to increasing the micellar particle size independently on the absence or presence of the loaded drug.

Empty PEO-PCL and PEO-PBCL micelles showed a near neutral zeta potential. Zeta-potential of particles increased by GE11 surface modification of both PCL- and PBCL- based micelles ($p < 0.05$; one-way ANOVA, Tukey's *posthoc* test), which has also been observed among different types of polymeric micelles.[201] This change in measurements further confirms the success of peptide conjugation. Drug encapsulation in plain and GE11 modified micelles led to an increase in micellar ZP as well.

Modification of micellar shells with GE11 did affect the CMC for both PCL and PBCL micelles (**Table 5.2**), leading to a significant decrease in micellar thermodynamic stability ($p < 0.05$; one-way ANOVA, Tukey's *posthoc* test). Moreover, micelles containing benzyl groups in their core were identified having a much lower CMC compared to the ones with PCL cores irrespective of peptide modification ($p < 0.05$; one-way ANOVA, Tukey's *posthoc* test).

Incubation of plain- or GE11-modified PBCL based micelles with SDS did not affect the kinetic stability of these structures, whereas a substantial decrease in the intensity of PCL-based micelles was observed following incubation with SDS (**Figure 5.2A-B**).

Table 5.2. Characterization of polymeric micelles.

Mixed micelles	Size (nm)	PDI	ZP (mV)	CMC (nM)	EE (%)
PEO-PCL	56.5 ± 0.5 [a]	0.24	-0.75 ± 0.21 [a]	368 ± 0.02 [a]	-
GE11-PCL	53.5 ± 0.1 [b]	0.23	-3.48 ± 0.55 [a,b]	419 ± 0.05 [b]	-
PEO-PCL + A83	54.3 ± 0.1 [c]	0.20	-9.91 ± 0.64 [c]	-	74.0 ± 2.8 [a,b]
GE11-PCL + A83	55.3 ± 0.1 [d]	0.22	-16.8 ± 1.48 [d]	-	72.1 ± 3.5 [a]
PEO-PBCL	39.9 ± 0.3 [e]	0.21	0.99 ± 0.36 [a]	95 ± 0.02 [c]	-
GE11-PBCL	41.5 ± 0.2 [f]	0.26	-5.16 ± 0.78 [b]	167 ± 0.01 [b]	-
PEO-PBCL + A83	40.1 ± 0.2 [e]	0.18	-6.92 ± 1.98 [b,c]	-	79.5 ± 1.4 [b,c]
GE11-PBCL + A83	42.2 ± 0.3 [f]	0.16	-16.0 ± 2.55 [d]	-	80.8 ± 2.1 [c]

* Letters superscripted in each column indicate the results after statistical analysis (one-way ANOVA, Tukey's posthoc test). Values ($n = 3$) bearing the same letters are not significantly different from each other ($p > 0.05$), and in the opposite case, their differences are significant ($p < 0.05$).

PEO-PCL and GE11-PCL micelles showed an average encapsulation efficiency of 74.0 and 72.1% for A83B4C63, respectively. This value for PEO-PBCL and GE11-PBCL micelles was 79.5 and 80.8%, respectively (**Table 5.2**). In general, PBCL-based micelles showed higher encapsulation of A83B4C63, without or with peptide on their surfaces ($p < 0.05$; unpaired t-test). In both micellar core structures, no

difference in the encapsulation of A83B4C63 between plain and GE11 modified ones was observed (p < 0.05, one-way ANOVA). Furthermore, > 70% of the drug was released from the PCL micellar cores within 8 h (72.6% for PEO-PCL micelles and 88.8% for GE11-PCL micelles), as shown in **Figure 5.2C,** whereas PBCL micelles showed < 50% drug release at that same time point (42.7% for PEO-PBCL micelles, and 29.5% for GE11-PCL micelles, on average). While drug release for PCL micelles was nearly 100% at 48 h, only 65.7% and 68.9% of the A83B4C63 was released from PEO-PBCL and GE11-PBCL micelles, respectively, at that same time point.
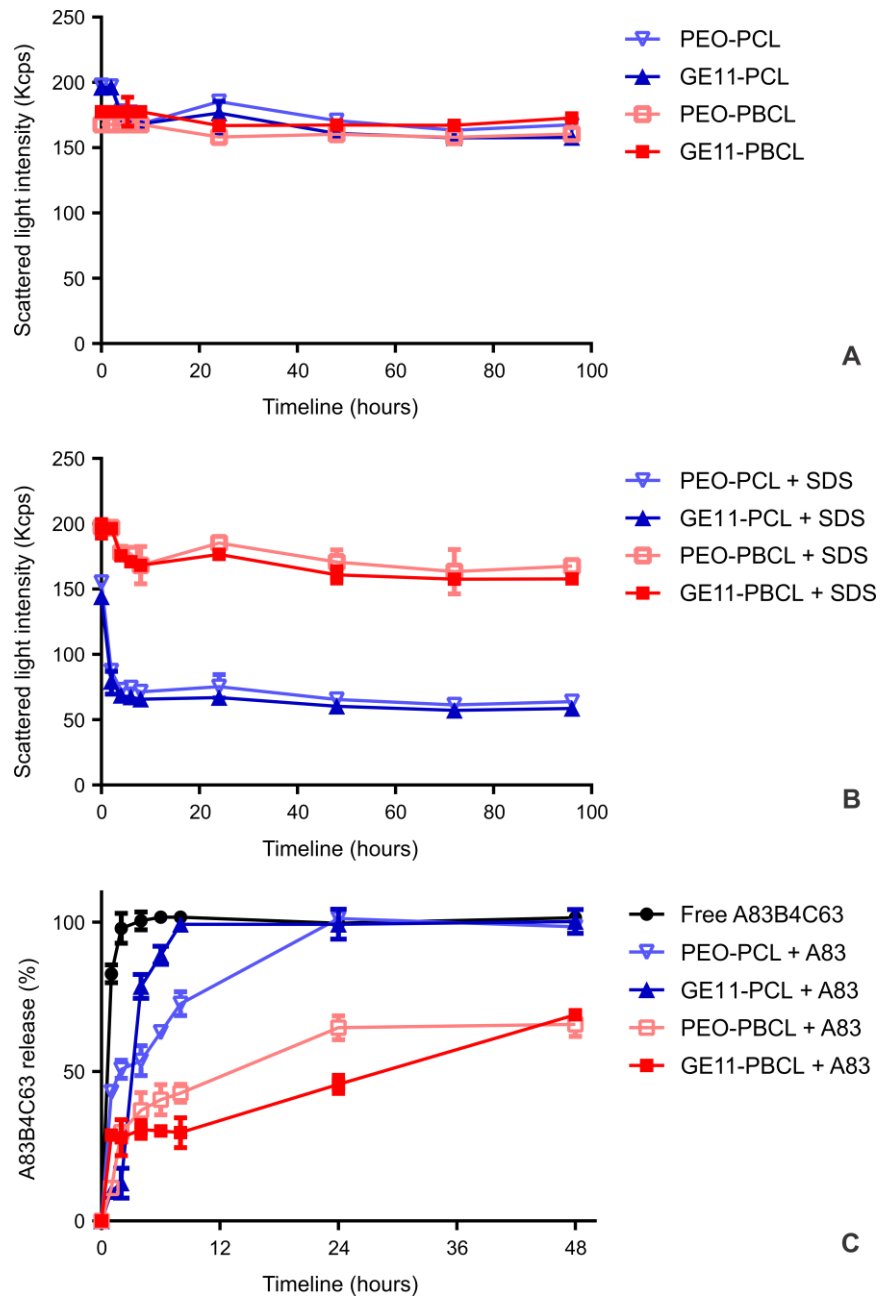
Figure 5.2. Micellar kinetic stability profile. (A): in water. (B): in presence of sodium dodecyl sulfate (SDS, 6 mg/mL). (C): Graph in shows the *in vitro* release of A83B4C63 as free drug and as plain and GE11 micellar formulations.

5.3.2 Binding mode and binding free energy of GE11 *versus* EGF to EGFR

The predicted human EGFR binding site for the GE11 peptide was found to be different from that of EGF (**Figure 5.3**). The free energy for binding interactions calculated for GE11/EGFR and EGF/EGFR complexes were −163.43 Kj/Mol (−39.06 Kcal/Mol) and −621.68 (−148.58 Kcal/Mol), respectively (**Table 5.3**). This difference in binding free energies for these two ligands indicates that EGF binding is 3.8 times more spontaneous, and is consistent with previous observations reported in the literature [279]. **Figure 5.S3** shows the interacting side-chain amino acid residues involved in both complexes during the MD simulations. The Root Mean Square Deviation (RMSD) of backbone, ligand positional RMSD, and Root Mean Square Fluctuation (RMSF) of the EGFR side chain were also computed (**Figure 5.S3A-C**). The backbone RMSD of GE11/EGFR and EGF/EGFR complex shows reasonable stability for the EGFR backbone during the MD simulation of both complexes. However, we observed higher stability for the EGF complexed with the EGFR in the ligand positional mode compared to that of GE11 (**Figure 5.S3B**).
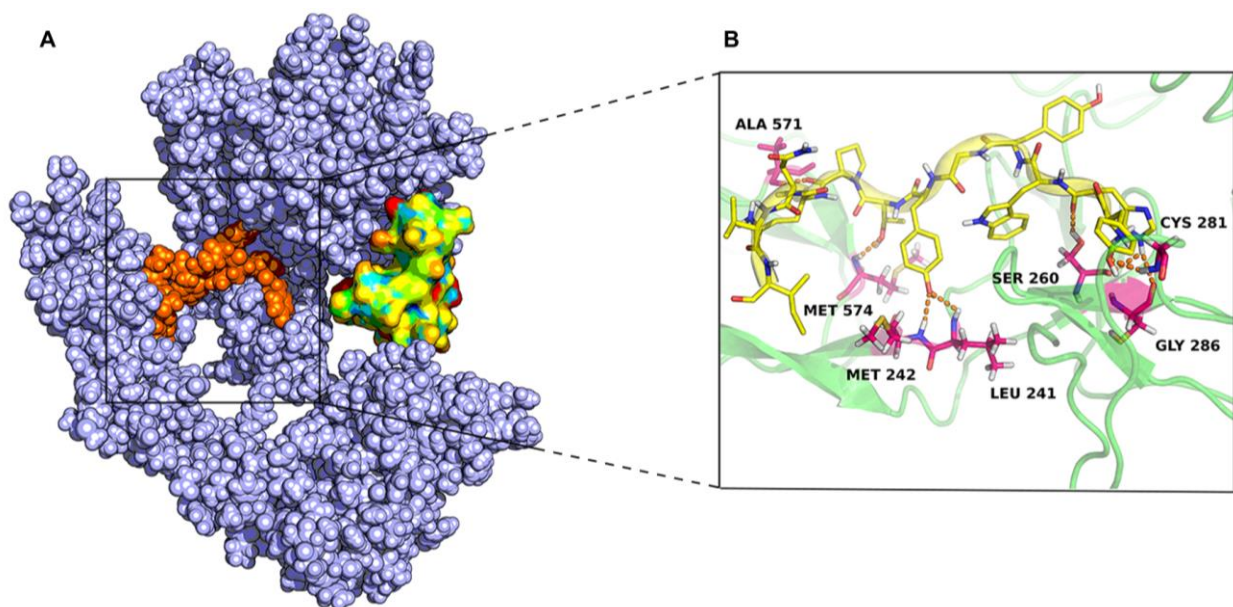
Figure 5.3. Molecular dynamics simulations using the crystal structure of human EGFR. (A): Prediction of the binding site of EGF (in yellow) and GE11 (in red) with EGFR. (B): Identification of the main intermolecular bindings between GE11 and EGFR.

Table 5.3. Calculated free energy of binding to EGFR for EGF and GE11 (MMPBSA). The free energy of binding was calculated by summing the Van Der Waal, SASA, and Electrostatic energy and subtracting the Polar solvation energy.

EGFR ligand	Van der Waal energy (KJ/mol)	Electrostatic energy (KJ/mol)	Polar solvation energy (KJ/mol)	SASA energy (KJ/mol)	Binding energy (KJ/mol)
EGF	−558.426 ± 33.4	−395.031 ± 116.3	392.68± 60.5	−60.908 ± 3.6	−621.68 ± 165.72
GE11	−234.07 ± 27.3	−192.73 ± 42.9	292.64 ± 66.2	−29.264 ± 3.5	−163.43 ± 33.08

5.3.3 GE11-containing micelles are highly internalized by EGFR-expressing cells

Fluorescent signals from Cy5.5-labelled polymeric micelles, quantified by flow cytometry analysis, indicated that the overall micellar uptake by SW620 cells was lower compared to HCT116 cells (**Figure 5.4**). Despite this difference in endocytosis rate, PCL- and PBCL-based micelles, with and without GE11 surface modification, exhibited similar uptake by SW620 cells. On the contrary, GE11- modified micelles showed enhanced uptake by HCT116 cells compared to the plain micelles (**Figure 5.4A**). The observation was in line with the level of EGFR expression in these two cell lines as measured by western blot (**Figure 5.S5**).

The effect of peptide density on micellar shell on the uptake of particles by SW620 and HCT116 cells was also tested for PBCL based micelles. The results showed a similar level of micellar uptake, irrespective of GE11 density, on SW620 cells. In contrast, increasing the levels of GE11 peptide on the micellar surface contributed to an increase in cell-associated fluorescence in EGFR-positive HCT116 cells. The exception was a non-significant difference between the uptake of micelles with 10 and 20 mol% of GE11, suggesting saturation of cell surface EGFR at the 10 % level. The confocal microscopy data (**Figure 5.S4**), confirmed the preferential internalization of GE11- micelles in HCT116 cells as compared to that of plain micelles or uptake in SW620 (EGFR negative) cells.
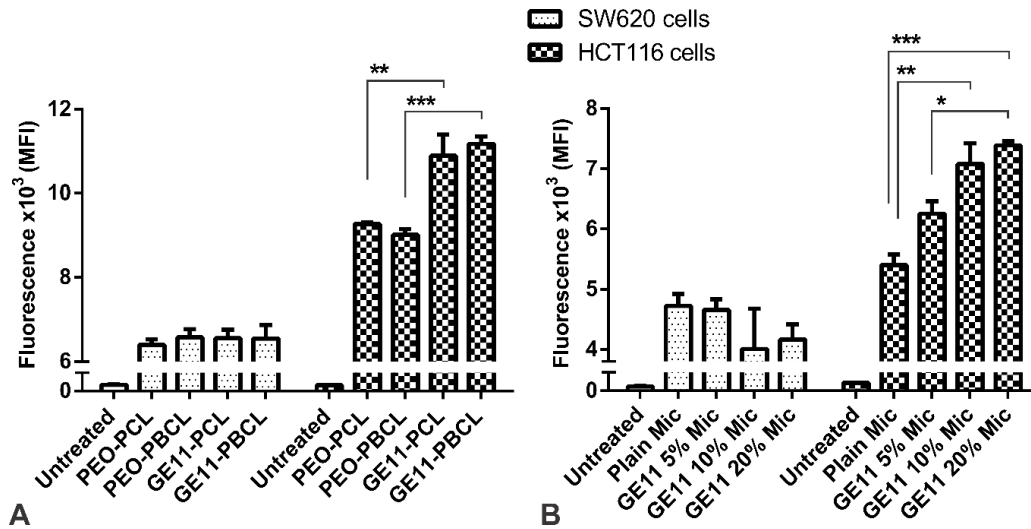
Figure 5.4. *In vitro* uptake of Cy5.5-labelled mix micelles by colorectal cancer cell lines. Flow cytometry data shows median fluorescence intensity (MFI) measured after 3 h treatment at 37 °C. (A): Effect of GE11 modification on PCL- and PBCL-based micelles. (B): Effect of PBCL-based micelles with different surface peptide densities. * $p < 0.05$, ** $p < 0.01$, *** $p < 0.001$. Data are presented as mean ± SEM.

5.3.4 *In vivo* distribution of GE11 modified versus plain polymeric micelles in orthotopic HCT116 Luc+ xenograft model

Live images of plain or GE11-modified micellar biodistribution following intravenous injection in orthotopic HCT116 Luc+ xenografted NIH III mice is shown in **Figure 5.5**. The tumor location was identified by luminescence imaging and used to estimate micellar accumulation in the tumor for different groups under study. Using this method, in live animals, higher tumor accumulation of Cy5.5-labelled PCL-based micelles (either plain or GE11- modified) was achieved at 2 h time point compared to the PBCL-based micelles ($p < 0.05$, unpaired t-test). However, over time this pattern was shifted in a way that at 6 h post-injections, the micellar fluorescence signals were comparable among all micelles under study. At 24 h time point, the tumor accumulation of PEO-PBCL micelles was higher than that of their counterparts (i.e., PEO-PCL micelles – $p < 0.05$; unpaired t-test).
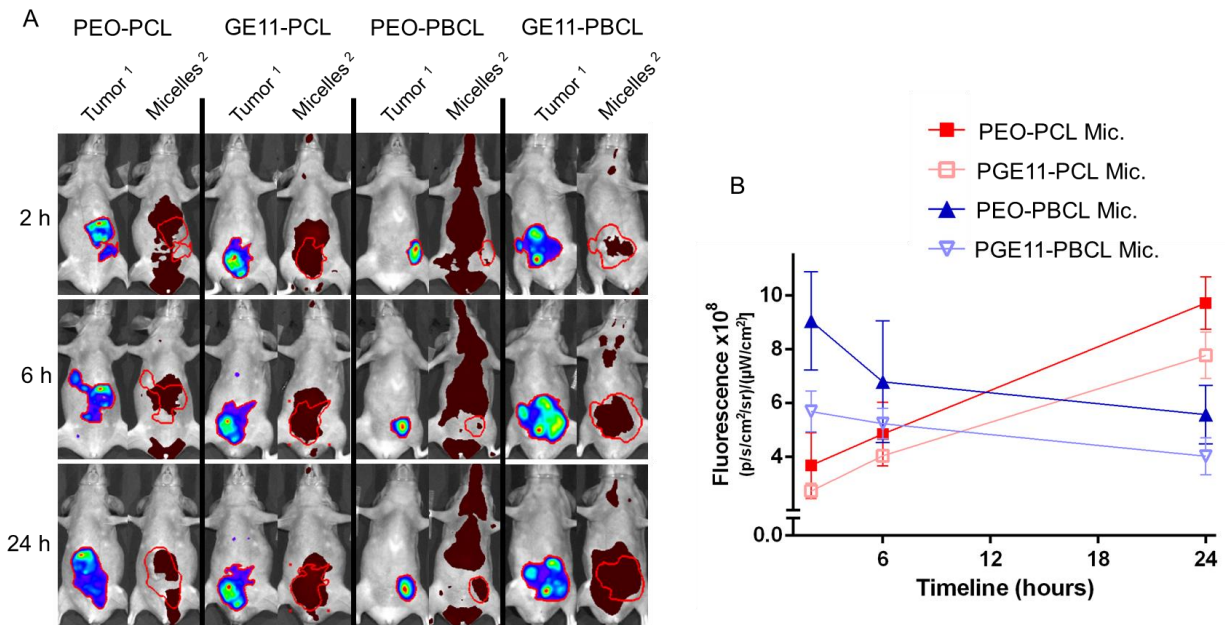
Figure 5.5. *In vivo* imaging of Cy5.5-tagged mixed micelles after 2, 6, and 24 h intravenous administration. (A): Each time-point contains one representative capture of luminescence (Tumor signal[1]) and fluorescence (Micelles[2]). (B): Graph shows fluorescence intensity coming from the Cy5.5-labeled polymeric micelles at the region co-localized with luminescence signals.

The above analysis in live animals provided an estimate over the distribution of different micellar formulation in orthotropic tumors. However, depending on the distribution of particles among organs that reside near the region where cecum is located, such as spleen and liver, an overestimation of micelle accumulation in the orthotopic tumor model may have occurred. The analysis of the excised organs contributed to a clearer insight about micellar biodistribution. This analysis was conducted at 24 h post-injection (**Figure 5.6**). Except for kidneys that showed a comparable distribution among PCL and PBCL micelles, all other examined main organs (i.e., liver, lungs, and heart) illustrated a considerably stronger fluorescent signal for PBCL-based micelles. A trend towards higher accumulation of PBCL-based micelles compared to PCL-based ones was also observed in the spleen, which was statistically not significant. The results suggest that all the prepared polymeric micellar systems were not able to cross the brain-blood barrier since no signal was detected in the brain.
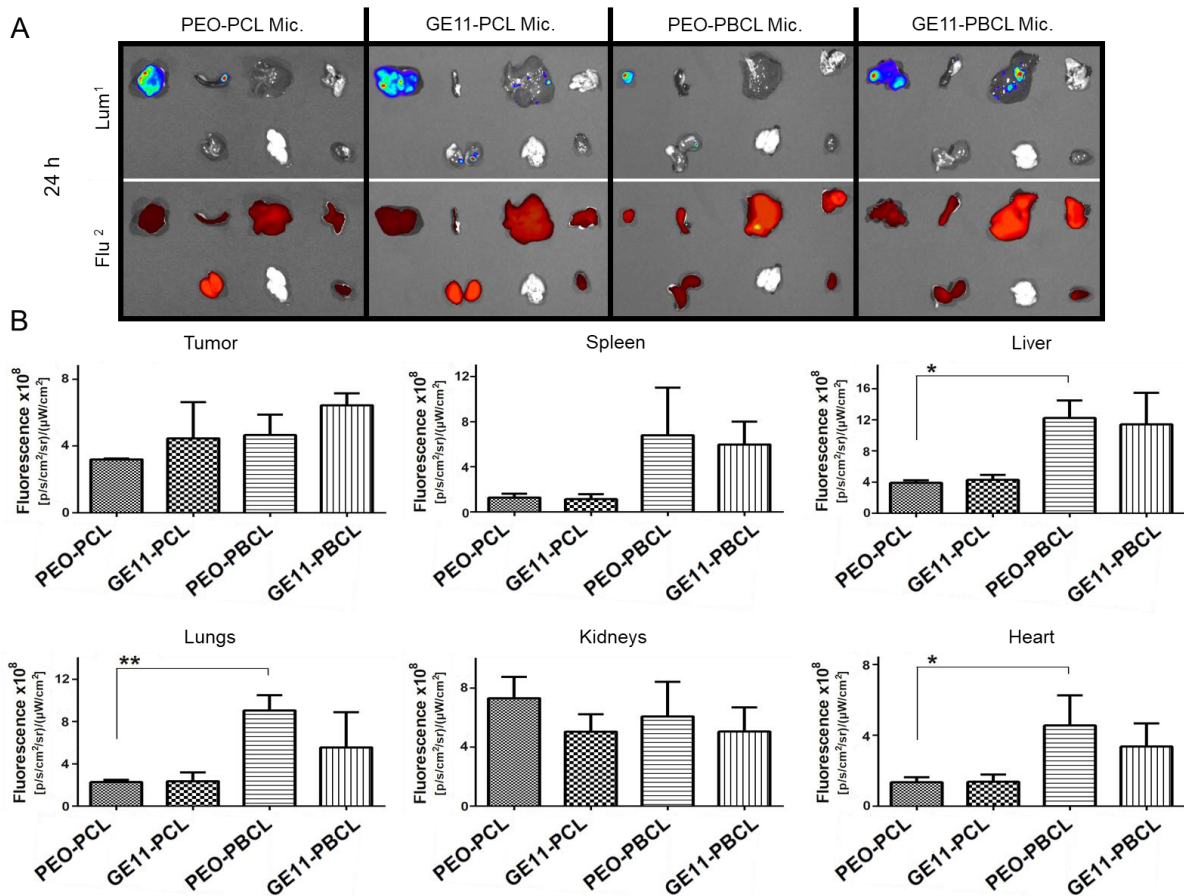
Figure 5.6. *Ex vivo* imaging of Cy5.5-tagged micelles 24 h after intravenous administration. (A): Images show (clockwise from bottom right corner) tumor, spleen, liver, lungs, heart, brain, and kidneys. Each excised organ is representative of one individual mouse from a group of three mice. Tumor signal[1]: Luminescence originated from the HCT116 luciferase positive cells; Micelles signal[2]: Fluorescence from the Cy5.5 dye present inside of the micelles. (B): The bar graphs represent the micelle accumulation in the organs after 24 h injection ± SEM. Unpaired t-test, * $p < 0.05$, ** $p < 0.01$.

Analysis of the excised intestines from animals with tumor growth pointed to a trend in increased accumulation of GE11-modified micelles compared to their plain (unmodified) counterparts, but the difference was not statistically significant (data now shown). More rapid clearance of PCL-based micelles within 24 h possibly through kidneys were observed. On the other hand, PBCL-based micelles appeared to stay longer in the circulation, showed higher levels in normal organs, and were mainly cleared by the liver since this organ presented the strongest fluorescence.

5.3.5 Therapeutic activity of A83B4C63 nano-formulations

We have conducted studies evaluating the anti-cancer activity of encapsulated A83B4C63 in plain versus GE11 modified micelles, against HCT116-Luc2+ *PTEN*-/- tumors *in vitro*, and *in vivo*. As shown in **Figure 5.7**, encapsulated A83B4C63 in PCL-based micelles appeared to be more effective in reducing cell proliferation compared to PBCL-based formulations of this drug, particularly when MTT assay was used. This observation was in line with a slower release of A83B4C63 from the PBCL based micelles. GE11 modification of the micellar surface contributed to enhancing the therapeutic activity of PBCL-based micellar formulations of A83B4C63 at drug concentrations ≥ 12.5 μM (**Figure 5.7D**). The effect of GE11 modification of micellar formulation was not observed for GE11-PCL micelles at least up to 50 μM of A83B4C63.
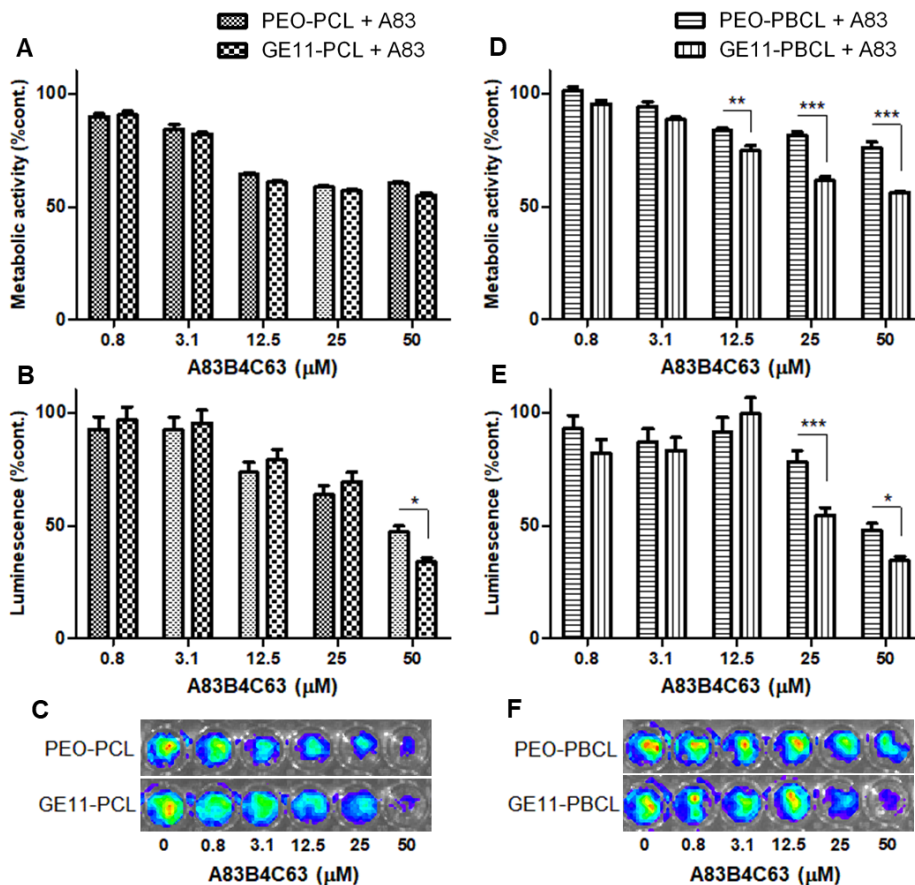
Figure 5.7. *In vitro* therapeutic activity of nano-formulated A83B4C63 in HCT116-Luc2+ *PTEN-/-* cells. After 48 h treatment, MTT assay was carried out using (A) PCL-based and (D) PBCL-based micelles. Luciferase activity was measured in parallel, through luminescence signal. (B and E): Data presented by bar graphs, as well as by the images (C and F) of cell culture plates. The experiments were done in triplicate and are expressed by mean ± SEM. Unpaired t-test, * $p < 0.05$, ** $p < 0.01$, *** $p < 0.001$.

PBCL-based micelles were able to provide a controlled release profile of the A83B4C63 compound within 48 h (e.g., the release from GE11-PBCL was 2.2-fold slower than GE11-PCL), as well as a higher tumor accumulation *in vivo* over the PCL-based ones at 24 h timepoint. Thus, because of these outcomes, the evaluation of the drug activity was performed using only nano-formulations composed of PEO-PBCL and GE11-PBCL micelles. The results of this study are summarized in **Figure 5.8**. The *in vivo* image of tumor growth in the longest surviving mice in each group is shown in **Figure 5.8A**. As shown here, the longest survival for mice receiving dextrose 5 % vehicle was 37 days, whereas this duration was elongated to 54

and 72 days for the longest surviving mice treated with plain and GE11 modified PBCL based micelles of A83B4C63, respectively. **Figure 5.8B** and C, the rate of tumor growth in the animal of different groups. Mice receiving dextrose was the first group in which the luminescence signal, from the orthotopically implanted CRC cells, reached the threshold level. This was followed by the group treated with plain PEO-PBCL formulation of A83B4C63 and, later, by the group that received the A83B4C63 loaded into GE11-PBCL micelles. The effect of GE11 modification on this formulation significantly contributed to lowering tumor growth when compared with the dextrose group at 37 days following initial treatment. (**Figure 5.8E**). Animals treated with dextrose and PEO-PBCL formulations presented a small impairment in weight gain (**Figure 5.8D**). The survival curve indicates that the A83B4C63 treatment using both formulations were effective in prolonging the mouse lifetime when compared with the dextrose group, even though the treatment was slightly more beneficial when the GE11-modified formulation was applied (**Figure 5.8E**).
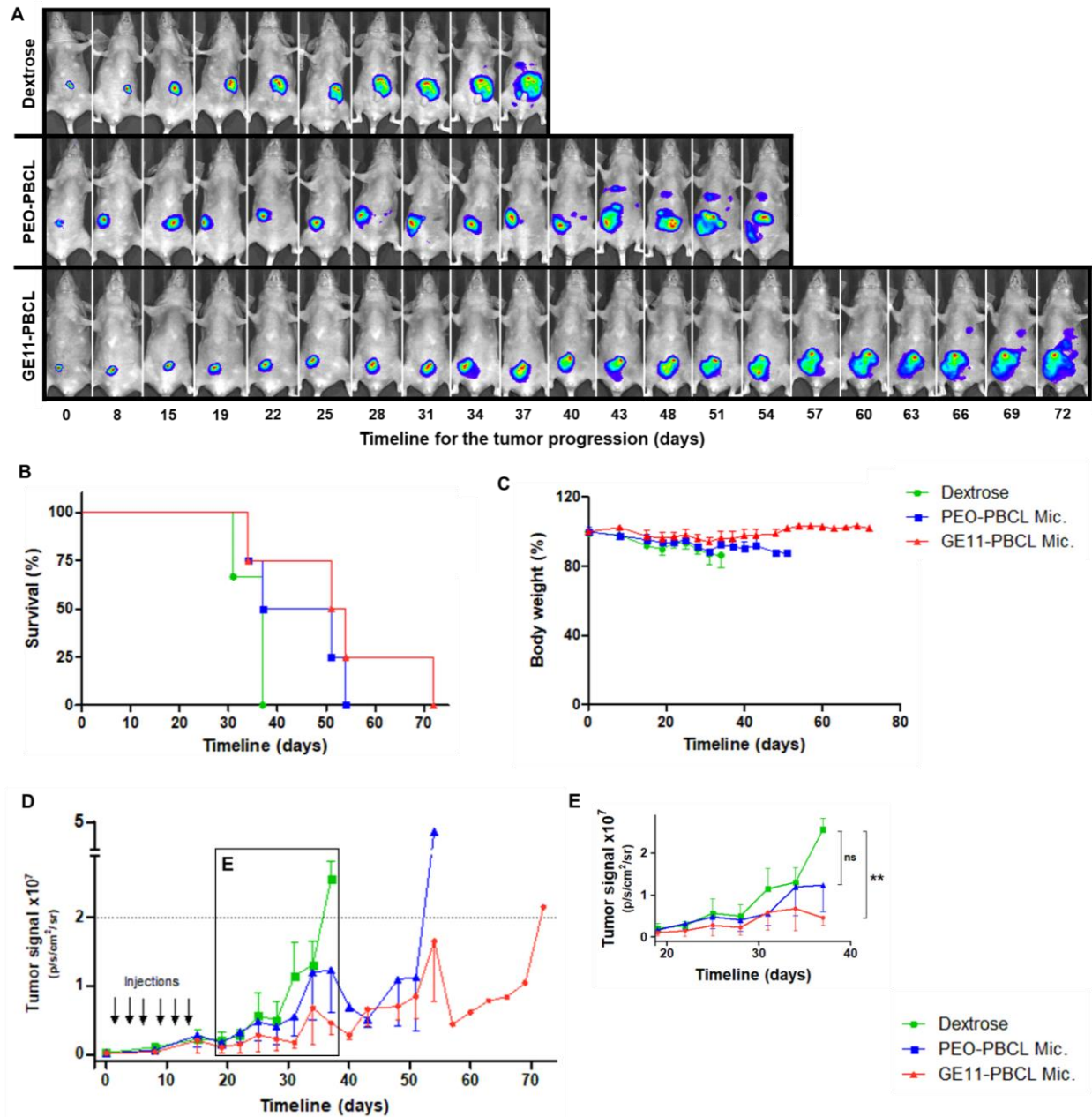
Figure 5.8. *In vivo* treatment with A83B4C63 loaded into PBCL-based micelles. NIH-III nude mice, implanted with HCT116-Luc2+ *PTEN-/-* cells orthotopically received 6 i.v. injections of 25 mg/Kg of the PNKP inhibitor. (A): Luminescence images of the individual mouse from each group that had the highest survival. (B): Survival curve for the three groups tested. (C): Mean percentage change in animal body weight. (D): Tumor growth monitoring throughout the timeline of the study. The dotted line shows the luminescence threshold, indicating the endpoint for each animal. (E): The highlight of important timepoints in the treatment course. Values are the mean of maximum 3-4 mice ± SEM (n = 3-4). Unpaired t-test, ^{ns} p > 0.05, ** p < 0.01.

5.4 Discussion

The main objective of the present study was to investigate the biodistribution of Cy5.5-labelled polymeric micelles and the therapeutic activity of A83B4C63 nano-formulations using a relevant CRC animal model. In cancer research, pre-clinical *in vivo* studies have a tremendous importance towards the optimization of therapeutic and diagnostic approaches. Human CRC xenografts are usually developed in immune-deficient mice by inoculating cells/tumor ectopically or orthotopically. In the first method, the cancer implantation takes place in the subcutaneous flank of the animals and although it is the most common strategy, this is not considered to be a realistic model and lacks clinical relevance. On the other hand, orthotopic models are designed to display the CRC tumors in a more natural tumor microenvironment (i.e., tumor located in the mouse intestine), and in consequence, more similarities in cancer cell differentiation, angiogenesis, amount of stroma and metastasis have been identified when compared to the actual patterns from patients. In line with other similar reports on this form of CRC mouse model, we also found metastatic regions among the majority of the inoculated mice, highlighting spleen and liver as well as lungs that are commonly reported as an organ for finding metastasis. The brain was the only organ no mouse presented luminescence signal.[342–344]

Synthetized block copolymers were designed to have, in the polycaprolactone core-forming segments, a degree of polymerization (DP) around 25. The polymeric micelles prepared in this study showed better micellar characteristics, overall, in contrast to micelles previously prepared using similar di-block copolymers, but with shorter length (DP ~ 10), especially regarding their critical micellar concentration lower. In that previous report, their CMC values were respectively ~ 3.7 µM and ~ 0.8 µM for PCL- and PBCL-based micelles, which were much higher than what we found here (~ 0.39 µM and ~ 0.13 µM for PCL- and PBCL-based micelles, respectively), indicating that our polymeric micelles had a superior thermodynamic stability.[250] Moreover, we have found that higher DP was crucial for improving micellar core capacity to efficiently load and provide a sustained release for a couple of PNKP inhibitor

candidates, that are currently being optimized and/or tested in our research group, for CRC treatment.[267] The lack of benzyl groups among PCL-based nano-formulations may have contributed to this fast drug release behavior. By observing the chemical structure of A83B4C63 molecule, previously described, many aromatic rings can be found in its composition, which may have enhanced the interaction within the cores from PBCL-based micelles through intermolecular bonds (i.e., π–π stacking),[345] leading to more prolonged drug retention inside those micellar formulations.

Micellar shells of both PCL- and PBCL-based micelles were modified by GE11, and our *in vitro* cell uptake experiments confirmed the widely known affinity between this dodecapeptide and the EGF-receptor. Only the EGFR-positive HCT116 cells showed enhancement in the uptake of GE11-containing micelles, whereas among EGFR-negative SW620 cells, no difference was observed when compared to micelles with unmodified shells. After GE11 discovery and characterization, little has been done regarding peptide optimization, especially towards a lower proteolytic degradation in the presence of human serum.[279,323] More recently, this peptidic sequence was reported to present poor stability against proteolysis ($t_{1/2} \sim 1$ h), which confirms the need for more investigation about its improvement in stability against chemical degradation.[320] An interesting approach seems to be the peptide cyclization, which has already been implemented with successful outcomes. This issue represents a special concern when the peptide is attached to the surface of nanoparticles, given their longer *in vivo* circulation.[206,346]

MD simulation analysis confirmed the lower affinity of GE11 towards human EGFR in contrast with the physiological ligand by calculating the binding free energy for both interactions. This finding is in agreement with different data reporting higher dissociation constants for GE11 ($Kd \sim 4.59 \times 10^{-4}$ M) relatively to EGF ($Kd \sim 1.77 \times 10^{-7}$ M).[279,324] We also corroborated another MD simulation pointing out for the fact that the GE11 binding site is near EGF binding pocket,[281] but in our prediction, we further identified that their binding site, actually, does not overlap. In that study, Ongarora *et al.*[281] highlighted only two amino acid residues (one tyrosine and one isoleucine) belonging to GE11 as the main stabilizers

of the interaction with EGFR. In contrast, our analysis suggested more amino acid residues (total of 7) for the peptide-receptor binding.

Biodistribution of the injected polymeric micelles throughout the mice's body was assessed by imaging the rodents alive, under anesthesia, and by separately imaging their excised organs. Our micellar nano-constructs were tracked through the near-infrared (NIR) fluorophore Cy5.5, which was covalently grafted to a core-forming segment from the triblock copolymers. *Ex vivo* images of the organs revealed that, after 24 h injections, the highest accumulation of PCL-based micelles (either unmodified or GE11 shell-modified ones) was found in the kidneys. The sieving coefficient of glomerular basement membranes, from kidneys, has been previously characterized by using dextran and is generally known that macromolecules above 10 nm are mostly retained in the blood circulation.[306,347,348] Taken together, we can suggest that PCL-based micelles (particle size ~ 55 nm) may have undergone dissociation, which is in accordance with their poor stability data foregoing, so that most of the fluorescence signal detected in this organ may have come from the PEO-*b*-PCL-*b*-P(CL-*g*-Cy5.5) unimers, instead of the actual formulation. The enhancement of micellar tumor accumulation was accomplished due to a combined effect of micellar core and shell modifications. Benzyl grafts on the core-forming segment contributed to the formation of micelles with a more compacted core, and consequently, more stable in the blood circulation, which is reflected by the overall higher accumulation of PBCL-based micelles among the organs. On the other hand, the attachment of GE11 peptide to the shell-forming segment increased cell internalization, given the stronger interaction of surface-modified micelles with those cancer cells, highly expressing EGFR. Thus, the combination of both micellar modifications seems the best strategy for enhancing their potential for delivering payloads into tumors.

Our *in vitro* results showed that the encapsulated A83B4C63 into PCL-based micelles was overall more cytotoxic for the cells than the compound loaded with PBCL-based micelles. One of the main reasons for this observation may be the fast drug release among these micelles, allowing the free drug to act

longer among the plated cells, which in an *in vivo* perspective, is not desirable due to the lack of tumor specificity that the drug nanocarrier confers to the encapsulated small molecule. The role of the GE11 micellar surface modification on cytotoxicity of A83B4C63 was more prominent among PBCL-based micelles, and the significance could be detected by both readouts (i.e., MTT assay and luminescence), especially in the 25 µM concentration.

Mice were treated with A83B4C63 loaded into PBCL-based micelles since they were advantageous over the PCL-based micelles in the biodistribution and *in vitro* cytotoxicity studies. The aggressiveness of tumors in this present model, especially because of the absence of PTEN, was found to be very high. Mice without any treatment or individuals from the other groups that had higher tumor growth at the beginning of the injections experienced a very rapid tumor progression with metastasis in almost all the organs. Even so, mice that received GE11-modified micelles were slightly more benefited than the ones treated with plain micelles, and an improvement in drug efficacy was observed over the non-modified formulation, which can be seen by a lower luminescence signal throughout the study course as well as by the prolonged survival of mice from this group.

5.5 Conclusion

The biodistribution and drug activity study of our prepared mix micelles was investigated in conditions that are very close to an actual CRC scenario since human cancer cells were inoculated orthotopically into the mice. PBCL-based micelles presented a superior half-life in blood circulation when compared with PCL-based ones. Even though the micellar shell modification with GE11 contributed alone for higher *in vitro* uptake by HCT116 cells, the outcomes *in vivo* did not follow the same pattern. Only when micellar core- and shell-modification were taken into account together, an enhancement in tumor accumulation was observed. Therefore, despite the differences in micellar structures that may occur after loading a hydrophobic payload into the micellar core, our data demonstrated the real capacity of GE11-PBCL micelles to enhance drug delivery into the CRC tumors, given their great tropism to tumors. In fact, the therapeutic activity of A83B4C63 towards PTEN-negative CRC cells was slightly more pronounced in the group that EGFR was targeted by using the GE11 peptide.

5.7 Supplementary Information

Table 5.S1. Polymer composition of the prepared mixed micelles.

Polymers / Drug	Cy5.5-labelled micelles				Micelles loaded with A83B4C63			
	PEO-PCL	GE11-PCL	PEO-PBCL	GE11-PBCL	PEO-PCL	GE11-PCL	PEO-PBCL	GE11-PBCL
PEO-*b*-PCL	8.0	6.8	-	-	10	8.8	-	-
GE11-PEO-*b*-PCL	-	1.2	-	-	-	1.2	-	-
PEO-*b*-PCL-*b*-P(CL-*g*-Cy5.5)	2.0	2.0	-	-	-	-	-	-
PEO-*b*-PBCL	-	-	9.4	8.0	-	-	10	8.6
GE11-PEO-*b*-PBCL	-	-	-	1.4	-	-	-	1.4
PEO-*b*-PBCL-*b*-P(CL-*g*-Cy5.5)	-	-	0.6	0.6	-	-	-	-
A83B4C63	-	-	-	-	3	3	3	3
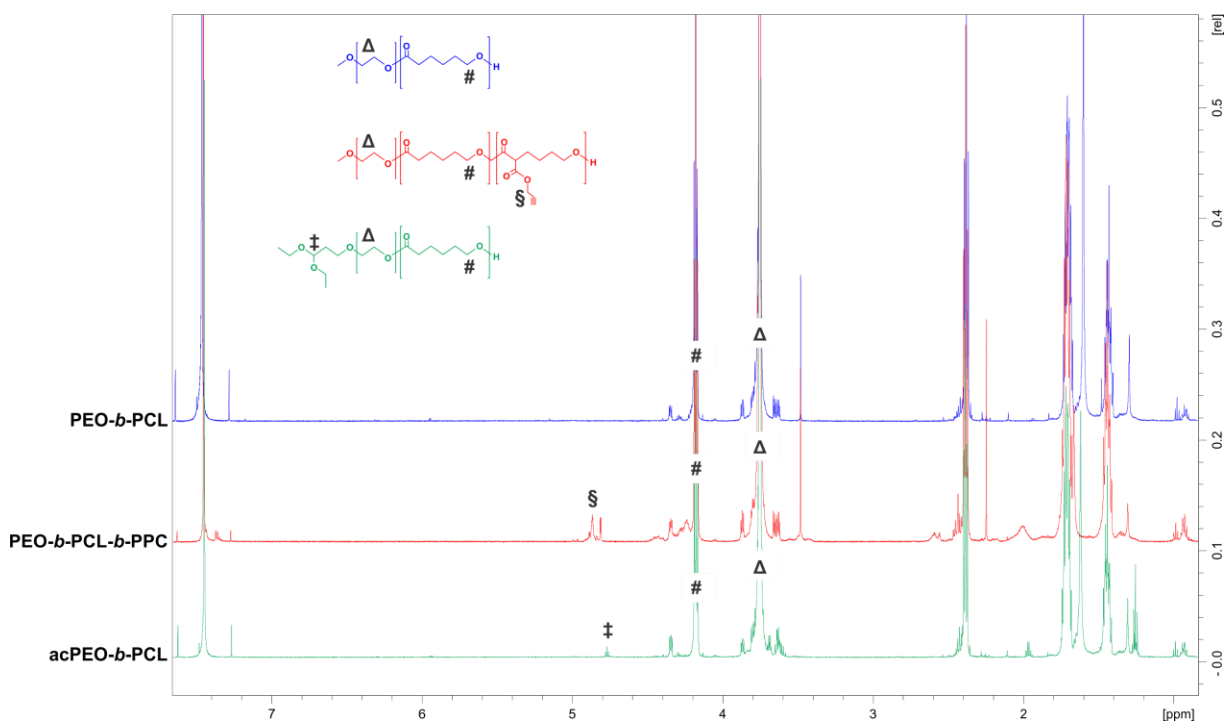
Figure 5.S1. ^{1}H NMR spectra of block copolymers that formed the PCL-based micelles.
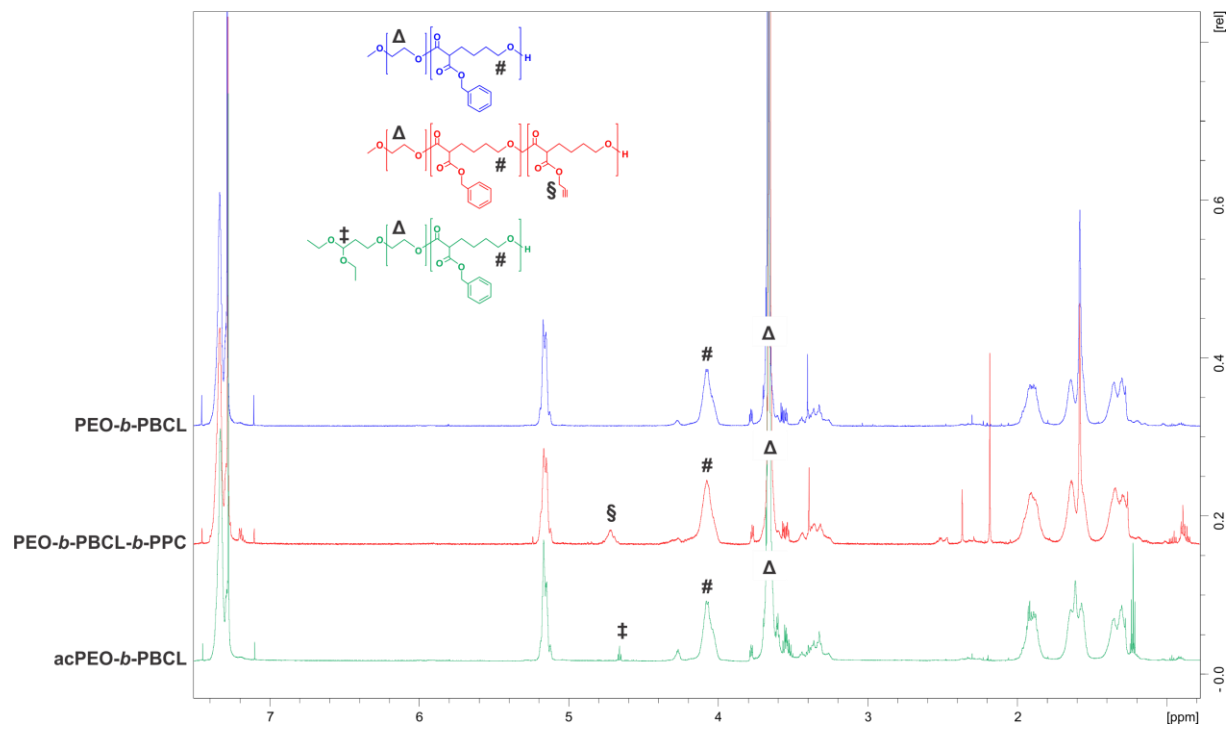
Figure 5.S2. ^{1}H NMR spectra of block copolymers that formed the PBCL-based micelles.
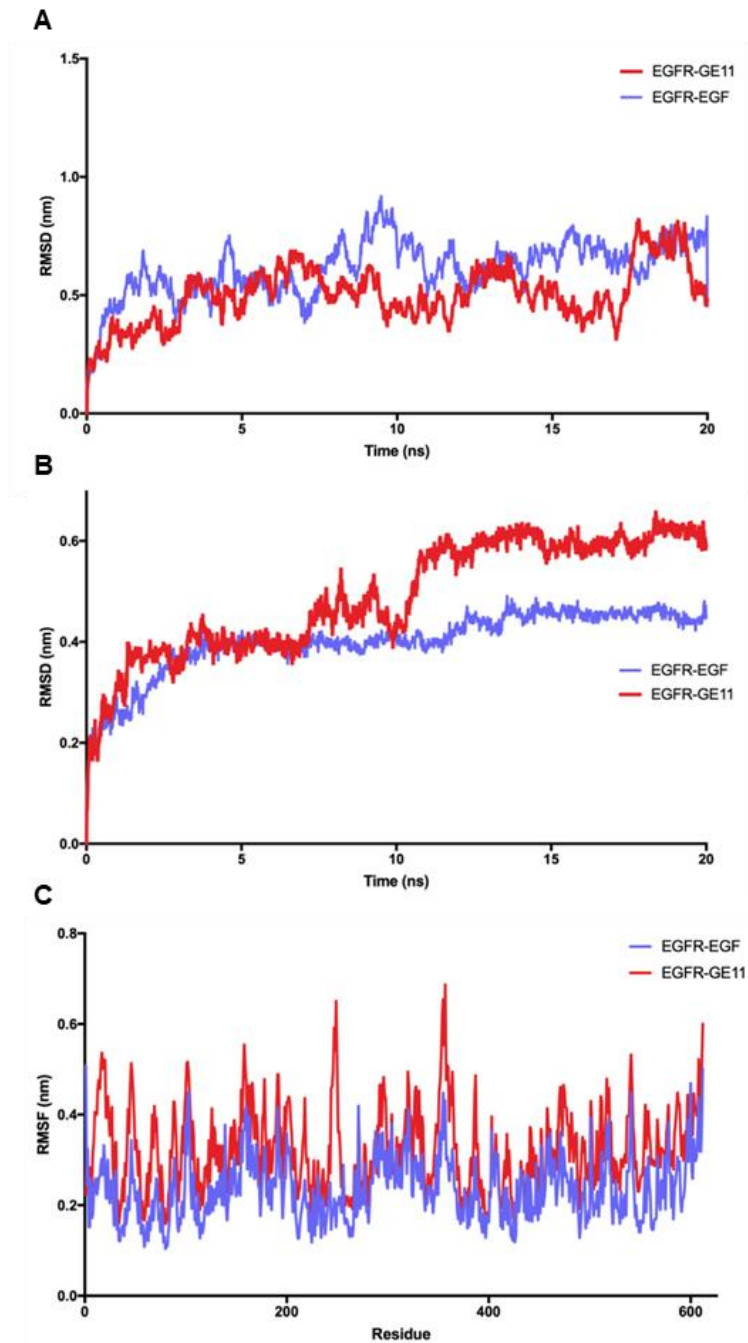
Figure 5.S3. (A): Root Mean Square Deviation (RMSD) of the EGFR backbone in complex with GE11 (red line) and EGF (blue line). (B): ligand positional RMSD of GE11 (red line) and EGF (blue line) in complex with EGFR. (C): Root Mean Square Fluctuation of the EGFR side chain in complex with GE11 (red line) and EGF (blue line).
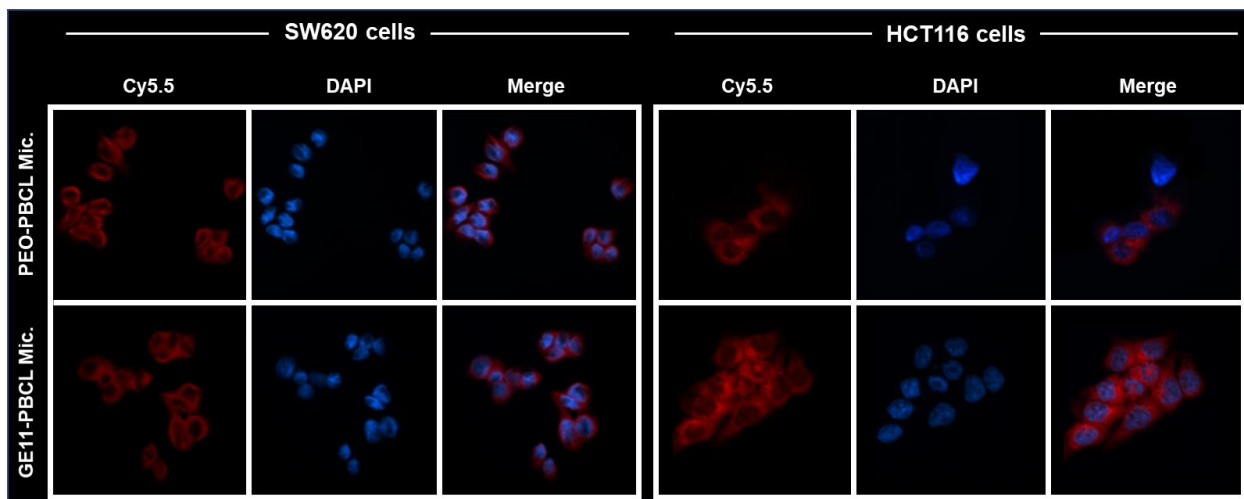
Figure 5.S4. The uptake of Cy5.5-labelled mix micelles by HCT116 and SW620 colorectal cancer cell lines after 3 h incubation at 37 °C. (A): Plain micelles; (B): GE11 modified micelles. Confocal microscopic images represent nuclear stain DAPI (blue) alone, Cy5.5 (red) alone, and the merged dyes.
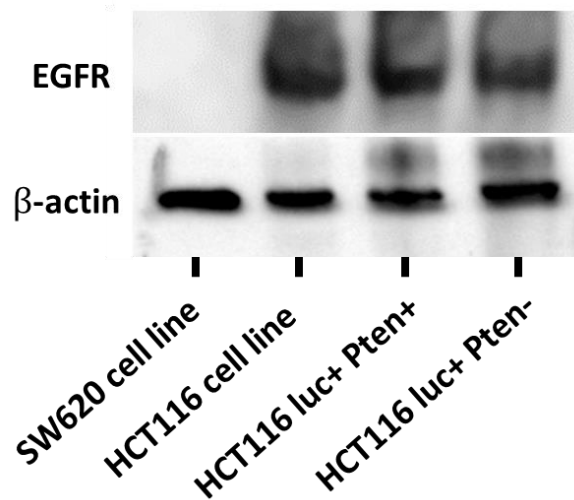
Figure 5.S5. Analysis of EGFR expression. The western blot data shows that the levels of EGFR expression were not changed after the genetic modifications in the HCT116 cells.

Chapter Six

Surface modification of polymeric micelles with monoclonal antibodies for

targeting colorectal cancer cells

6.1 Introduction

Human epidermal growth factor receptor 1 (HER1), also known as epidermal growth factor receptor (EGFR), is a 170-kDa glycoprotein containing transmembrane, intra-, and extracellular domains. Its external portion has an affinity for some endogenous ligands, such as epidermal growth factor (EGF), transforming growth factor-alfa (TGF-α), amphiregulin, betacellulin, and epiregulin. The binding of these ligands induces phosphorylation and formation of homo- or heterodimers with other members of the growth factor receptor family (i.e., HER2, HER3, and HER4). Overexpression of EGFR is commonly observed in tumors from epithelial origin, including colorectal, esophageal, gastric, prostate, renal, ovarian, and breast cancer. Additionally, its expression is related to poor prognosis and high resistance to different therapies, since this receptor plays a critical role in regulating cellular survival, proliferation, and differentiation.[333,349]

Different strategies for inhibiting EGFR have been tested in cancer treatment due to the high relevance of this receptor for the cellular processes. For instance, small molecule-based inhibitors of EGFR-tyrosine kinase activity, such as Gefitinib and Erlotinib, are FDA approved for pancreatic, lung, and other cancers. The use of monoclonal antibodies (mAbs) against EGFR, is also a clinically relevant strategy in the treatment of EGFR expressing tumors due to their high specificity to the target. Cetuximab, Matuzumab, and Panitumumab are respectively chimeric, humanized, and human anti-EGFR mAbs, commercially available in the market, and clinically used in the treatment of colorectal cancers (CRC), either as monotherapy or in combination with other therapeutic agents. One relevant requirement for the success of these therapies is the genetic profile of the patient's tumor, especially regarding the expression of EGFR as well as the mutation in K-ras protein. Tumors mainly composed of wild-type K-ras are sensitive to the therapy, while mutated K-ras types are irresponsive.[350,351]

In addition to the direct receptor blocking of anti-EGFR antibodies, which ultimately results in inhibition of favorable pathways for cancer cell growth, especially suppression of apoptosis, cell cycle

progression, and metastasis, those therapeutic antibodies also present another mechanism of action.[199] The antibody-dependent cellular cytotoxicity (ADCC) has been vastly reported in contributing to the elimination of tumors. Since panitumumab is an IgG2 molecule, a weaker ADCC activity would be expected compared to the cetuximab, which is an IgG1. However, a recent study indicated that panitumumab is quite effective in triggering ADCC by neutrophils and monocytes.[352]

Carcinoembryonic antigen-related cell adhesion molecule 6 (CEACAM6), also called CD66c, is a single-chain glycoprotein (37 kDa), anchored to the plasma membrane without transmembrane or intracellular domains. As its name indicates, its role relates to cell adhesion, being intimately associated with integrin $\alpha_v\beta_3$, fibronectin and vitronectin. Its overexpression in CRC has been associated with the worse prognosis and high risk of relapse in patients.[353–355] Recently, EGF/EGFR-dependent processes associated with metastasis, such as cytoskeletal rearrangement, cell invasion, and migration, have been shown to be mediated by CEACAM6. Moreover, this receptor was found to enhance EGFR-activation upon EGF binding, enhancing proliferation and cell growth.[356] In previous studies, CEACAM6 was also identified abundantly on colon HCT116 spheres that were isolated from HCT116 monolayers and can be used as a CRC stem cell marker, co-expressing with established cancer stem cell markers, such as the CD133.[7,357]

Because of the frequent demand for combining mAb treatment with chemotherapy, the development of antibody-drug conjugates (ADCs) has been the focus of increasing attention by pharmaceutical companies. The advantage is the simultaneous delivery of two therapeutic entities in one formulation, to cancer cells.[134] The limitation of ADCs is the need for the internalization of antibody for effective delivery of conjugated drug, the requirement for the presence of functional groups on the drug molecule, restrictions in the number of drug molecules that can be attached to one antibody and the question over drug activity following conjugation to the antibody of interest.[174] Therefore, the attachment of mAbs to drug nanocarriers is considered a great alternative to solve these problems. Nano-sized delivery systems have shown to be an effective approach to passively target tumors due to the enhanced

permeation and retention (EPR) effect.[358] Antibody on the surface of these nanocarriers can enhance their internalization to the tumor cells and/or increase carrier homing in the tumor tissue contributing to enhanced drug specificity for cancer versus normal cells.

Several drug nano-formulation, including nanoparticles, liposomes, and polymeric micelles bearing monoclonal antibodies against EGFR have been developed over the past years.[274,275,310] Such nanocarriers confer active drug targeting by preventing EGFR from forming dimers and losing the ability to trigger its intracellular kinase domain and the subsequent downstream cellular signaling. The inactivated-receptor is recognized by the cell and cleared from the plasma membrane, leading to its internalization, along with the therapy.[317]

In the present study, polymeric micelles based on poly(ethylene oxide)-*block*-poly(α-benzyl carboxylate-ε-caprolactone), PEO-*b*-PBCL, containing mAb molecules on their surface, denoted here as immuno-micelles, were developed for improving the delivery of payloads to CRC tumors. Monoclonal antibodies against EGFR and CEACAM6 were chosen for this purpose to target EGFR expressing colorectal cancer cells and cancer stem cells. The near-infrared (NIR) Cy5.5 fluorophore was loaded into the developed micellar systems for a dual purpose, which includes micelle traceability, allowing a quantitative assessment of nanoparticle fate, as well as prediction of loading and release of hydrophobic drugs into our immuno-micelles since this dye can be considered a model drug for early development stage.[359,360]

6.2 Methods

6.2.1 Materials

Maleimide polyethylene oxide (mal-PEO, 5 KDa) was purchased from JenKem Technology Inc. (Allen, TX, USA). α-Benzyl carboxylate-ε-caprolactone (BCL monomer) was obtained from Alberta Research Chemicals Inc. (Edmonton, AB, Canada). Stannous octoate (Tin-II 2-ethyl hexanoate) was acquired from Sigma Aldrich (St. Louis, MO, USA), and further purified by vacuum distillation. Cyanine 5.5

(Cy 5.5) was purchased from LumiProbe LLC (Hallandale Beach, FL, USA). Vectibix® (Panitumumab, anti-EGFR) was obtained from Cross Cancer Institute, and the anti-CD66c antibody was obtained from BD Pharmingen (San Jose, CA, USA, #555749). Most of SDS-PAGE equipment and solutions were obtained from (Biorad, USA). All other chemicals were reagent grade.

6.2.2 Polymer synthesis and micelle preparation

Di-block copolymers composed of mal-PEO-*b*-PBCL were synthesized by ring-opening polymerization of BCL using mal-PEO as initiator, more specifically its hydroxyl end group, as well as stannous octoate as the catalyst, according to previous reports.[361] Briefly, mal-PEO (0.5 g), BCL (0.8 g) and purified stannous octoate (3 drops) were added to an ampoule and sealed under reduced pressure. The polymerization reaction was processed at 120 °C for 3 h. Then, the mixture of polymers, unreacted monomers, and catalyst, was dissolved in dichloromethane (DCM) followed by polymer precipitation in hexane and impurity removal. Polymer structure was confirmed by ^{1}H nuclear magnetic resonance (^{1}H-NMR) using a 600-MHz Bruker spectrometer (Bruker Instruments, Inc., Billerica, MA, USA). Micelles were formed by dissolving copolymer (9 mg) with and without Cy5.5 (0.1 mg) in acetone, adding dropwise in water under constant stirring, and incubating overnight. Polymeric micelles (3 mg/mL polymer concentration) were centrifuged (~ 10,000 x g) and filtered (0.22 µm) to remove any suspended aggregates.

6.2.3 Preparation of polymeric immuno-micelles

Anti-EGFR or anti-CD66c antibodies (1.4 mg) were thiolated using 2-iminothiolane (0.025 mg) in phosphate-buffered saline (PBS, pH 7.9) for 1 h at room temperature under gentle stirring. The solution was dialyzed against PBS for 2 h to remove the unreacted 2-imidothiolane. The coupling of thiolated antibodies into maleimide-containing micelles was carried out by mixing both solutions and incubation

overnight under minimal agitation. Three different amounts of thiolated panitumumab were added to micelles (2 mg polymer concentration) so that antibody/polymer molar ratios of 1:200, 1:100, and 1:50 (mol/mol) were tested. For anti-CD66c conjugation, the antibody/polymer ratio used was 1:100 (mol/mol). After that, remaining unreacted maleimide groups were inactivated with β-mercaptoethanol. Finally, the immuno-micelles were eluted through a Sepharose chromatography column for purification from unreacted antibodies. Micelles presenting no antibody on their surface (plain-micelles) were prepared under similar conditions as a negative control. Qualitative assessment of antibody conjugation was carried out using sodium dodecyl sulfate-polyacrylamide gel electrophoresis (SDS-PAGE), and protein bands were visualized upon staining with Bio-Safe Coomassie premixed solution (#1610786, Bio-Rad).

6.2.4 Release of Cy5.5 from micellar systems

Solutions containing Panitumumab immuno-micelles, plain-micelles, and free Cy5.5 were placed into separate Spectra/Por dialysis bags (MWCO = 3.5 KDa). The dialysis bags were sealed with clips and placed in a beaker with 300 mL double-distilled water and incubated at 37 °C in a shaker. After 0, 2, 8, and 24 h, a 150-μL sample was taken from inside the dialysis bag, then the volume was restored by adding 150 μL ddH$_2$O. To maintain the sink conditions, outside media were discarded and replaced with fresh ddH$_2$O at each time point. Cy5.5 was quantified at 673/707 nm (excitation/emission) using a microplate fluorescence reader (Synergy H1, BioTek Winooski, VT, USA).

6.2.5 CRC cells

Human colorectal cancer cells, HCT116, and SW620 cells were used for cell uptake studies. Both cell lines were cultured using Dulbecco's modified eagle's medium (DMEM) supplemented with 10% fetal bovine serum, 100 IU/mL penicillin, and 100 IU/mL streptomycin in a humidified atmosphere of 5% CO$_2$ at 37 °C. Additionally, a stem-like cell population from HCT116 cells was isolated. Colon sphere cultures were obtained by collecting the supernatant of confluent HCT116 cells and plating on ultralow attachment

plates (Corning, Acton, MA, USA) using EpiCult-C Human Medium Kit from StemCell Technologies (GmbH, Germany)

6.2.6 Cell uptake studies

Cells were seeded in 24-well plates (80,000-100,000 cells/well) and incubated for 24 h at 37 °C. Then, cells were incubated with immuno-micelles containing either anti-EGFR or anti-CD66c antibodies (prepared using antibody:polymer ratio of 1:100) and with plain-micelles. The final concentration of Cy5.5 of 0.2 μg/mL per well for 3 h at 37 °C. Competition experiment was carried using only Panitumumab (100 μg/mL) so that free antibodies were added to the culture media 2 h prior to the treatment with Panitumumab-micelles. All the experiments were done in triplicate. After the incubation, both cells were washed three times with PBS, fixed (4% paraformaldehyde for 15 minutes), and analyzed using a flow cytometer (BD FACS Canto™ II). 10,000 single cells were measured from each sample.

6.2.7 Statistical analysis

Data are reported as mean ± standard error of mean (SEM). Statistical analysis was carried out using one-way ANOVA followed by Tukey's multiple comparison test (GraphPad Prism, La Jolla, CA, USA). Differences were considered statistically significant for $p < 0.05(*)$, $p < 0.01(**)$, and $p < 0.001(***)$.
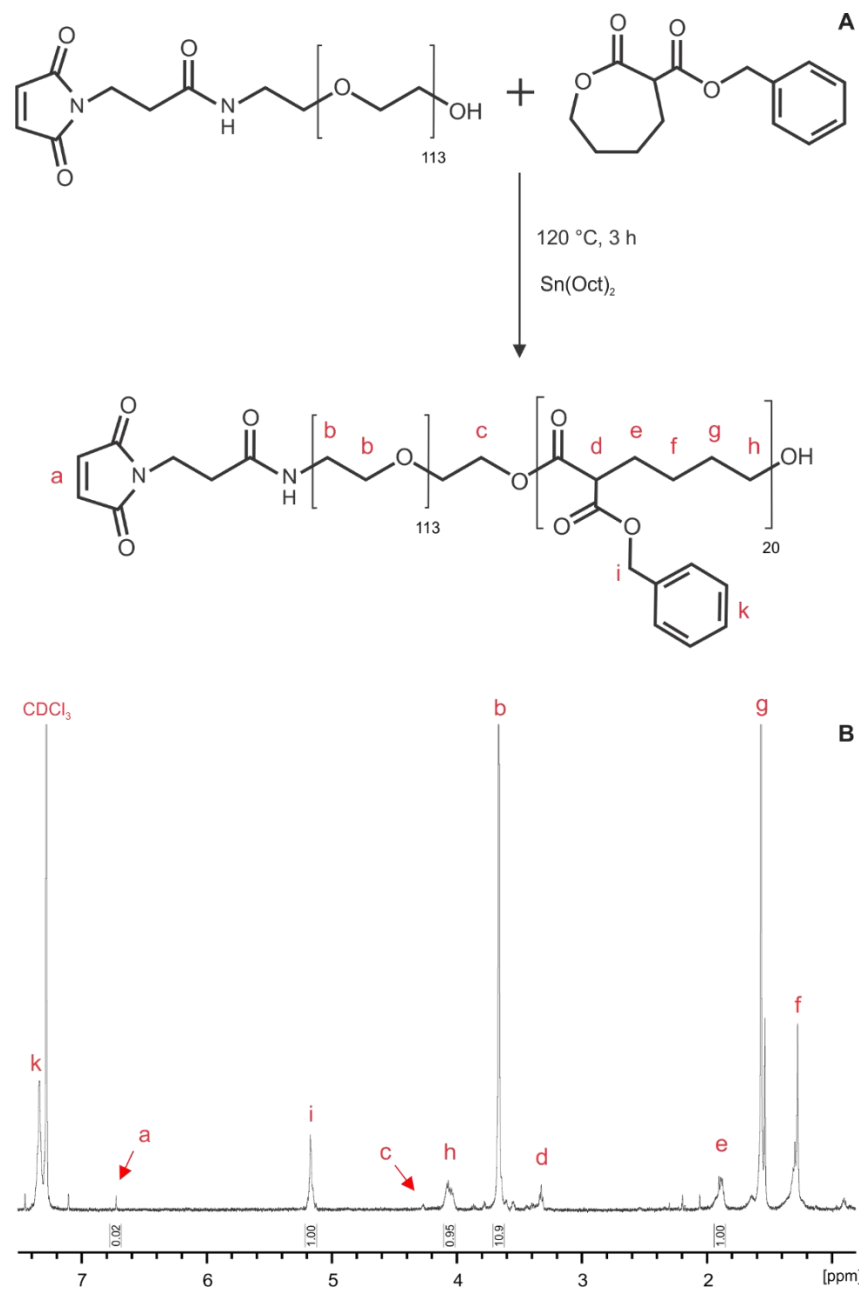
Figure 6.1. (A): Schematic synthesis of maleimide-PEO-*block*-PBCL block copolymers, along with some details about the polymerization reaction, such as temperature (120 °C), time (3 h), and catalyst (stannous octoate). (B): ^{1}H NMR spectrum of mal-PEO$_{114}$-*b*-PBCL$_{20}$ block copolymer dissolved in deuterated chloroform (CDCl$_3$), containing peak assignments (in red) and integration for selected proton signals (between vertical bars).

6.3 Results and discussion

6.3.1 Polymer characterization

^{1}H NMR spectra revealed that the polymerization reaction was successful, but the yield of the reaction was only around 66%. The degree of polymerization for the PBCL segment was 19.9, as determined by the comparison of methylene signals from PEO (-C**H₂**C**H₂**O-, δ = 3.65 ppm) and PBCL (-OC**H₂**-, δ = 4.05 ppm) blocks (**Figure 6.1**). This was lower compared to the theoretical DP, calculated based on the amount of PEO and BCL initially added (DP = 30), and maybe primarily due to the temperature used for the reaction (120 °C). In our first attempts using PEG functionalized with maleimide, the usual temperature of 140 °C showed a substantial degradation of maleimide groups. Thus, although the reaction yield here was slightly compromised, polymerization at 120 °C led to a reduced maleimide loss (~ 30%).

Number average molecular weight (Mn) was found to be 9,900 g/mol (PEO$_{114}$-*block*-PBCL$_{20}$), in which hydrophilic and hydrophobic portions had similar Mn's (PEO ~ 5,000 g/mol and PBCL ~ 5,000 g/mol, respectively). According to our previous studies, such copolymers are known to form polymeric micelles with suitable physicochemical properties. Different studies have indicated the benefits of having benzyl groups in the micellar core-forming segments, especially for improving micelle stability, loading, and release of model hydrophobic drugs.[250,267,345,362] Conversely, our research group has indicated that for suitable drug loading and release using micelles formed by PEO-*b*-poly(ε-caprolactone), without benzyl pendant groups, the length of hydrophobic segments must be increased for an optimum outcome, such as PEO ~ 5,000 g/mol and PCL ~ 13,000.[363]
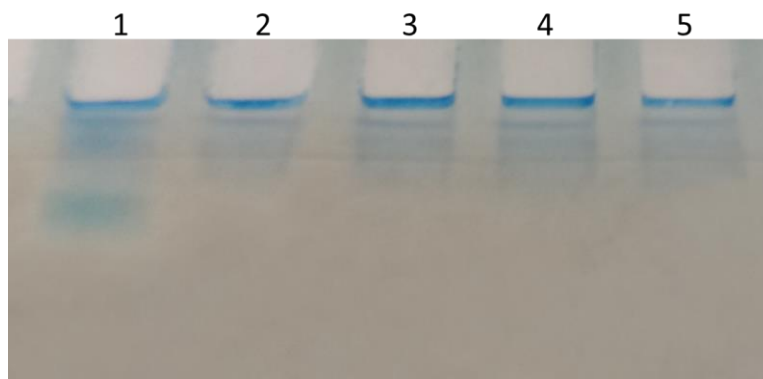
Figure 6.2. Electrophoretic profile of (well #1): free Panitumumab, (well #2): plain-micelles, and Panitumumab-micelles formed with antibody:polymer ratio of (well #3) 1:50, (well #4) 1:100, and (well #5) 1:200.

6.3.2 Cy5.5-loaded micelles and immune-micelles

An electrophoretic approach was selected for the qualitative assessment of antibody conjugation since this technique relies on a separation step before protein staining. As shown in SDS-PAGE data (**Figure 6.2**), the protein band related to the free antibody was not observed in the other groups and, although plain-micelles still got stained, a slightly stronger bands were visualized among immuno-micelles, compared to the plain-micelles.

Encapsulation of Cy5.5 into plain micellar structures led to high levels of entrapment (> 90%). Also, sustained rates of Cy5.5 was observed from both plain- and Panitumumab-modified micelles (**Figure 6.3**). Encapsulation efficiency was 97.6%, and Cy5.5 loading was 1.04% for plain-micelles. Moreover, at 24 h, only 26% and 31% of the dye was released from plain- and Panitumumab-micelles, respectively. [359]
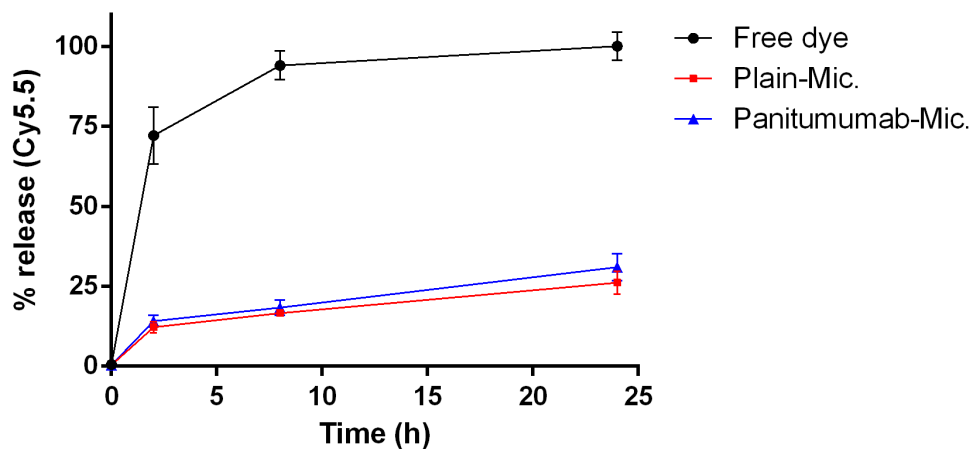
Figure 6.3. *In vitro* release profile of Cy5.5 among free and Cy.5.5-loaded polymeric micelles micellar structures.

Polymeric micelles showed a narrow size distribution (PDI < 0.3). Plain micelles and Panitumumab-micelles (prepared using antibody/polymer molar ratios of 1:100) had PDI = 0.25 ± 0.03 and PDI = 0.28 ± 0.03, respectively (**Figure 6.4A**). The particle size of micelles was significantly increased by antibody conjugation (p < 0.01, Anova followed by Tukey test). As presented in **Figure 6.4B,** plain-micelles were characterized with a hydrodynamic diameter of 54.3 ± 4.6 nm, whereas Panitumumab-micelles were almost 2-fold larger: 99.3 ± 11.0 nm; 100.3 ± 3.5 nm; and 114.7 ± 14.6 nm, when antibody:polymer ratio was 1:200; 1:100; and 1:50, respectively (**Figures 6.4B**).
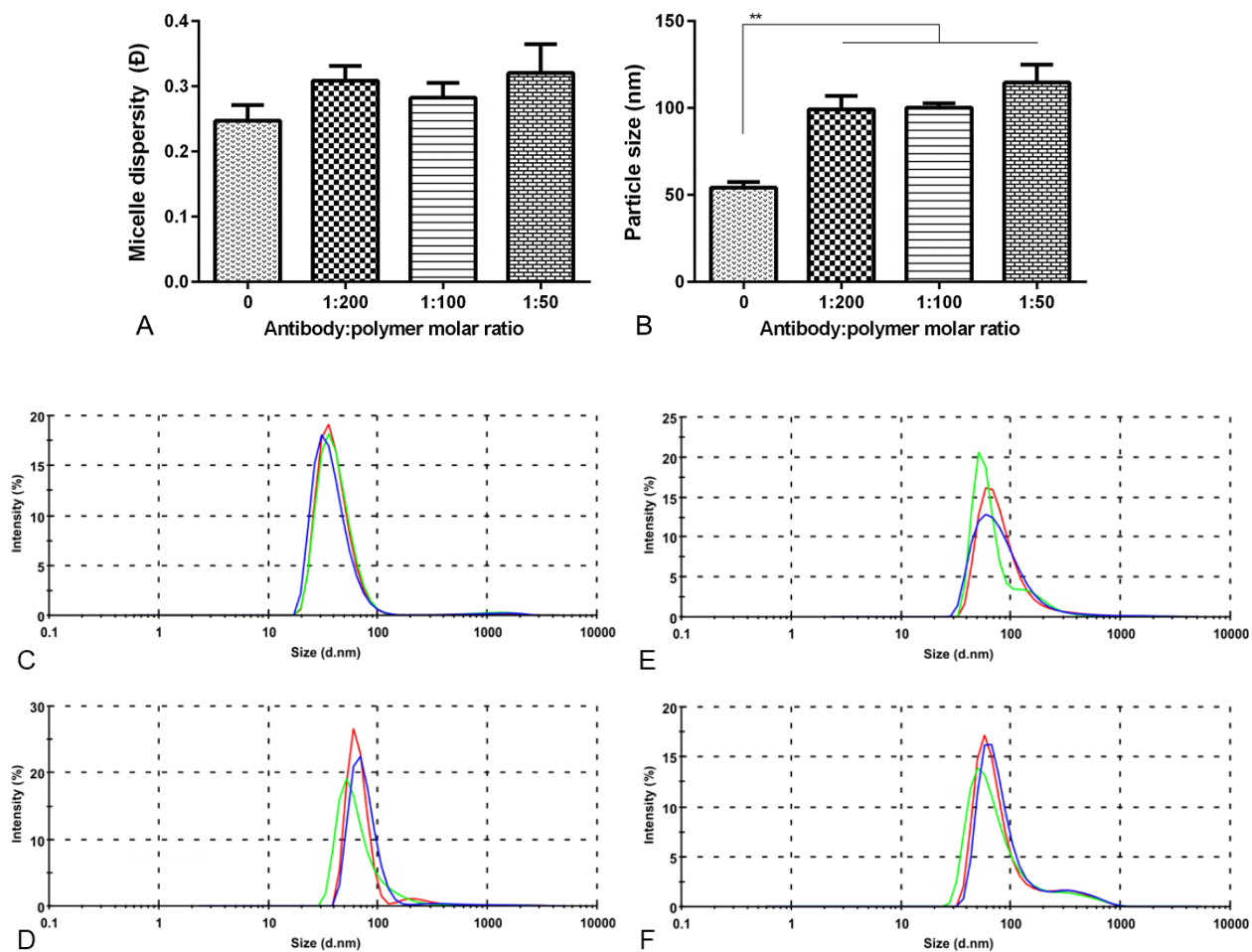
Figure 6.4. Physicochemical characterization of polymeric micelles and Panitumumab-based immuno-micelles. (A): Data indicating dispersity (Đ) in micelle size distribution. (B): Graph on particle size, in which the data were also plotted as size distribution against micelle intensity for each sample, namely (C) plain-micelles and Panitumumab-micelles formed using antibody:polymer ratios of (D) 1:200, (E): 1:100, and (F): 1:50.

6.3.3 Cell uptake studies

In vitro uptake of Panitumumab-micelles was assessed using two CRC cells, one expressing EGFR (HCT116 cells) and another without EGFR-expression (SW620 cells). Similarly, polymeric micelles containing anti-CD66c antibody on their surface, denoted as CD66c-micelles, were incubated with HCT116 cells (lower CD66c expression) as well as with colon spheres isolated from HCT116 cells (higher CD66c

expression). We then determined if those antibody surface modifications could significantly improve the uptake of Cy5.5-labeled polymeric micelles by CRC cells having different levels of both targeted-receptors.
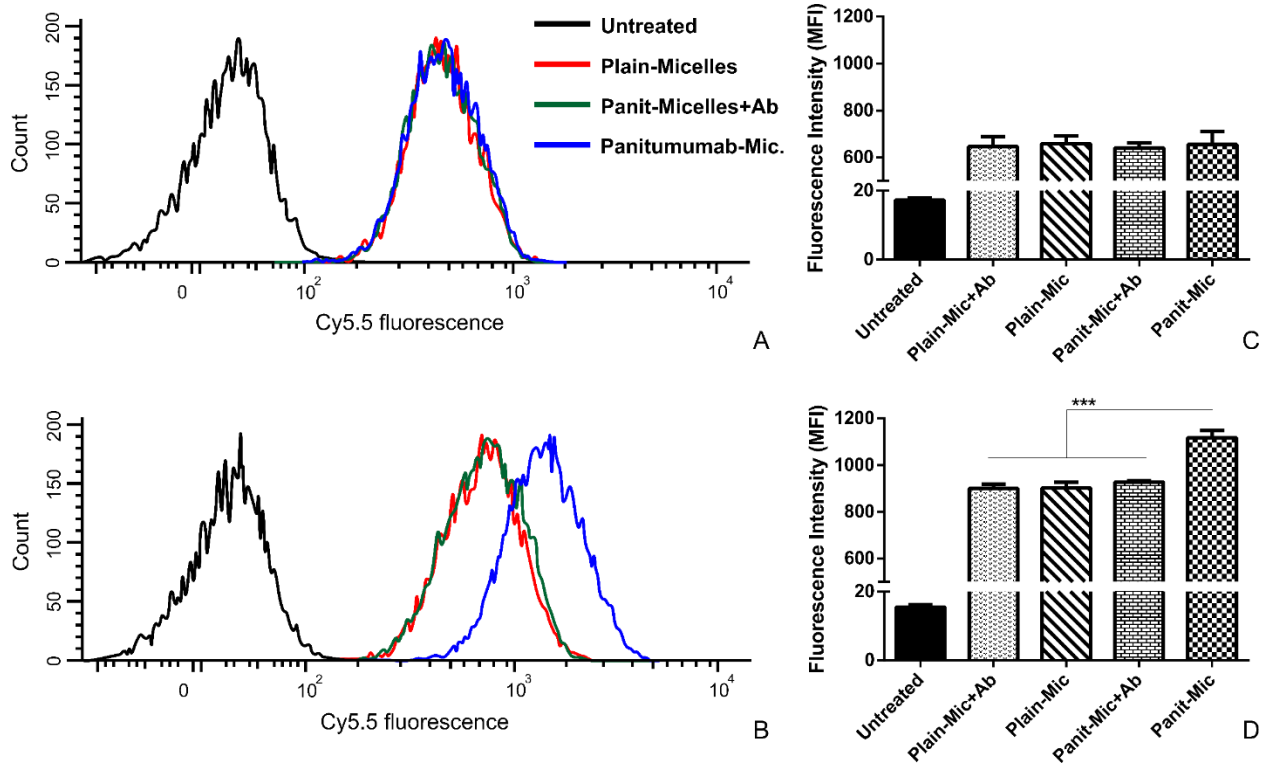
Figure 6.5. *In vitro* uptake of Cy5.5-containing Panitumumab-micelles by SW620 (top panels) and HCT116 (bottom panels) cells. (A and B): Histograms indicate the distribution of Cy5.5 fluorescence intensity among different samples after measurement of 10,000 single cells. (C and D): Bar graphs show the median fluorescence intensity (MFI) for each treatment.

According to flow cytometry analyses, the endocytic activity among HCT116 cells seems to be higher than the one among SW620 cells, since fluorescence signals from Cy5.5-labelled plain-micelles were, overall, lower in the latter cell line. Comparing the uptake of plain- and Panitumumab-micelles by SW620 cells, similar MFI values were noticed (**Figure 6.5C**). On the other hand, the uptake of plain-micelles by HCT116 cells was found significantly lower ($p < 0.001$) compared to the EGFR-targeting immuno-

micelles (MFI = 899 ± 15.9 versus MFI = 1117 ± 25.2), confirming the role of EGFR in boosting Panitumumab-micelle internalization (**Figure 6.5D**). Additionally, a competition study revealed that pre-treatment with free Panitumumab drastically reduced this enhancement, resulting in an uptake profile similar to the group treated with plain-micelles.
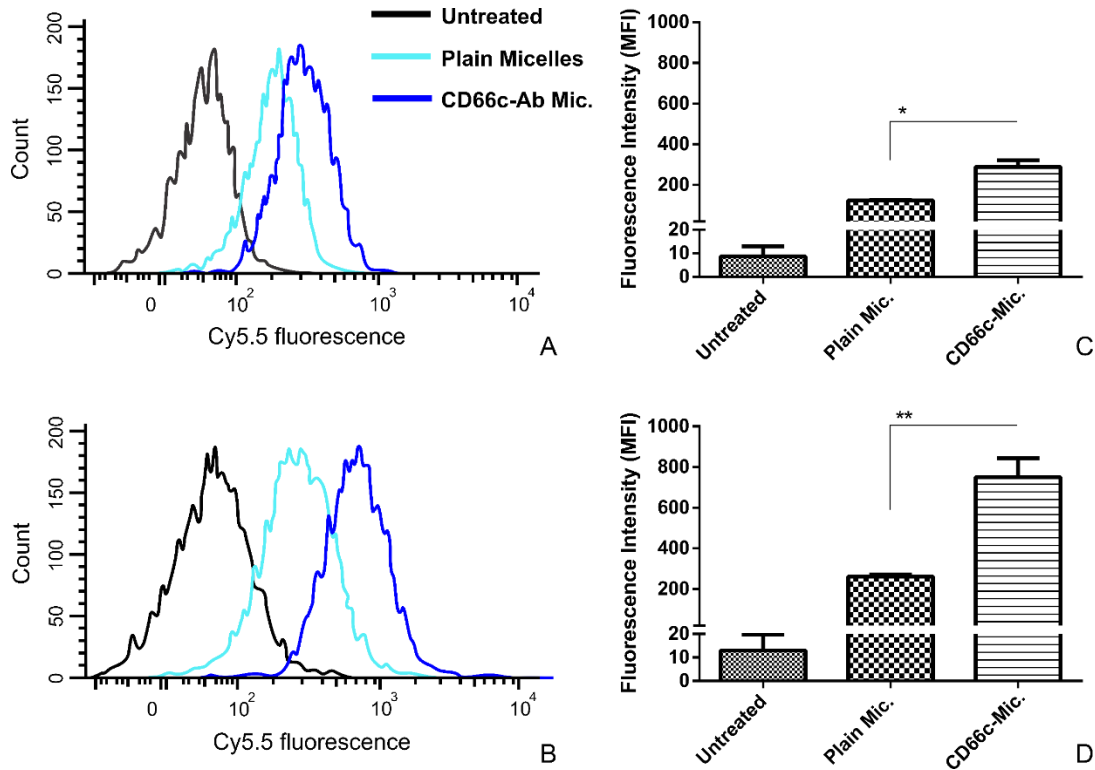
Figure 6.6. Cell uptake of CD66c-micelles using HCT116 (top panels) cells, as well as colon spheres isolated from HCT116 (bottom panels) cells. (A and B): Histograms indicate the distribution of Cy5.5 fluorescence intensity among test and control groups after analysis of 10,000 events. (C and D): Bar graphs show median fluorescence intensity (MFI).

Surface-modification of polymeric micelles with anti-CD66c antibody contributed to increasing micelle uptake in both cell populations of HCT116 cells. As indicated in **Figure 6.6C**, fluorescence intensity for HCT116 cell line treated with plain micelles was 124 ± 2.6, while treatment with CD66c-micelles led to a fluorescence intensity shift to 289 ± 23.4, which is 2.3 times higher (p < 0.05). Similarly, **Figure 6.6D**

shows that the uptake of CD66c-micelles by stem-like HCT116 cells (MFI = 750 ± 45.7) was 2.9-fold higher (p < 0.01) than the uptake of plain-micelles (MFI = 261 ± 13.7). The delivery of STAT3 inhibitors encapsulated in PEO-PBCL micelles decorated with antibody anti-CD38 significantly improved therapeutic efficiency against multiple myeloma in pre-clinical studies. Therefore, the preferential accumulation we observed here among stem-like CRC cells has a great potential to impact drug delivery and chemotherapy outcomes in a positive manner, especially because this cancer cell population has been robustly suggested to contribute with higher drug resistance traits as well as with cancer relapse.[361]

6.4 Conclusion

In summary, surface modification of polymeric micelles with anti-EGFR anti-CD66c was successfully accomplished using maleimide-functionalized PEO and sulfhydryl groups anchored from lysine residues (i.e., amines) on antibody molecules. Further studies are required to validate a method for quantifying antibody density on the surface of our polymeric micelles. Panitumumab-micelles were associated with EGFR-overexpressing CRC cells compared to plain micelles, and the uptake of CD66c-micelles was significantly higher in whole HCT116 cell and its CD66 overexpressing sub-population when compared to the plain-micelles. Therefore, developed immune-micellar constructs were considered suitable candidates to deliver cytotoxic drugs to HCT116 xenografts and stem cell subpopulation, respectively.

Chapter Seven

General Discussion, Conclusion, and Future Directions

7.1 General Discussion

Targeted drug delivery for cancer treatment has been yearning for a long time. Paul Ehrlich dreamed, after his discovery of selective staining for gram-positive bacteria in 1882, that one day, a "magic bullet" would be developed for selective elimination of cancers, leaving the surrounding healthy tissues undamaged. Unfortunately, the advances in cancer biology have shown the immense complexity and heterogeneity of this pathological condition, and the development of that dreamed, single, and specific therapy to cure cancer turns out to be an elusive and unrealistic approach. The 1989 Nobel laureate in physiology/medicine Dr. Harold Varmus referred to cancer as a "cell like Grendel [*mythologic monster*], a distorted version of our own selves". In fact, every feature of cancer cells is rooted in a corrupted process available among normal cell populations, which makes the search for cancer-specific targets very challenging. The central point of this thesis was to take advantage of the fact that some receptors are upregulated in certain types of cancer so that ligands with affinity to those receptors can enhance specificity of the drug formulation to tumors.[150]

In the first research project (Chapter 2), the main objective was to assess whether or not the proteolytically stable cyclic decapeptide C18.4DK (WXEAAYQkFL), conjugated with Cy5.5, could be used as a targeted drug delivery platform to treat breast cancer cells. The sub-nanometer scale of this formulation led to a distinct *in vivo* pharmacokinetic profile than the nano-delivery systems reported in the other chapters. Rapid clearance through kidneys and liver was observed, which indicated a lack of prolonged stability in the blood. Interestingly, this formulation was able to cross the blood-brain barrier, reaching the brain (**Figure 2.10B**); and because of its capacity to overcome this barrier, which is known to contain cells very tightly connected with one another, this model drug delivery system may be an interesting alternative approach in cases of highly rigid tumors, with necrotic and hypoxic regions and low diffusion rates.[4,5,206]

The target of C18.4DK peptide has been recently proposed by Soudy *et al*.[223] to be keratin-1 (KRT1). In Chapter 3, this protein was also targeted by using the linear engineered P18.4 peptidic sequence. Interestingly, one of the natural ligands for KRT1 is the high-molecular-weight kininogen (HK),[364,365] which is also endogenously specific for other two receptors: complement component 1q receptor (gC1qR), and urokinase-type plasminogen activator receptor (uPAR).[191,366] Those receptors are known for tumor-targeting purposes due to their often upregulation in specific types of cancer. Lyp-1 peptide and its analogs have been extensively reported for binding to gC1qR,[367–370] as well as AE105, AE147, and others for uPAR-targeting systems.[371–373] Similarly, the P18.4 peptide has been successfully utilized by surface-modifying various nanocarriers, such as liposomes loaded with doxorubicin,[194,195] traceable polymeric micelles,[250] and plasmid lipoplexes,[196] as well as for peptide-drug conjugation[222,374] and breast cancer diagnosis.[375] Our results indicated, for the first time, that P18.4 peptide can also contribute to enhancing internalization of siRNA into cancer cells (**Figure 3.5 and 3.6**), although we found that the siRNA uptake enhancement did not lead to higher MCL-1 downregulation under current experimental conditions. A possible reason for this finding maybe because of the high stability of the polyamine/siRNA complex, leading to a limited siRNA dissociation. Another explanation could be due to the saturation of the RNAi machinery, given the wide gap between 200 and 300 nM siRNA dose. Also, there is a possibility of MCL-1 upregulation by other compensatory cell pathways in response to the treatment.

The biodistribution in mice of polymeric micelles was investigated by varying the chemical structure and/or the molecular weight of the core-forming segments of micellar structures. In line with previous studies, the benzyl-caprolactone block with a degree of polymerization of 20 (i.e., PEO_{114}-$PBCL_{20}$) was selected in Chapter 4. The *in vivo* fate of micelles bearing the EGFR-targeting peptide GE11 or the mock peptide HW12 was assessed by PET imaging.[216,250] As showed in **Figure 4.S2**, the radiotracer ^{64}Cu was successfully incorporated into the chelating agent NOTA, and significantly different behavior was

observed *in vivo* if only ^{64}Cu-NOTA is injected (**Figure 4.S3**). The analysis of accumulation into ectopic

HCT116 subcutaneous xenograft tumors (**Figure 4.5**) revealed that the surface-modification with GE11 led

to a higher PET signal only by taking into account the values of SUV_{max} (p < 0.05), but the p-number for

SUV_{mean} was higher than 0.05 (i.e., p = 0.08). This was quite interesting because the SUV_{mean} is determined

by considering the entire tumor region, while SUV_{max} is generated by focusing on the regions with the

highest PET intensities. Therefore, the data provided quantitative means to indicate that the GE11-

micelles were more highly accumulated in the tumor periphery, whereas the tumor core was not

significantly affected by the EGFR-targeting of nanocarriers, suggesting a poor diffusion of our micelles

inside the cancerous tissue.

In Chapter 5, the biodistribution and accumulation into orthotopic HCT116 xenograft tumors were

assessed through NIR imaging (**Figure 5.5**). Cy5.5-labeled micelles composed of PEO-*b*-PCL and PEO-*b*-

PBCL copolymers, with and without GE11 decoration, were concomitantly challenged so that by

comparing only PEO-PBCL micelles with GE11-PBCL counterparts, no significance in tumor accumulation

enhancement was observed, similar to the outcome from PET SUV_{mean} values. However, by analyzing the

effect of modifications on micellar surface and core in parallel, the tumor NIR fluorescence intensity was

significantly higher in the groups treated with PEO-PBCL and GE11-PBCL micelles when compared to the

one that received PEO-PCL micelles. This was in line with our previous observations on P18.4 modified

PEO-PBCL micelles that have shown a higher accumulation in orthotopic MDA-MB-231 tumors compared

to their PEO-PCL counterparts.[250] The higher tumor accumulation of PEO-PBCL is attributed to the higher

stability of these micelles leading to longer circulation times in blood for them in comparison to PEO-PCL

based micelles. Overall, the results of both studies show that the high circulation time of polymeric

micelles can enhance the chance for EPR effect of plain micelles, downplaying the effect of targeting

peptide in leading to a meaningful increase in micellar tumor accumulation. Whether peptide modification

of nanoparticle surfaces can enhance the preferential interaction of nanocarriers with tumor cells over normal cells within the tumor microenvironment is not known.

We then tried to investigate the effect of EGFR-targeting peptide modification of micellar structures in increasing the therapeutic activity of drugs in colorectal cancer models. Our collaborators from Chemistry Department (Dr. Dennis Hall Lab, University of Alberta) have designed a novel and potent PNKP inhibitor denoted as A83B4C63. The drug was loaded into polymeric micelles composed of PEO_{114}-b-$PBCL_{25}$ copolymers. The degree of polymerization of the PBCL segment was increased in comparison to the one used for PET imaging. This modification was performed based on previous data on the encapsulation of A83B4C63, aiming for a more controlled release profile of the compound. The disruption of PNKP has been characterized to affect the viability of cancer cells by itself minimally but sensitizes tumors to DNA-damaging therapies. Moreover, simultaneous disruption of PNKP with PTEN protein is known to trigger cell death, through a phenomenon called synthetic lethality.[267,329,330] In a similar way, the concomitant inhibition of many pairs of proteins that leads to cell death have already been identified in several cancers, such as the down-regulation of PTEN and PARP.[328] Taking advantage of this mechanism, mice bearing orthotopic HCT116 tumor xenografts, without PTEN expression (i.e., HCT116 PTEN -/-), were treated with A83B4C63 drug, loaded into plain or GE11-micelles. The results pointed to a trend for a better outcome (i.e., higher cell toxicity) among mice treated with EGFR-targeted nano-formulation (**Figure 5.8**). Given the frequent PTEN down-regulation observed among CRC cells in patients, the delivery of PNKP inhibitors has a great potential to bring unprecedented clinical success since two efficient strategies for targeting cancer cells are being applied: synthetic lethality only within cancer cell population because of their loss in PTEN expression while normal cells are left healthy since they are PTEN positive; and enhancement in cell internalization of the drug in cancer cells by targeting EGFR, which are minimally expressed in healthy cells. Individualized therapies that carefully consider specific traits of a given cell population tends to be the answer for reaching highly efficient and safe therapies against cancer. In the

case of our proposed nano-formulation, CRC patients would have to be checked for PTEN expression, and the population presenting low levels of PTEN protein would be eligible for the treatment. Then, the targeted delivery systems carrying PKNP inhibitors would possibly exert the role of that dreamed "magic bullet".

In the last research project (Chapter 6), our goal toward the development of active-tumor targeting drug nanocarriers was pursued in a slightly different way from the other chapters. The ligand molecules selected this time to enhance specificity to CRC cells were monoclonal antibodies, instead of peptidic sequences. Two antibodies were used for micellar surface-modification, one was anti-EGFR and the other anti-CD66c. Recently, our research group has reported on the anti-CD38 antibody conjugation approach for targeting multiple myeloma (MM) cells.[361] CD38, also known as cyclic ADP ribose hydrolase, is a highly expressed receptor in MM, and the monoclonal antibody Daratumumab is a FDA-approved therapeutic indicated for this condition. One important difference between the goal of that study from targeting CRC tumors is the formation of solid tumors, which is not the case in MM. The diffusion of imunomicelles into the tumor core maybe even more significantly compromised when compared to peptide-modified micelles, due to their much larger hydrodynamic particle size (**Figure 6.4**). Nevertheless, the clinical application of anti-EGFR antibodies may be considered an advantage over the use of novel non-FDA approved peptides in the drug development process for drug targeting to cancer.

Different chemistries were employed for coupling the tumor-targeting ligands to polymeric micelles or drugs in this thesis. For peptide attachment, synthesized acetal PEO blocks were de-protected to unmask aldehyde motifs, then imine conjugation with primary amines from peptidic sequences was carried out, followed by reduction of the imine for linkage stabilization. For monoclonal antibody coupling, functionalized PEO with maleimide groups were commercially obtained, and thiolation was chemically performed using a reagent that binds to the exposed amines in the antibody molecule. The interesting feature of these chemical modifications is their ease applicability to other circumstances so that new

therapeutic cargos and/or ligands can be introduced according to the structure and nature of those entities. Concerning the overall feasibility of coupling peptide and antibody molecules on the surface of nanoparticles, peptides are advantageous over antibodies. The attachment of peptides on pegylated liposomes, for instance, has been accomplished with success using pre- or post-insertion methods, whereas antibodies are only inserted after the nanoparticle formation. This disadvantage of antibodies relates to the fact that their proper 3D configuration is essential for maintaining their specificity to the target, though their binding is usually tighter than peptides.[376–378]

7.2 General conclusion

Characteristic features or hallmarks of cancer cells, such as angiogenesis, metabolic reprogramming, cell survival/apoptosis, metastasis, therapy resistance, and others, are the result of abnormal expressions of important players for cell biology, including cell-surface proteins. Ligand molecules that have a high affinity to upregulated receptors on the cancer plasma membrane represent an important avenue to improve the specificity of drug formulations towards tumor cells. However, it is crucial to keep in mind that it may be rare to identify a truly cancer-specific receptor that is expressed only by cancer cells and without any expression in non-cancerous ones. In all research projects of this thesis, the ligand molecules were used to target cell-surface proteins overexpressed in the targeted cancer cell population, namely KRT1, EGFR, and CD66c, but with some levels of expression among healthy cell population.

The proteolytically stable, KRT1-targeting C18.4DK peptide can be conjugated with chemotherapeutic agents due to the encouraging *in vivo* outcomes with the model drug Cy5.5. This peptide-drug conjugate was characterized with a substantial affinity to breast cancer, marked by rapid drug delivery and clearance from the body. New chemistries for C18.4DK conjugation with other therapeutic small molecules can also be tested to improve pharmacokinetic profiles further.

Polymeric micelles showed great versatility for carrying different types of payloads, including siRNA, Cy5.5, and A83B4C63, depending on the chemical structure of the core that accommodates these cargos. In this context, the use of chemically flexible PEO-PCL based nanocarriers with functional core structures was of great advantage. Chemical modifications, through specific pendant group attachments, allowed the proper loading of siRNA negatively-charged molecules, as well as highly hydrophobic small-molecule entities (i.e., Cy5.5 and A83B4C63). In addition, the functionality of the PEO end provided opportunities for the attachment of different peptide as well as monoclonal antibody ligands to the polymeric nanocarriers.

Overall, our results indicate that the central hypothesis was answered positively, *in vitro*, since all the ligands used in this study exerted some enhancement in the interaction with cancer cells over the healthy ones. Though the benefit *in vivo* was not as clear as the *in vitro* results, as a limited benefit in the increase of tumor homing by peptide modified polymeric micelles over plain ones was observed. Nevertheless, peptide modification of nanocarriers appeared to enhance the therapeutic activity of an incorporated drug, despite no significant effect in nanocarrier homing in primary tumors. This may be attributed to better delivery of the drug to cancer cells in the tumor micro-environment of primary tumor or towards the metastatic site. The targeted small molecules (e.g., peptide-drug conjugates) showed rapid tumor accumulation and fast systemic clearance of these agents in the mouse model. Peptide-modified polymeric micelles, on the other hand, showed an advantage in terms of accommodating higher payloads of diverse chemicals, and enhanced interaction with the target cells, *in vitro*. These nanocarriers did not show significant benefit in enhancing accumulation of nanocarrier in solid tumors, *in vivo* since the effect of ligands on their accumulation into tumors may have been mostly overshadowed by passive targeting of the nanocarrier structures by the EPR effect, as well as by a possible higher retention in the liver due to the surface decoration with ligands that may have caused a higher recognition by Kupffer cells, as vastly discussed in the literature.[379] Nevertheless, the EGFR targeted nanocarriers showed an improved

therapeutic outcome for the loaded inhibitor of PNKP, A83B4C63, in PTEN negative CRC in orthotopic CRC models, possibly by changing the intratumoral distribution of loaded drug towards cancer over normal cells within the tumor microenvironment.

7.3 Limitations

Regarding the biodistribution study of C18.4DK conjugated with Cy5.5, an important control group could have been used, which is a mock peptide with no affinity to MDA-MB-231 cells conjugated with the fluorophore. Although different studies show the *in vivo* biodistribution of free Cy5.5, this dye conjugated to a similar cyclic peptidic sequence would be of great importance, especially in terms of tumor accumulation and clearance.

In chapter three, the reported P18.4-modified siRNA delivery system was tested with only one cancer cell line in the experiment of siRNA activity. Perhaps, using a wider variety of cancer cells, the role of the peptide surface modification would have been more meaningful for other cell types. Our preliminary study using the plain siRNA delivery system indicated that the ratio and dose may vary depending on the cell type for achieving substantial downregulation.

The biodistribution study of our polymeric micelles that relied on the PET imaging was performed using ectopic CRC mouse model, whereas the one employing NIR optical imaging used orthotopic CRC mouse model. The comparison between techniques would have been more accurate if in both cases CRC cells could have been injected orthotopically, but the lack of a platform that could take the PET imaging, and at the same time, detecting the exact location of the tumors (e.g., luminescence or another approach) made the experiment non-feasible for our purpose.

In the investigation on the therapeutic activity of A83B4C63 drug on PTEN-negative CRC cells, the EGFR-targeting formulation would possibly have led to a statistical significance over the plain micellar

form if the number of mice was higher. The surgery for the development of orthotopic CRC cells in mice is very delicate and extensive so that only a few animals were injected in a couple of days of the procedure.

Chapter 6 is an initial study on the development of antibody-modified polymeric micelles to target EGFR. One of the main limitations of this study was the physical encapsulation of Cy5.5 for investigating the cell uptake study. A similar approach reported on the previous chapter needs to be pursued, aiming for a covalent attachment of the fluorophore to the polymer. Otherwise, the released Cy5.5 from the micelles may significantly interfere in the accuracy of measurements.

7.4 Future Directions

In this thesis, we looked at the effect of nanoparticle drug delivery by passive targeting (represented in **figure 7.1.A**) versus ligand modification of small molecules (represented in **Figure 7.1.B**) and nanocarriers (represented in **Figure 7.1.C**) in increasing the specific interaction of contrast/imaging agents or drugs with cancer over normal cells/tissues.
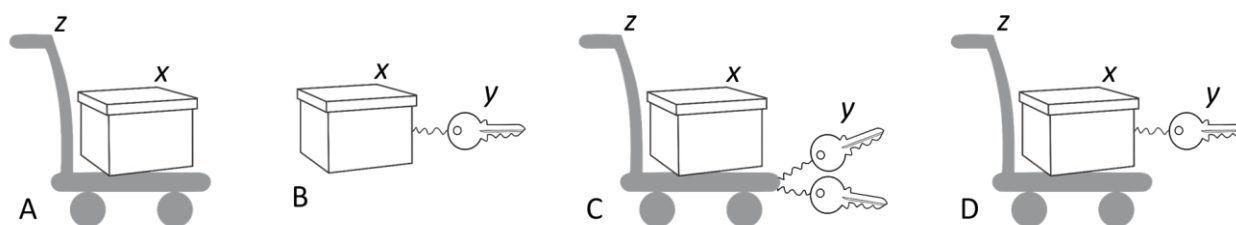
Figure 7.1. Schematic representation of different tumor targeting systems. (A): Drug encapsulated in a surface-plain nanocarrier. (B): Ligand-drug conjugate. (C): Drug encapsulated in a surface-decorated nanocarrier. (D): Proposed strategy to encapsulate a ligand-drug conjugate. Major components are identified with low-case letters (x = drug, y = ligand, z = nanocarrier).

The non-EPR approach, through use of peptide-model drug conjugates, was shown to be effective in targeting of solid tumors for a short period of time following i.v. administration (~ 2h). Future

investigations in this regard should focus on assessing the effect of this approach on the targeting and therapeutic index of actual drugs for cancer therapy. Similar to antibody-drug conjugates, peptide drug conjugates can be designed for this purpose. The drug mertansine (also called DM1), which is 25- to 500-fold more potent than paclitaxel, could be evaluated after conjugation with C18.4DK peptide, aiming to reduce the serious side effects of this compound in its free form.[380] Additionally, in light of the fast clearance of the peptide-Cy5.5 conjugate from the systemic circulation, the approach may be deemed useful for cancer cell detection and imaging. So the potential application of the developed system in guided therapy may be investigated.

Regarding investigation on biodistribution studies of polymeric micelles in cancer mouse models, we provided here a foundation for combining NIR and PET imaging concomitantly in the same experimental design. Different chemical modifications on micellar core and/or shell can be more powerfully evaluated by relying on both techniques, especially in more complex animal models, such as in metastatic ones. Functional NIR fluorophores operating in the second near-infrared window (1000–1700 nm) should be validated to improve imaging resolution, though some challenges still need to be addressed. One issue observed for longer wavelength cyanine fluorophores is a significant quenching caused by solvatochromism in biological fluids and other polar solvents.

Modulation of gene expression by different nucleic acid structures requires the use of efficient delivery systems. Here, an optimized strategy to transfect MDA-MB-435 cells with siRNA molecules was reported, we might look at using this transfection agent to evaluate its capacity to deliver more than one nucleic acid entity, not necessarily being siRNA. The co-delivery of multiple types of nucleic acids in a single system can serve as a powerful tool for more-effective complementary therapeutics. Some studies using PEI-based polyplexes have shown both *in vitro* and *in vivo* that the codelivery of DNA and siRNA to breast MDA-MB-231 cell line resulted in 20-fold higher plasmid transfection and 2-fold higher siRNA transfection, as compared to the respective single-nucleotide delivery.[381,382]

Since PNKP is an enzyme involved in the DNA repair machinery, the therapy combining A83B4C63 drug with radiotherapy or some DNA-damaging agents, such as irinotecan, melphalan, and others, could be a promising approach to treat cancer cells with a normal PTEN expression. Furthermore, new small molecules are being investigated for further improving PNKP inhibition, as well as for targeting another enzyme also involved in DNA repair, called ERCC1-XPF. Because those novel compounds may have substantial chemical differences, they would have to be assessed regarding encapsulation efficiency and release profile using polymeric micelles formed by PEO-PBCL and, perhaps, other types of copolymers. Then, *in vitro* and *in vivo* studies need to be performed.

We showed that our immunomicelles, formed by surface modification using full-length antibody molecules, were preferentially internalized by the cell populations expressing their receptor-based antigen at *in vitro* level. However, because of the potential off-targets relate to the Fc portion, as well as due to their larger size, other related molecules would be more suitable for the *in vivo* experiments.

Finally, future strategies can look at the delivery of ligand modified small molecules by nano-drug delivery systems as an alternative strategy in drug targeting. An example of potential could be the encapsulation of folate-drug conjugates. Many studies have reported on the conjugation of folate and cytotoxic agents,[383–385] and parallelly, different investigations are showing the feasibility of folate encapsulation in nanocarriers.[386–388] As represented in **Figure 7.1.D**, the combination of both approaches could greatly direct the delivery of such therapeutics into cancer cells.

References

(1) Bauer, S., Wiest, R., Nolte, L.-P., and Reyes, M. (2013) A survey of MRI-based medical image analysis for brain tumor studies. *Phys. Med. Biol. 58*, R97–R129.
(2) Hanahan, D., and Weinberg, R. A. (2011) Hallmarks of Cancer: The Next Generation. *Cell 144*, 646–674.
(3) Hanahan, D., and Weinberg, R. A. (2000) The Hallmarks of Cancer. *Cell 100*, 57–70.
(4) Marongiu, F., Serra, M., and Laconi, E. (2018) Development versus Evolution in Cancer Biology. *Trends Cancer 4*, 342–348.
(5) Burgos-Panadero, R., Lucantoni, F., Gamero-Sandemetrio, E., Cruz-Merino, L. de la, Álvaro, T., and Noguera, R. (2019) The tumour microenvironment as an integrated framework to understand cancer biology. *Cancer Lett. 461*, 112–122.
(6) Bussard, K. M., and Smith, G. H. (2012) Human Breast Cancer Cells Are Redirected to Mammary Epithelial Cells upon Interaction with the Regenerating Mammary Gland Microenvironment In-Vivo. *PLoS ONE* (Welm, A. L., Ed.) *7*, e49221.

(7) Gemei, M., Mirabelli, P., Di Noto, R., Corbo, C., Iaccarino, A., Zamboli, A., Troncone, G., Galizia, G., Lieto, E., Del Vecchio, L., and Salvatore, F. (2013) CD66c is a novel marker for colorectal cancer stem cell isolation, and its silencing halts tumor growth *in vivo*. *Cancer 119*, 729–738.

(8) Hopkins, A. L., and Groom, C. R. (2002) The druggable genome. *Nat. Rev. Drug Discov. 1*, 727–730.

(9) Gurevich, E. V., and Gurevich, V. V. (2014) Therapeutic Potential of Small Molecules and Engineered Proteins, in *Arrestins - Pharmacology and Therapeutic Potential*, pp 1–12. Springer Berlin Heidelberg, Berlin, Heidelberg.

(10) Imming, P., Sinning, C., and Meyer, A. (2006) Drugs, their targets and the nature and number of drug targets. *Nat. Rev. Drug Discov. 5*, 821–834.

(11) Al-Lawati, H., Binkhathlan, Z., and Lavasanifar, A. (2019) Nanomedicine for the effective and safe delivery of non-steroidal anti-inflammatory drugs: A review of preclinical research. *Eur. J. Pharm. Biopharm. 142*, 179–194.

(12) Hoyer, D., and Boddeke, H. W. G. M. (1993) Partial agonists, full agonists, antagonists: dilemmas of definition. *Trends Pharmacol. Sci. 14*, 270–275.

(13) Adams, S. (2009) Toll-like receptor agonists in cancer therapy. *Immunotherapy 1*, 949–964.

(14) Ralff, M. D., Lulla, A. R., Wagner, J., and El-Deiry, W. S. (2017) ONC201: a new treatment option being tested clinically for recurrent glioblastoma. *Transl. Cancer Res. 6*, S1239–S1243.

(15) Feng, Y., Zhou, J., Li, Z., Jiang, Y., and Zhou, Y. (2016) Small Molecular TRAIL Inducer ONC201 Induces Death in Lung Cancer Cells: A Preclinical Study. *PLoS ONE* (Hsieh, Y.-H., Ed.) *11*, e0162133.

(16) Wang, G., Wang, X., Yu, H., Wei, S., Williams, N., Holmes, D. L., Halfmann, R., Naidoo, J., Wang, L., Li, L., Chen, S., Harran, P., Lei, X., and Wang, X. (2013) Small-molecule activation of the TRAIL receptor DR5 in human cancer cells. *Nat. Chem. Biol. 9*, 84–89.

(17) Bush, K. (1983) Screening and Characterization of Enzyme Inhibitors as Drug Candidates. *Drug Metab. Rev. 14*, 689–708.

(18) Swinney, D. C. (2004) Biochemical mechanisms of drug action: what does it take for success? *Nat. Rev. Drug Discov. 3*, 801–808.

(19) Neubig, R. R., Spedding, M., Kenakin, T., and Christopoulos, A. (2003) International Union of Pharmacology Committee on Receptor Nomenclature and Drug Classification. *Pharmacol. Rev. 55*, 597–606.

(20) Wan, S., and Coveney, P. V. (2011) Rapid and accurate ranking of binding affinities of epidermal growth factor receptor sequences with selected lung cancer drugs. *J. R. Soc. Interface 8*, 1114–1127.

(21) Morin-Ben Abdallah, S., and Hirsh, V. (2018) Irreversible tyrosine kinase inhibition of epidermal growth factor receptor with afatinib in EGFR activating mutation–positive advanced non-small-cell lung cancer. *Curr. Oncol. 25*, 9.

(22) Waibel, R., Treichler, H., Schaefer, N. G., van Staveren, D. R., Mundwiler, S., Kunze, S., Kuenzi, M., Alberto, R., Nuesch, J., Knuth, A., Moch, H., Schibli, R., and Schubiger, P. A. (2008) New Derivatives of Vitamin B12 Show Preferential Targeting of Tumors. *Cancer Res. 68*, 2904–2911.

(23) Zwicke, G. L., Mansoori, G. A., and Jeffery, C. J. (2012) Utilizing the folate receptor for active targeting of cancer nanotherapeutics. *Nano Rev. 3*, 18496.

(24) Krall, N., Scheuermann, J., and Neri, D. (2013) Small Targeted Cytotoxics: Current State and Promises from DNA-Encoded Chemical Libraries. *Angew. Chem. Int. Ed. 52*, 1384–1402.

(25) Allison, R. R., and Sibata, C. H. (2010) Oncologic photodynamic therapy photosensitizers: A clinical review. *Photodiagnosis Photodyn. Ther. 7*, 61–75.

(26) Lin, C.-M., Usama, S. M., and Burgess, K. (2018) Site-Specific Labeling of Proteins with Near-IR Heptamethine Cyanine Dyes. *Molecules 23*, 2900.

(27) Hue, J. J., Lee, H.-J., Jon, S., Nam, S. Y., Yun, Y. W., Kim, J.-S., and Lee, B. J. (2013) Distribution and accumulation of Cy5.5-labeled thermally cross-linked superparamagnetic iron oxide nanoparticles in the tissues of ICR mice. *J. Vet. Sci. 14*, 473–479.

(28) Shirata, C., Kaneko, J., Inagaki, Y., Kokudo, T., Sato, M., Kiritani, S., Akamatsu, N., Arita, J., Sakamoto, Y., Hasegawa, K., and Kokudo, N. (2017) Near-infrared photothermal/photodynamic therapy with indocyanine green induces apoptosis of hepatocellular carcinoma cells through oxidative stress. *Sci. Rep. 7*, 13958.

(29) Doyle, S. K., Pop, M. S., Evans, H. L., and Koehler, A. N. (2016) Advances in discovering small molecules to probe protein function in a systems context. *Curr. Opin. Chem. Biol. 30*, 28–36.

(30) Booij, M. T., and Van De Kerkhof, P. C. M. (2011) Acitretin revisited in the era of biologics. *J. Dermatol. Treat. 22*, 86–89.

(31) Henninot, A., Collins, J. C., and Nuss, J. M. (2018) The Current State of Peptide Drug Discovery: Back to the Future? *J. Med. Chem. 61*, 1382–1414.

(32) Xiao, Y.-F., Jie, M.-M., Li, B.-S., Hu, C.-J., Xie, R., Tang, B., and Yang, S.-M. (2015) Peptide-Based Treatment: A Promising Cancer Therapy. *J. Immunol. Res. 2015*, 1–13.

(33) Marqus, S., Pirogova, E., and Piva, T. J. (2017) Evaluation of the use of therapeutic peptides for cancer treatment. *J. Biomed. Sci. 24*, 1–15.

(34) AlDeghaither, D., Smaglo, B. G., and Weiner, L. M. (2015) Beyond peptides and mAbs—current status and future perspectives for biotherapeutics with novel constructs. *J. Clin. Pharmacol. 55*, S4–S20.

(35) Roxin, Á., and Zheng, G. (2012) Flexible or fixed: a comparative review of linear and cyclic cancer-targeting peptides. *Future Med. Chem. 4*, 1601–1618.

(36) Sato, A. K., Viswanathan, M., Kent, R. B., and Wood, C. R. (2006) Therapeutic peptides: technological advances driving peptides into development. *Curr. Opin. Biotechnol. 17*, 638–642.

(37) Ajani, J. A. (2002) Role of Octreotide in Cancer and Therapy- Related Complications. *Oncology 16*, 1–3.

(38) Huang, X.-Q. (1997) Somatostatin: Likely the most widely effective gastrointestinal hormone in the human body. *World J. Gastroenterol. 3*, 201.

(39) Aranda, F., Vacchelli, E., Eggermont, A., Galon, J., Sautès-Fridman, C., Tartour, E., Zitvogel, L., Kroemer, G., and Galluzzi, L. (2013) Trial Watch: Peptide vaccines in cancer therapy. *OncoImmunology 2*, e26621.

(40) Brown, T. A., Byrd, K., Vreeland, T. J., Clifton, G. T., Jackson, D. O., Hale, D. F., Herbert, G. S., Myers, J. W., Greene, J. M., Berry, J. S., Martin, J., Elkas, J. C., Conrads, T. P., Darcy, K. M., Hamilton, C. A., Maxwel, G. L., and Peoples, G. E. (2019) Final analysis of a phase I/IIa trial of the folate-binding protein-derived E39 peptide vaccine to prevent recurrence in ovarian and endometrial cancer patients. *Cancer Med. 8*, 4678–4687.

(41) Prehn, R. T. (2006) An immune reaction may be necessary for cancer development. *Theor. Biol. Med. Model. 3*, 1–9.

(42) Filipazzi, P., Pilla, L., Mariani, L., Patuzzo, R., Castelli, C., Camisaschi, C., Maurichi, A., Cova, A., Rigamonti, G., Giardino, F., Di Florio, A., Asioli, M., Frati, P., Sovena, G., Squarcina, P., Maio, M., Danielli, R., Chiarion-Sileni, V., Villa, A., Lombardo, C., Tragni, G., Santinami, M., Parmiani, G., and Rivoltini, L. (2012) Limited Induction of Tumor Cross-Reactive T Cells without a Measurable Clinical Benefit in Early Melanoma Patients Vaccinated with Human Leukocyte Antigen Class I-Modified Peptides. *Clin. Cancer Res. 18*, 6485–6496.

(43) Laakkonen, P., and Vuorinen, K. (2010) Homing peptides as targeted delivery vehicles. *Integr. Biol. 2*, 326–337.

(44) Dave, N., and Liu, J. (2012) Biomimetic sensing based on chemically induced assembly of a signaling DNA aptamer on a fluid bilayer membrane. *Chem. Commun. 48*, 3718–3720.

(45) Koren, E., and Torchilin, V. P. (2012) Cell-penetrating peptides: breaking through to the other side. *Trends Mol. Med. 18*, 385–393.

(46) Xu, J., Khan, A. R., Fu, M., Wang, R., Ji, J., and Zhai, G. (2019) Cell-penetrating peptide: a means of breaking through the physiological barriers of different tissues and organs. *J. Controlled Release 309*, 106–124.

(47) Kalafatovic, D., and Giralt, E. (2017) Cell-Penetrating Peptides: Design Strategies beyond Primary Structure and Amphipathicity. *Molecules 22*, 1–38.

(48) Borrelli, A., Tornesello, A., Tornesello, M., and Buonaguro, F. (2018) Cell Penetrating Peptides as Molecular Carriers for Anti-Cancer Agents. *Molecules 23*, 1–28.

(49) Qvit, N., Rubin, S. J. S., Urban, T. J., Mochly-Rosen, D., and Gross, E. R. (2017) Peptidomimetic therapeutics: scientific approaches and opportunities. *Drug Discov. Today 22*, 454–462.

(50) Cirillo, D., Pentimalli, F., and Giordano, A. (2011) Peptides or Small Molecules? Different Approaches to Develop More Effective CDK Inhibitors. *Curr. Med. Chem. 18*, 2854–2866.

(51) Watson, J. D., and Crick, F. H. C. (1953) Molecular structure of nucleic acids. *Nature 171*, 737–738.

(52) Conde, J., Oliva, N., Atilano, M., Song, H. S., and Artzi, N. (2016) Self-assembled RNA-triple-helix hydrogel scaffold for microRNA modulation in the tumour microenvironment. *Nat. Mater. 15*, 353–363.

(53) Nikolova, E. N., Zhou, H., Gottardo, F. L., Alvey, H. S., Kimsey, I. J., and Al-Hashimi, H. M. (2013) A historical account of Hoogsteen base-pairs in duplex DNA. *Biopolymers 99*, 955–968.

(54) Aliabadi, H. M., Landry, B., Sun, C., Tang, T., and Uludağ, H. (2012) Supramolecular assemblies in functional siRNA delivery: Where do we stand? *Biomaterials 33*, 2546–2569.

(55) Setten, R. L., Rossi, J. J., and Han, S. (2019) The current state and future directions of RNAi-based therapeutics. *Nat. Rev. Drug Discov. 18*, 421–446.

(56) Cobb, M. (2017) 60 years ago, Francis Crick changed the logic of biology. *PLoS Biol. 15*, e2003243.

(57) Dimitriadis, G. J. (1978) Translation of rabbit globin mRNA introduced by liposomes into mouse lymphocytes. *Nature 274*, 923–924.

(58) Hajj, K. A., and Whitehead, K. A. (2017) Tools for translation: non-viral materials for therapeutic mRNA delivery. *Nat. Rev. Mater. 2*, 1–17.

(59) Kowalski, P. S., Rudra, A., Miao, L., and Anderson, D. G. (2019) Delivering the Messenger: Advances in Technologies for Therapeutic mRNA Delivery. *Mol. Ther. 27*, 710–728.

(60) Lee, Y., Kim, M., Han, J., Yeom, K.-H., Lee, S., Baek, S. H., and Kim, V. N. (2004) MicroRNA genes are transcribed by RNA polymerase II. *EMBO J. 23*, 4051–4060.

(61) Nana-Sinkam, S. P., and Croce, C. M. (2013) Clinical Applications for microRNAs in Cancer. *Clin. Pharmacol. Ther. 93*, 98–104.

(62) Curtis, H. J., Sibley, C. R., and Wood, M. J. A. (2012) Mirtrons, an emerging class of atypical miRNA. *Wiley Interdiscip. Rev. RNA 3*, 617–632.

(63) Dong, Y., Siegwart, D. J., and Anderson, D. G. (2019) Strategies, design, and chemistry in siRNA delivery systems. *Adv. Drug Deliv. Rev. 144*, 133–147.

(64) Hanna, J., Hossain, G. S., and Kocerha, J. (2019) The Potential for microRNA Therapeutics and Clinical Research. *Front. Genet. 10*, 1–6.

(65) Acharya, R. (2019) The recent progresses in shRNA-nanoparticle conjugate as a therapeutic approach. *Mater. Sci. Eng. C 104*, 109928.

(66) Conejos-Sánchez, I., Gallon, E., Niño-Pariente, A., Smith, J. A., De la Fuente, A. G., Di Canio, L., Pluchino, S., Franklin, R. J. M., and Vicent, M. J. (2019) Polyornithine-based polyplexes to boost effective gene silencing in CNS disorders. *Nanoscale 10.1039.C9NR06187H*, 1–15.

(67) Brandão, P. R. de P., Titze-de-Almeida, S. S., and Titze-de-Almeida, R. (2019) Leading RNA Interference Therapeutics Part 2: Silencing Delta-Aminolevulinic Acid Synthase 1, with a Focus on Givosiran. *Mol. Diagn. Ther. 10.1007/s40291-019-00438–6*, 1–8.

(68) Yoon, S., and Rossi, J. J. (2018) Therapeutic Potential of Small Activating RNAs (saRNAs) in Human Cancers. *Curr. Pharm. Biotechnol. 19*, 604–610.

(69) Setten, R. L., Lightfoot, H. L., Habib, N. A., and Rossi, J. J. (2018) Development of MTL-CEBPA: Small Activating RNA Drug for Hepatocellular Carcinoma. *Curr. Pharm. Biotechnol. 19*, 611–621.

(70) Reebye, V., Saetrom, P., Mintz, P. J., Huang, K.-W., Swiderski, P., Peng, L., Liu, C., Liu, X., Lindkaer-Jensen, S., Zacharoulis, D., Kostomitsopoulos, N., Kasahara, N., Nicholls, J. P., Jiao, L. R., Pai, M., Spalding,

D. R., Mizandari, M., Chikovani, T., Emara, M. M., Haoudi, A., Tomalia, D. A., Rossi, J. J., and Habib, N. A. (2014) Novel RNA oligonucleotide improves liver function and inhibits liver carcinogenesis *in vivo*. *Hepatology 59*, 216–227.

(71) Castanotto, D., and Rossi, J. J. (2009) The promises and pitfalls of RNA-interference-based therapeutics. *Nature 457*, 426–433.

(72) Zhang, C., Li, G., Zhu, S., Zhang, S., and Fang, J. (2014) tasiRNAdb: a database of ta-siRNA regulatory pathways. *Bioinformatics 30*, 1045–1046.

(73) Kim, H., Kim, S.-T., Ryu, J., Kang, B.-C., Kim, J.-S., and Kim, S.-G. (2017) CRISPR/Cpf1-mediated DNA-free plant genome editing. *Nat. Commun. 8*, 14406.

(74) Sánchez-Rivera, F. J., and Jacks, T. (2015) Applications of the CRISPR–Cas9 system in cancer biology. *Nat. Rev. Cancer 15*, 387–393.

(75) Yan, M.-Y., Yan, H.-Q., Ren, G.-X., Zhao, J.-P., Guo, X.-P., and Sun, Y.-C. (2017) CRISPR-Cas12a-Assisted Recombineering in Bacteria. *Appl. Environ. Microbiol. 83*, 1–13.

(76) Cyranoski, D. (2016) CRISPR gene editing tested in a person. *Nature 539*, 479.

(77) Lu, Y., Huang, M., Deng, T., Zhou, X., Yu, K., Liang, M., Deng, L., Xue, J., Yi, X., Ding, Z., Gong, Y., Zhu, J., Wang, Y., Wang, Y., Song, J., Tong, R., Li, L., Huang, J., Na, F., Zhao, M., Chen, C., Wei, Y., and Li, W. A phase I trial of PD-1 deficient engineered T cells with CRISPR/Cas9 in patients with advanced non-small cell lung cancer with PD-L1 expression. *Cancer Res. 78*, Abstract CT133.

(78) Martinez-Lage, M., Puig-Serra, P., Menendez, P., Torres-Ruiz, R., and Rodriguez-Perales, S. (2018) CRISPR/Cas9 for Cancer Therapy: Hopes and Challenges. *Biomedicines 6*, 105.

(79) Xia, L., Liu, Y., and Wang, Y. (2019) PD-1/PD-L1 Blockade Therapy in Advanced Non-Small-Cell Lung Cancer: Current Status and Future Directions. *The Oncologist 24*, S31–S41.

(80) McIvor, R. S. (2011) Therapeutic Delivery of mRNA: The Medium Is the Message. *Mol. Ther. 19*, 822–823.

(81) Hu, Q., Li, W., Hu, X., Hu, Q., Shen, J., Jin, X., Zhou, J., Tang, G., and Chu, P. K. (2012) Synergistic treatment of ovarian cancer by co-delivery of survivin shRNA and paclitaxel via supramolecular micellar assembly. *Biomaterials 33*, 6580–6591.

(82) Xing, J., Jia, C.-R., Wang, Y., Guo, J., and Cai, Y. (2012) Effect of shRNA targeting survivin on ovarian cancer. *J. Cancer Res. Clin. Oncol. 138*, 1221–1229.

(83) Cai, Y., Ma, W., Huang, X., Cao, L., Li, H., Jiang, Y., Lu, N., and Yin, Y. (2015) Effect of survivin on tumor growth of colorectal cancer *in vivo*. *Int. J. Clin. Exp. Pathol. 8*, 13267–13272.

(84) Mokhtary, P., Javan, B., Sharbatkhari, M., Soltani, A., and Erfani-Moghadam, V. (2018) Cationic vesicles for efficient shRNA transfection in the MCF-7 breast cancer cell line. *Int. J. Nanomedicine 13*, 7107–7121.

(85) Goklany, S., Lu, P., Godeshala, S., Hall, A., Garrett-Mayer, E., Voelkel-Johnson, C., and Rege, K. (2019) Delivery of TRAIL-expressing plasmid DNA to cancer cells *in vitro* and *in vivo* using aminoglycoside-derived polymers. *J. Mater. Chem. B 7*, 7014–7025.

(86) Hoon, S., Zhou, B., Janda, K., Brenner, S., and Scolnick, J. (2011) Aptamer selection by high-throughput sequencing and informatic analysis. *BioTechniques 51*.

(87) Haßel, S. K., and Mayer, G. (2019) Aptamers as Therapeutic Agents: Has the Initial Euphoria Subsided? *Mol. Diagn. Ther. 23*, 301–309.

(88) Lakhin, A. V., Tarantul, V. Z., and Gening, L. V. (2013) Aptamers: Problems, Solutions and Prospects. *Acta Naturae 5*, 34–43.

(89) Lipman, N. S., Jackson, L. R., Trudel, L. J., and Weis-Garcia, F. (2005) Monoclonal Versus Polyclonal Antibodies: Distinguishing Characteristics, Applications, and Information Resources. *ILAR J. 46*, 258–268.

(90) Liu, J. K. H. (2014) The history of monoclonal antibody development – Progress, remaining challenges and future innovations. *Ann. Med. Surg. 3*, 113–116.

(91) Rader, R. A. (2008) (Re)defining biopharmaceutical. *Nat. Biotechnol. 26*, 743–751.

(92) Evens, R. P., and Kaitin, K. I. (2014) The Biotechnology Innovation Machine: A Source of Intelligent Biopharmaceuticals for the Pharma Industry—Mapping Biotechnology's Success. *Clin. Pharmacol. Ther. 95*, 528–532.

(93) Heidelberger, M. (1929) A Quantitative Study of the Precipitin Reaction between Type III Pneumococcus Polysaccharide and Purified Homologous Antibody. *J. Exp. Med. 50*, 809–823.

(94) Smith, S. L. (1996) Ten years of Orthoclone OKT3 (muromonab-CD3): a review. *J. Transpl. Coord. 6*, 109–121.

(95) Jefferis, R. (2012) Isotype and glycoform selection for antibody therapeutics. *Arch. Biochem. Biophys. 526*, 159–166.

(96) Schroeder, H. W., and Cavacini, L. (2010) Structure and function of immunoglobulins. *J. Allergy Clin. Immunol. 125*, S41–S52.

(97) Liu, H., and May, K. (2012) Disulfide bond structures of IgG molecules: Structural variations, chemical modifications and possible impacts to stability and biological function. *mAbs 4*, 17–23.

(98) Lacy, E. R., Baker, M., and Brigham-Burke, M. (2008) Free sulfhydryl measurement as an indicator of antibody stability. *Anal. Biochem. 382*, 66–68.

(99) Van Buren, N., Rehder, D., Gadgil, H., Matsumura, M., and Jacob, J. (2009) Elucidation of Two Major Aggregation Pathways in an IgG2 Antibody. *J. Pharm. Sci. 98*, 3013–3030.

(100) Liu, H., Nowak, C., Andrien, B., Shao, M., Ponniah, G., and Neill, A. (2017) Impact of IgG Fc-Oligosaccharides on Recombinant Monoclonal Antibody Structure, Stability, Safety, and Efficacy. *Biotechnol. Prog. 33*, 1173–1181.

(101) Subedi, G. P., and Barb, A. W. (2015) The Structural Role of Antibody N-Glycosylation in Receptor Interactions. *Structure 23*, 1573–1583.

(102) Chames, P., Van Regenmortel, M., Weiss, E., and Baty, D. (2009) Therapeutic antibodies: successes, limitations and hopes for the future. *Br. J. Pharmacol. 157*, 220–233.

(103) Pillay, V., Gan, H. K., and Scott, A. M. (2011) Antibodies in oncology. *New Biotechnol. 28*, 518–529.

(104) Santos, M. L. dos, Quintilio, W., Manieri, T. M., Tsuruta, L. R., and Moro, A. M. (2018) Advances and challenges in therapeutic monoclonal antibodies drug development. *Braz. J. Pharm. Sci. 54*, e01007.

(105) Shirai, H., Kidera, A., and Nakamura, H. (1999) H3-rules: identification of CDR-H3 structures in antibodies. *FEBS Lett. 455*, 188–197.

(106) Battaglin, F., Puccini, A., Ahcene Djaballah, S., and Lenz, H.-J. (2019) The impact of panitumumab treatment on survival and quality of life in patients with RAS wild-type metastatic colorectal cancer. *Cancer Manag. Res. 11*, 5911–5924.

(107) Nelson, A. L. (2010) Antibody fragments: Hope and hype. *mAbs 2*, 77–83.

(108) Ahmad, Z. A., Yeap, S. K., Ali, A. M., Ho, W. Y., Alitheen, N. B. M., and Hamid, M. (2012) scFv Antibody: Principles and Clinical Application. *Clin. Dev. Immunol. 2012*, 1–15.

(109) Rodrigo, G., Gruvegård, M., and Van Alstine, J. (2015) Antibody Fragments and Their Purification by Protein L Affinity Chromatography. *Antibodies 4*, 259–277.

(110) Bannas, P., Hambach, J., and Koch-Nolte, F. (2017) Nanobodies and Nanobody-Based Human Heavy Chain Antibodies As Antitumor Therapeutics. *Front. Immunol. 8*, 1–13.

(111) Ingram, J. R., Schmidt, F. I., and Ploegh, H. L. (2018) Exploiting Nanobodies' Singular Traits. *Annu. Rev. Immunol. 36*, 695–715.

(112) Könning, D., Zielonka, S., Grzeschik, J., Empting, M., Valldorf, B., Krah, S., Schröter, C., Sellmann, C., Hock, B., and Kolmar, H. (2017) Camelid and shark single domain antibodies: structural features and therapeutic potential. *Curr. Opin. Struct. Biol. 45*, 10–16.

(113) Klein, C., Sustmann, C., Thomas, M., Stubenrauch, K., Croasdale, R., Schanzer, J., Brinkmann, U., Kettenberger, H., Regula, J. T., and Schaefer, W. (2012) Progress in overcoming the chain association issue in bispecific heterodimeric IgG antibodies. *mAbs 4*, 653–663.

(114) Labrijn, A. F., Janmaat, M. L., Reichert, J. M., and Parren, P. W. H. I. (2019) Bispecific antibodies: a mechanistic review of the pipeline. *Nat. Rev. Drug Discov. 18*, 585–608.

(115) Wang, Q., Chen, Y., Park, J., Liu, X., Hu, Y., Wang, T., McFarland, K., and Betenbaugh, M. J. (2019) Design and Production of Bispecific Antibodies. *Antibodies 8*, 43.

(116) Przepiorka, D., Ko, C.-W., Deisseroth, A., Yancey, C. L., Candau-Chacon, R., Chiu, H.-J., Gehrke, B. J., Gomez-Broughton, C., Kane, R. C., Kirshner, S., Mehrotra, N., Ricks, T. K., Schmiel, D., Song, P., Zhao, P., Zhou, Q., Farrell, A. T., and Pazdur, R. (2015) FDA Approval: Blinatumomab. *Clin. Cancer Res. 21*, 4035–4039.

(117) Nagorsen, D., Kufer, P., Baeuerle, P. A., and Bargou, R. (2012) Blinatumomab: A historical perspective. *Pharmacol. Ther. 136*, 334–342.

(118) Vazquez-Lombardi, R., Phan, T. G., Zimmermann, C., Lowe, D., Jermutus, L., and Christ, D. (2015) Challenges and opportunities for non-antibody scaffold drugs. *Drug Discov. Today 20*, 1271–1283.

(119) Feldwisch, J., Tolmachev, V., Lendel, C., Herne, N., Sjöberg, A., Larsson, B., Rosik, D., Lindqvist, E., Fant, G., Höidén-Guthenberg, I., Galli, J., Jonasson, P., and Abrahmsén, L. (2010) Design of an Optimized Scaffold for Affibody Molecules. *J. Mol. Biol. 398*, 232–247.

(120) Löfblom, J., Feldwisch, J., Tolmachev, V., Carlsson, J., Ståhl, S., and Frejd, F. Y. (2010) Affibody molecules: Engineered proteins for therapeutic, diagnostic and biotechnological applications. *FEBS Lett. 584*, 2670–2680.

(121) Lorey, S., Fiedler, E., Kunert, A., Nerkamp, J., Lange, C., Fiedler, M., Bosse-Doenecke, E., Meysing, M., Gloser, M., Rundfeldt, C., Rauchhaus, U., Hänssgen, I., Göttler, T., Steuernagel, A., Fiedler, U., and Haupts, U. (2014) Novel Ubiquitin-derived High Affinity Binding Proteins with Tumor Targeting Properties. *J. Biol. Chem. 289*, 8493–8507.

(122) Rothe, C., and Skerra, A. (2018) Anticalin® Proteins as Therapeutic Agents in Human Diseases. *BioDrugs 32*, 233–243.

(123) Sha, F., Salzman, G., Gupta, A., and Koide, S. (2017) Monobodies and other synthetic binding proteins for expanding protein science. *Protein Sci. 26*, 910–924.

(124) Silacci, M., Baenziger-Tobler, N., Lembke, W., Zha, W., Batey, S., Bertschinger, J., and Grabulovski, D. (2014) Linker Length Matters, Fynomer-Fc Fusion with an Optimized Linker Displaying Picomolar IL-17A Inhibition Potency. *J. Biol. Chem. 289*, 14392–14398.

(125) Hosse, R. J., Rothe, A., and Power, B. E. (2006) A new generation of protein display scaffolds for molecular recognition. *Protein Sci. 15*, 14–27.

(126) Škrlec, K., Štrukelj, B., and Berlec, A. (2015) Non-immunoglobulin scaffolds: a focus on their targets. *Trends Biotechnol. 33*, 408–418.

(127) Orlova, A., Wallberg, H., Stone-Elander, S., and Tolmachev, V. (2009) On the Selection of a Tracer for PET Imaging of HER2-Expressing Tumors: Direct Comparison of a 124I-Labeled Affibody Molecule and Trastuzumab in a Murine Xenograft Model. *J. Nucl. Med. 50*, 417–425.

(128) Eshhar, Z., Waks, T., Gross, G., and Schindler, D. G. (1993) Specific activation and targeting of cytotoxic lymphocytes through chimeric single chains consisting of antibody-binding domains and the γ or δ subunits of the immunoglobulin and T-cell receptors. *Proc Natl Acad Sci USA 90*, 720–724.

(129) Dotti, G., Savoldo, B., and Brenner, M. (2009) Fifteen Years of Gene Therapy Based on Chimeric Antigen Receptors: "Are We Nearly There Yet?" *Hum. Gene Ther. 20*, 1229–1239.

(130) Kosti, P., Maher, J., and Arnold, J. N. (2018) Perspectives on Chimeric Antigen Receptor T-Cell Immunotherapy for Solid Tumors. *Front. Immunol. 9*, 1–9.

(131) Ramos, C. A., and Dotti, G. (2011) Chimeric antigen receptor (CAR)-engineered lymphocytes for cancer therapy. *Expert Opin. Biol. Ther. 11*, 855–873.

(132) Liu, F., and Saif, M. W. (2017) T cell optimization for the treatment of pancreatic cancer. *Expert Opin. Biol. Ther. 17*, 1493–1501.

(133) Neelapu, S. S., Locke, F. L., Bartlett, N. L., Lekakis, L. J., Miklos, D. B., Jacobson, C. A., Braunschweig, I., Oluwole, O. O., Siddiqi, T., Lin, Y., Timmerman, J. M., Stiff, P. J., Friedberg, J. W., Flinn, I. W., Goy, A., Hill, B. T., Smith, M. R., Deol, A., Farooq, U., McSweeney, P., Munoz, J., Avivi, I., Castro, J. E., Westin, J. R., Chavez, J. C., Ghobadi, A., Komanduri, K. V., Levy, R., Jacobsen, E. D., Witzig, T. E., Reagan, P., Bot, A., Rossi, J., Navale, L., Jiang, Y., Aycock, J., Elias, M., Chang, D., Wiezorek, J., and Go, W. Y. (2017) Axicabtagene Ciloleucel CAR T-Cell Therapy in Refractory Large B-Cell Lymphoma. *N. Engl. J. Med. 377*, 2531–2544.

(134) Beck, A., and Reichert, J. M. (2014) Antibody-drug conjugates: Present and future. *mAbs 6*, 15–17.

(135) Upadhyay, P., Sarker, S., Ghosh, A., Gupta, P., Das, S., Ahir, M., Bhattacharya, S., Chattopadhyay, S., Ghosh, S., and Adhikary, A. (2019) Transferrin-decorated thymoquinone-loaded PEG-PLGA nanoparticles exhibit anticarcinogenic effect in non-small cell lung carcinoma *via* the modulation of miR-34a and miR-16. *Biomater. Sci. 7*, 4325–4344.

(136) Sun, B., Deng, C., Meng, F., Zhang, J., and Zhong, Z. (2016) Robust, active tumor-targeting and fast bioresponsive anticancer nanotherapeutics based on natural endogenous materials. *Acta Biomater. 45*, 223–233.

(137) Jule, E., Nagasaki, Y., and Kataoka, K. (2003) Lactose-Installed Poly(ethylene glycol)-Poly(D,L-lactide) Block Copolymer Micelles Exhibit Fast-Rate Binding and High Affinity toward a Protein Bed Simulating a Cell Surface. A Surface Plasmon Resonance Study. *Bioconjug. Chem. 14*, 177–186.

(138) He, H., Liu, L., Morin, E. E., Liu, M., and Schwendeman, A. (2019) Survey of Clinical Translation of Cancer Nanomedicines—Lessons Learned from Successes and Failures. *Acc. Chem. Res. 52*, 2445–2461.

(139) Bertrand, N., Wu, J., Xu, X., Kamaly, N., and Farokhzad, O. C. (2014) Cancer nanotechnology: The impact of passive and active targeting in the era of modern cancer biology. *Adv. Drug Deliv. Rev. 66*, 2–25.

(140) Yang, C., Wu, T., Qi, Y., and Zhang, Z. (2018) Recent Advances in the Application of Vitamin E TPGS for Drug Delivery. *Theranostics 8*, 464–485.

(141) Dong, X., Mattingly, C. A., Tseng, M. T., Cho, M. J., Liu, Y., Adams, V. R., and Mumper, R. J. (2009) Doxorubicin and Paclitaxel-Loaded Lipid-Based Nanoparticles Overcome Multidrug Resistance by Inhibiting P-Glycoprotein and Depleting ATP. *Cancer Res. 69*, 3918–3926.

(142) Collnot, E.-M., Baldes, C., Wempe, M. F., Hyatt, J., Navarro, L., Edgar, K. J., Schaefer, U. F., and Lehr, C.-M. (2006) Influence of vitamin E TPGS poly(ethylene glycol) chain length on apical efflux transporters in Caco-2 cell monolayers. *J. Controlled Release 111*, 35–40.

(143) Collnot, E.-M., Baldes, C., Schaefer, U. F., Edgar, K. J., Wempe, M. F., and Lehr, C.-M. (2010) Vitamin E TPGS P-Glycoprotein Inhibition Mechanism: Influence on Conformational Flexibility, Intracellular ATP Levels, and Role of Time and Site of Access. *Mol. Pharm. 7*, 642–651.

(144) Nowack, B., Krug, H. F., and Height, M. (2011) 120 Years of Nanosilver History: Implications for Policy Makers. *Environ. Sci. Technol. 45*, 1177–1183.

(145) Matsumura, Y., and Maeda, H. (1986) A New Concept for Macromolecular Therapeutics in Cancer Chemotherapy: Mechanism of Tumoritropic Accumulation of Proteins and the Antitumor Agent Smancs. *Cancer Res. 46*, 6387–6392.

(146) Shi, J., Kantoff, P. W., Wooster, R., and Farokhzad, O. C. (2017) Cancer nanomedicine: progress, challenges and opportunities. *Nat. Rev. Cancer 17*, 20–37.

(147) Danhier, F. (2016) To exploit the tumor microenvironment: Since the EPR effect fails in the clinic, what is the future of nanomedicine? *J. Controlled Release 244*, 108–121.

(148) Wilhelm, S., Tavares, A. J., Dai, Q., Ohta, S., Audet, J., Dvorak, H. F., and Chan, W. C. W. (2016) Analysis of nanoparticle delivery to tumours. *Nat. Rev. Mater. 1*, 1–12.

(149) Bulbake, U., Doppalapudi, S., Kommineni, N., and Khan, W. (2017) Liposomal Formulations in Clinical Use: An Updated Review. *Pharmaceutics 9*, 1–33.

(150) Nichols, J. W., and Bae, Y. H. (2014) EPR: Evidence and fallacy. *J. Controlled Release 190*, 451–464.

(151) Rosenblum, D., Joshi, N., Tao, W., Karp, J. M., and Peer, D. (2018) Progress and challenges towards targeted delivery of cancer therapeutics. *Nat. Commun. 9*, 1410.

(152) Zhang, X.-L., Pang, W., Hu, X.-T., Li, J.-L., Yao, Y.-G., and Zheng, Y.-T. (2014) Experimental primates and non-human primate (NHP) models of human diseases in China: current status and progress. *Zool. Res. 35*, 447–464.

(153) Anchordoquy, T. J., Barenholz, Y., Boraschi, D., Chorny, M., Decuzzi, P., Dobrovolskaia, M. A., Farhangrazi, Z. S., Farrell, D., Gabizon, A., Ghandehari, H., Godin, B., La-Beck, N. M., Ljubimova, J., Moghimi, S. M., Pagliaro, L., Park, J.-H., Peer, D., Ruoslahti, E., Serkova, N. J., and Simberg, D. (2017) Mechanisms and Barriers in Cancer Nanomedicine: Addressing Challenges, Looking for Solutions. *ACS Nano 11*, 12–18.

(154) Schädlich, A., Caysa, H., Mueller, T., Tenambergen, F., Rose, C., Göpferich, A., Kuntsche, J., and Mäder, K. (2011) Tumor Accumulation of NIR Fluorescent PEG–PLA Nanoparticles: Impact of Particle Size and Human Xenograft Tumor Model. *ACS Nano 5*, 8710–8720.

(155) Geng, Y., Dalhaimer, P., Cai, S., Tsai, R., Tewari, M., Minko, T., and Discher, D. E. (2007) Shape effects of filaments versus spherical particles in flow and drug delivery. *Nat. Nanotechnol. 2*, 249–255.

(156) Amoozgar, Z., and Yeo, Y. (2012) Recent advances in stealth coating of nanoparticle drug delivery systems. *Wiley Interdiscip. Rev. Nanomed. Nanobiotechnol. 4*, 219–233.

(157) van Vlerken, L. E., Duan, Z., Little, S. R., Seiden, M. V., and Amiji, M. M. (2008) Biodistribution and Pharmacokinetic Analysis of Paclitaxel and Ceramide Administered in Multifunctional Polymer-Blend Nanoparticles in Drug Resistant Breast Cancer Model. *Mol. Pharm. 5*, 516–526.

(158) Lancet, J. E., Uy, G. L., Cortes, J. E., Newell, L. F., Lin, T. L., Ritchie, E. K., Stuart, R. K., Strickland, S. A., Hogge, D., Solomon, S. R., Stone, R. M., Bixby, D. L., Kolitz, J. E., Schiller, G. J., Wieduwilt, M. J., Ryan, D. H., Hoering, A., Banerjee, K., Chiarella, M., Louie, A. C., and Medeiros, B. C. (2018) CPX-351 (cytarabine and daunorubicin) Liposome for Injection Versus Conventional Cytarabine Plus Daunorubicin in Older Patients With Newly Diagnosed Secondary Acute Myeloid Leukemia. *J. Clin. Oncol. 36*, 2684–2692.

(159) Sharma, B., Crist, R. M., and Adiseshaiah, P. P. (2017) Nanotechnology as a Delivery Tool for Precision Cancer Therapies. *AAPS J. 19*, 1632–1642.

(160) Oh, J. Y., Kim, H. S., Palanikumar, L., Go, E. M., Jana, B., Park, S. A., Kim, H. Y., Kim, K., Seo, J. K., Kwak, S. K., Kim, C., Kang, S., and Ryu, J.-H. (2018) Cloaking nanoparticles with protein corona shield for targeted drug delivery. *Nat. Commun. 9*.

(161) Tavares, A. J., Poon, W., Zhang, Y.-N., Dai, Q., Besla, R., Ding, D., Ouyang, B., Li, A., Chen, J., Zheng, G., Robbins, C., and Chan, W. C. W. (2017) Effect of removing Kupffer cells on nanoparticle tumor delivery. *Proc. Natl. Acad. Sci. 114*, E10871–E10880.

(162) Van Rooijen, N., and Sanders, A. (1996) Kupffer cell depletion by liposome-delivered drugs: Comparative activity of intracellular clodronate, propamidine, and ethylenediaminetetraacetic acid. *Hepatology 23*, 1239–1243.

(163) Galanis, E., Carlson, S. K., Foster, N. R., Lowe, V., Quevedo, F., McWilliams, R. R., Grothey, A., Jatoi, A., Alberts, S. R., and Rubin, J. (2008) Phase I Trial of a Pathotropic Retroviral Vector Expressing a Cytocidal Cyclin G1 Construct (Rexin-G) in Patients With Advanced Pancreatic Cancer. *Mol. Ther. 16*, 979–984.

(164) Matsumura, Y., Gotoh, M., Muro, K., Yamada, Y., Shirao, K., Shimada, Y., Okuwa, M., Matsumoto, S., Miyata, Y., Ohkura, H., Chin, K., Baba, S., Yamao, T., Kannami, A., Takamatsu, Y., Ito, K., and Takahashi, K. (2004) Phase I and pharmacokinetic study of MCC-465, a doxorubicin (DXR) encapsulated in PEG immunoliposome, in patients with metastatic stomach cancer. *Ann. Oncol. 15*, 517–525.

(165) Suzuki, R., Takizawa, T., Kuwata, Y., Mutoh, M., Ishiguro, N., Utoguchi, N., Shinohara, A., Eriguchi, M., Yanagie, H., and Maruyama, K. (2008) Effective anti-tumor activity of oxaliplatin encapsulated in transferrin–PEG-liposome. *Int. J. Pharm. 346*, 143–150.

(166) Miller, K., Cortes, J., Hurvitz, S. A., Krop, I. E., Tripathy, D., Verma, S., Riahi, K., Reynolds, J. G., Wickham, T. J., Molnar, I., and Yardley, D. A. (2016) HERMIONE: a randomized Phase 2 trial of MM-302

plus trastuzumab versus chemotherapy of physician's choice plus trastuzumab in patients with previously treated, anthracycline-naïve, HER2-positive, locally advanced/metastatic breast cancer. *BMC Cancer 16*, 352.

(167) Park, J. W., Hong, K., Kirpotin, D. B., Colbern, G., Shalaby, R., Baselga, J., Shao, Y., Nielsen, U. B., Marks, J. D., Moore, D., Papahadjopoulos, D., and Benz, C. C. (2002) Anti-HER2 Immunoliposomes: Enhanced Efficacy Attributable to Targeted Delivery. *Clin. Cancer Res. 8*, 1172–1181.

(168) Gargett, T., Abbas, M. N., Rolan, P., Price, J. D., Gosling, K. M., Ferrante, A., Ruszkiewicz, A., Atmosukarto, I. I. C., Altin, J., Parish, C. R., and Brown, M. P. (2018) Phase I trial of Lipovaxin-MM, a novel dendritic cell-targeted liposomal vaccine for malignant melanoma. *Cancer Immunol. Immunother. 67*, 1461–1472.

(169) Von Hoff, D. D., Mita, M. M., Ramanathan, R. K., Weiss, G. J., Mita, A. C., LoRusso, P. M., Burris, H. A., Hart, L. L., Low, S. C., Parsons, D. M., Zale, S. E., Summa, J. M., Youssoufian, H., and Sachdev, J. C. (2016) Phase I Study of PSMA-Targeted Docetaxel-Containing Nanoparticle BIND-014 in Patients with Advanced Solid Tumors. *Clin. Cancer Res. 22*, 3157–3163.

(170) MacDiarmid, J. A., Mugridge, N. B., Weiss, J. C., Phillips, L., Burn, A. L., Paulin, R. P., Haasdyk, J. E., Dickson, K.-A., Brahmbhatt, V. N., Pattison, S. T., James, A. C., Al Bakri, G., Straw, R. C., Stillman, B., Graham, R. M., and Brahmbhatt, H. (2007) Bacterially Derived 400 nm Particles for Encapsulation and Cancer Cell Targeting of Chemotherapeutics. *Cancer Cell 11*, 431–445.

(171) Siefker-Radtke, A., Zhang, X., Guo, C. C., Shen, Y., Pirollo, K. F., Sabir, S., Leung, C., Leong-Wu, C., Ling, C.-M., Chang, E. H., Millikan, R. E., and Benedict, W. F. (2016) A Phase l Study of a Tumor-targeted Systemic Nanodelivery System, SGT-94, in Genitourinary Cancers. *Mol. Ther. 24*, 1484–1491.

(172) Senzer, N., Nemunaitis, J., Nemunaitis, D., Bedell, C., Edelman, G., Barve, M., Nunan, R., Pirollo, K. F., Rait, A., and Chang, E. H. (2013) Phase I Study of a Systemically Delivered p53 Nanoparticle in Advanced Solid Tumors. *Mol. Ther. 21*, 1096–1103.

(173) Davis, M. E., Zuckerman, J. E., Choi, C. H. J., Seligson, D., Tolcher, A., Alabi, C. A., Yen, Y., Heidel, J. D., and Ribas, A. (2010) Evidence of RNAi in humans from systemically administered siRNA via targeted nanoparticles. *Nature 464*, 1067–1070.

(174) de Goeij, B. E., and Lambert, J. M. (2016) New developments for antibody-drug conjugate-based therapeutic approaches. *Curr. Opin. Immunol. 40*, 14–23.

(175) Yaghoubi, S., Karimi, M. H., Lotfinia, M., Gharibi, T., Mahi-Birjand, M., Kavi, E., Hosseini, F., Sineh Sepehr, K., Khatami, M., Bagheri, N., and Abdollahpour-Alitappeh, M. (2019) Potential drugs used in the antibody–drug conjugate (ADC) architecture for cancer therapy. *J. Cell. Physiol. 235*, 31–64.

(176) Reth, M. (2013) Matching cellular dimensions with molecular sizes. *Nat. Immunol. 14*, 765–767.

(177) Kung Sutherland, M. S., Walter, R. B., Jeffrey, S. C., Burke, P. J., Yu, C., Kostner, H., Stone, I., Ryan, M. C., Sussman, D., Lyon, R. P., Zeng, W., Harrington, K. H., Klussman, K., Westendorf, L., Meyer, D., Bernstein, I. D., Senter, P. D., Benjamin, D. R., Drachman, J. G., and McEarchern, J. A. (2013) SGN-CD33A: a novel CD33-targeting antibody–drug conjugate using a pyrrolobenzodiazepine dimer is active in models of drug-resistant AML. *Blood 122*, 1455–1463.

(178) Sun, A., and Benet, L. Z. (2020) Late-Stage Failures of Monoclonal Antibody Drugs: A Retrospective Case Study Analysis. *Pharmacology 10.1159/000505379*, 1–19.

(179) Ma, L., Wang, C., He, Z., Cheng, B., Zheng, L., and Huang, K. (2017) Peptide-Drug Conjugate: A Novel Drug Design Approach. *Curr. Med. Chem. 24*, 1–24.

(180) Xuan, W., Peng, Y., Deng, Z., Peng, T., Kuai, H., Li, Y., He, J., Jin, C., Liu, Y., Wang, R., and Tan, W. (2018) A basic insight into aptamer-drug conjugates (ApDCs). *Biomaterials 182*, 216–226.

(181) Ding, H., Altai, M., Rinne, S. S., Vorobyeva, A., Tolmachev, V., Gräslund, T., and Orlova, A. (2019) Incorporation of a Hydrophilic Spacer Reduces Hepatic Uptake of HER2-Targeting Affibody–DM1 Drug Conjugates. *Cancers 11*, 1168.

(182) Huang, H., Wu, T., Shi, H., Wu, Y., Yang, H., Zhong, K., Wang, Y., and Liu, Y. (2019) Modular Design of Nanobody-drug Conjugates for Targeteddelivery of Platinum Anticancer Drug with MRI Contrast Agent. *Chem. Commun. 55*, 5175–5178.

(183) Oller-Salvia, B., Sánchez-Navarro, M., Giralt, E., and Teixidó, M. (2016) Blood–brain barrier shuttle peptides: an emerging paradigm for brain delivery. *Chem. Soc. Rev. 45*, 4690–4707.

(184) Li, Y., Zheng, X., Gong, M., and Zhang, J. (2016) Delivery of a peptide-drug conjugate targeting the blood brain barrier improved the efficacy of paclitaxel against glioma. *Oncotarget 7*, 79401–79407.

(185) Lewis Phillips, G. D., Li, G., Dugger, D. L., Crocker, L. M., Parsons, K. L., Mai, E., Blattler, W. A., Lambert, J. M., Chari, R. V. J., Lutz, R. J., Wong, W. L. T., Jacobson, F. S., Koeppen, H., Schwall, R. H., Kenkare-Mitra, S. R., Spencer, S. D., and Sliwkowski, M. X. (2008) Targeting HER2-Positive Breast Cancer with Trastuzumab-DM1, an Antibody-Cytotoxic Drug Conjugate. *Cancer Res. 68*, 9280–9290.

(186) McCombs, J. R., and Owen, S. C. (2015) Antibody Drug Conjugates: Design and Selection of Linker, Payload and Conjugation Chemistry. *AAPS J. 17*, 339–351.

(187) Staudacher, A. H., and Brown, M. P. (2017) Antibody drug conjugates and bystander killing: is antigen-dependent internalisation required? *Br. J. Cancer 117*, 1736–1742.

(188) Hasan, A. A. K., Zisman, T., and Schmaier, A. H. (1998) Identification of cytokeratin 1 as a binding protein and presentation receptor for kininogens on endothelial cells. *Proc. Natl. Acad. Sci. 95*, 3615–3620.

(189) Collard, C. D., Montalto, M. C., Reenstra, W. R., Buras, J. A., and Stahl, G. L. (2001) Endothelial Oxidative Stress Activates the Lectin Complement Pathway. *Am. J. Pathol. 159*, 1045–1054.

(190) Labudova, M., Tomaskova, J., Skultety, L., Pastorek, J., and Pastorekova, S. (2009) The Nucleoprotein of Lymphocytic Choriomeningitis Virus Facilitates Spread of Persistent Infection through Stabilization of the Keratin Network. *J. Virol. 83*, 7842–7849.

(191) Kolte, D., Osman, N., Yang, J., and Shariat-Madar, Z. (2011) High Molecular Weight Kininogen Activates B_2 Receptor Signaling Pathway in Human Vascular Endothelial Cells. *J. Biol. Chem. 286*, 24561–24571.

(192) Tang, S., Huang, W., Zhong, M., Yin, L., Jiang, H., Hou, S., Gan, P., and Yuan, Y. (2012) Identification Keratin 1 as a cDDP-resistant protein in nasopharyngeal carcinoma cell lines. *J. Proteomics 75*, 2352–2360.

(193) Marimpietri, D., Petretto, A., Raffaghello, L., Pezzolo, A., Gagliani, C., Tacchetti, C., Mauri, P., Melioli, G., and Pistoia, V. (2013) Proteome Profiling of Neuroblastoma-Derived Exosomes Reveal the Expression of Proteins Potentially Involved in Tumor Progression. *PLoS ONE 8*, e75054.

(194) Shahin, M., Soudy, R., Aliabadi, H. M., Kneteman, N., Kaur, K., and Lavasanifar, A. (2013) Engineered breast tumor targeting peptide ligand modified liposomal doxorubicin and the effect of peptide density on anticancer activity. *Biomaterials 34*, 4089–4097.

(195) Shahin, M., Soudy, R., El-Sikhry, H., Seubert, J. M., Kaur, K., and Lavasanifar, A. (2013) Engineered peptides for the development of actively tumor targeted liposomal carriers of doxorubicin. *Cancer Lett. 334*, 284–292.

(196) Mohammed-Saeid, W., Soudy, R., Tikoo, R., Kaur, K., Verrall, R. E., and Badea, I. (2018) Design and Evaluation of Gemini Surfactant-Based Lipoplexes Modified with Cell-Binding Peptide for Targeted Gene Therapy in Melanoma Model. *J. Pharm. Pharm. Sci. 21*, 363–375.

(197) Brandt, B., Meyer-Staeckling, S., Schmidt, H., Agelopoulos, K., and Buerger, H. (2006) Mechanisms of *egfr* Gene Transcription Modulation: Relationship to Cancer Risk and Therapy Response. *Clin. Cancer Res. 12*, 7252–7260.

(198) Ping Wee, and Zhixiang Wang. (2017) Epidermal Growth Factor Receptor Cell Proliferation Signaling Pathways. *Cancers 9*, 52.

(199) Sigismund, S., Avanzato, D., and Lanzetti, L. (2018) Emerging functions of the EGFR in cancer. *Mol. Oncol. 12*, 3–20.

(200) Zou, Y., Xia, Y., Meng, F., Zhang, J., and Zhong, Z. (2018) GE11-Directed Functional Polymersomal Doxorubicin as an Advanced Alternative to Clinical Liposomal Formulation for Ovarian Cancer Treatment. *Mol. Pharm. 15*, 3664–3671.

(201) Mondal, G., Kumar, V., Shukla, S. K., Singh, P. K., and Mahato, R. I. (2016) EGFR-Targeted Polymeric Mixed Micelles Carrying Gemcitabine for Treating Pancreatic Cancer. *Biomacromolecules 17*, 301–313.

(202) Soleymani Abyaneh, H., Soleimani, A., Vakili, M., Soudy, R., Kaur, K., Cuda, F., Tavassoli, A., and Lavasanifar, A. (2018) Modulation of Hypoxia-Induced Chemoresistance to Polymeric Micellar Cisplatin: The Effect of Ligand Modification of Micellar Carrier Versus Inhibition of the Mediators of Drug Resistance. *Pharmaceutics 10*, 196–213.

(203) Duxbury, M. S., Ito, H., Benoit, E., Waseem, T., Ashley, S. W., and Whang, E. E. (2004) A Novel Role for Carcinoembryonic Antigen-Related Cell Adhesion Molecule 6 as a Determinant of Gemcitabine Chemoresistance in Pancreatic Adenocarcinoma Cells. *Cancer Res. 64*, 3987–3993.

(204) Lewis-Wambi, J. S., Cunliffe, H. E., Kim, H. R., Willis, A. L., and Jordan, V. C. (2008) Overexpression of CEACAM6 promotes migration and invasion of oestrogen-deprived breast cancer cells. *Eur. J. Cancer 44*, 1770–1779.

(205) Steiner, N., Hajek, R., Nachbaur, D., Borjan, B., Sevcikova, S., Göbel, G., and Gunsilius, E. (2019) Levels of CEACAM6 in Peripheral Blood Are Elevated in Patients with Plasma Cell Disorders: A Potential New Diagnostic Marker and a New Therapeutic Target? *Dis. Markers 2019*, 1–6.

(206) Raghuwanshi, Y., Etayash, H., Soudy, R., Paiva, I., Lavasanifar, A., and Kaur, K. (2017) Proteolytically Stable Cyclic Decapeptide for Breast Cancer Cell Targeting. *J. Med. Chem. 60*, 4893–4903.

(207) Schrama, D., Reisfeld, R. A., and Becker, J. C. (2006) Antibody targeted drugs as cancer therapeutics. *Nat. Rev. Drug Discov. 5*, 147–159.

(208) van der Meel, R., Vehmeijer, L. J. C., Kok, R. J., Storm, G., and van Gaal, E. V. B. (2013) Ligand-targeted particulate nanomedicines undergoing clinical evaluation: Current status. *Adv. Drug Deliv. Rev. 65*, 1284–1298.

(209) Sun, H., Zhu, X., Lu, P. Y., Rosato, R. R., Tan, W., and Zu, Y. (2014) Oligonucleotide Aptamers: New Tools for Targeted Cancer Therapy. *Mol. Ther. 3*, e182.

(210) Junutula, J. R., Raab, H., Clark, S., Bhakta, S., Leipold, D. D., Weir, S., Chen, Y., Simpson, M., Tsai, S. P., Dennis, M. S., Lu, Y., Meng, Y. G., Ng, C., Yang, J., Lee, C. C., Duenas, E., Gorrell, J., Katta, V., Kim, A., McDorman, K., Flagella, K., Venook, R., Ross, S., Spencer, S. D., Lee Wong, W., Lowman, H. B., Vandlen, R., Sliwkowski, M. X., Scheller, R. H., Polakis, P., and Mallet, W. (2008) Site-specific conjugation of a cytotoxic drug to an antibody improves the therapeutic index. *Nat. Biotechnol. 26*, 925–932.

(211) Khan, D. R., Webb, M. N., Cadotte, T. H., and Gavette, M. N. (2015) Use of Targeted Liposome-based Chemotherapeutics to Treat Breast Cancer. *Breast Cancer Basic Clin. Res. 9*, 1–5.

(212) Wu, C.-H., Kuo, Y.-H., Hong, R.-L., and Wu, H.-C. (2015) α-Enolase–binding peptide enhances drug delivery efficiency and therapeutic efficacy against colorectal cancer. *Sci. Transl. Med. 7*, 290ra91.

(213) Ladner, R. C., Sato, A. K., Gorzelany, J., and de Souza, M. (2004) Phage display-derived peptides as therapeutic alternatives to antibodies. *Drug Discov. Today 9*, 525–529.

(214) Soudy, R., Byeon, N., Raghuwanshi, Y., Ahmed, S., Lavasanifar, A., and Kaur, K. (2017) Engineered Peptides for Applications in Cancer-Targeted Drug Delivery and Tumor Detection. *Mini-Rev. Med. Chem. 17*.

(215) Gray, B. P., and Brown, K. C. (2014) Combinatorial Peptide Libraries: Mining for Cell-Binding Peptides. *Chem. Rev. 114*, 1020–1081.

(216) Li, Z., Zhao, R., Wu, X., Sun, Y., Yao, M., Li, J., Xu, Y., and Gu, J. (2005) Identification and characterization of a novel peptide ligand of epidermal growth factor receptor for targeted delivery of therapeutics. *FASEB J. 19*, 1978–1985.

(217) Wang, S., Noberini, R., Stebbins, J. L., Das, S., Zhang, Z., Wu, B., Mitra, S., Billet, S., Fernandez, A., Bhowmick, N. A., Kitada, S., Pasquale, E. B., Fisher, P. B., and Pellecchia, M. (2013) Targeted Delivery of Paclitaxel to EphA2-Expressing Cancer Cells. *Clin. Cancer Res. 19*, 128–137.

(218) Zhang, J., Spring, H., and Schwab, M. (2001) Neuroblastoma tumor cell-binding peptides identified through random peptide phage display. *Cancer Lett. 171*, 153–164.

(219) Askoxylakis, V., Zitzmann, S., Mier, W., Graham, K., Krämer, S., von Wegner, F., Fink, R. H. A., Schwab, M., Eisenhut, M., and Haberkorn, U. (2005) Preclinical Evaluation of the Breast Cancer Cell-Binding Peptide, p160. *Clin. Cancer Res. 11*, 6705–6712.

(220) Ahmed, S., Mathews, A. S., Byeon, N., Lavasanifar, A., and Kaur, K. (2010) Peptide Arrays for Screening Cancer Specific Peptides. *Anal. Chem. 82*, 7533–7541.

(221) Soudy, R., Gill, A., Sprules, T., Lavasanifar, A., and Kaur, K. (2011) Proteolytically Stable Cancer Targeting Peptides with High Affinity for Breast Cancer Cells. *J. Med. Chem. 54*, 7523–7534.

(222) Soudy, R., Chen, C., and Kaur, K. (2013) Novel Peptide–Doxorubicin Conjugates for Targeting Breast Cancer Cells Including the Multidrug Resistant Cells. *J. Med. Chem. 56*, 7564–7573.

(223) Soudy, R., Etayash, H., Bahadorani, K., Lavasanifar, A., and Kaur, K. (2017) Breast Cancer Targeting Peptide Binds Keratin 1: A New Molecular Marker for Targeted Drug Delivery to Breast Cancer. *Mol. Pharm. 14*, 593–604.

(224) Ahmed, S., and Kaur, K. (2009) The Proteolytic Stability and Cytotoxicity Studies of l-Aspartic Acid and l-Diaminopropionic Acid derived β-Peptides and a Mixed α/β-Peptide. *Chem. Biol. Drug Des. 73*, 545–552.

(225) Kaiser, E., Colescott, R. L., Bossinger, C. D., and Cook, P. I. (1970) Color Test for Detection of Free Terminal Amino Groups in the Solid-Phase Synthesis of Peptides. *Anal. Biochem. 34*, 595–598.

(226) Irwin, C. R., Favis, N. A., Agopsowicz, K. C., Hitt, M. M., and Evans, D. H. (2013) Myxoma Virus Oncolytic Efficiency Can Be Enhanced Through Chemical or Genetic Disruption of the Actin Cytoskeleton. *PLoS ONE 8*, e84134.

(227) Chariou, P. L., Lee, K. L., Wen, A. M., Gulati, N. M., Stewart, P. L., and Steinmetz, N. F. (2015) Detection and Imaging of Aggressive Cancer Cells Using an Epidermal Growth Factor Receptor (EGFR)-Targeted Filamentous Plant Virus-Based Nanoparticle. *Bioconjug. Chem. 26*, 262–269.

(228) Pauletti, G. M., Okumu, F. W., and Borchardt, R. T. (1997) Effect of Size and Charge on the Passive Diffusion of Peptides Across Caco-2 Cell Monolayers via the Paracellular Pathway. *Pharm. Res. 14*, 164–168.

(229) Gudmundsson, O. S., Jois, S. D. S., Velde, D. G. V., Siahaan, T. J., Wang, B., and Borchardt, R. T. (1999) The effect of conformation on the membrane permeation of coumarinic acid- and phenylpropionic acid-based cyclic prodrugs of opioid peptides. *J. Pept. Res. 53*, 383–392.

(230) Golemis, E. A., Scheet, P., Beck, T. N., Scolnick, E. M., Hunter, D. J., Hawk, E., and Hopkins, N. (2018) Molecular mechanisms of the preventable causes of cancer in the United States. *Genes Dev. 32*, 868–902.

(231) Herrera, V. L., Colby, A. H., Ruiz-Opazo, N., Coleman, D. G., and Grinstaff, M. W. (2018) Nucleic acid nanomedicines in Phase II/III clinical trials: translation of nucleic acid therapies for reprogramming cells. *Nanomed. 13*, 2083–2098.

(232) Chakraborty, C., Sharma, A. R., Sharma, G., Doss, C. G. P., and Lee, S.-S. (2017) Therapeutic miRNA and siRNA: Moving from Bench to Clinic as Next Generation Medicine. *Mol. Ther. - Nucleic Acids 8*, 132–143.

(233) Tai, W. (2019) Current Aspects of siRNA Bioconjugate for *In Vitro* and *In Vivo* Delivery. *Molecules 24*, 1–25.

(234) Saw, P. E., and Song, E.-W. (2019) siRNA therapeutics: a clinical reality. *Sci. China Life Sci.*

(235) Kaczmarek, J. C., Kowalski, P. S., and Anderson, D. G. (2017) Advances in the delivery of RNA therapeutics: from concept to clinical reality. *Genome Med. 9*, 1–16.

(236) Cooper, B. M., and Putnam, D. (2016) Polymers for siRNA Delivery: A Critical Assessment of Current Technology Prospects for Clinical Application. *ACS Biomater. Sci. Eng. 2*, 1837–1850.

(237) Garg, S. M., Falamarzian, A., Vakili, M. R., Aliabadi, H. M., Uludağ, H., and Lavasanifar, A. (2016) Polymeric micelles for *MCL-1* gene silencing in breast tumors following systemic administration. *Nanomed. 11*, 2319–2339.

(238) Bolesta, E., Pfannenstiel, L. W., Demelash, A., Lesniewski, M. L., Tobin, M., Schlanger, S. E., Nallar, S. C., Papadimitriou, J. C., Kalvakolanu, D. V., and Gastman, B. R. (2012) Inhibition of Mcl-1 Promotes Senescence in Cancer Cells: Implications for Preventing Tumor Growth and Chemotherapy Resistance. *Mol. Cell. Biol. 32*, 1879–1892.

(239) Thomas, L. W., Lam, C., and Edwards, S. W. (2010) Mcl-1; the molecular regulation of protein function. *FEBS Lett. 584*, 2981–2989.

(240) Xiao, Y., Nimmer, P., Sheppard, G. S., Bruncko, M., Hessler, P., Lu, X., Roberts-Rapp, L., Pappano, W. N., Elmore, S. W., Souers, A. J., Leverson, J. D., and Phillips, D. C. (2015) MCL-1 Is a Key Determinant of Breast Cancer Cell Survival: Validation of MCL-1 Dependency Utilizing a Highly Selective Small Molecule Inhibitor. *Mol. Cancer Ther. 14*, 1837–1847.

(241) Raab, M., Kobayashi, N. F., Becker, S., Kurunci-Csacsko, E., Krämer, A., Strebhardt, K., and Sanhaji, M. (2019) Boosting the apoptotic response of high-grade serous ovarian cancers with *CCNE1* amplification to paclitaxel *in vitro* by targeting APC/C and the pro-survival protein MCL-1. *Int. J. Cancer*.

(242) Wertz, I. E., Kusam, S., Lam, C., Okamoto, T., Sandoval, W., Anderson, D. J., Helgason, E., Ernst, J. A., Eby, M., Liu, J., Belmont, L. D., Kaminker, J. S., O'Rourke, K. M., Pujara, K., Kohli, P. B., Johnson, A. R., Chiu, M. L., Lill, J. R., Jackson, P. K., Fairbrother, W. J., Seshagiri, S., Ludlam, M. J. C., Leong, K. G., Dueber, E. C., Maecker, H., Huang, D. C. S., and Dixit, V. M. (2011) Sensitivity to antitubulin chemotherapeutics is regulated by MCL1 and FBW7. *Nature 471*, 110–114.

(243) Aliabadi, H. M., Maranchuk, R., Kucharski, C., Mahdipoor, P., Hugh, J., and Uludağ, H. (2013) Effective response of doxorubicin-sensitive and -resistant breast cancer cells to combinational siRNA therapy. *J. Controlled Release 172*, 219–228.

(244) Basu, A., and Sridharan, S. (2017) Regulation of anti-apoptotic Bcl-2 family protein Mcl-1 by S6 kinase 2. *PLoS ONE 12*, e0173854.

(245) Karami, H., Baradaran, B., Esfehani, A., Sakhinia, M., and Sakhinia, E. (2014) Down-Regulation of Mcl-1 by Small Interference RNA Induces Apoptosis and Sensitizes HL-60 Leukemia Cells to Etoposide. *Asian Pac. J. Cancer Prev. 15*, 629–635.

(246) Cao, F., Gong, Y.-B., Kang, X.-H., Lu, Z.-H., Wang, Y., Zhao, K.-L., Miao, Z.-H., Liao, M.-J., and Xu, Z.-Y. (2019) Degradation of MCL-1 by bufalin reverses acquired resistance to osimertinib in EGFR-mutant lung cancer. *Toxicol. Appl. Pharmacol. 379*, 114662.

(247) Fernandes, C., Suares, D., and Yergeri, M. C. (2018) Tumor Microenvironment Targeted Nanotherapy. *Front. Pharmacol. 9*, 1230.

(248) Nagasaki, Y., Kutsuna, T., Iijima, M., Kato, M., and Kazunori, K. (1995) Formyl-Ended Heterobifunctional Poly(ethylene oxide): Synthesis of Poly(ethylene oxide) with a Formyl Group at One End and a Hydroxyl Group at the Other End. *Bioconjug. Chem. 6*, 231–233.

(249) Xiong, X.-B., Uludağ, H., and Lavasanifar, A. (2009) Biodegradable amphiphilic poly(ethylene oxide)-*block*-polyesters with grafted polyamines as supramolecular nanocarriers for efficient siRNA delivery. *Biomaterials 30*, 242–253.

(250) Garg, S. M., Paiva, I. M., Vakili, M. R., Soudy, R., Agopsowicz, K., Soleimani, A. H., Hitt, M., Kaur, K., and Lavasanifar, A. (2017) Traceable PEO-poly(ester) micelles for breast cancer targeting: The effect of core structure and targeting peptide on micellar tumor accumulation. *Biomaterials 144*, 17–29.

(251) Lavasanifar, A., Samuel, J., and Kwon, G. S. (2001) Micelles self-assembled from poly(ethylene oxide)-*block*-poly(N-hexyl stearate l-aspartamide) by a solvent evaporation method: effect on the solubilization and haemolytic activity of amphotericin B. *J. Controlled Release 77*, 155–160.

(252) Stewart, D. P., Koss, B., Bathina, M., Perciavalle, R. M., Bisanz, K., and Opferman, J. T. (2010) Ubiquitin-Independent Degradation of Antiapoptotic MCL-1. *Mol. Cell. Biol. 30*, 3099–3110.

(253) Sun, C.-Y., Shen, S., Xu, C.-F., Li, H.-J., Liu, Y., Cao, Z.-T., Yang, X.-Z., Xia, J.-X., and Wang, J. (2015) Tumor Acidity-Sensitive Polymeric Vector for Active Targeted siRNA Delivery. *J. Am. Chem. Soc. 137*, 15217–15224.

(254) Sun, T.-M., Du, J.-Z., Yao, Y.-D., Mao, C.-Q., Dou, S., Huang, S.-Y., Zhang, P.-Z., Leong, K. W., Song, E.-W., and Wang, J. (2011) Simultaneous Delivery of siRNA and Paclitaxel via a "Two-in-One" Micelleplex Promotes Synergistic Tumor Suppression. *ACS Nano 5*, 1483–1494.

(255) Peng, Y., Huang, J., Xiao, H., Wu, T., and Shuai, X. (2018) Codelivery of temozolomide and siRNA with polymeric nanocarrier for effective glioma treatment. *Int. J. Nanomedicine 13*, 3467–3480.

(256) Zou, S., Cao, N., Cheng, D., Zheng, R., Wang, J., Zhu, K., and Shuai, X. (2012) Enhanced apoptosis of ovarian cancer cells via nanocarrier-mediated codelivery of siRNA and doxorubicin. *Int. J. Nanomedicine 7*, 3823–3835.

(257) Cao, N., Cheng, D., Zou, S., Ai, H., Gao, J., and Shuai, X. (2011) The synergistic effect of hierarchical assemblies of siRNA and chemotherapeutic drugs co-delivered into hepatic cancer cells. *Biomaterials 32*, 2222–2232.

(258) Lu, Y., Zhong, L., Jiang, Z., Pan, H., Zhang, Y., Zhu, G., Bai, L., Tong, R., Shi, J., and Duan, X. (2019) Cationic micelle-based siRNA delivery for efficient colon cancer gene therapy. *Nanoscale Res. Lett. 14*.

(259) Xiong, X.-B., and Lavasanifar, A. (2011) Traceable Multifunctional Micellar Nanocarriers for Cancer-Targeted Co-delivery of MDR-1 siRNA and Doxorubicin. *ACS Nano 5*, 5202–5213.

(260) Won, Y.-Y., Sharma, R., and Konieczny, S. F. (2009) Missing pieces in understanding the intracellular trafficking of polycation/DNA complexes. *J. Controlled Release 139*, 88–93.

(261) Yook, S., Cai, Z., Lu, Y., Winnik, M. A., Pignol, J.-P., and Reilly, R. M. (2016) Intratumorally Injected ^{177}Lu-Labeled Gold Nanoparticles: Gold Nanoseed Brachytherapy with Application for Neoadjuvant Treatment of Locally Advanced Breast Cancer. *J. Nucl. Med. 57*, 936–942.

(262) Xing, Y., Zhao, J., Conti, P. S., and Chen, K. (2014) Radiolabeled Nanoparticles for Multimodality Tumor Imaging. *Theranostics 4*, 290–306.

(263) Hoshyar, N., Gray, S., Han, H., and Bao, G. (2016) The effect of nanoparticle size on *in vivo* pharmacokinetics and cellular interaction. *Nanomed. 11*, 673–692.

(264) Ambade, A. V., Savariar, E. N., and Thayumanavan, S. (2005) Dendrimeric Micelles for Controlled Drug Release and Targeted Delivery. *Mol. Pharm. 2*, 264–272.

(265) Winkler, M., Raupp, Y. S., Köhl, L. A. M., Wagner, H. E., and Meier, M. A. R. (2014) Modified Poly(ε-caprolactone)s: An Efficient and Renewable Access via Thia-Michael Addition and Baeyer–Villiger Oxidation. *Macromolecules 47*, 2842–2846.

(266) Mahmud, A., Xiong, X.-B., and Lavasanifar, A. (2006) Novel Self-Associating Poly(ethylene oxide)-*block*-poly(ε-caprolactone) Block Copolymers with Functional Side Groups on the Polyester Block for Drug Delivery. *Macromolecules 39*, 9419–9428.

(267) Shire, Z., Vakili, M. R., Morgan, T. D. R., Hall, D. G., Lavasanifar, A., and Weinfeld, M. (2018) Nanoencapsulation of Novel Inhibitors of PNKP for Selective Sensitization to Ionizing Radiation and Irinotecan and Induction of Synthetic Lethality. *Mol. Pharm. 15*, 2316–2326.

(268) Harari, P. M., Allen, G. W., and Bonner, J. A. (2007) Biology of Interactions: Antiepidermal Growth Factor Receptor Agents. *J. Clin. Oncol. 25*, 4057–4065.

(269) Sasaki, T., Hiroki, K., and Yamashita, Y. (2013) The Role of Epidermal Growth Factor Receptor in Cancer Metastasis and Microenvironment. *BioMed Res. Int. 2013*, 1–8.

(270) Rayego-Mateos, S., Rodrigues-Diez, R., Morgado-Pascual, J. L., Valentijn, F., Valdivielso, J. M., Goldschmeding, R., and Ruiz-Ortega, M. (2018) Role of Epidermal Growth Factor Receptor (EGFR) and Its Ligands in Kidney Inflammation and Damage. *Mediators Inflamm. 2018*, 1–22.

205

(271) Yu, X., Zhao, X., Zhang, J., Li, Y., Sheng, P., Ma, C., Zhang, L., Hao, X., Zheng, X., Xing, Y., Qiao, H., Qu, L., and Zhu, D. (2019) Dacomitinib, a new pan-EGFR inhibitor, is effective in attenuating pulmonary vascular remodeling and pulmonary hypertension. *Eur. J. Pharmacol. 850*, 97–108.

(272) Li, N., Nguyen, H. H., Byrom, M., and Ellington, A. D. (2011) Inhibition of Cell Proliferation by an Anti-EGFR Aptamer. *PLoS ONE* (Lewin, A., Ed.) *6*, e20299.

(273) Kang, M. K., Mao, W., Lee, J. B., and Yoo, H. S. (2017) Epidermal growth factor (EGF) fragment-guided anticancer theranostic particles for pH-responsive release of doxorubicin. *Int. J. Pharm. 519*, 104–112.

(274) Liao, C., Sun, Q., Liang, B., Shen, J., and Shuai, X. (2011) Targeting EGFR-overexpressing tumor cells using Cetuximab-immunomicelles loaded with doxorubicin and superparamagnetic iron oxide. *Eur. J. Radiol. 80*, 699–705.

(275) Zalba, S., Contreras, A. M., Haeri, A., ten Hagen, T. L. M., Navarro, I., Koning, G., and Garrido, M. J. (2015) Cetuximab-oxaliplatin-liposomes for epidermal growth factor receptor targeted chemotherapy of colorectal cancer. *J. Controlled Release 210*, 26–38.

(276) Roovers, R. C., Vosjan, M. J. W. D., Laeremans, T., el Khoulati, R., de Bruin, R. C. G., Ferguson, K. M., Verkleij, A. J., van Dongen, G. A. M. S., and van Bergen en Henegouwen, P. M. P. (2011) A biparatopic anti-EGFR nanobody efficiently inhibits solid tumour growth. *Int. J. Cancer 129*, 2013–2024.

(277) Master, A. M., and Sen Gupta, A. (2012) EGF receptor-targeted nanocarriers for enhanced cancer treatment. *Nanomed. 7*, 1895–1906.

(278) Chu, W.-Y., Tsai, M.-H., Peng, C.-L., Shih, Y.-H., Luo, T.-Y., Yang, S.-J., and Shieh, M.-J. (2018) pH-Responsive Nanophotosensitizer for an Enhanced Photodynamic Therapy of Colorectal Cancer Overexpressing EGFR. *Mol. Pharm. 15*, 1432–1444.

(279) Li, Z., Zhao, R., Wu, X., Sun, Y., Yao, M., Li, J., Xu, Y., and Gu, J. (2005) Identification and characterization of a novel peptide ligand of epidermal growth factor receptor for targeted delivery of therapeutics. *FASEB J. 19*, 1978–1985.

(280) Lee, D., Lee, Y. M., Kim, J., Lee, M. K., and Kim, W. J. (2015) Enhanced tumor-targeted gene delivery by bioreducible polyethylenimine tethering EGFR divalent ligands. *Biomater. Sci. 3*, 1096–1104.

(281) Ongarora, B. G., Fontenot, K. R., Hu, X., Sehgal, I., Satyanarayana-Jois, S. D., and Vicente, M. G. H. (2012) Phthalocyanine–Peptide Conjugates for Epidermal Growth Factor Receptor Targeting. *J. Med. Chem. 55*, 3725–3738.

(282) DeJesus, O. T. (2012) Synthesis of [^{64}Cu]Cu-NOTA-Bn-GE11 for PET Imaging of EGFR-Rich Tumors. *Curr. Radiopharm. 5*, 15–18.

(283) Dissoki, S., Hagooly, A., Elmachily, S., and Mishani, E. (2011) Labeling approaches for the GE11 peptide, an epidermal growth factor receptor biomarker. *J. Label. Compd. Radiopharm. 54*, 693–701.

(284) Rahmanian, N., Hosseinimehr, S. J., Khalaj, A., Noaparast, Z., Abedi, S. M., and Sabzevari, O. (2017) ^{99m}Tc-radiolabeled GE11-modified peptide for ovarian tumor targeting. *DARU J. Pharm. Sci. 25*, 13.

(285) Chen, C.-J., Chan, C.-H., Lin, K.-L., Chen, J.-H., Tseng, C.-H., Wang, P.-Y., Chien, C.-Y., Yu, H.-M., and Lin, W.-J. (2019) ^{68}Ga-labelled NOTA-RGD-GE11 peptide for dual integrin and EGFR-targeted tumour imaging. *Nucl. Med. Biol. 68–69*, 22–30.

(286) Striese, F., Sihver, W., Gao, F., Bergmann, R., Walther, M., Pietzsch, J., Steinbach, J., and Pietzsch, H.-J. (2018) Exploring pitfalls of ^{64}Cu-labeled EGFR-targeting peptide GE11 as a potential PET tracer. *Amino Acids 50*, 1415–1431.

(287) Klutz, K., Schaffert, D., Willhauck, M. J., Grünwald, G. K., Haase, R., Wunderlich, N., Zach, C., Gildehaus, F. J., Senekowitsch-Schmidtke, R., Göke, B., Wagner, E., Ogris, M., and Spitzweg, C. (2011) Epidermal Growth Factor Receptor-targeted 131I-therapy of Liver Cancer Following Systemic Delivery of the Sodium Iodide Symporter Gene. *Mol. Ther. 19*, 676–685.

(288) Klutz, K., Willhauck, M. J., Dohmen, C., Wunderlich, N., Knoop, K., Zach, C., Senekowitsch-Schmidtke, R., Gildehaus, F.-J., Ziegler, S., Fürst, S., Göke, B., Wagner, E., Ogris, M., and Spitzweg, C. (2011) Image-

Guided Tumor-Selective Radioiodine Therapy of Liver Cancer After Systemic Nonviral Delivery of the Sodium Iodide Symporter Gene. *Hum. Gene Ther. 22*, 1563–1574.

(289) Urnauer, S., Schmohl, K. A., Tutter, M., Schug, C., Schwenk, N., Morys, S., Ziegler, S., Bartenstein, P., Clevert, D.-A., Wagner, E., and Spitzweg, C. (2019) Dual-targeted NIS polyplexes—a theranostic strategy toward tumors with heterogeneous receptor expression. *Gene Ther. 26*, 93–108.

(290) Yu, H.-M., Chen, J.-H., Lin, K.-L., and Lin, W.-J. (2015) Synthesis of ^{68}Ga-labeled NOTA-RGD-GE11 heterodimeric peptide for dual integrin and epidermal growth factor receptor-targeted tumor imaging. *J. Label. Compd. Radiopharm. 58*, 299–303.

(291) Parmar, A., Pascali, G., Voli, F., Lerra, L., Yee, E., Ahmed-Cox, A., Kimpton, K., Cirillo, G., Arthur, A., Zahra, D., Rahardjo, G., Liu, G. J., Lengkeek, N., Saletta, F., Charil, A., Kavallaris, M., and Vittorio, O. (2018) *In vivo* [^{64}Cu]CuCl$_2$ PET imaging reveals activity of Dextran-Catechin on tumor copper homeostasis. *Theranostics 8*, 5645–5659.

(292) Chen, K., Li, Z.-B., Wang, H., Cai, W., and Chen, X. (2008) Dual-modality optical and positron emission tomography imaging of vascular endothelial growth factor receptor on tumor vasculature using quantum dots. *Eur. J. Nucl. Med. Mol. Imaging 35*, 2235–2244.

(293) Chen, F., Hong, H., Zhang, Y., Valdovinos, H. F., Shi, S., Kwon, G. S., Theuer, C. P., Barnhart, T. E., and Cai, W. (2013) *In Vivo* Tumor Targeting and Image-Guided Drug Delivery with Antibody-Conjugated, Radiolabeled Mesoporous Silica Nanoparticles. *ACS Nano 7*, 9027–9039.

(294) Hu, H., Li, D., Liu, S., Wang, M., Moats, R., Conti, P. S., and Li, Z. (2014) Integrin α$_2$β$_1$ targeted GdVO$_4$:Eu ultrathin nanosheet for multimodal PET/MR imaging. *Biomaterials 35*, 8649–8658.

(295) Lee, H.-Y., Li, Z., Chen, K., Hsu, A. R., Xu, C., Xie, J., Sun, S., and Chen, X. (2008) PET/MRI Dual-Modality Tumor Imaging Using Arginine-Glycine-Aspartic (RGD)-Conjugated Radiolabeled Iron Oxide Nanoparticles. *J. Nucl. Med. 49*, 1371–1379.

(296) Hong, H., Zhang, Y., Engle, J. W., Feng, L., Yang, Y., Nayak, T. R., Goel, S., Bean, J., Theuer, C. P., Barnhart, T. E., Liu, Z., and Cai, W. (2012) *In Vivo* Targeting and Imaging of Tumor Vasculature with Radiolabeled, Antibody-Conjugated Nanographene. *ACS Nano 6*, 2361–2370.

(297) Liu, Z., Cai, W., He, L., Nakayama, N., Chen, K., Sun, X., Chen, X., and Dai, H. (2007) *In vivo* biodistribution and highly efficient tumour targeting of carbon nanotubes in mice. *Nat. Nanotechnol. 2*, 47–52.

(298) Chen, F., Hong, H., Goel, S., Graves, S. A., Orbay, H., Ehlerding, E. B., Shi, S., Theuer, C. P., Nickles, R. J., and Cai, W. (2015) *In Vivo* Tumor Vasculature Targeting of CuS@MSN Based Theranostic Nanomedicine. *ACS Nano 9*, 3926–3934.

(299) Yang, M., Cheng, K., Qi, S., Liu, H., Jiang, Y., Jiang, H., Li, J., Chen, K., Zhang, H., and Cheng, Z. (2013) Affibody modified and radiolabeled gold–Iron oxide hetero-nanostructures for tumor PET, optical and MR imaging. *Biomaterials 34*, 2796–2806.

(300) Wadas, T., Wong, E., Weisman, G., and Anderson, C. (2007) Copper Chelation Chemistry and its Role in Copper Radiopharmaceuticals. *Curr. Pharm. Des. 13*, 3–16.

(301) Leier, S. (2018) Chemoselective bioconjugation reactions of tyrosine residues for application in PET radiochemistry. University of Alberta, Edmonton.

(302) Richer, S., Medina, A., Bergman, C., Pink, D., Raturi, A., Wuest, M., Lin, R., Steinmetz, N., Lewis, J., and Wuest, F. (2017) Smart Tobacco Mosaic Virus-based Nanoparticles for Targeted MolecularImaging of Cancer. *J. Label. Compd. Radiopharm. 23rd International Symposium on Radiopharmaceutical Sciences*, Poster 124, S280.

(303) McKay, C. S., and Finn, M. G. (2014) Click Chemistry in Complex Mixtures: Bioorthogonal Bioconjugation. *Chem. Biol. 21*, 1075–1101.

(304) Schlesinger, J., Rajander, J., Ihalainen, J. A., Ramesh, D., Eklund, P., Fagerholm, V., Nuutila, P., and Solin, O. (2011) Isomerism of [^{64}Cu-NOTA-Bn]-Labeled Radiotracers: Separation of Two Complex Isomers

and Determination of Their Interconversion Energy Barrier Using Ion Pair Chromatography. *Inorg. Chem. 50*, 4260–4271.

(305) Fukukawa, K., Rossin, R., Hagooly, A., Pressly, E. D., Hunt, J. N., Messmore, B. W., Wooley, K. L., Welch, M. J., and Hawker, C. J. (2008) Synthesis and Characterization of Core–Shell Star Copolymers for *In Vivo* PET Imaging Applications. *Biomacromolecules 9*, 1329–1339.

(306) Lazzara, M. J., and Deen, W. M. (2001) Effects of plasma proteins on sieving of tracer macromolecules in glomerular basement membrane. *Am. J. Physiol.-Ren. Physiol. 281*, F860–F868.

(307) Schmidt, M. M., and Wittrup, K. D. (2009) A modeling analysis of the effects of molecular size and binding affinity on tumor targeting. *Mol. Cancer Ther. 8*, 2861–2871.

(308) Arnold, M., Sierra, M. S., Laversanne, M., Soerjomataram, I., Jemal, A., and Bray, F. (2017) Global patterns and trends in colorectal cancer incidence and mortality. *Gut 66*, 683–691.

(309) Wu, K., Zhai, M. Z., Weltzien, E. K., Cespedes Feliciano, E. M., Meyerhardt, J. A., Giovannucci, E., and Caan, B. J. (2019) Non-alcoholic fatty liver disease and colorectal cancer survival. *Cancer Causes Control 30*, 165–168.

(310) Chen, X., Xu, J., Guo, Q., Wang, L., Yang, Y., Guo, H., Gu, N., Zhang, D., Qian, W., Hou, S., Li, J., Dai, J., Guo, Y., and Wang, H. (2016) Therapeutic efficacy of an anti-PD-L1 antibody based immunocytokine in a metastatic mouse model of colorectal cancer. *Biochem. Biophys. Res. Commun. 480*, 160–165.

(311) Smith, A. J., Driman, D. K., Spithoff, K., Hunter, A., McLeod, R. S., Simunovic, M., and Langer, B. (2010) Guideline for optimization of colorectal cancer surgery and pathology. *J. Surg. Oncol. 101*, 5–12.

(312) Siddiqui, A. D., and Piperdi, B. (2010) KRAS Mutation in Colon Cancer: A Marker of Resistance to EGFR-I Therapy. *Ann. Surg. Oncol. 17*, 1168–1176.

(313) Troiani, T., Martinelli, E., Napolitano, S., Vitagliano, D., Ciuffreda, L. P., Costantino, S., Morgillo, F., Capasso, A., Sforza, V., Nappi, A., De Palma, R., D'Aiuto, E., Berrino, L., Bianco, R., and Ciardiello, F. (2013) Increased TGF-α as a Mechanism of Acquired Resistance to the Anti-EGFR Inhibitor Cetuximab through EGFR-MET Interaction and Activation of MET Signaling in Colon Cancer Cells. *Clin. Cancer Res. 19*, 6751–6765.

(314) Edwards, M. S., Chadda, S. D., Zhao, Z., Barber, B. L., and Sykes, D. P. (2011) A systematic review of treatment guidelines for metastatic colorectal cancer. *Colorectal Dis. 14*, e31–e47.

(315) Ida Genta, Enrica Chiesa, Barbara Colzani, Tiziana Modena, Bice Conti, and Rossella Dorati. (2017) GE11 Peptide as an Active Targeting Agent in Antitumor Therapy: A Minireview. *Pharmaceutics 10*, E2.

(316) Langer, R. (1998) Drug Delivery and Targeting. *Nature 392*, 5–10.

(317) Tebbutt, N., Pedersen, M. W., and Johns, T. G. (2013) Targeting the ERBB family in cancer: couples therapy. *Nat. Rev. Cancer 13*, 663–673.

(318) Ono, M., and Kuwano, M. (2006) Molecular Mechanisms of Epidermal Growth Factor Receptor (EGFR) Activation and Response to Gefitinib and Other EGFR-Targeting Drugs. *Clin. Cancer Res. 12*, 7242–7251.

(319) Gil, D., and Schrum, A. G. (2013) Strategies to stabilize compact folding and minimize aggregation of antibody-based fragments. *Adv. Biosci. Biotechnol. 4*, 73–84.

(320) Hossein-Nejad-Ariani, H., Althagafi, E., and Kaur, K. (2019) Small Peptide Ligands for Targeting EGFR in Triple Negative Breast Cancer Cells. *Sci. Rep. 9*.

(321) Vlieghe, P., Lisowski, V., Martinez, J., and Khrestchatisky, M. (2010) Synthetic therapeutic peptides: science and market. *Drug Discov. Today 15*, 40–56.

(322) Song, S., Liu, D., Peng, J., Deng, H., Guo, Y., Xu, L. X., Miller, A. D., and Xu, Y. (2009) Novel peptide ligand directs liposomes toward EGF-R high-expressing cancer cells *in vitro* and *in vivo*. *FASEB J. 23*, 1396–1404.

(323) Zarschler, K., Prapainop, K., Mahon, E., Rocks, L., Bramini, M., Kelly, P. M., Stephan, H., and Dawson, K. A. (2014) Diagnostic nanoparticle targeting of the EGF-receptor in complex biological conditions using single-domain antibodies. *Nanoscale 6*, 6046–6056.

(324) Kuo, W.-T., Lin, W.-C., Chang, K.-C., Huang, J.-Y., Yen, K.-C., Young, I.-C., Sun, Y.-J., and Lin, F.-H. (2015) Quantitative Analysis of Ligand-EGFR Interactions: A Platform for Screening Targeting Molecules. *PLoS ONE* (Lee, J. W., Ed.) *10*, e0116610.

(325) Mickler, F. M., Möckl, L., Ruthardt, N., Ogris, M., Wagner, E., and Bräuchle, C. (2012) Tuning Nanoparticle Uptake: Live-Cell Imaging Reveals Two Distinct Endocytosis Mechanisms Mediated by Natural and Artificial EGFR Targeting Ligand. *Nano Lett. 12*, 3417–3423.

(326) Truebenbach, I., Zhang, W., Wang, Y., Kern, S., Höhn, M., Reinhard, S., Gorges, J., Kazmaier, U., and Wagner, E. (2019) Co-delivery of pretubulysin and siEG5 to EGFR overexpressing carcinoma cells. *Int. J. Pharm. 569*, 118570.

(327) Kotelevets, L., Scott, M. G. H., and Chastre, E. (2018) Targeting PTEN in Colorectal Cancers, in *Targeted Therapy of Colorectal Cancer Subtypes* (Jordan, P., Ed.), pp 55–73. Springer International Publishing, Cham.

(328) Mendes-Pereira, A. M., Martin, S. A., Brough, R., McCarthy, A., Taylor, J. R., Kim, J., Waldman, T., Lord, C. J., and Ashworth, A. (2009) Synthetic lethal targeting of PTEN mutant cells with PARP inhibitors. *EMBO Mol. Med. 1*, 315–322.

(329) Mereniuk, T. R., El Gendy, M. A. M., Mendes-Pereira, A. M., Lord, C. J., Ghosh, S., Foley, E., Ashworth, A., and Weinfeld, M. (2013) Synthetic Lethal Targeting of PTEN-Deficient Cancer Cells Using Selective Disruption of Polynucleotide Kinase/Phosphatase. *Mol. Cancer Ther. 12*, 2135–2144.

(330) Sadat, S., Paiva, I. M., Shire, Z., Morgan, T. D. R., Busheri, F. K., Hall, D. G., Weinfeld, M., and Lavasanifar, A. (2020) Nano-delivery of PNKP inhibitor exhibits synthetic lethality in PTEN-deficient colorectal cancer xenograft mice. *Unpubl. Data*.

(331) Topel, Ö., Çakır, B. A., Budama, L., and Hoda, N. (2013) Determination of critical micelle concentration of polybutadiene-*block*-poly(ethyleneoxide) diblock copolymer by fluorescence spectroscopy and dynamic light scattering. *J. Mol. Liq. 177*, 40–43.

(332) Owen, S. C., Chan, D. P. Y., and Shoichet, M. S. (2012) Polymeric micelle stability. *Nano Today 7*, 53–65.

(333) Ferguson, K. M., Berger, M. B., Mendrola, J. M., Cho, H.-S., Leahy, D. J., and Lemmon, M. A. (2003) EGF Activates Its Receptor by Removing Interactions that Autoinhibit Ectodomain Dimerization. *Mol. Cell 11*, 507–517.

(334) Pettersen, E. F., Goddard, T. D., Huang, C. C., Couch, G. S., Greenblatt, D. M., Meng, E. C., and Ferrin, T. E. (2004) UCSF Chimera—A visualization system for exploratory research and analysis. *J. Comput. Chem. 25*, 1605–1612.

(335) Morris, G. M., Huey, R., Lindstrom, W., Sanner, M. F., Belew, R. K., Goodsell, D. S., and Olson, A. J. (2009) AutoDock4 and AutoDockTools4: Automated docking with selective receptor flexibility. *J. Comput. Chem. 30*, 2785–2791.

(336) Trott, O., and Olson, A. J. (2010) AutoDock Vina: Improving the speed and accuracy of docking with a new scoring function, efficient optimization, and multithreading. *J. Comput. Chem. 31*, 455–461.

(337) Sousa da Silva, A. W., and Vranken, W. F. (2012) ACPYPE - AnteChamber PYthon Parser interfacE. *BMC Res. Notes 5*, 367.

(338) Abraham, M. J., Murtola, T., Schulz, R., Páll, S., Smith, J. C., Hess, B., and Lindahl, E. (2015) GROMACS: High performance molecular simulations through multi-level parallelism from laptops to supercomputers. *SoftwareX 1–2*, 19–25.

(339) Kumari, R., Kumar, R., Open Source Drug Discovery Consortium, and Lynn, A. (2014) *g_mmpbsa*—A GROMACS Tool for High-Throughput MM-PBSA Calculations. *J. Chem. Inf. Model. 54*, 1951–1962.

(340) Bondareva, A., Downey, C. M., Ayres, F., Liu, W., Boyd, S. K., Hallgrimsson, B., and Jirik, F. R. (2009) The Lysyl Oxidase Inhibitor, β-Aminopropionitrile, Diminishes the Metastatic Colonization Potential of Circulating Breast Cancer Cells. *PLoS ONE 4*, e5620.

(341) Lee, C., Kim, J.-S., and Waldman, T. (2004) *PTEN* Gene Targeting Reveals a Radiation-Induced Size Checkpoint in Human Cancer Cells. *Cancer Res. 64*, 6906–6914.

(342) Tseng, W., Leong, X., and Engleman, E. (2007) Orthotopic Mouse Model of Colorectal Cancer. *J. Vis. Exp. 10*, 484–488.

(343) Céspedes, M. V., Espina, C., García-Cabezas, M. A., Trias, M., Boluda, A., Gómez del Pulgar, M. T., Sancho, F. J., Nistal, M., Lacal, J. C., and Mangues, R. (2007) Orthotopic Microinjection of Human Colon Cancer Cells in Nude Mice Induces Tumor Foci in All Clinically Relevant Metastatic Sites. *Am. J. Pathol. 170*, 1077–1085.

(344) Rapic, S., Vangestel, C., Verhaeghe, J., Van den Wyngaert, T., Hinz, R., Verhoye, M., Pauwels, P., Staelens, S., and Stroobants, S. (2017) Characterization of an Orthotopic Colorectal Cancer Mouse Model and Its Feasibility for Accurate Quantification in Positron Emission Tomography. *Mol. Imaging Biol. 19*, 762–771.

(345) Shi, Y., van Steenbergen, M. J., Teunissen, E. A., Novo, L., Gradmann, S., Baldus, M., van Nostrum, C. F., and Hennink, W. E. (2013) Π-Π Stacking Increases the Stability and Loading Capacity of Thermosensitive Polymeric Micelles for Chemotherapeutic Drugs. *Biomacromolecules 14*, 1826–1837.

(346) Danhier, F., Le Breton, A., and Préat, V. (2012) RGD-Based Strategies To Target Alpha(v) Beta(3) Integrin in Cancer Therapy and Diagnosis. *Mol. Pharm. 9*, 2961–2973.

(347) Deen, W. M., Lazzara, M. J., and Myers, B. D. (2001) Structural determinants of glomerular permeability. *Am. J. Physiol.-Ren. Physiol. 281*, F579–F596.

(348) Lawrence, M. G., Altenburg, M. K., Sanford, R., Willett, J. D., Bleasdale, B., Ballou, B., Wilder, J., Li, F., Miner, J. H., Berg, U. B., and Smithies, O. (2017) Permeation of macromolecules into the renal glomerular basement membrane and capture by the tubules. *Proc. Natl. Acad. Sci. 114*, 2958–2963.

(349) Meira, D. D., Nóbrega, I., Almeida, V. H. de, Mororó, J. S., Cardoso, A. M., Silva, R. L. A., Albano, R. M., and Ferreira, C. G. (2009) Different antiproliferative effects of matuzumab and cetuximab in A431 cells are associated with persistent activity of the MAPK pathway. *Eur. J. Cancer 45*, 1265–1273.

(350) Rivera, F., Vega-Villegas, M. E., Lopez-Brea, M. F., and Marquez, R. (2008) Current situation of Panitumumab, Matuzumab, Nimotuzumab and Zalutumumab. *Acta Oncol. 47*, 9–19.

(351) Whittle, J. R., Lickliter, J. D., Gan, H. K., Scott, A. M., Simes, J., Solomon, B. J., MacDiarmid, J. A., Brahmbhatt, H., and Rosenthal, M. A. (2015) First in human nanotechnology doxorubicin delivery system to target epidermal growth factor receptors in recurrent glioblastoma. *J. Clin. Neurosci. 22*, 1889–1894.

(352) Shim, H. (2011) One target, different effects: a comparison of distinct therapeutic antibodies against the same targets. *Exp. Mol. Med. 43*, 539–549.

(353) Jantscheff, P., Terracciano, L., Lowy, A., Glatz-Krieger, K., Grunert, F., Micheel, B., Brümmer, J., Laffer, U., Metzger, U., Herrmann, R., and Rochlitz, C. (2003) Expression of CEACAM6 in Resectable Colorectal Cancer: A Factor of Independent Prognostic Significance. *J. Clin. Oncol. 21*, 3638–3646.

(354) Kim, K. S., Kim, J.-T., Lee, S.-J., Kang, M. A., Choe, I. S., Kang, Y. H., Kim, S.-Y., Yeom, Y. I., Lee, Y.-H., Kim, J. H., Kim, K. H., Kim, C. N., Kim, J. W., Nam, M.-S., and Lee, H. G. (2013) Overexpression and clinical significance of carcinoembryonic antigen-related cell adhesion molecule 6 in colorectal cancer. *Clin. Chim. Acta 415*, 12–19.

(355) Johnson, B., and Mahadevan, D. (2015) Emerging Role and Targeting of Carcinoembryonic Antigen-related Cell Adhesion Molecule 6 (CEACAM6) in Human Malignancies. *Clin. Cancer Drugs 2*, 100–111.

(356) Chiang, W.-F., Cheng, T.-M., Chang, C.-C., Pan, S.-H., Changou, C. A., Chang, T.-H., Lee, K.-H., Wu, S.-Y., Chen, Y.-F., Chuang, K.-H., Shieh, D.-B., Chen, Y.-L., Tu, C.-C., Tsui, W.-L., and Wu, M.-H. (2017) Carcinoembryonic antigen-related cell adhesion molecule 6 (CEACAM6) promotes EGF receptor signaling of oral squamous cell carcinoma metastasis via the complex N-glycosylation. *Oncogene 37*, 116–127.

(357) Zhang, F., Sun, H., Zhang, S., Yang, X., Zhang, G., and Su, T. (2017) Overexpression of PER3 Inhibits Self-Renewal Capability and Chemoresistance of Colorectal Cancer Stem-Like Cells via Inhibition of Notch and β-Catenin Signaling. *Oncol. Res. 25*, 709–719.

(358) Thanki, K., Kushwah, V., and Jain, S. (2015) Recent Advances in Tumor Targeting Approaches, in *Targeted Drug Delivery : Concepts and Design*, pp 41–112. Springer International Publishing, Cham.

(359) Hennink, W. E., Shi, Y., and Van Nostrum, C. F. (2016) Amphiphilic block copolymers for delivery of active agents. *Pat. WO 16/024861*, 1–36.

(360) Xu, C., Li, H., Zhang, K., Binzel, D. W., Yin, H., Chiu, W., and Guo, P. (2019) Photo-controlled release of paclitaxel and model drugs from RNA pyramids. *Nano Res. 12*, 41–48.

(361) Huang, Y.-H., Vakili, M., Molavi, O., Morrissey, Y., Wu, C., Paiva, I., Soleimani, A., Sanaee, F., Lavasanifar, A., and Lai, R. (2019) Decoration of Anti-CD38 on Nanoparticles Carrying a STAT3 Inhibitor Can Improve the Therapeutic Efficacy Against Myeloma. *Cancers 11*, 248.

(362) Carstens, M. G., Jong, P. H. J. L. F. de, van Nostrum, C. F., Kemmink, J., Verrijk, R., Leede, L. G. J. de, Crommelin, D. J. A., and Hennink, W. E. (2008) The effect of core composition in biodegradable oligomeric micelles as taxane formulations. *Eur. J. Pharm. Biopharm. 68*, 596–606.

(363) Aliabadi, H. M., Mahmud, A., Sharifabadi, A. D., and Lavasanifar, A. (2005) Micelles of methoxy poly(ethylene oxide)-*b*-poly(ε-caprolactone) as vehicles for the solubilization and controlled delivery of cyclosporine A. *J. Controlled Release 104*, 301–311.

(364) Hasan, A. A. K., Zisman, T., and Schmaier, A. H. (1998) Identification of cytokeratin 1 as a binding protein and presentation receptor for kininogens on endothelial cells. *Proc. Natl. Acad. Sci. 95*, 3615–3620.

(365) Astern, J. M., Pendergraft, W. F., Falk, R. J., Jennette, J. C., Schmaier, A. H., Mahdi, F., and Preston, G. A. (2007) Myeloperoxidase Interacts with Endothelial Cell-Surface Cytokeratin 1 and Modulates Bradykinin Production by the Plasma Kallikrein-Kinin System. *Am. J. Pathol. 171*, 349–360.

(366) Mahdi, F. (2002) Factor XII interacts with the multiprotein assembly of urokinase plasminogen activator receptor, gC1qR, and cytokeratin 1 on endothelial cell membranes. *Blood 99*, 3585–3596.

(367) Park, J.-H., von Maltzahn, G., Xu, M. J., Fogal, V., Kotamraju, V. R., Ruoslahti, E., Bhatia, S. N., and Sailor, M. J. (2010) Cooperative nanomaterial system to sensitize, target, and treat tumors. *Proc. Natl. Acad. Sci. 107*, 981–986.

(368) Paasonen, L., Sharma, S., Braun, G. B., Kotamraju, V. R., Chung, T. D. Y., She, Z.-G., Sugahara, K. N., Yliperttula, M., Wu, B., Pellecchia, M., Ruoslahti, E., and Teesalu, T. (2016) New p32/gC1qR Ligands for Targeted Tumor Drug Delivery. *ChemBioChem 17*, 570–575.

(369) Zhang, X., Wang, F., Shen, Q., Xie, C., Liu, Y., Pan, J., and Lu, W. (2018) Structure Reconstruction of LyP-1: ^{L}c(LyP-1) Coupling by Amide Bond Inspires the Brain Metastatic Tumor Targeted Drug Delivery. *Mol. Pharm. 15*, 430–436.

(370) Li, C., Wang, Y., Zhang, X., Deng, L., Zhang, Y., and Chen, Z. (2013) Tumor-targeted liposomal drug delivery mediated by a diseleno bond-stabilized cyclic peptide. *Int. J. Nanomedicine 8*, 1051–1062.

(371) Ahmed, M. S., Bin Salam, A., Yates, C., Willian, K., Jaynes, J., Turner, T., and Abdalla, M. (2017) Double-receptor-targeting multifunctional iron oxide nanoparticles drug delivery system for the treatment and imaging of prostate cancer. *Int. J. Nanomedicine 12*, 6973–6984.

(372) Abdalla, M. O., Karna, P., Sajja, H. K., Mao, H., Yates, C., Turner, T., and Aneja, R. (2011) Enhanced noscapine delivery using uPAR-targeted optical-MR imaging trackable nanoparticles for prostate cancer therapy. *J. Controlled Release 149*, 314–322.

(373) Hansen, L., Unmack Larsen, E. K., Nielsen, E. H., Iversen, F., Liu, Z., Thomsen, K., Pedersen, M., Skrydstrup, T., Nielsen, N. Chr., Ploug, M., and Kjems, J. (2013) Targeting of peptide conjugated magnetic nanoparticles to urokinase plasminogen activator receptor (uPAR) expressing cells. *Nanoscale 5*, 8192.

(374) Raghuwanshi, Y., Etayash, H., Soudy, R., Paiva, I., Lavasanifar, A., and Kaur, K. (2017) Proteolytically Stable Cyclic Decapeptide for Breast Cancer Cell Targeting. *J. Med. Chem. 60*, 4893–4903.

(375) Etayash, H., Jiang, K., Azmi, S., Thundat, T., and Kaur, K. (2015) Real-time Detection of Breast Cancer Cells Using Peptide-functionalized Microcantilever Arrays. *Sci. Rep. 5*, 13967.

(376) Ishida, T., Iden, D. L., and Allen, T. M. (1999) A combinatorial approach to producing sterically stabilized (Stealth) immunoliposomal drugs. *FEBS Lett. 460*, 129–133.

(377) Moreira, J. N., Ishida, T., Gaspar, R., and Allen, T. M. (2002) Use of the Post-Insertion Technique to Insert Peptide Ligands into Pre-Formed Stealth Liposomes with Retention of Binding Activity and Cytotoxicity. *Pharm. Res. 19*, 265–269.

(378) Nosova, A. S., Koloskova, O. O., Nikonova, A. A., Simonova, V. A., Smirnov, V. V., Kudlay, D., and Khaitov, M. R. (2019) Diversity of PEGylation methods of liposomes and their influence on RNA delivery. *Med. Chem. Commun. 10*, 369–377.

(379) Torchilin, V. (2008) Antibody-modified liposomes for cancer chemotherapy. *Expert Opin. Drug Deliv. 5*, 1003–1025.

(380) LoRusso, P. M., Weiss, D., Guardino, E., Girish, S., and Sliwkowski, M. X. (2011) Trastuzumab Emtansine: A Unique Antibody-Drug Conjugate in Development for Human Epidermal Growth Factor Receptor 2-Positive Cancer. *Clin. Cancer Res. 17*, 6437–6447.

(381) Lu, S., Morris, V. B., and Labhasetwar, V. (2015) Codelivery of DNA and siRNA via Arginine-Rich PEI-Based Polyplexes. *Mol. Pharm. 12*, 621–629.

(382) Thapa, B., Kc, R., Bahniuk, M., Schmitke, J., Hitt, M., Lavasanifar, A., Kutsch, O., Seol, D.-W., and Uludag, H. (2019) Breathing New Life into TRAIL for Breast Cancer Therapy: Co-Delivery of pTRAIL and Complementary siRNAs Using Lipopolymers. *Hum. Gene Ther. 30*, 1531–1546.

(383) Reddy, J. A., Westrick, E., Santhapuram, H. K. R., Howard, S. J., Miller, M. L., Vetzel, M., Vlahov, I., Chari, R. V. J., Goldmacher, V. S., and Leamon, C. P. (2007) Folate Receptor-Specific Antitumor Activity of EC131, a Folate-Maytansinoid Conjugate. *Cancer Res. 67*, 6376–6382.

(384) Vlahov, I. R., Wang, Y., Kleindl, P. J., and Leamon, C. P. (2008) Design and regioselective synthesis of a new generation of targeted chemotherapeutics. Part II: Folic acid conjugates of tubulysins and their hydrazides. *Bioorg. Med. Chem. Lett. 18*, 4558–4561.

(385) Vlahov, I. R., Vite, G. D., Kleindl, P. J., Wang, Y., Santhapuram, H. K. R., You, F., Howard, S. J., Kim, S.-H., Lee, F. F. Y., and Leamon, C. P. (2010) Regioselective synthesis of folate receptor-targeted agents derived from epothilone analogs and folic acid. *Bioorg. Med. Chem. Lett. 20*, 4578–4581.

(386) Alborzi, S., Lim, L.-T., and Kakuda, Y. (2013) Encapsulation of folic acid and its stability in sodium alginate-pectin-poly(ethylene oxide) electrospun fibres. *J. Microencapsul. 30*, 64–71.

(387) Ariyarathna, I. R., and Karunaratne, D. N. (2015) Use of chickpea protein for encapsulation of folate to enhance nutritional potency and stability. *Food Bioprod. Process. 95*, 76–82.

(388) Ruiz-Rico, M., Pérez-Esteve, É., Lerma-García, M. J., Marcos, M. D., Martínez-Máñez, R., and Barat, J. M. (2017) Protection of folic acid through encapsulation in mesoporous silica particles included in fruit juices. *Food Chem. 218*, 471–478.

Appendix

Experiments for siRNA delivery optimization aiming the down regulating of luciferase protein expression into MDA-MB-231-Luc+ (A) and HCT116-Luc+ (B) cancer cells. Block copolymers with different degree of polymerization (DP) for the caprolactone segments were tested >> DP=10, DP=15, and DP=20. Moreover, two siRNA:polymer ratios were also tested >> 1:16 and 1:32).
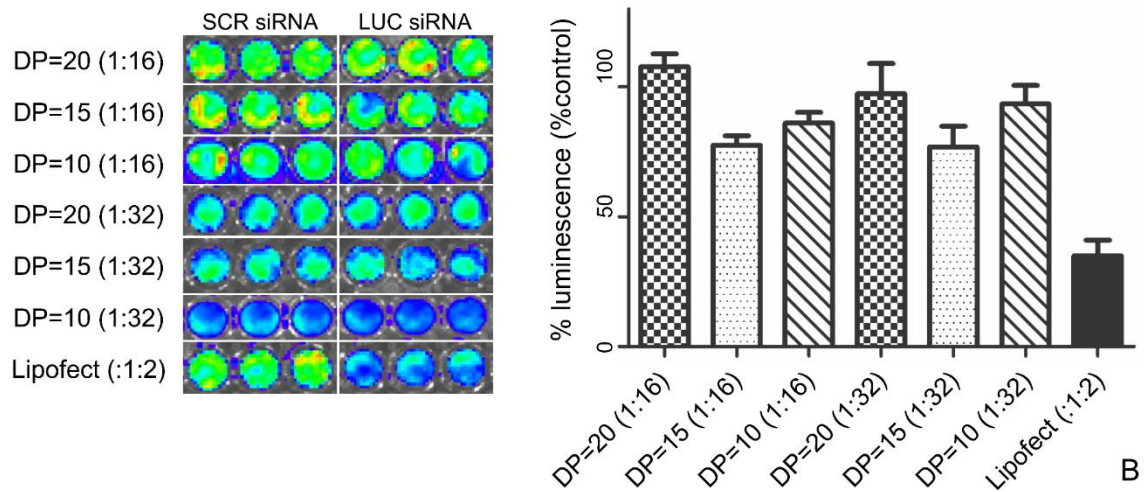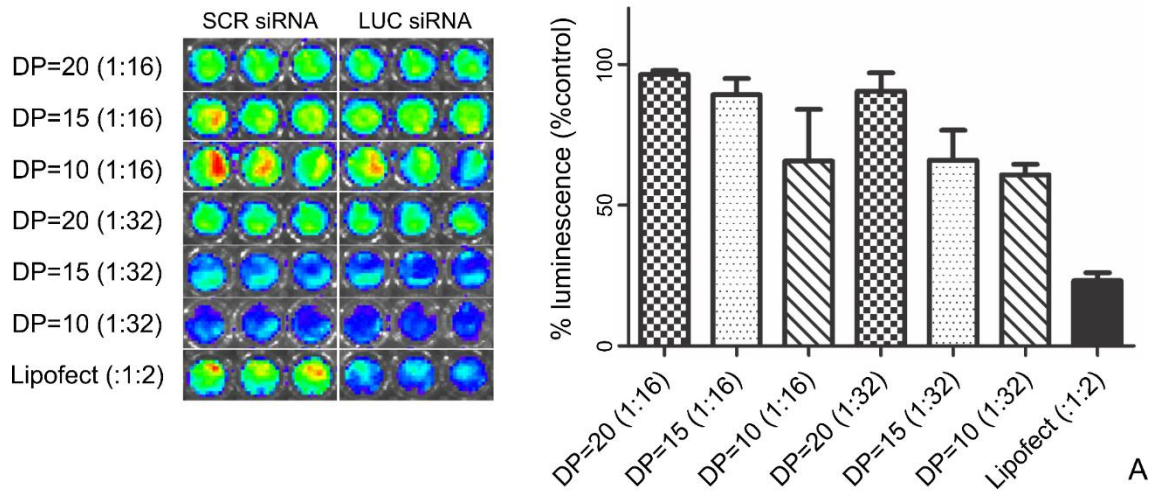
Experiments for siRNA delivery optimization aiming the down regulating of PNKP protein expression into HCT116 CRC cell line. Block copolymers with DP=10, DP=15, and DP=20 for the caprolactone segments were tested. The siRNA:polymer ratio was 1:32.
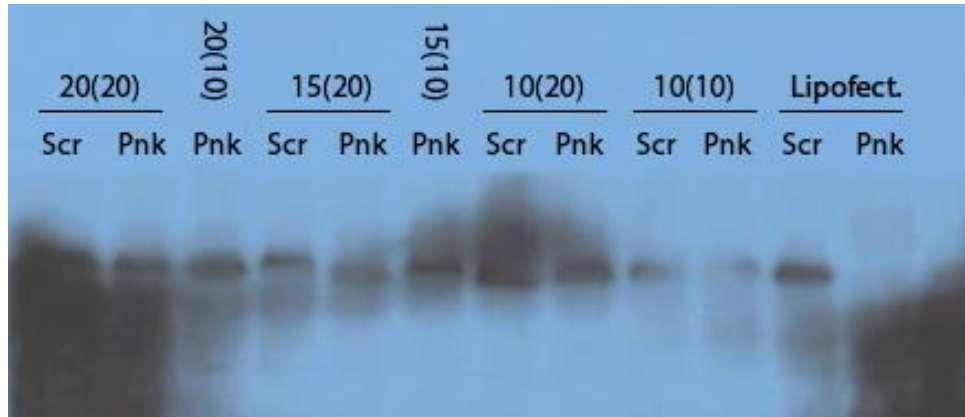
Experiments for siRNA delivery aiming the down regulating of PNKP protein expression into HCT116 CRC cell line. Testing different commercially available transfecting agents. (Available online at the following address: _https://www.rjhbiosciences.com/transfecting-colon-cancer-hct-116-cells-with-rjh-reagents-to-silence-polynucleotide-kinase-3-phosphatase-pnkp-expression_).

Testimonial:

Transfecting Colon Cancer HCT-116 Cells with RJH Reagents to silence Polynucleotide Kinase 3'-Phosphatase (PNKP) Expression

Methodology

Colon cancer HCT-116 cells (ATCC) were seeded and grown in 6-well plates overnight before transfection with siRNA complexes. A specific siRNA against Polynucleotide Kinase 3'-Phosphatase (PNKP; obtained from IDT) was formulated with LipofectamineTM 2000 and the RJH transfection reagents, as recommended by the respective manufacturers (see below for speci?c siRNA:transfection reagent ratios used). As a control, a scrambled siRNA was also formulated with the same reagents and used in cell treatments. The cells were transfected in complete tissue culture medium (DMEM + 10% FBS, 1% Pen/Strep) at siRNA concentration of 50 nM, and allowed to incubate with the formulated siRNAs for additional 2 days. The cells were harvested and processed for western blot analysis according to the established procedures. The blots were stained with an in-house generated polyclonal antibody and visualized using chemoluminescence.
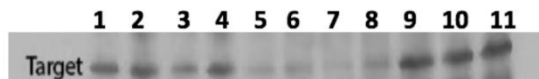
Figure 1

The indicated lanes in the western blot correspond to the following treatments:
1) untreated cells
2) cells exposed to scrambled siRNA/Lipo-2000 (1:2)
3) cells exposed to PNKP siRNA/Lipo-2000 (1:2)
4) cells exposed to scrambled siRNA/Lipo-2000 (1:4)
5) cells exposed to PNKP siRNA/Lipo-2000 (1:4)
6) cells exposed to PNKP siRNA/ALL-Fect (1:6)
7) cells exposed to PNKP siRNA/293-Fect (1:6)
8) cells exposed to PNKP siRNA/Prime-Fect (1:6)
9) cells exposed to scrambled siRNA/ALL-Fect (1:6)
10) cells exposed to siRNA/293-Fect (1:6)
11) cells exposed to scrambled siRNA/Prime-Fect (1:6)

Results

The lanes treated with the scrambled siRNA (#2, 4, 9, 10, and 11) gave band intensities equivalent to the untreated cells (#1), irrespective of the transfection reagent used. With PNKP specific siRNA treatments, significant reductions in the band intensities were evident; LipofectamineTM 2000 at ratio of 1:4 was more potent than 1:2 (siRNA:reagent respectively). All 3 RJH reagents were effective in reducing the PKNP protein levels, indicating the versatility of the reagents. Note that highest silencing was seen with 293-Fect in this study. All 3 RJH reagents, ALL-Fect, 293-Fect and Prime-Fect were effective in silencing the chosen target by 80-90%, based on semi-quantitative densitometric analysis.